Numerical analysis of a fluid droplet subject to acoustic waves

Xuan Meng

Infrastructure & Environment Research Division School of Engineering

Submitted in fulfilment of the requirements for the
Degree of Doctor of Philosophy

The University of Glasgow

October, 2018

Abstract

Efficient and rigorous acoustic solvers that enable high frequency sweep application over a wide range of frequencies are of great interest due to their practical importance in many engineering, physical problems or life science research that involve acoustic radiation, such as engine noise analysis, acoustic simulation in micro-fluidics and the design of lab device, etc. There is room for reduction of cost on experimental systems that can be investigated and optimised through numerical modelling of physical processes on the micro-scale level [297]. The major difficulty that arises is the inconsistency of materials, time scales and fast oscillation nature of the solution that leads to unstable results for conventional numerical methods. However, analytical solutions are infeasible for large problems with complex geometries and sophisticated boundary conditions. Hence, the vital need for efficient solvers.

In this research the development of computational methods for acoustic application is presented. The proposed method is applied to the study of propagating waves in particular to simulate acoustic phenomena in micro-droplet actuated by leaky Surface Acoustic Waves on a lithium niobate ($LiNbO_3$) substrate. Explicitly, we introduce a new computational method for the analysis of fluids subjected to high frequency mechanical forcing. Here we solve the Helmholtz equation in the frequency domain, applying higher order Lobatto hierarchical finite element approximation in H^1 space [10], where both pressure field and geometry are independently approximated with arbitrary and heterogeneous polynomial order. Meanwhile, a time dependent acoustic solver with arbitrary input signals is also proposed and implemented. The development of extended computational methods for the solution of the Helmholtz equation with polychromatic waves is presented, where Fourier transformation is applied to switch the incident wave and solution space from the frequency domain to the temporal domain. Consequently, the implementation and convergence rate of the numerical methods are demonstrated with benchmark problems. The numerical method is an extension of the conventional higher order finite element method and as such it relies on the definition of basis functions. In this

work we implement a set of basis functions using integrated Legendre polynomials (Lobatto polynomial). Two type of basis functions are presented and compared. Therefore, the significant improvements in efficiency is demonstrated using a Lobatto hierarchical basis compared with a Legendre type basis. Moreover, a novel error estimation and automatic adaptivity scheme is outlined based on an existing *a priori* error estimator [256]. The accuracy and efficiency of the proposed object oriented (predefined error level) *a priori* error estimator is validated through numerical assessments on a three-dimensional spherical problem and compared with uniformly h and p adaptivities. The simple and generic features of the proposed scheme allow fast frequency sweeps with low computational cost for multiple frequencies acoustic application. The current finite element approach is executed in parallel with pre-partitioned domain, which guarantees the optimal computational speed with minimal computational effort for large problems. Overall, the benefits of using the proposed acoustic solver is explained in detail.

Finally, we illustrate the model's performance using an example of a micro-droplet actuated by a surface acoustic wave (SAW), which has vast applications in micro-fluidics and micro-rheology at high frequency. Conclusions are drawn, and future directions are pointed out.

The proposed finite element technology is implemented in the University of Glasgow in-house open-source finite element parallel computational code, MoFEM (Mesh Oriented Finite Element Method) [199]. All algorithms and examples are publicly available for download and testing.

List of Figures

List of Tables

Acknowledgement

First of all, I would like to thank my family, my mom (Wu YingQi), my grandparents (Wu YongXiang, Li XingHua) and dad for their support financially and spiritually. My wife has been working hard to support my family, she has the endless enthusiasm to always encourage me from depression, and helped me overcome the difficulties. My mom keeps encouraging me, she is always telling me to go back to study instead of accompanying her. I would not have completed my research without my family.

I would like to give my deepest gratitude to my supervisors: Dr Łukasz Kaczmarczyk and Dr Julien Reboud. I appreciated them for offering me the PhD opportunity in first place. I thank them for their inspiring supervision, their constant encouragement and their thoughtful advice. Their insights into the underlying physics and experiences with research helped me get through the hardest part of my research. This work could not possibly have been completed without their fully supports.

Secondly, I would like to send my gratitude to Professor Chris Pearce, he has been one of my annual progression convenors from the beginning of my study. His in-depth knowledge in many fields of engineering and computational mechanics has been invaluable, along with his corrections and guidance on my research directions.

Thirdly, I would like to give a big special thanks to Professor Jonathan Cooper, for his encouragements and help on finding the topics for my PhD, I would not be able to have started this PhD without his numerous helps.

I would like to thank Dr Andrew McBride for his advises and suggestions on my Thesis. I would like to thank Dr Robert Simpson for his advise and expertise in boundary element methods and acoustic problems.

In addition to these, the school of engineering is like another family to me, I have enjoyed my research life in the office, surrounded by my dear colleagues.

I would like to also thank all the members of the MoFEM team at Glasgow University, school of engineering, for their contribution to the program.

I would like to also thank all the members of the Bioelectronics team at Glasgow University, school of engineering, for their images and data provided based on experiments.

And last but not least, I would like to thank the MOAB and PETSc developer team, for their contribution on the two efficient numerical tools.

Declaration of Authorship

I hereby declare that all the original works in this thesis are carried out by myself under the supervision of Doctor Łukasz Kaczmarczyk and Doctor Julien Reboud, and it is based on research conducted in the Computational Mechanics Group, School of Engineering, The University of Glasgow. The research was taken during the period of Jan 2014 to June 2017. The copyright of this thesis belongs to the author under the terms of the United Kingdom Copyright acts. No part of this article has been submitted elsewhere for any other degree or qualification and it is all my own work unless referenced to the contrary in the text. Parts of this work have been published in the following:

Conferences

Xuan Meng, Łukasz Kaczmarczyk, & Julien Reboud. (2015). Acoustic Hierarchical Finite Element on Unstructured Higher Order Geometry. *In Proceedings of the British Society of Rheology Winter Meeting 2015: Microrheology and Microfluidics*, Wolfson Medical Building, University of Glasgow, UK, 14th - 15th December 2015

[1] Meng Xuan, Reboud Julien, & Kaczmarczyk Łukasz. (2016). Acoustic Wave Propagation in Microfluidic Application with Hierarchical Finite Element. *In Proceedings of the 24th UK Conference of the Association for Computational Mechanics in Engineering (ACME)*, Cardiff University, Cardiff, UK, 31 March - 1st April 2016

[2] Xuan Meng, Łukasz Kaczmarczyk, & Julien Reboud. (2017). A-Priori Error Estimator based Hierarchical p Adaptivity Scheme for Acoustic Problems. *In Proceedings of the 25th UK Conference of the Association for Computational Mechanics in Engineering (ACME)*, Birmingham University, Birmingham, UK, 11th - 13th April 2017

Notation and Nomenclature

Throughout the entire article, we adopt the following symbol and nomenclatures:

Abbreviations

- MoFEM = Mesh oriented finite element method
- MoAB = The Mesh-Oriented datABase
- PDE = Partial Differential Equation
- FEM = Finite element method
- GFEM = Generalized finite element method
- BC = Boundary condition
- BG = Bubnov Galerkin method
- PG = Petrov Galerkin method
- DPG = Discontinuous Petrov Galerkin method
- UWVF = Ultra-weak variational formulation
- PUFEM = Partition unity finite element method
- LS = Least square method
- LU = LU factorization
- ILU = Incomplete LU factorization
- JACOBI = diagonal scaling preconditioning
- PBJACOBI = Point block Jacobi preconditioner
- FGMRES = Flexible Generalized Minimal Residual method
- MUMPS = Multifrontal Massively Parallel Sparse direct Solver
- CG = Preconditioned conjugate gradient (PCG) iterative method
- CGS = Conjugate Gradient Squared method.

- BCGS = Bi-CGStab (Stabilised version of Bi-Conjugate Gradient Squared) method.
- MINRES = Minimum Residual method.
- NURBS = Non-Uniform Rational B-Splines
- PML = Perfectly matched layer
- DOF = Degree of freedoms
- BGT = Bayliss-Gunzburger-Turkel like absorbing boundary condition
- SAW = Surface acoustic wave
- LSAW = leaky surface acoustic wave
- $LiNbO_3$ = Lithium niobate
- IDT = Interdigital transducer

Symbols

- ρ material density
- ξ_f dynamic viscosity of fluid
- $Y = \frac{1}{\sigma} = \rho c$ stands for impedance coefficient
- Ω whole computational domain
- Ω_o domain of obstacle
- Ω_e element domain
- Γ_1 the Lipschitzian boundary of the scatterer
- Γ_∞ the Lipschitzian boundary of the artificial boundary
- ∇ the gradient operator in $\mathbb{R}^3$
- Δ the Laplacian operator in $\mathbb{R}^3$
- n outward normal to the boundaries. $\frac{\partial}{\partial n}$
- $\theta = arctan(y, x)$ in spherical or cylindrical coordinate systems
- $\phi = arctan(\sqrt{x^2 + y^2}/z)$ in spherical coordinate systems
- D diameter of a sphere / cylinder
- R radius of spherical / cylindrical domain
- r the distance of specific point from the origin in spherical or cylindrical coordinate systems
- $\mathbf{r}$ the spatial coordinate vector of points in domain

- $\omega = 2\pi f = \frac{2\pi}{T}$ angular frequency
- $k = \frac{\omega}{c}$ wave number
- $\lambda = \frac{2\pi}{k} = \frac{c}{f}$ the wave length
- $T = \frac{1}{f}$ wave period or signal duration.
- f frequency
- $c = \lambda f = \frac{\lambda}{T} = \frac{\omega}{k}$ wave speed (phase velocity)
- $\mathbf{d}$ the direction vector of incident plane wave
- L_2 square-integrable Sobolev space [230].
- H^1 more enhanced Sobolev space (Hilbert space)
- A_0 A.K.A. Φ_0 amplitude of the wave, real value for signal profile.
- $\Phi = \Phi_I + \Phi_S$ total wave potential
- $\Phi_I = \Phi_0 e^{\mathrm{i}k\mathbf{d}\cdot\mathbf{r}}$ incident wave potential
- Φ_S scattered (radiation) wave potential
- Φ_{Abs} absolute wave potential
- Φ_{fem} & Φ_{ref} Finite element solution and reference solution.
- Φ_a the analytical solution of acoustic potential Φ
- Φ_ϵ plain error in desired norm.
- η relative error in percent in desired norm.

MOAB Terminology

- **volume** computational domain encompasses vertices, curves, and surfaces.
- **blockset** a set which includes geometrical entities
- **edge** an entity representing a path between two end nodes and passes through mid-nodes if they exist in finite element tetrahedral meshset
- **node** an entity in MOAB represents a point in finite element mesh
- **nodeset** an entity set which contains nodes
- **sideset** an entity set which contains triangles

Contents

Chapter 1

Introduction

1.1 Background

1.1.1 Research Topic

Edward Jenner (1749-1823) was the father of modern vaccination and the pioneer of immunisation. He has saved millions of lives and increased the chances of survival from pandemic diseases like smallpox. Nowadays, the pharmaceutical industry conducts numerous experiments and studies each year, not only developing new vaccination techniques, but also new system of diagnosis. In current days, blood samples are taken manually using a syringe, then loaded into a centrifuge and processed for many hours to separate and collect the different parts of the blood sample. Afterwards, these separated parts are tested manually for a possible range of diseases. This whole process is expensive, energy intensive and the diagnostic duration is relatively long. Even worse, in some states of the world, there is lack of such testing facilities (no access to such facilities). Hence, novel diagnostic methods involving the manipulation of microchips and microfludics are open for extended researches. The goal is to integrate a comprehensive analysis and reaction system on small scale surfaces ($\leq 1cm^2$). Micro-fluidics and lab-on-a-chip (LOC) devices guaranteed the further development of portable point-of-care systems that could reduce the complexity of assays to facilitate the limited medical resources in low and middle income countries (LMICs) around the world [334].

The mechanical energy generated by acoustic waves can manipulate cells, fluids, and samples [150]. This poses a challenge to the in-depth study of acoustic waves propagating in fluids, which induces time average mean flow through acoustic streaming. The surface acoustic wave (SAW) device is known as one of the most frequently adopted ultrasonic transducers, which has been previously developed from 1940s [30]. It is used to actuate the micro liquid (droplet or bulk form) sitting on microfluidic chips [330, 335]. The motion of a droplet including jumping [284], pumping [133], jetting or atomisation [306, 258] and mixing [134] are highly depen-

Figure 1.1: Vision for a SAW-actuated device, as a reader and a cartridge to perform medical diagnostics, from Bioelectronics Group UoG.

dent on the acoustic power applied. The fast emerging SAW technologies played an important role in the development of microfluidic systems since the 1990s [292, 299]. The newly developed system of experiments with phononic lattices enables switching of acoustic wavelength as well as the shape of acoustic fields [270]. Through numerical modelling, the distribution of acoustic pressure and stress fields can be observed inside the droplet [188]. Alternatively, the phenomena that occur in physical experiments, like acoustic streaming at low power, water movement, jetting, or even nebulisation of droplets at higher power, can be fulfilled by adjusting the power, frequency of waves and shape of input source, or even the contact angle and height of the droplets [335].

This research lies at the interface between advanced modelling and experimental validation in biomedical engineering applications. Several innovative advances will be presented in the modelling of micro-fluids subject to high frequency acoustic waves necessary to capture their behaviour at micro-scales. The techniques developed will enable us to establish a continuum description, which allows solving problems where the classical time harmonic wave equation is no longer applicable.

There are various numerical simulation methods available to solve physical problems, such as: finite difference method, finite element method, boundary element method, mesh-less finite element method, finite volume method, etc. Due to limited contexts, the specified usages of other methods will not be addressed here, we will focus on only the finite element method in this work. The reason for choosing the finite element method is not merely because of its accuracy, but also for its economical computational cost and widely developed novel schemes like the various Galerkin methods and error estimation techniques.

The advantages of the FEM for solving acoustic problems are:

- Ability to capture complex geometries.
- Flexibility, with the availability of many error estimation techniques and advanced numerical tools.
- Ability to handle the union of different material properties with a proven track-record for stability and robustness.

- Convenient for coupling different physical problems and boundary conditions.

1.1.2 Fluid Mechanics

The original Pascal's Law was proposed based on Blaise Pascal's (1623-1662) experimental results [5]. He interpreted that the pressure applied in a confined incompressible fluid is transmitted equally in all directions within the fluid, in such a way that the initial pressure difference stays the same. It is expressed as:

$$\Delta P = \rho g \Delta h \tag{1.1}$$

where ΔP denotes the hydrostatic pressure given in Pascals unit, ρ is the density of the fluid, Δh is the height of the fluid above a certain level which has been predetermined (here the sign Δ represents the difference between a quantity at different positions, instead of the Laplace operator).

For an incompressible and isotropic Newtonian fluid, Sir Isaac Newton (1642-1727) the well-known scientists from the 17 century, proposed the linear relationship between the shear stress and the shear strain rate of fluids

$$\boldsymbol{\tau} = \mu \frac{\partial \mathbf{u}}{\partial y} \tag{1.2}$$

where $\boldsymbol{\tau}$ is the shear stress of the fluid, μ is a proportionality constant coefficient that representing the shear viscosity of the fluid, and $\frac{\partial \mathbf{u}}{\partial y}$ is the partial derivative of the velocity in the direction y parallel to the direction of shear stress and orthogonal to the direction of flow. Furthermore, a fluid is called non-Newtonian if the viscosity is dependent on the shear rate or the history of shear rate, in which case there is a non-linear relation between the shear strain rate and the shear stress that may involve a time dependant term. In practice, water and air are considered as realistic examples of newtonian fluids while, on the other hand, blood is a good example of non-newtonian fluids.

Daniel Bernoulli (1700-1782) [141] carried on Newton's research on inviscid flow, and derived the famous Bernoulli's principle named after the published book "Hydrodynamica" in 1738 [74]. Roughly speaking, the principle states that for an ideal fluid that has no viscosity (or relatively small value of viscous forces when compared to inertial forces), there exists a negative relationship between the speed of the fluid and the fluid pressure or fluid's potential energy.

In 1757, Leonhard Euler (1707-1783) introduced the Euler equation in his publication [145], which today is identifiable as a simplified version of the Navier-Stokes equation expressing conservation of momentum:

$$\rho \left(\frac{\partial}{\partial t} + \mathbf{u} \cdot \nabla \right) \mathbf{u} - \nabla \cdot \mathbf{T} + \nabla p = \mathbf{0} \tag{1.3}$$

following directly from Newton's second law, where ρ is the fluid density, t is the time, $\mathbf{u}$ is the fluid velocity vector and p and $\mathbf{T}$ are the fluid pressure and viscosity stress respectively.

In 1746, the one-dimensional wave equation describing the propagation of displacements along a string (vibration of string) was proposed by d'Alembert [3]. Subsequently, Euler and Bernoulli discovered the higher dimensional wave equation derived from the conservation of momentum and Bernoulli equation for flow field [224]. In article [92], 36 forms of acoustic wave equation derivations are outlined in specific terms.

The most significant breakthrough in the field of fluid flow was the formulation of the Navier-Stokes equation, named after Navier (1785-1836) and Stokes (1819-1903). The Navier-Stokes (N-S) equation is the culmination of many of the previously mentioned scientistss work, for instance, Newton; Laplace; Lagrange and so on. In the development of N-S equation, Navier first attempted to add a friction term to Euler's equation in 1822. Thereafter, in 1845, Stokes established Stokes law. The N-S equations arose from the application of Newton's second law to fluid motion, together with the assumption of the viscous flow, such that the stress in the fluid is equal to a viscous term (proportional to the gradient of velocity) plus a pressure term.

Osborne Reynolds (1842-1912) is best known for his contribution to the Reynolds number, Reynolds stress and the transition from streamline flow to turbulent fluid flow in pipes [272]. The Reynolds number is the ratio of inertial forces over viscous forces. A more viscous fluid will result in lower Reynolds number, or in other words, an inviscid fluid will have a large Reynolds number. Additionally, Osborne Reynolds introduced Reynolds-averaging, which is a way of separating the flow variables into the time averaged components and fluctuating components. This method can be applied to the Navier-Stokes equations resulting in the Reynolds-averaged Navier-Stokes (RANS) equations. Pertaining to the definition of Reynolds' stress $\rho\overline{u_i u_j}$ with index notation, where ρ is the density of the medium, u_i is the fluctuating velocity in $x_i = [x_1, x_2, x_3]$ coordinates. The stress term was introduced by Reynolds for the first time in 1895 [273]. In recent years, there have been seminal published discussions about the detailed usage of Reynolds' stress in different scenarios, such as: LeBlond, *et al.* in [210] and Lighthill in [216, 219, 217].

1.1.3 Simulation of Surface Acoustic Waves

It is widely accepted that acoustic problems have a vast range of uses in different physical applications and the study of life science. In the context of microfluidic, the applications encompass disease diagnostics, biochemical analysis, food industry, drug delivery, medical science, military, and aid to build the lab-on-chip (LOC) system [270, 89]. Results from numerical experiments can provide insight to the underlying physics of acoustic problems. Here we focus our attention on the development of a computational tool to aid the design of acoustic diagnostic devices (e.g. lab-on-chip). Through the in-depth study of acoustic fields inside a micro droplet, transducer design and related SAW parameters can be identified and improved, while also reducing the uncertainty from the system. Minor physical differences due to parameterization generally might not be observable in physical experiments but can be revealed by micro-scale numerical modelling [72]. Furthermore, numerical modelling is a low cost and economical efficient option. Once the connection between numerical and physical experiments is established, we can perform the

numerical test before setting up experiments with expensive devices [274].

In the pioneering works of Eckart and Lord Rayleigh [139, 268], the motion of fluid flow and the acoustic streaming caused by high intensity sound attenuation was introduced, and has since been further developed in various fields. That acoustic streaming phenomena inside micro liquid actuated by SAW can be used as a driving force to pump liquids was presented in [242, 243], in which the height of the channel and droplet, and amplitude of the waves was considered. In articles [299] and [330], it was also shown that the SAW can be exploited to drive a liquid droplet in a positive direction on a flat surface such as 128 degree Y cut lithium niobate ($LiNbO_3$), where droplets with different viscosities were taken into account.

In recent years, Shiokawa, Matsui and Ueda [291] led experiments regarding the manipulation of liquid droplets by applying SAW. The reaction of the droplets was discovered to be intimately dependent on the material and chemical condition of the solid surface. It was also found that the material from the droplets was ejected due to the strong SAW streaming force. Nonetheless, in their numerical assumptions, the viscosity damping and the internal reflections from solid-fluid interface and fluid-air interface are neglected [292].

Alghane *et al.* [17] applied the finite volume method in OpenFOAM [221] to examine the motion of acoustic waves in a liquid droplet sitting on a $LiNbO_3$ surface. The excitation of the fluid droplet was observed by solving the laminar incompressible Navier-Stokes equations. Furthermore, the article presumed that the SAW propagating inside the substrate and fluid obey certain displacement equations that limited the variation of motion of SAW before it incidents on the fluid object. In [283], two coupled-field analysis are provided. The work discusses the Nyborg's streaming theory and the fluid-solid interaction finite element formulation, it also introduces the idea of the complex SAW number to represent the exponential decay of leaky Rayleigh waves.

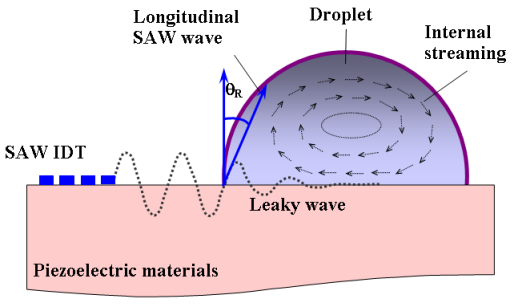

Figure 1.2: Acoustic streaming in liquid droplet caused by SAW [17]

Figure 1.2 illustrates the construction for such a system. A SAW that is generated from the alternating electric field through the interdigital transducer (IDT) will propagate alongside the solid-air interface until it reaches the solid-liquid interface. It will then change its form to that of a leaky SAW due to the longitudinal component of SAW being emitted into the droplet at a Rayleigh angle of Θ_R. The leaky SAW will produce longitudinal waves that will propagate into the fluid, and will further generate a body force acting on the fluid. The attenuation of magnitude of the longitudinal waves depends on the materials of the solid surface as well as the density of the liquid.

In articles [17, 291, 283, 222, 339], the nonlinear body force derived from the Reynolds' stress was mentioned as the main driving force behind the motion of the fluid (e.g acoustic streaming). The phenomenon is a result of the attenuation of the high intensity acoustic energy of the wave propagating in the medium. However, the Reynolds' stress did not result from any computational modelling processes but the assumption of the nonlinear acoustic streaming force. In 2012, Alghane, *et al.* [18] conducted experimental and numerical simulations on confined droplets actuated by SAW. In this work, the relationship between the height of the droplet, attenuation length of the SAW and the streaming flow were investigated, in which the attenuation of SAW was represented in closed form. The deformation of the droplet subject to high power SAW has been investigated by Schindler and his co-authors in [284], but the SAW radiation was neglected inside the droplet.

In 2013, Quintero and Simonetti [260] demonstrated the numerical simulation on how acoustic pressure fields, on the surface of a substrate, propagate into a droplet, with a frequency of 3.5MHz. In the assumption of Rayleigh wave transit to Stoneley wave instead of leaky surface acoustic wave (LSAW) inside the fluid, their model adopt the closed formula extracted from [323]. The coherent structure is not observed from simulation against [17]. The reflected waves from the internal surface of a droplet are not considered in their setup as well as the amount of energy dissipated due to solid-fluid interface.

In most recent times, Collins *et al.* [106] have demonstrated the effectiveness of size-selective particle concentration process from acoustic streaming generated by high-frequency SAW. The numerical solution simulated based on analytical forms have shown good agreement with the experimental results.

In [87], the acoustic pressure field has been numerically observed inside flat droplets actuated by SAW. The multiple reflections from the internal of a droplet shape chaotic cavity is considered. The asymmetry of droplet deformation is confirmed, but the mechanism related to the acoustic pressure and streaming have not yet been fully unveiled [274], the authors consider the viscosity as an important factor to support the existence of acoustic streaming inside a droplet, also a criterion to differentiate various types of acoustic streaming pattern. They presume the cavity of a droplet is an acoustic chaotic field in their setup.

The standard finite element numerical formulation for acoustic problems can be computationally expensive and unable to fully resolve the small wavelengths. Finite element modelling of such a problem also has been limited in its ability to handle the broad range of timescales. In particular, direct time integration techniques are computationally expensive because of the need to resolve the smallest timescale. To avoid the need of solving the 4 dimensional wave equation, the problem is expanded to polychromatic waves via Fourier transformation in both the time and frequency domain with respect to the input signal, solving the 3D Helmholtz equation instead. As shown in Figure 1.3b , it is presumed that the computational domain of a droplet (shown in purple) is a hemispherical shape with some contact angles. A SAW passes along a substrate then interacts with the droplet. To determine the boundary conditions (BCs) on the droplet, the incoming Rayleigh waves are expressed as a closed form analytical equation based on developments from [270] and [320] (1.3a). From a physical perspective, the incident Rayleigh wave carries energies while propagating through the substrate, and starts leaking energies into

the micro fluid. In this presumption, the Rayleigh wave generated from the input signal will be treated as a typical type of standing waves [245, 251]. The Rayleigh SAW travels with speed c_s, the wave speed is proportional to the stiffness of the material of the substrate. However, the wave which leaks to the droplet is a progressive wave, since the speed of the wave in the substrate and fluid are different. As a result, the wave observed in the fluid is a polychromatic wave.

A Fourier transform is then applied to the analytical equation of Rayleigh wave to establish the BCs. This allows us to solve for the propagation of the acoustic waves in the fluid droplet in the frequency domain, consequently it yields the pressure and velocity fields in the fluid which serves to calculate the acoustic Reynolds' stress and radiation force [187]. Theoretically, these nonlinear time averaged stress terms can be applied to solve the problem in the slow time scale using a direct time integration of Navier-Stokes equation for fluid flow to investigate the evolution of the droplet, specifically taking care of the surface tension. This final part of the problem is strongly nonlinear as a result of the evolving droplet geometry. Thus, the calculations of the acoustic wave in the fluid droplet are repeated for each time step at the slow time scale. The physical phenomena of fluid vortices and capillary wave inside the droplet incurred by acoustic actuation and streaming yet remain a challenging area, and have not yet been fully understood [89].

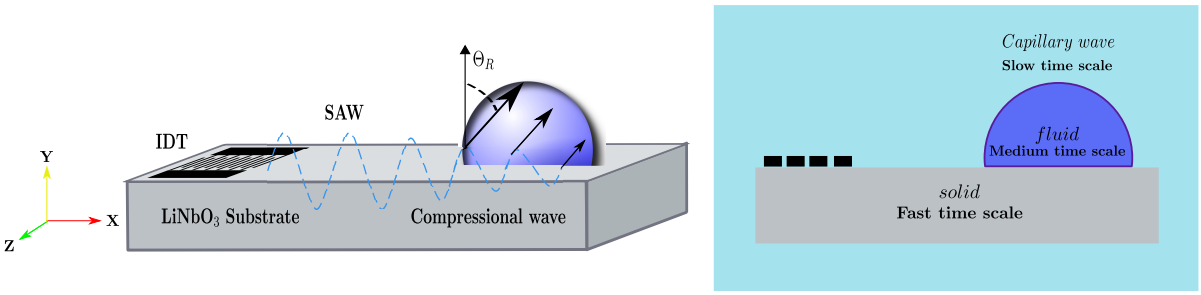

Figure 1.3: Surface acoustic waves application. (a) SAW actuation of a liquid drop on a $LiNbO_3$ piezoelectric surface, showing the leaky Rayleigh waves in the drop. (b) Illustration of the different timescales. grey = fast time scale, blue = medium time scale, Cyan = slow time scale

1.1.4 Numerical Methods on Solving Helmholtz Equation

It is a well known fact that the time harmonic acoustic problems governed by the Helmholtz equation face a major challenge in the non-coercive nature associated with extreme high frequencies [96]. Either its conditioning or its complexity will lead to intolerable computational costs. Many techniques and numerical methods have been developed and devised to tackle this issue for decades, such as least square finite element methods [166, 247, 313], discontinuous Galerkin method [146], the partition of unity methods [46], ultra-weak variational formulations [96, 178, 175, 97], and the higher-order finite element method which will be discussed in following chapters [183]. However, many of the methods suffer from ill-conditioning of the problem with fine mesh, instability of the system or the high computational costs arisen

from the complexity of the formulation.

In 2008, a two dimensional Helmholtz problem was solved on square domain near the scatterer by a novel locally enriched finite element method [301]. The idea behind is to enrich the local approximation basis by oscillatory functions. The proposed method proved the planar wave basis and provided accurate results near the scatterer, while the Bessel functions perform better in far fields. Furthermore, the required degrees of freedom per wavelength for accurate results with the proposed method are far less than the rule of thumb (10 nodal points per wavelength). Consequently, a hybrid combination of Bessel and plane wave basis for local enrichment are expected to deliver efficient calculation for the Helmholtz equation solved on large computational domain [207]. This type of method is categorised as the Trefftz type method, and originally introduced by Melenk and Babuška [232].

Generally speaking, the Trefftz methods exploit the *a priori* knowledge about the local behaviour of the solution function, and thus enrich the approximation spaces by well selected enrichment functions for the Helmholtz operator (e.g. spherical plane wave functions or Bessel functions) [207, 232]. The conditioning of the problem will be ultimately dependent on the chosen enrichment function space [43]. The efficiency of the partition of unity finite element method (PUFEM) method over the conventional FEM has been identified by Laghrouche *et al* in [203], through the specified angle of incidence for plane wave basis. Further in 2009, Huttunen *et al.* [176] have compared PUFEM with the ultra weak variational formulation (UWVF) on singular problem of L shaped domain. In later years, the partition of unity method has been further developed in two and three dimensional problems [204, 203, 201]. On the other hand, Lagrange multipliers applied on edges of elements enhanced the continuity of the solution. This technique can be coupled with wave solution based shape functions which leads to the reduction of the number of degrees of freedom (DOFs) compared to conventional Lagrange finite element methods[146, 147, 311]. In [205], the method is applied to solve Helmholtz problems with piecewise constant wavenumbers in the computational domain.

Alternatively, higher order finite element methods are proved to be efficient for solving the wave problems governed by the Helmholtz equation if accurate solutions are sought [103, 135, 72, 253, 288]. In essence, the hierarchical finite element basis can minimizes the computational costs associated with conventional higher order approximation basis, while further increasing the flexibility and scalability of approximation spaces. It should be kept in mind that the hierarchical higher order FEM can be coupled with various Galerkin methods and Trefftz methods. Since the higher order finite element method involves localised p enrichments, a goal oriented adaptivity scheme based on sufficient local error estimates can be devised to mitigate the dispersion effect and provide exponential convergence rate.

In this thesis we mainly focus on the acoustic part of the acoustic-fluid interaction problem for both monochromatic and polychromatic waves. First of all, a complete list of errors involved in numerical calculation are considered, and studied in edge elements. The stringent definition of qualified error estimator is then discussed. Secondly, the FEM solver for elliptic PDEs within the mesh oriented finite element method code (MoFEM) is developed, examples of thermal conductive problems are solved. Finally, numerical results are compared with commercial software (presented in Appendix).

In what follows, we build up the Helmholtz operator based on previous developed programming strategies (associated with elliptic type PDE), and then implement the relative L_2 and H_1 error estimation norms together with five benchmark examples. Initially, the problem of wave-guide and a plane wave impinging on the sound hard surface of a cylinder are considered, where solution convergence is studied for both geometry and multiple physical fields. Moreover, the numerical efficiency and accuracy of the *hp*-adaptivity in the context of the Helmholtz equation are investigated. The application of hierarchical finite element approximation together with generalized Duffy transformation drastically improves the computational efficiency and accuracy of the acoustic solver, while removing the singularity and uncertainty from numerical integration techniques [10, 137]. Subsequently, the problem of SAW actuation of a fluid droplet is considered. Using hierarchical finite element approximation basis (Lobatto and Legendre) on unstructured meshes [10], both acoustic potential (pressure) field and geometry are independently approximated with arbitrary and heterogeneous polynomial order.

In detailed exposition, the Rayleigh wave propagating on a SAW device medium can be regarded as a plane wave problem [291], which can be resolved with time-harmonic damped wave equation. Furthermore, a closed form leaky SAW is derived based on results and information from [270] and [320]. In our procedure, arbitrary signals can be applied to the medium. Analysis can be done in either frequency or time domain. Moreover, Reynolds' stress is retrieved from the acoustic velocity by taking unsteady part of the gradient of the acoustic potential multiplied by the density. In the sequel, the problem was expanded to polychromatic waves via Fourier transformation in both spatial domain and frequency domain with respect to the input signal. The acoustic pressure distribution inside a droplet is observed by manipulating the physical properties of the modelling, in order to further understand the underlying physics of the application.

1.2 Thesis Outline

The entire thesis is organized in 9 Chapters. It is outlined as follows:

Chapter 1 presents a general introduction and discussion on the historical background and fluid mechanics of current research. The main computational tools used throughout the thesis are also provided. In the $2nd$ Chapter, the derivation and formulation of the governing equations that describe acoustic waves propagating in an isotropic medium are explained in details. The different types of acoustic physical fields and waves with various phases are presented respectively, two types of incident waves and time dependant properties are included. In Chapter 3, the merits and limitations of hierarchical basis over conventional finite element shape functions are provided, as well as a brief introduction to modern refinement techniques. Then, the significant features of hierarchical Legendre type approximation basis are expounded in details. Moreover, the derivation process and implementation procedure of Lobatto basis is finally presented with tetrahedron elements.

Chapter 4, first, comprehensively introduces all type of errors occurring while solving practical physical problems. Secondly, various Galerkin methods associated

with finite element analysis are briefly explained. The criterion of qualified error estimator as well as the description of various type of error estimation techniques are presented in the following sections, which include *a priori* and *a posteriori* error estimators. The numerical accuracy and efficiency of existing error estimators are examined and demonstrated for elliptic type operator. The idea of error estimation on one dimensional elliptic type problems can be extended to three dimensions.

In Chapter 5, the governing equation of time harmonic convected wave equation and relevant boundary conditions are reviewed. The linear system of equations derived from variational formulation are given next, which is ready to be solved. The measurements of dispersion error and relative error are then provided to test the feasibility and accuracy of the finite element system of linear equations. In the next section, both monochromatic waves and arbitrary polychromatic input signals with time dependant solver are proposed and implemented in the acoustic solver. Finally, numerical assessments are presented based on finite element results from four benchmark problems, in order to demonstrate the performance of the proposed solver.

In Chapter 6, the distributed memory parallel computation algorithm, complex-real transformation and generalized Duffy transformation integration are proposed and implemented respectively, in order to alleviate the factorization memory during matrix evaluation process. The measurements to assess the rigorousness and robustness of the proposed algorithms are introduced and tested, such as: efficiency, speedup and the conditioning of the system matrix, etc. with the current solver. The superior property of p adaptivity with current settings are demonstrated based on previous numerical results.

In what follows, the *a priori* error estimator is introduced for Helmholtz type problems in Chapter 7. The error estimator is tested in both one, two and three dimensions, and its accuracy and rigorousness are established. Moreover, the proposed error estimator is coupled with automatic p adaptivity scheme, its performance is assessed through comparison with uniform h & p adaptivity on benchmark problems. All results are validated with two and three dimensional benchmark examples.

In the $8th$ Chapter of this thesis, initially, applications of micro-droplet actuated by SAW propagating on $LiNbO_3$ substrate are presented, with closed form of Rayleigh wave (SAW). The acoustic radiation pressure and Reynolds' stress are introduced. Then, the numerical simulations are conducted with various initial physical parameters, the shape and material of droplet are changed constantly to encompass different experimental scenarios. Comparison is made, and the novelty of the current method is demonstrated.

In the final Chapter, conclusions are made, and directions for future works are recommended.

1.3 Computational Tools

There are many computational tools available. In order to construct a numerical tool for analysis of a micro-fluid subjected to acoustic waves in three dimension, here the following softwares were used:

1. MoFEM: A mesh oriented finite element parallel computation software, it uses the hierarchical shape functions ([10, 295]) with arbitrary and heterogeneous orders as well as the automatic h & p refinement, Legendre, Jacobi and Lobatto basis are implemented. Comprehensive solution spaces available are L_2, H^1, $H(div)$ and $H(curl)$. (See Appendix A.1-A.19 for definition)

2. PETSc: A portable multi-processor scientific application designed to solve the partial differential equations raised in various physical problems, (e.g, linear system of equations like $Ax = b$) vast amount of solvers and pre-conditioners are available (e.g. FGMRES).

3. MOAB: A mesh oriented data base adopted in MoFEM, aimed to store meshes, organise and retrieve the mesh data.

4. Cubit: A graphical user interface 3D mesh generation software. All mesh data generated by Cubit are stored into Moab.

5. Paraview: The post-processing software used to visualize the mesh and the solution fields observed.

6. Matlab: Matlab can be used to solve the small to medium scale system of linear equations, and the edge element error analysis can be done within Matlab once the results are extracted from Mofem and translated into a readable file for Matlab.

7. Docker: Open platform provides container enables MoFEM users and developers to execute any physical applications across arbitrary platforms without the burden of reimplementation, rebuild.

Chapter 2

The Derivation of Acoustic Wave Equations

In the previous chapter, the origins of fluid mechanics were briefly introduced and described with Euler equations. However, the underlying motions and physics of acoustic waves inside fluids still remain unknown.

In this chapter, the governing equations of an inviscid fluid in linear motion are introduced and used, together with the assumption of irrotationality and Bernoulli's equation, to derive the convected homogeneous wave equation with unknown acoustic velocity potential. Furthermore, the linearised Euler equation is taken as the basis from which a convected wave equation with an acoustic pressure field as an unknown is derived. At the last stage, the wave equation is then simplified to give a Helmholtz equation under the assumption of a time harmonic wave in the spatial domain. Finally, the various physical fields associated with different types of waves are briefly explained.

2.1 Mathematical Formulation

Theoretically, every non-dimensional total physical field of fluid can be decomposed into two parts, namely the base-flow (steady part) and the perturbation parts, such as the pressure field: $p_T = p + p_0$. In this derivation, the notation $_T$ means the total quantity.

2.1.1 The Basic Conservation Equations

The basic equations that describe the motion of a fluid encompass two parts: the conservation of mass and momentum terms at the fluid parcel level. To be more precise, the compressibility of a fluid introduces an additional term related to thermal

dynamics. The conservation of mass is defined as:

$$\frac{\partial \rho_T}{\partial t} = -\nabla \cdot (\rho_T \mathbf{u}_T) \tag{2.1}$$

which describes the mass flux over (flow into and leave) a fluid body in the absence of external forces. The notation ρ_T denotes the total density of the fluid. And the momentum equation is defined as:

$$\rho_T \left[\frac{\partial \mathbf{u}_T}{\partial t} + (\mathbf{u}_T \cdot \nabla)\mathbf{u}_T \right] = \nabla \cdot \boldsymbol{\sigma} \tag{2.2}$$

the total field of density ρ_T, fluid velocity $\mathbf{u}_T$ and stress tensor $\boldsymbol{\sigma}$. If we consider the rate of change of a given quantity within a fluid body as a function of position, we thus introduce the material (substantive) derivative:

$$\frac{D\rho_T}{Dt} = \frac{\partial \rho_T}{\partial t} + u\frac{\partial \rho_T}{\partial x} + v\frac{\partial \rho_T}{\partial y} + w\frac{\partial \rho_T}{\partial z} = \frac{\partial \rho_T}{\partial t} + \mathbf{u}_T \cdot \nabla \rho_T \tag{2.3}$$

where $\mathbf{u} = [u, v, w]$ is the velocity vector. And the material derivative builds relationship between Lagrangian and Eulerian descriptions of fluid motion. Hence, the conservation of mass equation can be rewritten in the form:

$$\frac{D\rho_T}{Dt} = -\rho_T \nabla \cdot \mathbf{u}_T \tag{2.4}$$

and the conservation of momentum:

$$\rho_T \frac{D\mathbf{u}_T}{Dt} + \rho_T(\mathbf{u}_T \cdot \nabla)\mathbf{u}_T - \nabla \cdot \mathbf{T}_T + \nabla p_T = \mathbf{0} \tag{2.5}$$

where $\mathbf{T}_T$ is the viscous stress tensor. In case of incompressible fluid, the term $(\mathbf{u}_T \cdot \nabla)\mathbf{u}_T = \nabla \cdot (\mathbf{u}_T \otimes \mathbf{u}_T) = \mathbf{0}$. In the assumption of an ideal flow at low density and pressure with moderate temperature [92] Thus, the thermodynamics of an ideal fluid can be expressed as the equation of state:

$$\frac{Dp_T}{Dt} - \left(\frac{\partial p_T}{\partial \rho_T}\right)_s \frac{D\rho_T}{Dt} = \left(\frac{\partial p_T}{\partial s}\right)_{\rho_T} \frac{Ds}{Dt} \tag{2.6}$$

Equation (2.6) is defined on the basis of a moderate temperature, and the subscript s is the entropy [92]. It is envisaged that the entropy of a fluid element does not change with time, thus yields $\frac{Ds}{Dt} = 0$ [92]. And the adiabatic speed of sound is: $c_T^2 = \left(\frac{\partial p_T}{\partial \rho_T}\right)_s$, in an isentropic (adiabatic and reversible) ideal fluid can be rewritten as:

$$c_T^2 = \left(\frac{\partial p_T}{\partial \rho_T}\right)_s = \gamma \frac{p_T}{\rho_T} \tag{2.7}$$

where γ is the heat capacity ratio. Combining the equation of state (2.6) with expression (2.7) and the equation of mass (2.4), the equation of state is reduced to:

$$\frac{Dp_T}{Dt} = -\rho_T c_T^2 \nabla \cdot \mathbf{u}_T \tag{2.8}$$

which describes the conversation of energy [29]. Thus, the full set of Euler equations comprises the mass Eqn. (2.1), the momentum Eqn. (2.5), and the equation of state (2.8).

2.1.2 Linearised Bernoulli Equation

The physical fields represented in the Euler equations can be expressed in two parts: a steady mean flow part (the base flow quantity) and an unsteady perturbation part. Both the steady and unsteady parts of each field are substituted into the Euler equations. Therefore, the steady Euler equations for the base flow are described as:

$$\nabla \cdot (\rho_0 \mathbf{u}_0) = 0 \tag{2.9a}$$

$$\nabla p_0 + \rho_0 (\mathbf{u}_0 \cdot \nabla)\mathbf{u}_0 + \rho_0 \frac{D\mathbf{u}_0}{dt} = 0 \tag{2.9b}$$

$$\nabla p_0 \cdot \mathbf{u}_0 + \rho_0 c_0^2 \nabla \cdot \mathbf{u}_0 = 0 \tag{2.9c}$$

for the inviscid incompressible flow. Here the material derivative for the base flow: $\frac{D}{dt} = \frac{\partial}{\partial t} + \mathbf{u}_0 \cdot \nabla$ is introduced. The unsteady part of linearised Euler equations are:

$$\frac{D\rho}{dt} + \mathbf{u} \cdot \nabla \rho_0 + \rho_0 \nabla \cdot \mathbf{u} + \rho \nabla \cdot \mathbf{u}_0 = 0 \tag{2.10a}$$

$$\nabla p + \rho_0 \frac{D\mathbf{u}}{dt} + \rho_0 \left(\mathbf{u} \cdot \nabla\right) \mathbf{u}_0 + \rho \left(\mathbf{u}_0 \cdot \nabla\right) \mathbf{u}_0 = 0 \tag{2.10b}$$

$$\nabla p_0 \cdot \mathbf{u} + \frac{Dp}{dt} + \rho_0 c_0^2 \nabla \cdot \mathbf{u} + \rho_0 c^2 \nabla \cdot \mathbf{u}_0 = 0 \tag{2.10c}$$

which consists of three unknowns. The solutions of the first set of equations (2.9) are commonly used as input in the second set (2.10) of Euler equations.

2.1.3 Convected Wave Equation

The linearised Euler equations are generally too complex and computationally expensive to solve, as they contain three unknown functions (potentially five). Since thermal effects, such as heating or damping are proportional to $\gamma - 1$, where γ here represents the adiabatic index (heat capacity ratio), they are extremely weak in liquid [110]. In the absence of thermal energy exchange, and neglecting the viscosity of fluid and the perturbation of the base field, we can further simplify the Bernoulli's equation and identify it as a particular form of momentum Eqn. (2.5). The Bernoulli's equation describes the velocity potential, velocity and pressure of a fluid element travelling along a streamline. Under the assumptions of irrotational, inviscid and unsteady flow where $\mathbf{u} = \nabla\Phi$, the linearised Bernoulli's equation is defined as:

$$\frac{\rho_0}{c_0^2}\frac{\partial \Phi}{\partial t} + \frac{\rho_0 \mathbf{u}_0}{c_0^2} \cdot \nabla\Phi + \rho = 0 \tag{2.11}$$

where the full derivation which is omitted here can be found in [264]. The linearised Euler equations can describe both steady and perturbed parts of the fluid field. The

wave equation (the celebrated d'Alembert equation) can be derived by substituting Eqn. (2.11) into the conservation of mass Eqn. (2.10a):

$$\frac{\rho_0}{c_0^2}\frac{D^2\Phi}{dt^2} - \nabla\cdot(\rho_0\nabla\Phi) + \frac{\rho_0}{c_0^2}\frac{D\Phi}{dt}\nabla\cdot\mathbf{u}_0 = 0 \tag{2.12}$$

In the case of an incompressible flow, the velocity field is divergence free, and the acoustic potential wave equation is rewritten as:

$$\frac{D^2\Phi}{dt^2} - c_0^2\Delta\Phi = 0 \tag{2.13}$$

for which the solution function can be either plane or spherical waves. The material derivative under time harmonic assumption is defined as: $\frac{D}{dt} = \mathrm{i}\omega + \mathbf{u}_0\cdot\nabla$. The resulting wave equation enables computationally efficient solutions for various acoustic fields at high frequency compared with the linearized Euler equation.

2.1.4 Time Harmonic Helmholtz Governing Equations

Under the assumption of a time harmonic wave, the homogeneous wave equation for the propagation of acoustic potential in an ideal medium is

$$\nabla^2\Phi(\mathbf{r},t) = \frac{1}{c^2}\frac{\partial^2\Phi(\mathbf{r},t)}{\partial t^2} \tag{2.14}$$

the subscript $_0$ is dropped due to assumption of uniform flow. $\mathbf{r}$ is the position vector and c is the wave speed. Where the time and frequency dependent solution can be written in the form:

$$\Phi(\mathbf{r},\omega) = \int_{-\infty}^{\infty}\Phi(\mathbf{r},t)e^{\mathrm{i}\omega t}dt \tag{2.15}$$

through Forward Fourier transformation. ω is the angular frequency and i is the imaginary number when it is not a subscript. c denotes the speed of the wave propagating in the medium which depends on the material properties. Simultaneously,

$$\Phi(\mathbf{r},t) = \frac{1}{2\pi}\int_{-\infty}^{\infty}\Phi(\mathbf{r},\omega)e^{-\mathrm{i}\omega t}d\omega \tag{2.16}$$

through the Backward FT. Hence, substituting (2.16) into (2.14) we get

$$\frac{1}{2\pi}\int_{-\infty}^{\infty}\Delta\Phi(\mathbf{r},\omega)e^{-\mathrm{i}\omega t}d\omega - \frac{1}{c^2 2\pi}\int_{-\infty}^{\infty}\frac{\partial^2\Phi(\mathbf{r},\omega)}{\partial t^2}e^{-\mathrm{i}\omega t}d\omega = 0 \tag{2.17}$$

From the above we can identify that:

$$\Phi(\mathbf{r},t) = \Phi(\mathbf{r},\omega)e^{-\mathrm{i}\omega t} \tag{2.18}$$

which yields the steady part of the wave equation, the so called scalar Helmholtz equation. The existence and uniqueness of the Helmholtz equation solution has been demonstrated in the 1950s [107, 211, 172]. Thanks to the lower dimensionality of the Helmholtz equation compared to the wave equation, we can retrieve the

time dependent solution by simply applying the inverse Fourier transformation to the solution of the H^1 elliptic Helmholtz equation. Hence, the steady part of the homogeneous wave equation for the propagation of acoustic waves in an isotropic, ideal medium is defined as:

$$(\Delta + k^2)\Phi(\mathbf{r}) = 0, \quad k = \frac{\omega}{c} \text{ in } \Omega \tag{2.19}$$

where $k \in \mathbb{C}$ is referred to as the acoustic wave number. It can be expressed in the form $k = k_r(1 + i\delta)$, where δ refers to the loss tangent and k_r is the real part of the wavenumber [234]. In essence, it represents the number of amplitudes per 2π length. Consequently, $\Omega \subset \mathbb{R}^3$ is the computational domain. In the case of a homogeneous isotropic medium, such as glass, c is taken as a constant. $\Phi(\mathbf{r})$ will be replaced by Φ in some cases from now on for brevity. Any Φ that satisfies Eqn. (2.18) represents an acoustic potential, and so by the principle of superposition, does any sum over Φ [281].

2.2 Acoustic Waves and Physical Fields

2.2.1 Acoustic Fields

If solving for the above equation results in an acoustic potential Φ, since the components of the velocity $(m \cdot s^{-1})$ vector satisfy the scalar wave equation [138], the velocity field of the acoustic wave can be retrieved from the gradient of the acoustic potential as:

$$\mathbf{u} = \nabla\Phi \tag{2.20}$$

and the acoustic pressure (Pascal) is given by:

$$p = -\mathrm{i}\omega\rho\Phi \tag{2.21}$$

2.2.2 Polychromatic Wave

The polychromatic wave can be expanded as a sum of monochromatic waves through the use of the Fourier transform. At any point $\mathbf{r}$ in space, there exists an acoustic potential function $\Phi(\mathbf{r}, t)$ as a superposition integral of time harmonic waves at different amplitudes, frequencies and phases.

$$\Phi(\mathbf{r}, t) = \frac{1}{2\pi}\int_{-\infty}^{\infty} \Phi(\mathbf{r})e^{-\mathrm{i}\omega t}d\omega \tag{2.22}$$

2.2.3 Acoustic Intensity

The acoustic intensity $I(\mathbf{r})$ is the acoustic power per unit area $(W \cdot m^{-2})$, which is given by [281] :

$$I(\mathbf{r}) = 2\langle\Phi^2(\mathbf{r}, t)\rangle \tag{2.23}$$

where the notation $< \cdot >$ denotes the average of time interval over one acoustic wave period but less than the whole time duration of the pulse wave. Thus, the acoustic power $P(t)$ (W) crossing into an area S perpendicular to the propagation direction of the acoustic wave is defined as:

$$P(t) = \int_S I(\mathbf{r}, t) dS \tag{2.24}$$

And the acoustic energy (Joules) observed in a given period is as follows:

$$E(t) = \int_t P(t) dt \tag{2.25}$$

Since $\Phi(\mathbf{r}, t) = \Phi(\mathbf{r}) e^{\mathrm{i}2\pi f t}$ for monochromatic time harmonic waves,

$$2\Phi^2(\mathbf{r}, t) = 2\Phi^2(\mathbf{r})[\cos(\omega t) + \mathrm{i}\sin(\omega t)] \tag{2.26}$$

where it is seen that the intensity of a monochromatic wave is equal to the square of the absolute value of its complex amplitude, and that it is time independent.

The acoustic intensity for a polychromatic wave is given by [281] as:

$$\begin{aligned} I(\mathbf{r}, t) &= 2\langle \Phi^2(\mathbf{r}, t) \rangle = \\ &= 2 \left\langle \left\{ \frac{1}{2} \left[\Phi(\mathbf{r}, t) + \Phi^*(\mathbf{r}, t) \right] \right\}^2 \right\rangle \\ &= \frac{1}{2} \langle \Phi^2(\mathbf{r}, t) \rangle + \frac{1}{2} \langle \Phi^{*2}(\mathbf{r}, t) \rangle + \langle \Phi(\mathbf{r}, t) \Phi^*(\mathbf{r}, t) \rangle \\ &= |\Phi(\mathbf{r}, t)|^2 \end{aligned} \tag{2.27}$$

where it has been assumed that the wave is quasi-monochromatic with central frequency f_0 and spectral width $\Delta f \ll f_0$, and that the time average operation $\langle \cdot \rangle$ is taken over a duration longer than one cycle $\frac{1}{f_0}$ but shorter than $\frac{1}{\Delta f}$. Pertaining to Eqn. (2.16), the oscillation of the first two terms in Eqn.(2.27) has been averaged out due to the fact that their frequencies are approximately $2f_0$ and $-2f_0$ respectively. The third term has a frequency difference of the order of $\Delta f \ll f_0$ which varies slowly with the time averaging operation. Therefore, the acoustic intensity for polychromatic waves is the same as for monochromatic waves, and is the absolute squared value of acoustic potential function.

2.2.4 The Plane Wave Function

The complex amplitude plane wave is a solution of the Helmholtz equation and has the following form:

$$\Phi(\mathbf{r}) = A_0 e^{-\mathrm{i}k\mathbf{n}\cdot\mathbf{r}} e^{-\mathrm{i}\omega t} \tag{2.28}$$

where A_0 is the complex envelope or amplitude, and the wavenumber k can be vector-valued $\mathbf{k}$ if $\mathbf{n}$ is a scalar. The plane wave is an idealization of spherical waves propagating in a far field. A plane wave propagating in the direction $\mathbf{n}$ is a periodic function of $\mathbf{n}$ and t with spatial period λ and temporal period $T = \frac{1}{f}$.

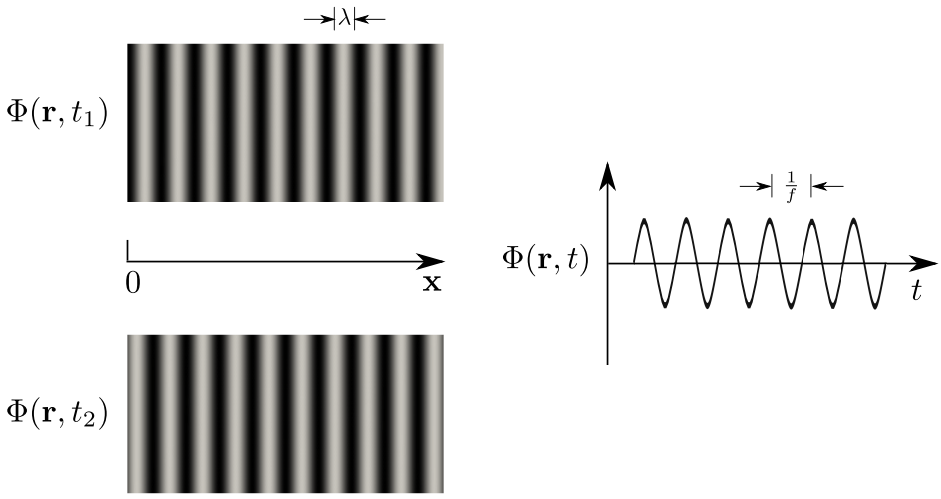

Figure 2.1: The illustration of a plane wave function, travelling in the x direction as periodic function of x with spatial period (wavelength) λ and a periodic function of t with temporal period $\frac{1}{f}$

2.2.5 The Spherical Wave Function

The spherical wave is also a solution function of the Helmholtz equation and has the generic form:

$$\Phi(\mathbf{r}) = \frac{A_0}{\mathbf{r} - \mathbf{r_0}} e^{-i\mathbf{k}\cdot[\mathbf{r}-\mathbf{r_0}]} \tag{2.29}$$

that satisfies the Green's functions, where $\mathbf{r_0}$ is the position of the wave's source point, and its wave fronts are concentric spheres centered at this point. The volume source force is defined as: $f(\mathbf{r}) = \delta(\mathbf{r} - \mathbf{r_0})$ for the inhomogeneous Helmholtz equation.

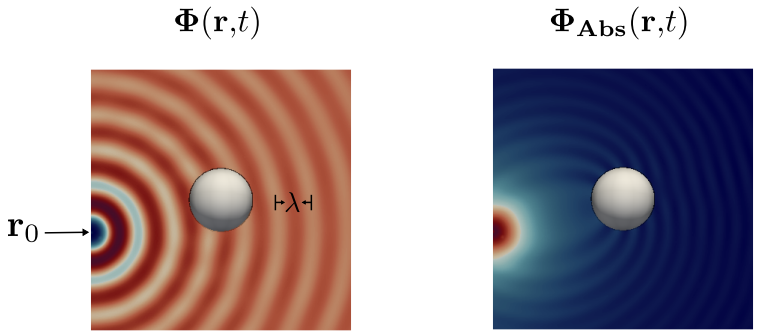

Figure 2.2: The illustration of a spherical wave function, total potential Φ and absolute potential $\Phi_{Abs} = |\Phi(\mathbf{r}, t)|$ is the absolute value of total acoustic potential (magnitude), where $\mathbf{r}_0$ is the source point

If the propagation medium is a composite material in the micro-scale or if there are multiple materials varying in space, such as a fluid-solid interaction problem, we need to impose an additional boundary condition that defines continuity of the wave over material boundaries [202].

Chapter 3

Hierarchical Higher Order Approximation Basis

In the preceding chapter, the derivation of the Helmholtz equation is described in detail. The acoustic field inside a fluid can be obtained by solving the Helmholtz equation with a numerical method such as the finite element method. One of the key factors that determines the efficiency of the finite element method is the type of basis used in the approximation spaces.

In this Chapter, the Legendre type hierarchical approximation basis is introduced. It is implemented in the acoustic solver in MoFEM, which has the flexibility to allow arbitrary user-defined basis sets. First, different refinement techniques are reviewed briefly. Then, the Legendre type polynomials are described in detail. Then, the matrix form of the tetrahedral shape functions with Cartesian coordinates are presented. This is followed by a short discussion on the efficient and accurate numerical integration algorithm, which is also implemented in MoFEM to an arbitrary order. Finally, the remainder of this chapter is devoted to the derivation and discussion of the tetrahedron hierarchical shape functions of different entities. Throughout this entire thesis, these hierarchical type basis functions for simplex elements (vertex, edge, triangle and tetrahedron) will be employed for numerical assessments.

3.1 Introduction

Conventional higher-order shape functions are limited to directly represent the approximated solution $\mathbf{u}_{fem}$ at the node points. It should be noted that u_{fem} can be a scalar value for acoustic problems. During the refinement process, the whole set of shape functions have to be replaced at each step. On the other hand, hierarchical shape functions have particular implications for local p enrichment. They can support the local p enrichment in a better way than other available methods.

Since the higher-order nodal shape functions used in higher-order finite element methods require a new set of functions after increasing polynomial orders, a plain new mesh must be generated (see Graph 3.1). A set of hierarchical modal shape functions will allow unchanged lower order functions to be augmented with additional higher order functions with increasing the order p, without any re-meshing. In Solin *et al.* [296], and Ainsworth and Coyle [10], the expressions, derivations and predefined conformity of hierarchical shape functions are explained in detail, the scalar and vector hierarchical shape functions for different type of elements are discussed. Furthermore, in [199] MoFEM documentation, the example of local refinement with a hierarchical approximation basis applied on different physical and engineering problems is also available.

In the hierarchical basis construction process, the number of degrees of freedom (DOFs) are associated with entities and additional vertices. This feature allows us to construct a heterogeneous order of approximation such that the order of approximation basis can be assigned independently on each entity. For example, for 1^{st} order hierarchical finite element shape functions ($p = 1$), the associated shape function type is merely the nodes. The merits of hierarchical shape functions in finite element codes are worth mentioning. They not only save computational time for higher order polynomials, but they also reduce the computational complexity related to mesh generation. They also substantially raise the convergence rate of the numerical solution compare to finite element with conventional shape functions. Notably, the increment of approximation basis can be quite frequent with p adaptivity of FEM when dealing with a large number of time steps. Moreover, the lower p order basis contains shape function types, such as node and edge that can be stored, and retrieved for further usages with higher order $p+1$ basis (MOAB [308]). The crucial fact is that the hierarchical basis are designed for local p enrichment since adjacent elements with different approximation orders can coexist.

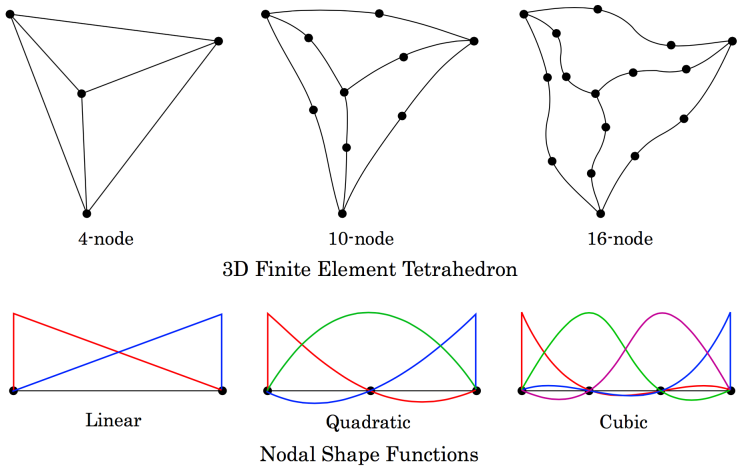

Figure 3.1: Example of curvilinear higher-order tetrahedrons and nodal shape functions [190, 109]

3.2 Finite Element Solution Refinement Techniques

There are generally five types of refinement:

h-refinement is refining the finite element solution by reducing the size of elements, equivalently adding more elements. h refinement is the most straight forward approach which can be done at the mesh generation level. However, it commonly leads to detrimental effects such as poor mesh quality and weak convergence rate.

p-refinement is another well known method to refine the solution by increasing the order of the approximation basis as a whole. In this approach the mesh is not divided but new nodes are added on the elements.

hp-refinement is a combination of h and p refinement, which is proved to exhibit an exponential convergence rate [36].

Localised refinement is either non-uniform h or p refinement that focuses on specific areas that exhibits a singularity or poor solution.

r-refinement is similar in idea to the localised h refinement, except that the number of DOFs (elements) remains unchanged. Instead, this approach moves existing nodes to concentrate them around problematic zones (stretching of nodes) to improve the accuracy in those areas. However, this method often suffers from ill-conditioned elements [233].

3.3 Lobatto Shape Functions

3.3.1 Legendre Type Polynomials

The Legendre type polynomials were originally constructed based on the Gram-Schmidt orthogonalization process that satisfies the Legendre differential equation [171]. Their roots coincide with the integration points of Gauss quadrature rules on edge elements. The most popular definition of Legendre polynomials of degree n for higher-order shape functions are defined as:

$$L_n(\bar{\zeta}) = \frac{2n-1}{n}\bar{\zeta}L_{n-1}(\bar{\zeta}) - \frac{n-1}{n}L_{n-2}(\bar{\zeta}), \text{ for } n = 2, 3, \ldots, N \tag{3.1}$$

where $-1 \leq \bar{\zeta} \leq 1$ for the first order functions, $L_0(\bar{\zeta}) = 1$ and $L_1(\bar{\zeta}) = \bar{\zeta}$. They satisfy the Legendre equation:

$$(1-\bar{\zeta}^2)\frac{d^2y}{d\bar{\zeta}^2} - 2\bar{\zeta}\frac{dy}{d\bar{\zeta}} + n(n+1)y = 0 \tag{3.2}$$

where $y \equiv L_n(\bar{\zeta})$. The alternative form can be defined by the differential relation:

$$L_n(\bar{\zeta}) = \frac{1}{2^n n!}\frac{d^n}{d\bar{\zeta}^n}(\bar{\zeta}^2-1)^n, \text{ for } n = 0, 1, 2, \ldots, N \tag{3.3}$$

The Legendre basis have orthogonality property in L_2 space,

$$\int_{-1}^{1} L_n(\bar{\zeta}) L_m(\bar{\zeta}) d\bar{\zeta} = \delta_{mn} \frac{2}{2n+1} = \begin{cases} \frac{2}{2n+1}, & \text{for } n = m. \\ 0, & \text{otherwise.} \end{cases} \tag{3.4}$$

And the recurrence relationship between Legendre polynomials is defined as:

$$L_n(\bar{\zeta}) = \frac{1}{2n+1} \left(\frac{d}{d\bar{\zeta}} L_{n+1}(\bar{\zeta}) - \frac{d}{d\bar{\zeta}} L_{n-1}(\bar{\zeta}) \right), \quad n \geq 1, \tag{3.5}$$

Thus, on node points:

$$L_n(1) = 1, \quad L_n(-1) = (-1)^n, \quad n \geq 0. \tag{3.6}$$

For a one dimensional edge element, the linear Legendre basis functions are defined as:

$$N_0 = 1 - \bar{\zeta} \quad N_1 = \bar{\zeta} \tag{3.7}$$

where $\bar{\zeta}$ is the local coordinate. The linear combination of Legendre polynomials can serve as shape functions for the finite element approximation. Consequently, the integrated Legendre polynomials are defined as:

$$l'_n(\zeta) = \int_{-1}^{\zeta} L_{n-1}(u) du = \frac{1}{2n+1} \left(L_n(\bar{\zeta}) - L_{n-2}(\bar{\zeta}) \right), \quad n \geq 2. \tag{3.8}$$

where $l'_0(\bar{\zeta}) = -1$ and $l'_1(\bar{\zeta}) = \bar{\zeta}$. $l'_n(\pm 1) = 0$ for $n \geq 2$.

The Legendre polynomials in one dimension are depicted in Figure 3.2. For details of Legendre type polynomial basis functions please see [296].

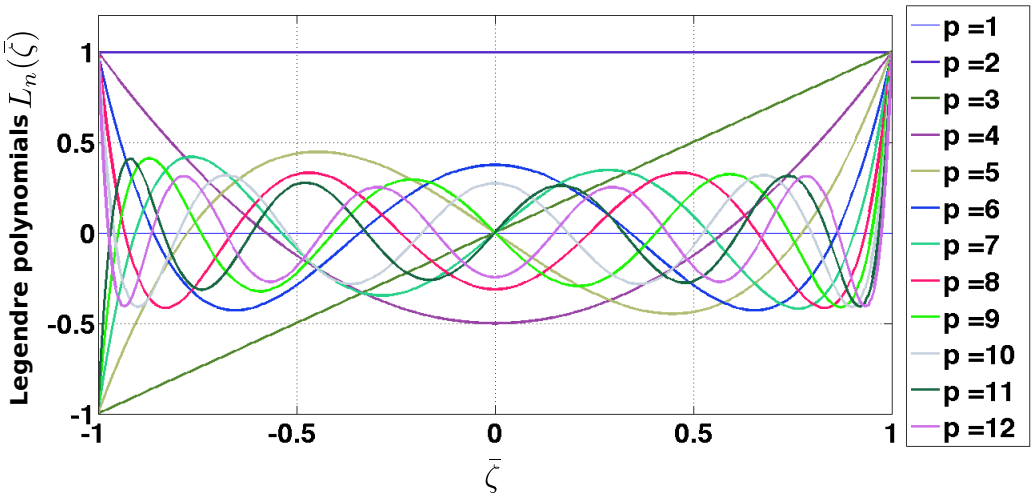

Figure 3.2: Example of Legendre polynomials L_n on an edge element

3.3.2 Construction of Tetrahedral Shape Functions

There are four entities of shape functions, written succinctly as vertex, edge, face and bubble (volume) functions. The various shape functions for tetrahedrons

are shown in Figures 3.4 and 3.6. These Figures exhibit the additional shape functions added on the basis of node shape functions depending on p. The interior bubble functions (face and volume) are internal, and vanish on the boundaries of the element, which has no adjacency with surrounding elements.

If a higher order approximation is adopted for p enrichment, except nodes, there will be additional degrees of freedom on the edges, faces and volumes. Consequently, there will be more shape functions on the foundation of the previous approximation order (Ainsworth [10]). In H^1 Hilbert space (see Appendix A.1.2.4 for detail), if the order on an element is p, then the number of DOFs on that element is:

$$DOFs_{\Omega_e} = 4 + 6(p^e_{E_i} - 1) + \frac{1}{2}(p^e_{F_i} - 2)(p^e_{F_i} - 1) + \frac{(p^e_{I_i} - 3)(p^e_{I_i} - 2)(p^e_{I_i} - 1)}{6} \quad (3.9)$$

where the order $p \in \mathbb{Z}$ is an integer, and $p^e_{E_i}$, $p^e_{F_i}$, $p^e_{I_i}$ correspond to the order of the ith edges, faces, and interiors of element e. In other words, the linear approximation basis has $p^e_{E_i} = p^e_{F_i} = p^e_{I_i} = 1$.

The Lobatto basis functions are derived from the modified integrated Legendre basis functions, thus inherit their hierarchical orthogonal property. The first order (linear) nodal shape functions of Lobatto type for a reference element is defined as:

$$l_0(\zeta) = \frac{1-\zeta}{2}, \quad l_1(\zeta) = \frac{1+\zeta}{2} \quad (3.10)$$

where the nodal shape functions are inherited by higher order basis with $p > 1$. These nodal shape functions of Legendre type guarantee the inter-element continuity ($l_i(\pm 1) = 0$ for $i \geq 2$). The p_{th} order Lobatto (integrated Legendre polynomials) basis are computed based on the $(p-1)_{th}$ Legendre basis:

$$l_i(\zeta) = \|L_{i-1}\|_2 \int_{-1}^{\zeta} L_{i-1}(\bar{\zeta}) d\bar{\zeta}, \quad \text{for } i = 2, 3, \ldots, p \quad (3.11)$$

where $\|L_{i-1}\|_2 = \sqrt{i - \frac{1}{2}}$, whereby $L_i(\zeta)$ is the Legendre basis of order i. The new shape function for hierarchical elements of Lobatto type has been implemented by the developer of MoFEM, its orthogonality property up to first order derivative in H^1 space can deliver coarser stiffness matrix together with the Duffy transformation of Gauss quadrature. Stringently speaking, they together lead to better conditioning for a sparse stiffness matrix with high wavenumbers [348, 296].

$$\int_{-1}^{1} \frac{dl_i}{d\zeta} \frac{dl_j}{d\zeta} d\zeta = \delta_{ij} \ , \quad \text{for } i \neq j \ \ \& \ \ i > 1 \text{ or } j > 1 \quad (3.12)$$

is the orthogonality condition of the Lobatto basis. The one dimensional edge integrated Legendre shape functions are shown in Figure 3.3.

The finite element solutions are based on a reference tetrahedron domain with $\left\{\bar{\boldsymbol{\zeta}} \in \mathbb{R}^3; -1 \leq \zeta_1, \zeta_2, \zeta_3; \zeta_1 + \zeta_2 + \zeta_3 \leq -1\right\}$. Thus, the affine coordinates are de-

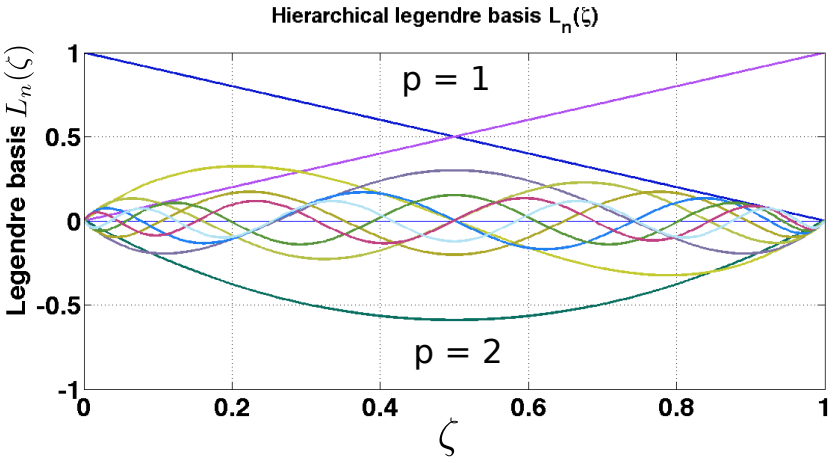

Figure 3.3: Example of shifted integrated hierarchical Legendre basis functions on edge element in $[0, 1]$

fined as:

$$\lambda_{1,T}(\bar{\boldsymbol{\zeta}}) = \frac{\zeta_2 + 1}{2}, \tag{3.13a}$$

$$\lambda_{2,T}(\bar{\boldsymbol{\zeta}}) = -\frac{\zeta_1 + \zeta_2 + \zeta_3 + 1}{2}, \tag{3.13b}$$

$$\lambda_{3,T}(\bar{\boldsymbol{\zeta}}) = \frac{\zeta_1 + 1}{2}, \tag{3.13c}$$

$$\lambda_{4,T}(\bar{\boldsymbol{\zeta}}) = \frac{\zeta_3 + 1}{2} \tag{3.13d}$$

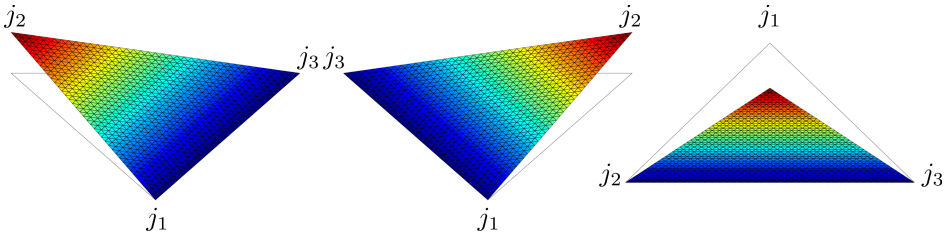

Figure 3.4: Hierarchical vertex basis for triangle, $p = 1$

The reference tetrahedron is illustrated as in Figure 3.5. These are also vertex shape functions $\psi_V^{j_i} = \lambda_{i_1,T}$ for $i = 1, ..., 4$ on each element. Each function $\psi_V^{j_i}$ is equal to one at the vertex j_i ($j_i = V_i$ for $i = 1, 2, 3$ on surface) and vanishes at the remaining vertices. The index i_1 is linked to the face F_{i_1} which does not include the vertex j_i. The vertex shape function ψ_V^{i,j_1} equal to unity at vertex j_1 of face F_i and vanishes at the other two vertices j_2 and j_3. Before introducing the quadratic basis, the so called kernel function is written as:

$$\mathbb{K}_i(\zeta) = \frac{l_{i+2}(\zeta)}{l_0(\zeta) l_1(\zeta)} \tag{3.14}$$

The edge shape functions are equivalent to the Lobatto polynomials on the edge they apply on, and equal to zero on all other five edges:

$$\psi_{E_i}^n = \lambda_{i_1,T} \lambda_{i_2,T} \mathbb{K}_{n-2}(\lambda_{i_1,T} - \lambda_{i_2,T}), \quad 2 \leq n \leq p_{E_i}^e \tag{3.15}$$

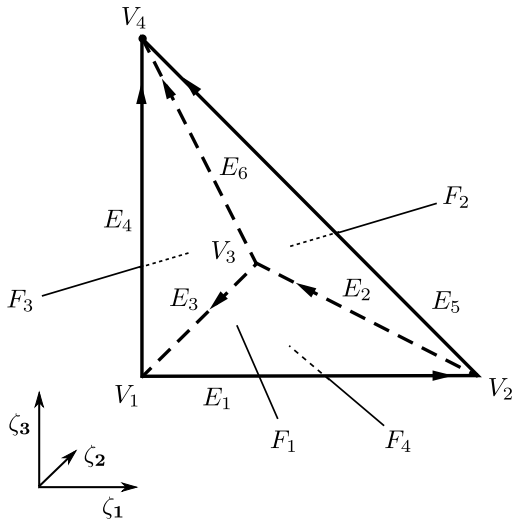

Figure 3.5: Example of the reference tetrahedron element e

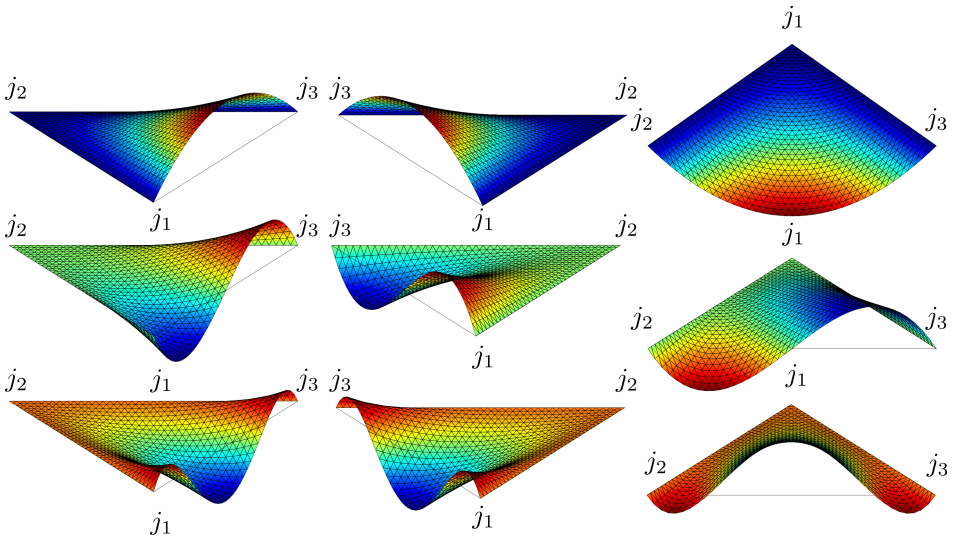

Figure 3.6: Hierarchical edge basis for triangle, $p = 2$ - 4

for E_i where $i = 1, \cdots, 6$.

The face functions only remain non-zero on the face F_i with $i = 1, ..., 4$. Assuming a triad of vertices V_a, V_b, and $V_c \in F_i$ with the lowest to the highest indices, this unique orientation of faces will have affine coordinates λ_a, λ_b and λ_c, such that they are, for each face F_i, have non-zero traces on itself ($\lambda_a(V_a) = \lambda_b(V_b) = \lambda_c(V_c) = 1$). Thus,

$$\psi_{F_i}^{n_1,n_2} = \lambda_a\lambda_b\lambda_c\mathbb{K}_{n_1-1}(\lambda_b - \lambda_a)\mathbb{K}_{n_2-1}(\lambda_a - \lambda_c), \quad 1 \leq n_1,\ n_2;\ \ n_1 + n_2 \leq p_{F_i}^e - 1 \tag{3.16}$$

Finally, the improved version of bubble functions:

$$\psi_I^{n_1,n_2,n_3} = \mathbb{K}_{n_1-1}(\lambda_{1,T} - \lambda_{2,T})\mathbb{K}_{n_2-1}(\lambda_{3,T} - \lambda_{2,T})\mathbb{K}_{n_3-1}(\lambda_{4,T} - \lambda_{2,T})\prod_{i=1}^{4}\lambda_{i,T}, \tag{3.17}$$

with $1 \leq n_1, n_2, n_3;\ n_1+n_2+n_3 \leq p_I^e-1$. The interior bubble shape functions vanish on the boundaries of the tetrahedron except in the interior. To conclude, equations

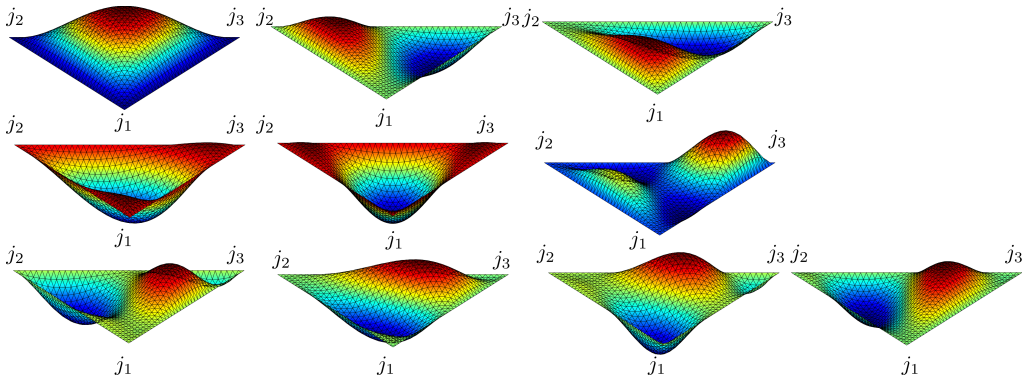

Figure 3.7: Hierarchical face basis for triangle and tetrahedron (the trace of triangle face function coincides with tetrahedron face function), $p = 3$ - 6

(3.13), (3.15), (3.16) and (3.17) together form a hierarchical basis for tetrahedrons in H^1 space. Since there exists an intrinsic inconsistency in approximation order between different entities, the conformity needs to be enforced together with the same ordering of nodes for adjacent edges and faces between finite elements [10].

As depicted in Figure 3.8(a) and (b), the hierarchical shape functions between edges and faces in 2D are conformed with its neighbouring entities. The key factor is to store and retrieve the approximation order and orientation of each of the mesh entities, which is made possible by MOAB tools [308] and MoFEM classes. The total number of DOFs (shape functions) for different entities on elements is outlined in Table 3.1.

Since different higher order DOFs are assigned to each mesh entity, this implies that the continuity needs to be assured by assigning the same approximation order across element boundaries, as shown in Figure 3.8 (b). Subsequently, the values of the neighbouring shape functions are identical for the shared entities between two or more adjacent elements. The order of the indices j_1, j_2 and j_3 should also follow the sense of direction of entities derived from a canonical order of connectivity in the finite element [307, 10]. Hence, identical node ordering is kept in adjacent entities. The detailed derivation and enforced (circumvented) conformity across elements are discussed in [199] and [10] with detailed derivations.

There are generally two ways to ensure the conformity around element boundaries, either enforce the conformity by changing the signs of coefficients or changing the global orientation. The global parametrisation is defined, and inherited locally to each element, to tackled the rotational invariance issue [10].

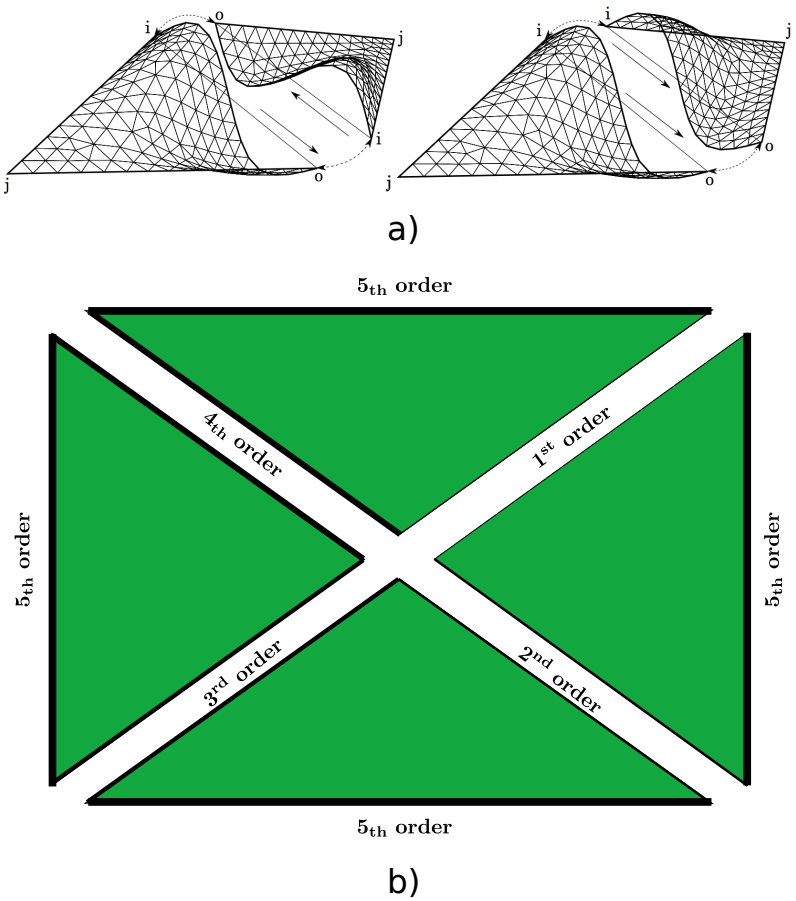

Figure 3.8: a) A priori conformity around 2D element boundaries, left: non-conforming geometry, right: conforming geometry. b) Continuity across element boundaries

Table 3.1: Table of p order for hierarchical shape functions in H^1 space with scalar field

Type	**Polynomial order**	**No. of shape functions**	**No. of nodes**
Vertex	p	1	4
Edge	$2 \leq p$	$p-1$	6
Face	$3 \leq p$	$(p-2)(p-1)/2$	4
Volume	$4 \leq p$	$(p-3)(p-2)(p-1)/6)$	1

In reference [6], the authors propose a novel hierarchical basis for simplex and compares it with existing hierarchical basis. They reveal that by orthogonalization of the face functions, they can sufficiently reduce the number of couplings between shape functions. As a result, their condition number grows with increasing polynomial order for the example of Laplace equation.

Thompson and Pinsky in [314] made a comparison between hierarchical shape

functions with Legendre, Fourier and Lagrange basis. They concluded that the use of hierarchical basis for the solution of the Helmholtz equation can deliver lower dispersion error than using a Lagrange basis. To date, the Lobatto, Bernstein and Lagrange basis have been employed to resolve the high frequency acoustic problem in [253]. Their numerical results demonstrate the effectiveness of the Lobatto and Bernstein basis over the Lagrange basis, and their superior interpolation properties.

In [325], computational times for different combinations of h & p refinements were investigated using a predefined error tolerance. The authors found that the p adaptivity with constant mesh size for elliptic type equations is said to be optimal with a predefined error tolerance. On the other hand, for a mesh domain with a singularity (e.g. L-shaped domain with a singularity at the corner), h refinement with fixed high polynomial order is preferred. This fact can be remedied by adopting the generalized Duffy transformation to eliminate the singularity on the computational domain [137]. Moreover, the frequency independent element matrices guarantee that faster frequency sweeps acoustic application will be computationally efficient (matrices can be stored and reused). Thus, in this circumstance, the polynomial shape functions have advantages over other conventional shape function spaces.

3.4 Numerical Integration for Hierarchical Shape Functions

Numerical integration should be performed over each element within the reference space $\bar{\Omega}$. A quadrature rule is said to have a degree of precision p if it can apply to integration of polynomials of degree up to p. It is defined inductively as:

$$\int_e \psi(x_i, y_i, z_i) d\mathbf{x} \approx \sum_{i=1}^{n} W_i^e \psi\left(\zeta_i^e, \eta_i^e, \xi_i^e\right) \tag{3.18}$$

where W_i, ζ_i, η_i and ξ_i denote the quadrature weights and nodes with respect to the element e on the mesh. The integrand ψ is any basis function to be integrated. The most commonly used quadrature rule is the Gaussian quadrature rule based on the Grundmann and Moller integration rule that appears frequently in the literature [164]. The expected total number of Gaussian points $\bar{n}$ is generally computed as:

$$\bar{n} = \frac{N!}{p!(N-p)!} \tag{3.19}$$

where $N = d + p + 1$, and d is the dimensional space [109]. The n points Gaussian quadrature rule is exact for polynomials of degree up to $2n - 1$. In our numerical simulation, a quadrature rule of $2p + 1$ for polynomial order p is employed for peace of mind. For short wavelength acoustic problems with linear elements, 10 integration points per wavelength are generally needed as a "rule of thumb" [344]. After the integral is computed over each reference element, the coordinate affine

transformation is performed from the reference space with coordinate $\bar{\Omega}(\zeta, \eta, \xi_i)$ to the physical space $\Omega(x, y, z)$. The Jacobian of the transformation is therefore equals to:

$$\mathbf{J} = \begin{bmatrix} \frac{\partial x}{\partial \eta} & \frac{\partial x}{\partial \zeta} & \frac{\partial x}{\partial \xi} \\ \frac{\partial y}{\partial \eta} & \frac{\partial y}{\partial \zeta} & \frac{\partial y}{\partial \xi} \\ \frac{\partial z}{\partial \eta} & \frac{\partial z}{\partial \zeta} & \frac{\partial z}{\partial \xi} \end{bmatrix} \tag{3.20}$$

with $\int_{\Omega}(\ldots)d\Omega = \int_{\bar{\Omega}}(\ldots)\,\|\mathbf{J}\|\,d\bar{\Omega}$ where the ellipses represents the integrands and $\|\mathbf{J}\|$ represents the determinant of Jacobian. The corresponding Gauss points and weights are hard coded in MoFEM for arbitrary polynomial orders to increase the efficiency of calculation [338, 164]. The generalized Duffy transformation is applied, in order to enhance the functionality of the standard integration rule. The Duffy transformation coupled with the Gaussian-Legendre quadrature rule solved the difficulties associated with the derivation of new sampling points and weights in three dimensional tetrahedron, see Appendix A.3.2 for details.

The discrete finite element solution is the sum of contributions from all shape functions for each entity. On arbitrary nodes, it is retrieved by

$$u_h(\bar{\mathbf{x}}) = \sum_{i=1}^{N^e_{dof}} \psi^e_i(\mathbf{x}) u^e_i \tag{3.21}$$

where u^e_i denotes the degrees of freedom on i_{th} entity of element e, and N^e_{dof} is the total number of shape functions contained in element e. All Gaussian points and weights retrieved from the generalised Duffy transformation are inserted into the above shape functions to calculate the right hand side vector and system matrix.

3.5 Cartesian Coordinates

In some circumstances we need the functional form of the boundary conditions (incident wave function), or we have the exact solution of a particular problem as a reference to test the accuracy of our finite element implementation. Thus, we demand the Cartesian coordinates at the Gaussian points in order to integrate over the computational domain Ω_e of element e. These coordinate matrices can be found by multiplying the existing natural nodal coordinates and the shape functions associated with these nodes.

$$\begin{bmatrix} x_1 & y_1 & z_1 \\ \vdots & \vdots & \vdots \\ x_{gg} & y_{gg} & z_{gg} \end{bmatrix} = \begin{bmatrix} N^1_1 & N^1_2 & N^1_3 & N^1_4 \\ \vdots & \vdots & \vdots & \\ N^{gg}_1 & N^{gg}_2 & N^{gg}_3 & N^{gg}_4 \end{bmatrix} \begin{bmatrix} x^{nd}_1 & y^{nd}_1 & z^{nd}_1 \\ x^{nd}_2 & y^{nd}_2 & z^{nd}_2 \\ x^{nd}_3 & y^{nd}_3 & z^{nd}_3 \\ x^{nd}_4 & y^{nd}_4 & z^{nd}_4 \end{bmatrix} \tag{3.22}$$

where gg is the total number of Gauss points on each tetrahedron element, and $\mathbf{x}^{nd}$ denotes the node coordinates (for more details please see $\langle ElementsOnEntities.hpp \rangle$ in MoFEM [190]). In case of surface (triangular) elements, the number of columns of matrices on the right hand side of Eqn. (3.22) is reduced to 3.

3.6 Concluding Remarks

In this chapter, the hierarchical higher order shape functions were introduced on the basis of Legendre type polynomials. The hierarchical approximation basis is constructed by increasing the order p of each of the entities of a specific element, which will eventually improve the number of virtual DOFs but leave the total amount of elements invariant. The traditional nodal higher order approximation basis requires re-meshing and replacing existing type of elements with new ones with different orders. The hierarchical approximation basis allowed the fast p adaptivity to be accessed without calculating a new set of shape functions or renumbering all the extensive nodes. It also encouraged the local p enrichment since the continuity of adjacent entities is enforced with uniform order and conformity across the element boundaries. This approach is beneficial when the time dependant problem is concerned with different inputs (multiple frequencies) in each time steps. The accuracy and efficiency of the proposed approximation basis will be verified with benchmark problems in the following chapters.

It should be noted that both Legendre and Lobatto hierarchical shape functions have been implemented, and efficiency and accuracy have been tested with various benchmark problems for different types of physical equations including Poisson equation, heat equation and Helmholtz equation.

Chapter 4

Introduction to Error Estimation Analysis

The primary goal of this Chapter is to briefly introduce the various errors and techniques for their estimation in the finite element method, as well as different types of Galerkin methods associated with variational formulations. The Galerkin methods are the backbone of the finite element method, different formulations of Galerkin methods can be specifically designed for a particular type of problems or equations.

Firstly, the global concept of "error" occurring in any simulations based on mathematical modelling is described. Secondly, the finite element method with various Galerkin methods are introduced. Then the criterion of a "good" error estimator is given. Finally, the error measures and estimations are outlined for Elliptic type benchmark problems.

4.1 Errors Occurring in Physical Problems

4.1.1 Mathematical Model Error

Let U be the exact physical quantity of interest, and u be the exact solution of the differential equation that describes this physical problem. Thus, the possible error is:

$$e_M = |U - u| \tag{4.1}$$

where $|\cdot|$ denotes H^1 seminorm. In general, the mathematical models are routinely less complicated than nature, therefore, $e_M > 0$ is always true. This type of error

can occur due to uncertainty in the problem data or fewer considered dimensions than the real world situation (e.g. 1D and 2D physical problems). The mathematical model error is also known as the "error of idealization" (See Babuška, [35]).

4.1.2 Approximation Error

Let u_h^* be an approximated solution on a single mesh with maximum element diameter h, then the approximation error is:

$$e_h^* = |u - u_h^*| \tag{4.2}$$

This type of error encompasses the entire errors on the computational domain whether it is caused by variational crimes or the numerical method for solving systems of linear equations.

4.1.3 Numerical Error

Since the finite element solution is obtained by way of several numerical techniques, like "quadrature rule", "discretization", "variational formulation", "direct method" or "iterative method" for systems of linear equations etc. Hence, it is reasonable to have the numerical error represented by the difference between an approximated FE solution u_h and the exact FE solution as:

$$e_N = |u_h^* - u_h| \tag{4.3}$$

This type of error normally includes: (1) round off errors, (2) error occurring during iteration processes or direct method for solving the system of linear equations, numerical integration, etc. (3) errors caused by computer codes due to the limitation of computer capacity.

4.1.4 Pollution Error

The pollution error caused by dispersion effects are exclusive to non-coercive type elliptic equations [132]. One of the special cases is the Helmholtz equation, when the wavenumber is increased, the Helmholtz equation loses its definiteness property [235]. The pollution error is denoted as:

$$e_D = |u_I - u_h| \tag{4.4}$$

The pollution error is equal to the interpolation solution (u_I) minus the finite element solution belonging to the same space. It could be regarded as part of the approximation errors. It is caused by the difference between the exact wavenumber and the wavenumber of the FE solution [44, 182]. Many attempts have been made in the literature to eliminate or reduce the pollution effects [50, 183, 181, 37, 123]. However, the dispersion effects are unavoidable in three dimensions, and most of the error estimators have difficulties in capturing the pollution errors efficiently.

4.1.5 Summary

Overall, the total error arising in any physical problem in arbitrary norm is defined as:

$$\|U - u_h\| \leq e_M + e_h^* + e_N \tag{4.5}$$

where the quantity of error we are primarily interested in is $e_h^* + e_N \approx |u - u_h|$.

4.2 Variational Crimes

The term variational crimes refer to mathematically violated rules caused by the numerical approximation process.

1. One needs to approximate the Lipschitz domain Ω by a polygonal domain Ω_h (e.g. for simplification, convex) for non-polygonal domain.
2. One needs to discretize the polygonal domain by a finite number of polygons (e.g line segments, triangles, tetrahedrons)
3. The numerical integration methods one applies to evaluate the integrands $a(u, v)$, etc.

These are the "crimes" required to commit during the numerical evaluation process. Pertaining to these above procedures, errors are incurred in each step. The first and second ones could be mitigated with mesh refinement techniques based on error estimators, the third one however is unavoidable. In addition, the error also appears during the process of solving the system of linear equations.

In case the particular method we apply to solve the system of linear equations is not exact, we need to exclude the approximation error generated by the method from the error estimator (e.g. *a posteriori* error indicators), in order to make the error estimator not too pessimistic. However, this type of error is generally negligible when compared to others. For a detailed explanation please see the book "Variational Crimes in the Finite Element Method" by Aziz, Abdul Kadir for reference [32].

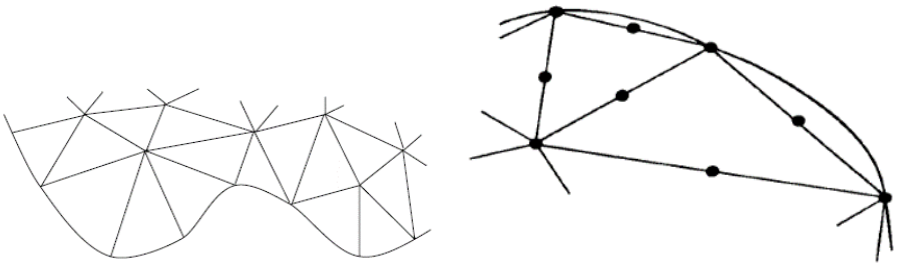

(a) (b)

Figure 4.1: Variational crime, (a) discretization (b) smoothness of boundary

4.3 A Brief Introduction to the Galerkin Methods

It is widely known that the original series of finite element books were written by Zienkiewicz and his co-author Cheung in 1967 [344]. The book was revised many times in the years after it was first published. The variational formulation with Galerkin methods has been developed consistently after it was found. The family of Galerkin methods includes the Bubnov Galerkin method, least square Galerkin method, discontinuous Galerkin method, discontinuous Petrov Galerkin method and more.

4.3.1 Bubnov Galerkin

The Bubnov-Galerkin method, named after the engineer Ivan Bubnov is the standard Galerkin method. Since the solution space V is infinite in the variational form of Eqn. (A.26) from appendices, the Galerkin method builds up the solution $\underline{u}_h$ belonging to the finite element subspace $V_h \in V$ such that $\underline{u}_h$, $\underline{v}_h \in V_h$.

$$\begin{cases} a(\underline{u}_h, \underline{v}) = f(\underline{v}), \forall \underline{u}_h \in V_h; \underline{v} \in V_h \\ \underline{u}_h(0) = \underline{u_0} \end{cases} \tag{4.6}$$

$$\underline{u}_h(\mathbf{x}) = \underline{u_0} + \sum_{i=1}^{n} \underline{u_i} \phi_i(\mathbf{x}) \tag{4.7}$$

where $\underline{u_i}$ is the value of the solution at nodal points (global degrees of freedom), and $\phi_i(\mathbf{x})$ are the i_{th} basis functions in the solution space that satisfies:

$$\begin{cases} \phi_i(\mathbf{x_j}) = \delta_{ij} \\ \delta_{ij} = 1 \ \text{ if } i = j, \ \text{ otherwise } \delta_{ij} = 0 \end{cases} \tag{4.8}$$

where δ_{ij} is the Kronecker's delta. In the Bubnov Galerkin method the solution space (also called the trial spaces) and test space are identical.

Theorem 4.3.1

$$a(\underline{u} - \underline{u}_h, \underline{v}) = l(\underline{v}) - a(\underline{u}_h, \underline{v}) = a(e_h, \underline{v}) = 0 \quad \forall \underline{u}_h \in V_h, \tag{4.9}$$

where e_h denotes the actual error. This relationship can be used as the foundation to develop the various error estimates in the following contexts.

Proof:

If we replace solution $\underline{u}$ in coercive bilinear form (A.26) by $\underline{u}_h \in V_h$, due to $V_h \subset V$ and $f \in V_h'$, with V_h' is the dual space of V_h. Hence, if the original bilinear form (A.26) is minus by the new generated coercive bilinear form, the desired result follows. Because the FE approximation error e_h is orthogonal to the finite test space (in Bubnov Galerkin the solution space as well) in the bilinear form, thus it is called the Galerkin Orthogonality condition (page 16 [14]). Finally, the orthogonality of the numerical error in the Galerkin projection described as:

$$a(e, \underline{v}_h) = 0 \ \forall \underline{v}_h \in V_h \subset V \tag{4.10}$$

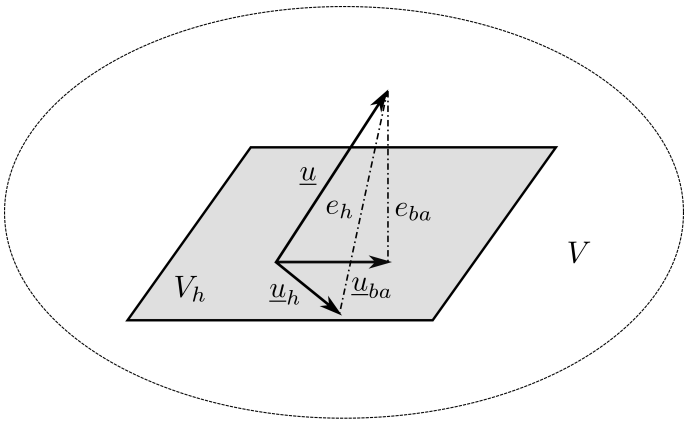

Figure 4.2: Galerkin orthogonality

Figure 4.2 illustrates the relationship between the approximation error and the finite element solution space. The best approximation error $e_{ba} = \|\underline{u} - \underline{u}_{ba}\|_V$ is the minimal distance between $\underline{u}$ and V_h, such that there exist a best approximation $\underline{u}_{ba} \in V_h$ of solution $\underline{u}$.

4.3.2 Least Square Galerkin Method

The least square Galerkin method was first proposed by Hughes and his co-authors in [174]. In his examples, the advection-diffusive equations were solved with embodied residuals from the strong form of the boundary value problem to

the weak form. This method is also related to the so called streamline upwind Petrov Galerkin method introduced by Brooks and Hughes [86]. In later years, the least square Galerkin method has been applied on the Helmholtz equation, for which the Bessel and plane wave basis are used to prove the convergence property of the method [236].

4.3.3 Petrov Galerkin Method

In the Petrov Galerkin method, the solution basis functions and test basis functions belong to different Hilbert spaces, which are the trial space and test spaces respectively. In order to stabilize the problem, special test spaces can be selected due to the instability of the original problem (e.g. advection diffusion problem in 1D with odd order, Runge's phenomenon occurs, the N-S equation with different physical quantities. See [155] and [259]). The idea is to enhance the solution spaces with emphasized information [298]. The various Petrov Galerkin methods are also known as mixed formulations in some articles due to their similar natural structures. In article [261], the hybrid Petrov Galerkin finite element method is applied to solve the Helmholtz equation with cavity problems.

4.3.4 Discontinuous Galerkin Method

The discontinuous Galerkin method was first proposed in 2000 [105]. Its basic idea is to enforce weak continuity (e.g. integrand is L_2 differentiable) on adjacent element boundaries, and employ discontinuous shape functions. The many variations of DG methods are examined and discussed in [24]. An interior penalty discontinuous Galerkin method with linear basis is developed to solve the Helmholtz equation in two and three dimensions in [148]. Through numerical analysis, the stability and accuracy of the proposed method is proven, with no mesh constraint. The plane wave basis with predefined directions were enriched on the polynomial basis, together with weak continuity on element boundaries by Lagrange multipliers. The results show good control on the dispersion effect and accuracy of the finite element solution [100].

Alternatively, the ultra weak variational formulation method uses discontinuous shape functions, and enforces continuity across element boundaries through the form of mixed boundary conditions (impedance BC) [124]. In many publications, the Helmholtz equation solved with the ultra weak variational formulation and plane wave basis has proven to have faster convergence rate when compared to the conventional Galerkin method with the finite element approach [96, 178, 177, 223].

4.3.5 Discontinuous Petrov Galerkin Method

The discontinuous Petrov Galerkin method was initially introduced in 2002 [81]. For the 1D transport equation, several numerical results illustrated that the optimal

stability of DPG compares to the Discontinuous Galerkin (DG) method. The newest breakthrough in this field was the optimal test function and the h and p adaptivity method [118, 117]. One of the major merits of this approach is the flexibility on easily adopted h & p adaptivity, due to its discontinuous characteristic between elements.

To date, unlike the DG method, the DPG method adopts a discontinuous trial function space with optimal stability. In other words, the estimated errors in L_2 norm are proved to be sufficiently small for both h refinement and p enrichment schemes, and additional flux terms across element boundaries are required.

The DPG method requires minimizing the residual in dual norm, thus it is a type of the minimum residual method as well. The choice of the test norm is vital since it requires that the error as well as the norm of the residual converge to zero. The DPG method succinctly contains *a posteriori* error estimator that is naturally carried out by the ultra-weak variational formulation [121].

Demkowicz *et al.* [119] discussed the conceptual framework of the ultra weak form adopted with the DPG method, and assessed the optimality of the method applied on Poisson equation. In addition, error estimates in terms of h & p adaptivity were identified. At last, uniform h refinement, h adaptivity and p adaptivity based on error residual were tested, the element error estimator extracted from element residual delivers exponential convergence rate for 2D Poisson equation [119]. The DPG method has been applied to one-dimensional Helmholtz problem in literature [347]. Additionally, a discontinuous Petrov Galerkin method formulation is introduced, in order to mitigate the phase error arising in Helmholtz problems with unstructured meshes in 2D. Most of all, results have been obtained through numerical assessments that demonstrate that the DPG method results in a smaller global numerical error than the DG method in two dimensional examples [125].

4.4 Definition of Error Estimates

4.4.1 Introduction

The various errors occurring during a computational process have been a principal source of concern in numerical simulations for decades. It is of paramount importance to measure, control, and mitigate the errors effectively.

Broadly speaking, error estimators are generally used as guidance for local mesh refinement in order to have an accurate as well as computationally inexpensive solutions. It also gives us an indicator as the measure of efficiency for the specific Galerkin method applied. Because for the majority of complicated applications, like Helmholtz and N-S equations, there is no analytical solution that exists, therefore many attempts to estimate the exact error are infeasible as well. The main goal of error estimators is to estimate the actual error, and subsequently provide an accurate error bounds for the exact error of a particular problem in functional norms (H^1, L_2 and energy).

In this section we will chiefly focus our attention on error estimators for finite element approximation and the Bubnov Galerkin method implemented with Elliptic boundary value problems. The definitions of an efficient error estimator will be inherited and advanced error estimators will be proposed and tested in three dimensions in the following chapters. Most of the definitions of error estimators presented in this section are obtained from books [116, 14] and [34].

4.4.2 Criterions of An Effective Error Estimators

The outstanding characteristics that a good error estimator should have are as follows:

- The error estimates should be accurate in the sense that the predicted error is close enough to the actual (unknown) error.
- The error estimates should be asymptotically correct in the sense that with increasing mesh density the error estimator should tend to zero at the same rate as the actual error.
- The error estimator should be as simple to implemented as possible, with the error estimator and bounds are computationally inexpensive to get when measured over the whole computational process of the particular analysis.
- Ideally, the error estimator should yield guaranteed, yet sharp upper and lower bounds of the actual error.
- The error estimator should be robust with regard to a wide range of applications, including non-linear problems.
- An implementation of the error estimator should be possible to facilitate an adaptive refinement process with the error estimate used to optimize the results (mesh) with respect to the computational goal.

4.5 Elliptic Type Boundary Value Problems

The two benchmark problems listed below are resolved to test the efficiency of the error measure throughout this chapter.

Benchmark Problem 1: Poisson equation

$$-\nabla^2 u = q(x) \text{ in } \Omega \in [0,1] \tag{4.11}$$

with Dirichlet boundary conditions:

$$u_{\partial\Omega_D} = 0 \text{ for } u \text{ on } \Gamma_D = 0,1 \tag{4.12}$$

The load coefficient $q(x)$ is chosen so that the exact solution has the form:

$$u(x) = \frac{x(1-x)}{2} \; \forall x \in \; \Omega = [0,1] \tag{4.13}$$

Alternatively, there is a second example of Poisson equation in higher dimensions with the analytical solution defined inductively as:

$$u(\mathbf{x}) = 1 + x^2 + y^2 + z^3 \; \forall x \in \; \Omega = (0,1) \times (0,1) \times (0,1) \tag{4.14}$$

And a Dirichlet boundary condition is manufactured as:

$$u_{\partial\Omega_D} = u(\mathbf{x}) \text{ for } u \text{ on } \Gamma_D \tag{4.15}$$

with source term $q(\mathbf{x}) = 4 + 6z$ by applying the Laplacian to the analytical formula.

Benchmark Problem 2: Linear, self-adjoint and positive-definite Dirichlet Elliptic equation Let $\Omega \subset \mathbb{R}^2$ be a Lipschitz domain with boundary $\partial\Omega$, we now consider the model problem similar to $-a(x)\Delta u + b(x)\nabla \cdot u + c(x)u$ with $a(x) = c(x) = 1, \; b(x) = 0$ such that:

$$-\nabla^2 u + u = q(x) \text{ in } \Omega \in [0,1] \tag{4.16}$$

with the Dirichlet boundary condition:

$$u_{\partial\Omega_D} = u_D \;\; \text{for } u \text{ on } \Gamma_D \tag{4.17}$$

Neumann boundary condition:

$$\frac{\partial u}{\partial n} = u_N \;\; \text{for } u \text{ on } \Gamma_N \tag{4.18}$$

where n represents the unit outward normal vector with respect to the boundary of the domain for which $n \in [L_\infty(\partial\Omega)]^n$. This problem is recognised as example 3 from Zienkiewicz and Zhu in [345], solving Helmholtz operator with unity wavenumber. It should be noted that Γ_N is the part of $\partial\Omega$ concerned by the Neumann BC such that $\overline{\Gamma_D} \cup \overline{\Gamma_N} = \partial\Omega$, which means Γ_D, Γ_N are disjoint. If $u_D = 0$ on $x = [0,1]$ and $\Gamma_N = \varnothing$ are chosen, the exact solution is defined as:

$$u(x) = x^2 - \frac{sinh(4x)}{sinh(4)} \tag{4.19}$$

Computational errors arise during the simulation of practical engineering problems. The objective of the error estimation process is to locate and minimize the

relative errors to a certain level (e.g. engineering accuracy) through h & p adaptivity refinement. We will not address all the methodologies regarding error estimation techniques, but only choose those that are robust and practically easy to implement with the model problems. The problem dependent regularity conditions resemble Eqn. (A.20) for $q(x) \in L_2(\Omega)$, $u_N \in L_2(\Gamma_N)$.

The weak form of problem 2 is an abridged version of Eqn. (A.25). The idea of $v = 0$ on Γ_D is extracted from the definition of trace operator (Lions, Magenes, [218]).

4.6 Introduction to *A Priori* Error Estimates

The *a priori* error estimator allows the estimation of the error prior to the calculation process of approximation solutions, which is mainly based on known information about the exact solutions in specified norms [34]. The majority of *a priori* error estimators in one dimension merely give the order of convergence in a manner as $\mathcal{O}(h^c)$ for finite element error in specific norms, where c is a positive constant.

The numerical analysis of *a priori* error estimators has been developed over a long time by different groups of researchers ([34, 275, 95, 328]). Theoretically, this particular type of estimator only tells us the rough information about how the asymptotic behaviour of the exact error changes with respect to the mesh parameters ($h \to 0$), broadly speaking, an upper and lower bound of the exact error. But it generally does not predict the concrete quantity of the error, due to lack of knowledge.There are also a few *a posteriori* error estimators with foundations based on *a priori* error estimators [95]. This section will be mainly devoted to common types of *a priori* error estimators for general elliptic type PDEs. The newly developed *a priori* error estimator specifically designed for the Helmholtz equation (coercive elliptic PDEs, became sign - indefinite when k is large) will be introduced in Chapter 6, after examining the h&p adaptivities in three dimensions.

Consider an Elliptic type equation as in section 4.5. The *a priori* error estimator for Elliptic type operator in L^p, H^1 and L_∞ norms can be defined as:

$$\begin{aligned}
&\|u - u_h\|_{H^1(\Omega)} = \|e_h\|_{H^1(\Omega)} \leq Ch^p \left\|u^{(p+1)}\right\|_{L_2(\Omega)} \\
&\|u - u_h\|_{L^p(\Omega)} = \|e_h\|_{L^p(\Omega)} \leq Ch^{p+1} \left\|u^{(p+1)}\right\|_{L^p(\Omega)} \quad 1 \leq p < \infty \\
&\|u - u_h\|_{L_\infty(\Omega)} = \|e_h\|_{L_\infty(\Omega)} \leq Ch^{p+1} \left\|u^{(p+1)}\right\|_{L_\infty(\Omega)}
\end{aligned} \tag{4.20}$$

where p is the order of the polynomial in each element, and $u^{(p)}$ is the p_{th} partial derivative of the solution [265, 11]. C is a mesh and solution independent constant. These estimates are element-wise, such that they can be calculated locally. Note that the choices of H^1, L_p and L_∞ norms covered all the required quantities of error that are problem independent [149]. As stated by Cea's Lemma, the exact approximation error is always bounded by the product of the best approximation

error and a mesh independent constant for coercive Elliptic equations. However, it is not the case for the Helmholtz equation. The Helmholtz equation is a special form of coercive PDE with increasing k number, it becomes sign - indefinite. The main drawback of generic *a priori* error estimators is that the constant C is unknown in most circumstances, as well as that the higher derivatives of the solution are hard to estimate. Hence, the predicted results of *a priori* error estimators tend to be pessimistic with bounds depending on unknown constants [102].

The *a priori* estimate bound for the error of Elliptic PDEs in energy norm can be highlighted by both Theorem 4.6.1 and Figures 4.3 and 4.4, such that the derivatives of the solution are equal to zero once the polynomial order reaches the analytical solution. We should notice that the derivatives of the solution inside the norm of the right hand side of Eqn. (4.20) increase as the polynomial order in each element is increased. Hence, if we want to have a proper upper bound for the error in the corresponding norms, we need to determine whether u has a derivative up to the polynomial order p or $p+1$. From the solutions of test problem 2 as shown in theorem 4.6.1, we know that the exact solution u is a cubic function, thus, we can use the basis functions up to order 3. For any orders $p > 3$, these simple *a priori* error estimators would give 0 in return (In fact, the Matlab program will generate extremely small meaningless floating point numbers (machine precision) instead of zero), since the finite element solution is exact. In other words, the cubic and quadratic approximation functions will both yield identical convergence rates when the solution u only has derivative up to order 2. But the cubic shape function is lack of efficiency for pursuing the same level of accuracy indeed. This observation remains in two dimensional problems as well. In some circumstances, the estimate of $u_h^{(p)} \approx u^{(p)}$ can be obtained in analytical form beforehand, such that it provides *a priori* error estimator [13]. For instance, the estimated partial derivatives of a solution can be determined by solving its 2D or 1D similar problems and then the error hardcoded in advance. The 3D Poisson equation example problem solved by MoFEM gives an identical observation as shown in Theorem 4.6.1. The right hand side norm of Theorem 4.6.1 is same as H^1 semi-norm of the solution u (u can be vector for different physical applications). The higher derivatives of solution u need to exist (in weak sense) in order to have the upper bound for approximation error. The regularity of u decides which Sobolev space it belongs, in other words, its weak derivatives up to p_{th} order.

Theorem 4.6.1

$$\|u - u_h\|_e \leq Ch^{\mu} \left\| \frac{\partial^{p+1} u}{\partial x^{p+1}} \right\|_{L_2(\Omega)} \tag{4.21}$$

where $\|\|_e$ denotes the energy norm, and μ is the rate of convergence depending on the polynomial order of solution space we use. In addition, the solution spaces of u depends on the regularity of the equation data itself and the shape of the computational domain Ω. In case of singularities at corners (L shape), the level of regularity for solution u is reduced. And C is independent of mesh size h and solution u.

Proof : See Babuška, chapter 6, [34] and [241] for details.

4.6.1 Numerical Results and Analysis

4.6.1.1 One Dimensional Analysis of Benchmark Problems

The benchmark problems 1 and 2 are solved with a uniform refinement. A common sequence can be observed from Figure 4.3(b) that $\|e\|_{L_2} < \|e\|_{L_\infty} < |e|_{H^1} < \|e\|_{H^1}$. This inequality states the fact that the error in the L_2 norm carries the least information about the error, while, the H^1 norm (in this case the energy norm as well) is the best norm to measure the error of the total energy in a physical problem. Precisely, it measures the weighted integrals of the squares of the errors over the domain. However, other norms are not obsolete, since they can measure the specific quantity of interest of the error. The L_2(root mean square) norm measures the average error for the function value of the solution itself, and the H^1 norm gives both the error in the solution and its partial derivatives in the L_2 norm up to first order. The L_∞(pointwise) norm gives us an indication of where the maximum error occurs in our system to aid the mesh refinement. At last, H^1 semi-norm measures the error in the gradient of the FE solution.

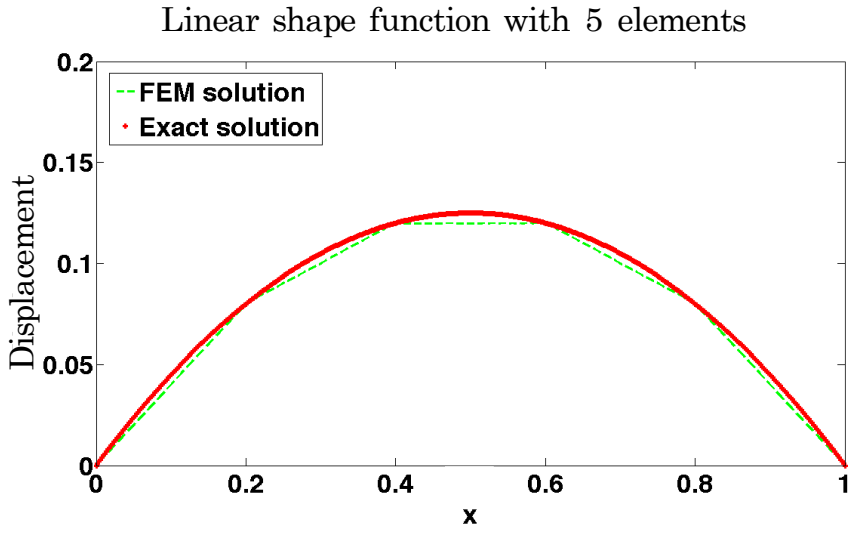

(a) FEM solution, problem 1

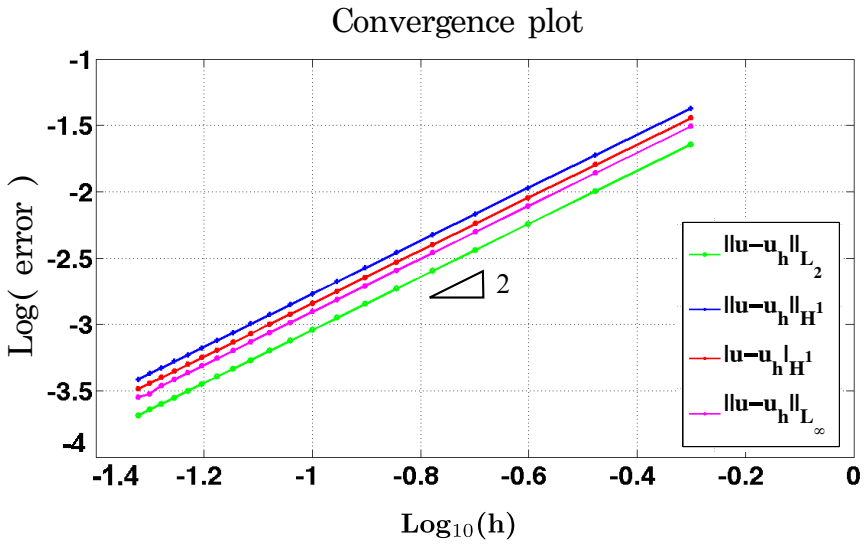

(b) Uniform enrichment, problem 1

Figure 4.3: FEM solutions of edge element benchmark problem 1, (a) approximated solution of benchmark problem 1, (b) convergence plot of uniform refinement, benchmark problem 1

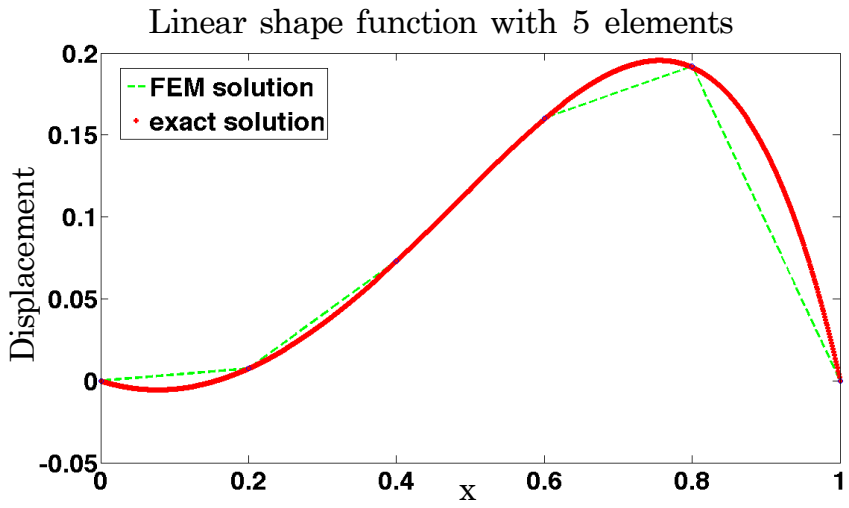

(a) FEM solution, problem 2

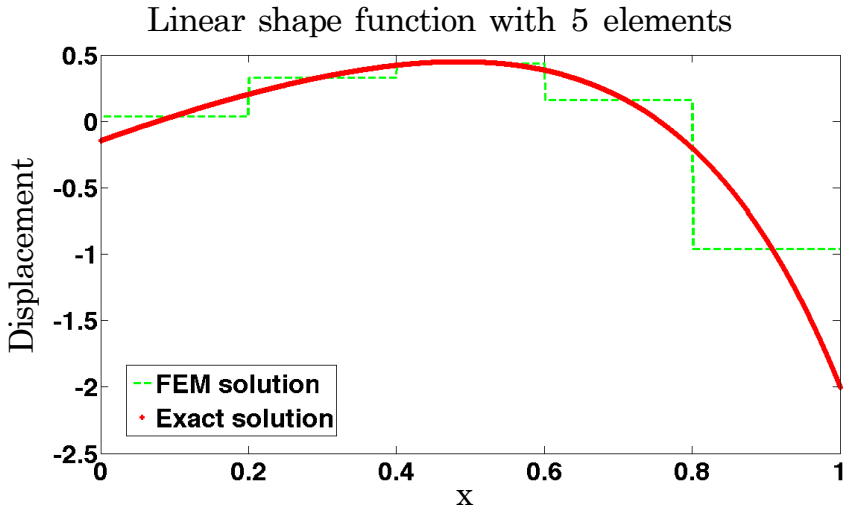

(b) Gradient of solution, problem 2

Figure 4.4: FEM solutions of edge element benchmark problem 2, (a) approximated solution of benchmark problem 2, (b) gradient of approximated solution of benchmark problem 2

In addition, the proportion of the gradient error is much more than the error of the solution itself for lower order elements. Thus it is reasonable to develop novel estimation techniques which could reduce such errors, or using higher order elements instead.

Theorem 4.6.2 *Let $p \in [1, \infty]$ be an integer, and m be a non-negative integer. Let V be the finite element subspace constructed on a regular partition Γ of Ω into triangular elements. In addition, let $s \in [0, 1]$ and $s \leq k \leq m+1$. Thus, there exists a constant C independent of the maximum element diameter h and the solution u such that for all $u \in W_p^k(\Omega)$, then the finite element solution satisfies:*

$$|u - u_h|_{W_p^k(K)} \leq C h_K^{k-s} |u|_{W_p^k(K)} \tag{4.22}$$

for every elements $k \in \Gamma$*, with assumptions if* $k > 1$*, then,* $\frac{2}{p} \leq m + 1$ *or* $m \geq 1$ *if* $p = 1$*.*

Proof See Ainsworth *et al.* [14].

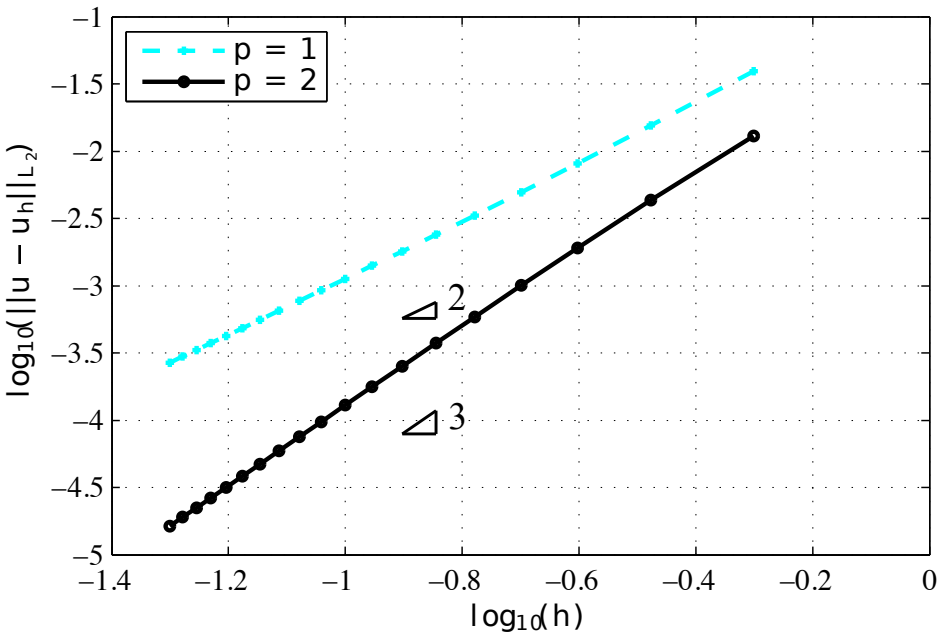

(a)

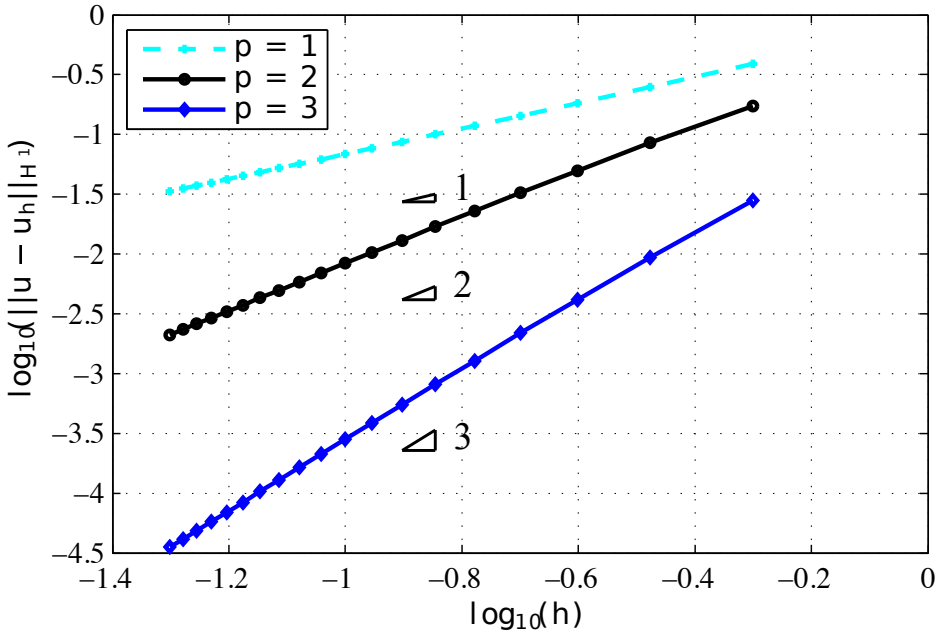

(b)

Figure 4.5: Uniform h refinement in (a) L_2 norm convergence plot of benchmark problem 2, and (b) H^1 norm convergence plot of benchmark problem 2. The triangles indicate the gradient slope

Figure 4.5 illustrate the rate of convergence of the approximation error in L_2 and H^1 norms respectively. The benchmark problem 2 is solved with the finite element method. It can be seen that the rate of convergence results match Eqn. (4.20) and Theorem 4.6.1 exactly with the same level of convergence rate. The h refinement exhibits algebraic convergence rates. The error converges asymptotically

order $\mathcal{O}(h^p)$ in H^1 norm. Moreover, the error of the solution itself (in L_2 norm) is superconvergent with order like $\mathcal{O}(h^{(p+1)})$.

4.6.1.2 Higher-Dimensional Analysis of Benchmark Problem One

In the documentation of MoFEM [199], there is a detailed tutorial on three dimensional non-linear Poisson equation solved by hierarchical FE approximation, thus the detailed procedure will not be addressed here. Moreover, the results can be validated by comparison to the analytical solution. In Figures 4.6 and 4.7, we solved the linear Poisson equation of problem 1 (second analytical solution) in a unit square cube discretized by 12 (coarse) and 1223 (fine) elements in total. We calculated the global actual error in H^1 norm, and uniformly enriched the approximation basis from order 1 to 7 with the total number of DOFs in the range from $15-1151$ DOFs (coarse mesh) and $478-82652$ DOFs (fine mesh).

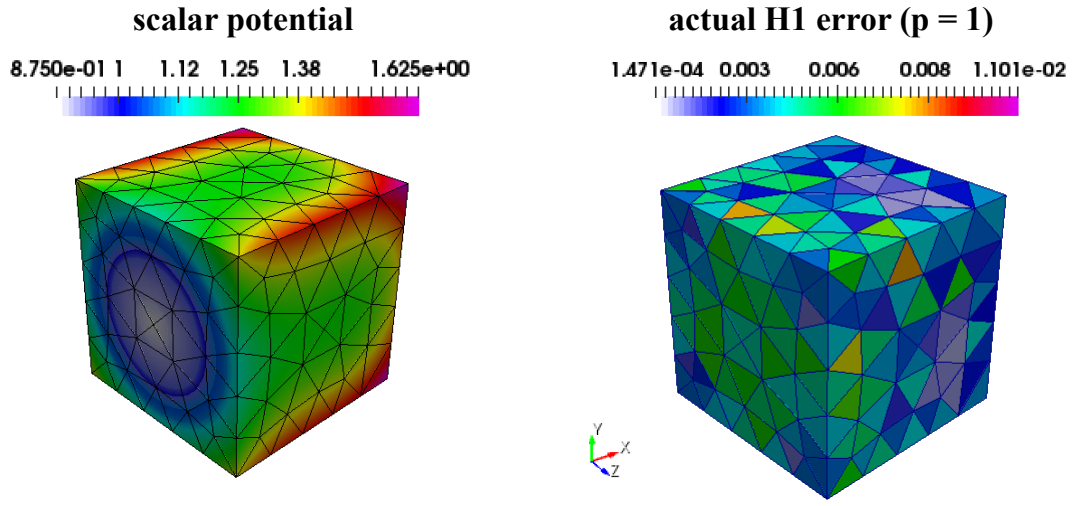

(a) scalar potential of Poisson equation (b) local error on computational domain

Figure 4.6: Poisson equation solved on unstructured mesh, scalar potential field and H^1 local exact relative error, 1223 elements

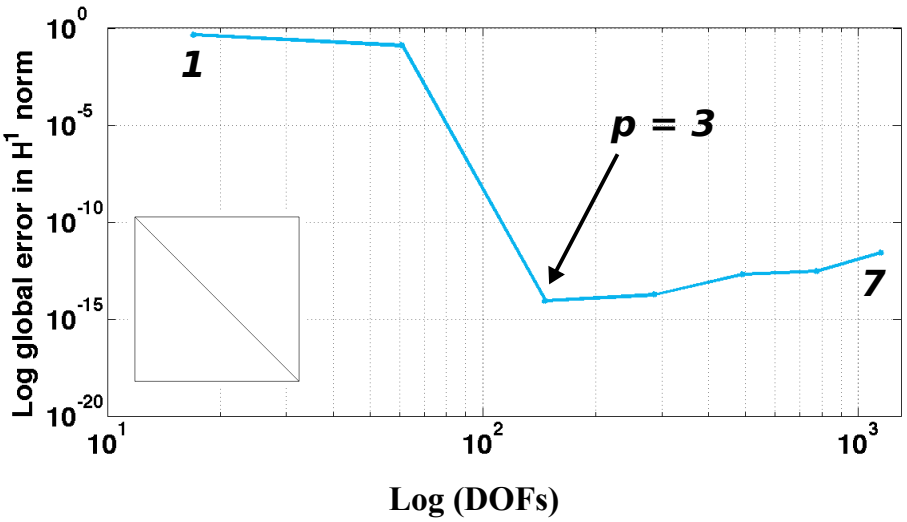

(a) coarse mesh

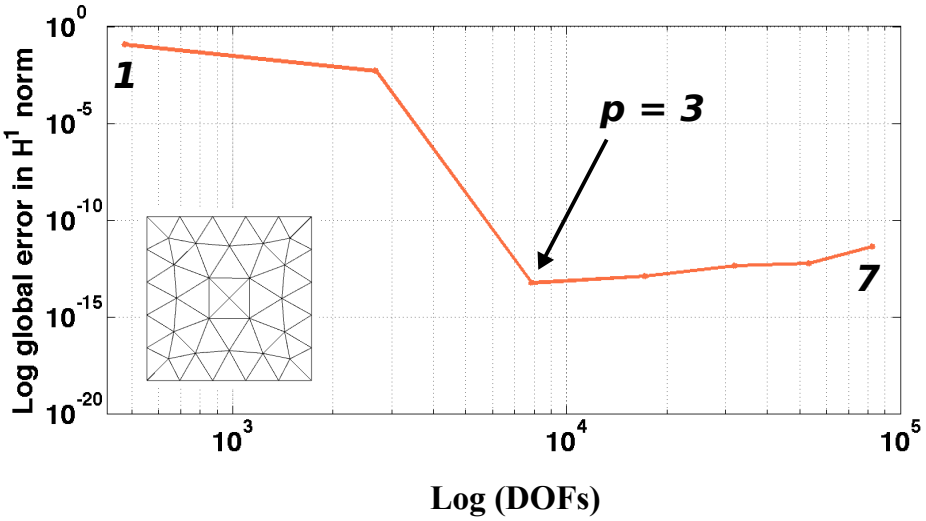

(b) regular unstructured mesh

Figure 4.7: Poisson equation solved on unstructured mesh, log global exact relative error in H^1 norm versus log number of DOFs. Uniform p enrichment.(a) 12 element, (b) 1223 elements

First of all, an exponential convergence rate can be observed from Figure 4.7 with p enrichment. Secondly, Figure 4.7 recovers the result of the one-dimensional application from the previous section that the error drops to zero when the polynomial order reaches 3, which is the order of the analytical solution exactly. However, we can see that the global errors slightly increase when increasing the order from 4 to 7. This is due to the deleterious effects of matrix condition and nodes generated by increasing orders. In fact, we have a floating number that is approximately zero ($\approx 1e-15$) on each node as local error when $p \geq 3$. But these numbers add up when we have plethora amount of nodes on the computational domain (round off errors). The error of the solution will remain zero once we reach the limitation of the polynomial order of the analytical solution. Consequently, any further attempts or

refinement steps will only gives us random extremely small floating point numbers (floating point operations) with machine precision. Hence, the accumulated local floating point errors grow with increasing p. We can control it by truncating the local error to significant figures. This is one way we can verify if the approximation basis used is correct. It should be borne in mind that the finite element solution can be reproduced with exactness, even if we use a coarser mesh than in the current example. This fact refers to Theorem (4.6.1) as well. It is also suggested by the authors of [325] such that the p enrichment performs better than the mesh refinement when solving Elliptic operators with smooth solutions, this is however not the case with singularities.

4.7 An Introduction to *A Posteriori* Error Estimates

This section is intended to briefly introduce the concepts behind *a posteriori* error estimates. The applications of error estimators applied to Elliptic PDEs can be found in Appendix B. In contrast to *a priori* error estimators, the *a posteriori* error estimator often requires extra calculation steps after the finite element solution is retrieved. It provides the explicit quantity of upper and lower bounds for the finite element error in specific norms such as $\|u - u_h\| \leq \epsilon$. The initial idea and pioneering work of *a posteriori* error estimators was first adapted on the one dimensional Elliptic boundary value problems by Babuška and Rheinboldt in 1978. Their error estimates enable locally element-wise error indication in order to aid adaptivity algorithms. Many variations of error estimators have been proposed hereafter [53, 47, 48, 34]. In 1984, Demkowicz identified an emerging concept of error estimation which is called "the element residual method" in the conference held in Lisbon [114]. The proposed method can be applied to many engineering and physical problems with slight modifications [33, 114, 115]. Around the 1980s, many *a posteriori* element-wise error estimation techniques were proposed due to an increasing demand for effective adaptivity schemes. These estimators were based on the foundation of *a priori* estimates and interpolation estimates. Some of them are heuristic and crude, however simple to implement, which leads to efficiency [113, 250]. Lately, Zienkiewicz and Zhu proposed a type of gradient recovered based method named the superconvergent patch recovery method. This type of estimator focuses on estimating the error in the gradient of solutions through enriching the gradient of the solution by interpolation techniques [343, 345]. In contrast, extrapolation methods could also provide global error indicators for h & p adaptivity schemes [303].

Several basic techniques of *a posteriori* error estimation were developed in the early 1990s, especially the notable result obtained by Verfürth for the Stokes problem and the Navier-Stokes problem [321]. Essentially, the explicit error estimator for a vast range of problems, including the non-linear problem, was discussed in [69]. Extensive research on element residual based methods have been conducted in the literature [12, 120]. They further extended the capability and scalability of the proposed methods to different types of problems and boundary conditions.

Noteworthy, generic *a priori* error estimators can only indicate the asymptotic rate of convergence as $h \to 0$. In the other aspect, they generally cannot offer the adaptable information of the actual error in an existing mesh with a fixed h value (Demkowicz, Oden and Strouboulis in [114], Bank and Weiser in [58]). Nevertheless, there are exceptions such as the *a posteriori* error evaluator that is based on the natural element residual property of its ultra weak variational formulation [82], as well as the *a priori* error estimators derived from the knowledge of the physics behind the problem, and the mesh resolutions. Even though, the majority of *a posteriori* error estimators can be applied as an independent measure to assess the quality of the approximation process without any *a priori* knowledge.

To date, there are mainly two types of *a posteriori* error estimators, explicit and implicit. Explicit means the input data is available in the problem, one only requires to compute the desired error quantities in a straightforward fashion. Implicit error estimators require to solve additional linear system of equations, in order to obtain a concrete value of the estimated error. Hence, the implicit error estimator is defined as an implicit function of the finite element approximated solution. On the other hand, the category can also be classified as element residual based error estimators and gradient recovery based estimators too.

4.8 Concluding Remarks

This chapter briefly introduced the measurements and the theorems related to the inconsistencies of solutions occurring within numerical modelling, namely, the simulation errors.

In Appendix B, five error estimation techniques that belong to the three main categories (explicit element residual method, implicit element residual method, element patch recovery method) have been assessed in one dimensional elements. These estimators are: explicit element residual method in L_2 norm, explicit element residual method in energy norm, implicit Dirichlet element residual method, implicit Neumann element residual method and superconvergent patch recovery method.

We can conclude that from the analysis of convergence property and the effectivity index, the explicit element residual method is the most sufficient and straightforward (less computational cost) to implement for test problems. On the other hand, the implicit element residual method is the most expensive to build during numerical simulations. Furthermore, it suffers from conditioning problems in higher dimensions ($d > 1$). The implicit *a posteriori* error estimator and Z-Z error estimator are proven to be the most accurate, even though the latter requires less computational time than the former by the nature of its arithmetic.

However, *a posteriori* error estimators require the calculated finite element solution before the errors can be estimated and require to solve an additional linear system of equations based on the finite element solution. Therefore, the *a posteriori* error estimators would be computationally ineffective to implement in higher dimensional problems, assuming that the size of the post-problems will dramatically

increase in three dimensions. Overall, there is a "trade off" between strict accuracy and computational costs of a proposed error estimator.

Furthermore, in this chapter, we demonstrated the effectiveness of p adaptivity compared to h adaptivity in one dimension. It is of practical importance to design the mesh and assign the element order based on the behaviours of the estimator in pre-asymptotic ranges [179]. Subsequently, it would be very computationally inefficient to apply the *a posteriori* error estimator in acoustic problems with high frequent frequency sweeps. On the other hand, there are several *a posteriori* estimators proposed and specifically designed to evaluate the pollution effects in one dimension, and effectivity index ranged from $1-3$ are observed [37, 39, 42]. Equally well, many numerical methodologies are discussed in order to exploit the existing error estimators which can accommodate the pollution effects caused by the highly oscillated character of Helmholtz problem [38, 40, 184]. Although they all performed better than the conventional finite element method with linear element, the results are somehow unsatisfactory [123]. Either complicated computations are required to achieve the goal (Quasi-Stabilized FEM), or methods are not available in higher dimensions (residual free bubble FEM). The *a posteriori* error estimators commonly dominate the asymptotic range and their performances on controlling the pollution errors in three dimensions still remain disappointing [8].

Chapter 5

Acoustic Problems with Assessment of h and p Adaptivity

This chapter mainly aims to evaluate the efficiency of uniform $h\&p$ adaptivity applied on three dimensional acoustic benchmark problems and the effects of pollution error related to domain length.

First of all, the time harmonic wave boundary value problem with arbitrary inhomogeneous boundary conditions is proposed. Several variations in generic applications are described in detail. The variational formulation is derived.

In the next part, the discussion on dispersion effect and pollution error in current developed measures is presented. The most popular techniques to reduce the pollution error are also introduced.

In the following section, the monochromatic benchmark problems are described. Subsequently, the polychromatic wave acoustic solver is proposed, detailing the implementation procedures, and the Fourier transformation is applied to transfer both incident wave and radiation wave fields from the spatial domain to the temporal domain. The variational formulation of the time dependant Helmholtz equation is given. Consequently, numerical analysis on uniform h and p refinement is performed, as well as studying the pollution error along the propagation direction of waves in three dimensions. Finally, conclusions are drawn.

5.1 The Three-Dimensional Exterior Boundary Value Problems

Follows the time harmonic Helmholtz equation derived in Chapter 3, we thus present the generic form of Helmholtz problems.

Let Ω be a domain in $\mathbb{R}^3$ with a smooth boundary and outward unit normal $\mathbf{n}$. In the assumption of a time harmonic wave, the steady part of the wave equation for the propagation of acoustic waves in an isotropic, homogeneous, ideal medium is defined inductively as

$$\nabla \cdot \nabla \Phi(\mathbf{r}) + k^2 \Phi(\mathbf{r}) = f(\mathbf{r}) \text{ in } \Omega \tag{5.1a}$$

$$\left(\frac{\partial \Phi(\mathbf{r})}{\partial n} + \mathrm{i}\sigma\Phi\right) = g \text{ on } \Gamma \tag{5.1b}$$

where the variation of $f(\mathbf{r})$ in (5.1a) is a source force term (e.g. a point source of acoustic wave). Equation (5.1b) is the mixed boundary condition with constant σ and where the value of g describes the type of boundary condition being implemented. If $g = 0$, the Robin boundary condition can be either the Dirichlet or Neumann BC in extreme cases, $Y = \rho c$ is therefore called the dimensionless impedance coefficient [88] ($\sigma = \frac{1}{\rho c}$ stands for admittance). When $\sigma \to \infty$ the boundary of the obstacle tends to soften, conversely, $\sigma \to 0$ defines a sound hard boundary. Acoustic problems with analytical solutions such as a wave guide, point source and plane wave impinging a sound hard / soft scatterer can be generated by setting appropriate boundary conditions.

5.1.1 Boundary Conditions for Benchmark Problem

Appropriate boundary conditions are essential for the set up of both benchmark examples and physical applications. The most generic boundary condition is the admittance boundary condition, which describes the behaviour of an acoustic medium as it reacts to waves incident on it. In the example of exterior boundary value problem where an incident wave (either plane or spherical) impinges a scatterer, the relation between the total field Φ, scattered field Φ_S and the incident field Φ_I is:

$$\Phi = \Phi_S + \Phi_I \tag{5.2}$$

5.1.1.1 Total Acoustic Potential

The following boundary conditions hold for the total field of acoustic potential Eqn. (2.18) and Eqn. (5.2):

$$\frac{\partial \Phi}{\partial r} = 0 \text{ on } \Gamma_N \tag{5.3a}$$

$$\Phi = 0 \text{ on } \Gamma_D \tag{5.3b}$$

$$\frac{\partial \Phi}{\partial r} - \mathrm{i}k\Phi = o\left(r^{-\frac{d-1}{2}}\right) \text{ as } r \to \infty \text{ on } \Gamma_\infty \tag{5.3c}$$

$d = 1, 2, 3$ is the dimension of space. In case of 3D, $\Phi = \mathcal{O}(r^{-1})$. The third equation above is called the Sommerfeld radiation condition, it describes the far field pattern

of the acoustic potential with no reflection from the artificial truncated boundary Γ_∞, in other words, for sufficiently big r in order to encompass the domain of interest (see Figures 5.1 and 5.2 for ref). Furthermore, Neumann BC imposed on Γ_N represents the sound-hard property of the scatterer, consistent with a rigid obstacle problem. Alternatively, Dirichlet BC on Γ_D satisfy the sound-soft property of the scatterer. For details of the derivation please see Ihlenburg [180]. A more readily applicable form of (5.3c) can be expressed as:

$$\lim_{R\to\infty} \int_{|r|=R} \left| \frac{\partial \Phi}{\partial r} - \mathrm{i}k\Phi \right|^2 d\Gamma = 0 \tag{5.4}$$

which is a non-local weaker integral form. Here the distance r covers a spherical domain centered at $r = 0$.

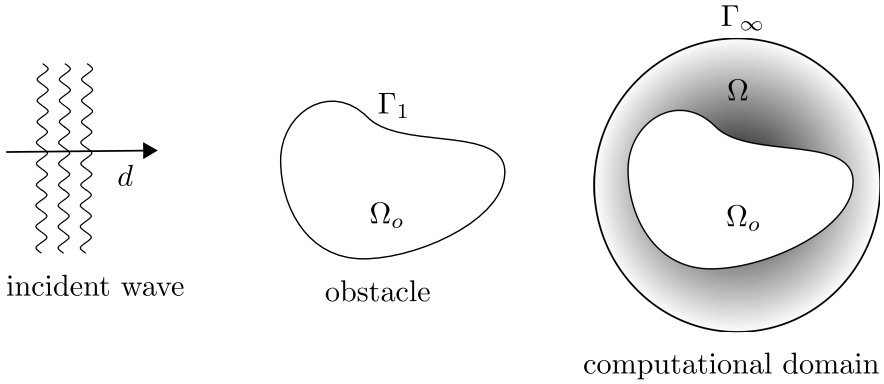

Figure 5.1: Example of exterior boundary value problem

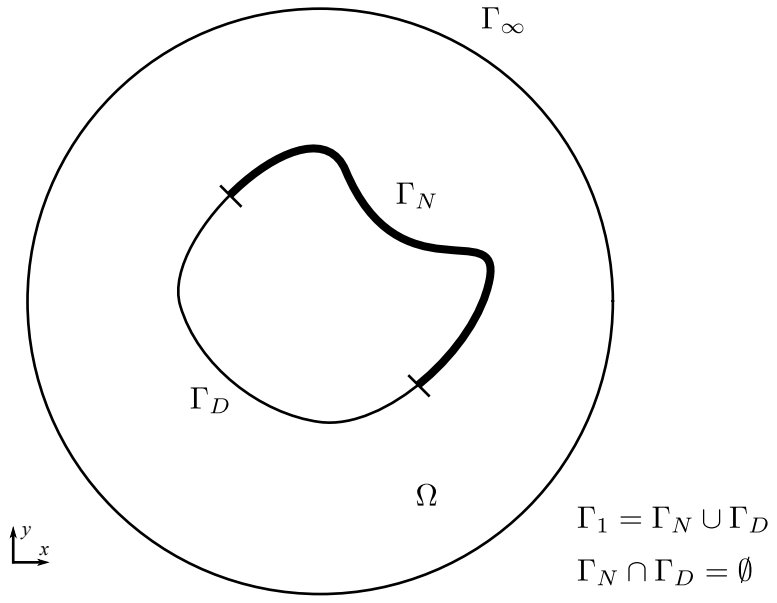

Figure 5.2: Schematic diagram of exterior boundary value problem, the boundary of the obstacle Γ_1 composed of Dirichlet and Neumann boundaries, and the exterior boundary Γ_∞.

The Sommerfeld radiation condition is applied on the artificial boundary truncated from the infinite domain as an asymptotic condition. Such a boundary condi-

tion requires special treatment to maintain a perfectly absorbing boundary. There are generally two ways to ensure this, either impose a variation of the absorbing BC on the truncated boundary, or through an assumed interpolation in the complement of the computational domain in order to restrict the reflection of waves from the boundary (Engquist [142], Bayliss [63], Bettess [75], Burnett [90]). Nevertheless, Berenger introduced the perfectly matched layer (PML) [67] which defines a finite thickness layer object to damp all the outgoing waves from the side of the scatterer.

Recent development has been conducted by Givoli and Keller [159, 193] on the Dirichlet-to-Neumann (D_tN) method which can be seen as an analytical impedance condition on the convex artificial boundary (e.g. circle, ellipse, sphere and ellipsoid) by employing a Fourier expansion of the D_tN non-local operator. The major drawback is that it generates symmetric sub-matrix associated with the degrees of freedom lying on the artificial boundary, storing such matrices is cumbersome for three dimensional high wave number problems (i.e. $ka \geq 40$). It is a non-local condition which contains an infinite series of trigonometric or spherical harmonic functions.

Since the Bayliss-Gunzburger-Turkel (BGT) like absorbing BC delivers the same accuracy as most of the methods stated above, importantly, it creates smaller systems of equations with better conditioning number than the others. Other quantitively similar boundary conditions include: Enquist and Majda absorbing BC, Pade approximations, and Feng operator, etc. These can be found in [208]. Thus, for simplicity, we implement the BGT first order condition for our numerical solution of benchmark problems with infinite exterior boundary (cf. Antoine [23], Tezaur [312]).

5.1.1.2 Scattered Acoustic Potential

As stated by Antoine in [23], all the current derivations of radiation BCs for acoustic problems in past literature have been tested. Equation (5.3c) has a generic analytical form given as:

$$\frac{\partial \Phi_S}{\partial r} - \mathrm{i}k\Phi_S = M\Phi_S \text{ on } \Gamma_\infty \tag{5.5}$$

where M is the operator satisfying the Sommerfeld radiation BC on the truncated boundary. It is often represented as a sequence of local operators. In this case, the desired solution is the acoustic radiation potential. The simplest expression is:

$$\frac{\partial \Phi_S}{\partial r} - \mathrm{i}k\Phi_S = -\frac{\zeta}{2}\Phi_S \tag{5.6}$$

where $\zeta = \frac{1}{R}$ in a circular boundary case represents the curvature of the scatterer surface. Consequently, the BGT like BC is:

$$\frac{\partial \Phi_S}{\partial r} - \mathrm{i}k\Phi_S = 0 \text{ on } \Gamma_\infty \tag{5.7}$$

in three dimensions, as well as in the situation where the artificial boundary is not far enough from the layer of the scatterer. The sufficiently higher order approximation

of M is compulsory in order to describe the absorption property of the domain boundary with better accuracy, thus the first order BGT like condition:

$$\frac{\partial \Phi_S}{\partial r} - \mathrm{i}k\Phi_S = -\frac{1}{2r}\Phi_S \text{ on } \Gamma_\infty \tag{5.8}$$

and the second order BGT like condition written as:

$$\frac{\partial \Phi_S}{\partial r} - \frac{1}{2(\mathrm{i}k - \frac{1}{r})}\Big(- 2k^2 - \frac{3\mathrm{i}k}{r} + \frac{3}{4r^2} - \frac{1}{r^2}\frac{\partial^2}{\partial \theta^2}\Big)\Phi_S = 0 \text{ on } \Gamma_\infty \tag{5.9}$$

where θ is the spherical coordinate. By combining equation (5.2) and equation (5.8), we can derive the explicit form of the local absorbing BC for the Helmholtz operator in the case of a BGT like first order BC (Bayliss [64, 23, 208]).

$$\frac{\partial \Phi}{\partial r} + \big(\frac{1}{2r} - \mathrm{i}k\big)\Phi = \frac{\partial \Phi_I}{\partial r} + \big(\frac{1}{2r} - \mathrm{i}k\big)\Phi_I \text{ on } \Gamma_\infty \tag{5.10}$$

The implicit mixed BC (5.3c) can now be replaced by (5.10). For the sake of simplicity, we will adopt the BGT condition of first order for numerical experiments. The most important point is that BGT type boundary conditions enable easy adoption (flexibility) to any finite element codes as well as a smaller computational domain which leads to better efficiency in 3D modelling. It has been proven that BGT boundary conditions with arbitrary orders can be applied to any convex artificial boundaries in exterior boundary value problems without loss of robustness [192].

Alternatively, we can impose the analytical solution Φ_{ref} of the benchmark problem on the artificial boundary, in order to have a better approximation on the exterior boundary [206]. The Robin type boundary condition is defined as:

$$\frac{\partial \Phi_S}{\partial r} - \mathrm{i}k\Phi_S = -(\frac{\partial \Phi_{ref}}{\partial r} + \mathrm{i}k\Phi_{ref}) \text{ on } \Gamma_\infty \tag{5.11}$$

Finally, we can write the BCs for the scattered solution of the Helmholtz equation as:

$$\nabla \cdot \nabla \Phi_S(\mathbf{r}) + k^2\Phi_S(\mathbf{r}) = f(\mathbf{r}) \text{ in } \Omega \tag{5.12a}$$
$$\nabla \Phi_S \cdot \mathbf{n} = \nabla \Phi_I \cdot \mathbf{n} \text{ on } \Gamma_N \tag{5.12b}$$
$$\Phi_S = \Phi_I \text{ on } \Gamma_D \tag{5.12c}$$
$$\nabla \Phi_S \cdot \mathbf{n} + \mathrm{i}\sigma\Phi_S = g \text{ as } r \to \infty \text{ on } \Gamma_\infty \tag{5.12d}$$

where equation (5.12b) and (5.12c) successively achieve the situations when the scatterer is sound-hard and sound-soft. In addition, Eqn. (5.12d) is the first-order BGT like BC when $\sigma = -k$ and $g = -\frac{\Phi_S}{2r}$ [64], and $\mathbf{n}$ denotes the outward normal vector to the boundary Γ_N.

5.1.2 Weak Variational Formulation of the Governing Equation

In this section, the acoustic radiation potential Φ_S is replaced by the solution u for convenience. A variational formulation of the problem (5.12) can be formulated as follows:

$$\begin{cases} \text{Find } u \in H^1(\Omega), & \text{such that} \\ a(u,v) = f(v) & \forall v \in H^1(\Omega) \end{cases}$$

where $a(\cdot,\cdot)$ is the symmetric bilinear form based on $a : H^1(\Omega) \times H^1(\Omega) \to \mathbb{C}$, to be clarified as:

$$a(u,v) = \int_\Omega \nabla u \cdot \nabla v \, d\Omega - k^2 \int_\Omega uv \, d\Omega + (\mathrm{i}k + M) \int_{\Gamma_\infty} uv \, d\Gamma \tag{5.13a}$$

$$f(v) = \int_\Omega fv \, d\Omega + \int_{\Gamma_\infty} g_2 v \, d\Gamma + \int_{\Gamma_1} g_1 v \, d\Gamma \tag{5.13b}$$

where $f \in H^{1*}$ is an antilinear functional (H^{1*} is the space of antilinear functionals in H^1 [180]), g_1 can be either equation (5.12b) or (5.12c) depending on the problem in hand. g_2 corresponds to the specific explicit form of the non-reflection boundary condition. To find the finite element solution u_h for Φ_S (from trial spaces for consistency), the domain Ω needs to be discretized into a set of element domains Ω_e with size h. Thus, our FE solution u_h and test functions v_h are built in H^1 space with a hierarchical basis. The subscript h will indicate the discrete version of quantities consistently in the following contexts. If we let the energy norm of the finite element solution be defined as:

$$\|u\|_e = \sqrt{\|\nabla u\|^2_{L_2(\Omega)} + k^2 \|u\|^2_{L_2(\Omega)}} \tag{5.14}$$

then,

Theorem 5.1.1 *(Existence and uniqueness of solution). Let $f \in H^{-1}(\Omega)$ and $g_i \in H^{-\frac{1}{2}}(\Gamma_i)$, for $i = 1, 2$. Thus, there exists a unique solution for the Helmholtz problem if the condition*

$$\|u\|_e \leq \zeta(\Omega, k)\big(\|f\|_{H^{-1}(\Omega)} + \sum_{i=1}^{2} \|g_i\|_{H^{-\frac{1}{2}}(\Gamma_i)} \big) \tag{5.15}$$

is satisfied. Where $\zeta(\Omega, k)$ is the dependence of ζ on the computational domain Ω and wave number k.

Proof see Strouboulis, Realino, and Babuska [300] for detailed proofs.

Finally, after discretization of the Galerkin method as discussed in section 4.3.1, the solution $u \approx u_h$, we end up with the linear system of equations:

$$\mathbf{KU} = \mathbf{F} \tag{5.16}$$

where $\mathbf{K}$ is the stiffness (system) matrix which contains the discretized bilinear form of chosen hierarchical shape functions, $\mathbf{U}$ contains the nodal DOFs u_i of the finite element solution u_h and $\mathbf{F}$ is the vector of the right hand side discretized linear form. The hierarchical higher order Lobatto type shape functions are used at element level (chapter 3). The Gaussian-Legendre quadrature rule coupled with the generalized Duffy transformation is applied to integrate over the computational domain in element level, in section 3.4 and Appendix A.3.2. The mesh geometry is represented by curvilinear tetrahedrons. The details about the used solver (e.g. direct solver) will be discussed in the following sections.

5.2 Measurement of Error Estimation for Helmholtz Equation

In this Section, the performance of Legendre type basis applied on three-dimensional problems will be assessed by the candidate analytical solutions. The most rigorous and robust combination of computational algorithms will be identified through numerical analysis.

5.2.1 Introduction

The main idea of error analysis is to find the optimal numerical scheme that facilitates fast frequency sweep for acoustic applications. There are two main categories of error estimator: *a priori* and a posteriori. The *a priori* error estimator is the estimation of the exact error before we reach the approximation solution, based on known information about the exact solutions in object specific norms [34].

This type of estimator merely gives the rough information about how the asymptotic behaviour of the exact error changes with respect to the mesh parameters (broadly speaking, an upper or lower bound of the exact error), but it does not provide the concrete quantity of the error.

Several basic algorithms for *a posteriori* error estimators were developed in the early 1990s, most noticeable of which was that result obtained by Verfüth in [321] for the Stokes problem and the Navier-Stokes problem. The major drawback of *a posteriori* error estimators is that they require knowledge of the finite element solution prior to the estimated error. In [13], Ainsworth gives a detailed comparison between different types of error estimators, whilst clarifying the requirements and criterions to be satisfied for standard error estimators. The analysis of *a posteriori* error estimators can be found in Appendix B.

The paramount issue for the Helmholtz equation is the dispersion effect that depends highly on the size of the wavenumber [123]. As the wavenumber is increased, the Helmholtz type Elliptic equation loses its coercivity [235]. The dispersion effect is a function associated with f, h, p and the number of DOFs which converges at

the order of $\mathcal{O}\left(k\left(\frac{kh}{2p}\right)^{2p}\right)$ [183]. The dispersion effect can be improved by careful choice of some periodic shape functions, modification of bilinear form and Fourier transform of the numerical quadrature for regular oscillators and the ultra-weak variational formulation (Iserles, Arieh in [186] and [185], Babuska and Sauter in [51], Gabard, Gamallo and Huttunen in [151], Wang, *et al.* in [327]). Despite these methods, incrementing the order of polynomial basis is proven to mitigate the pollution error at small computational cost and minimal size of result file [253]. Impressively, in recent research, Beriot, Prinn and Gabard proved the robustness of hierarchical approximation basis and showed that using higher orders can effectively reduce approximation error with minimal effort. They also developed a p-FEM strategy by implementing *a priori* error estimator [72] that accounts for the wavenumber. Based on the definition of *a priori* error estimators, an effective hierarchical p adaptivity scheme with minimal computational cost can be derived, which can locally enrich the approximation space of individual elements in a mesh.

5.2.2 Pollution Error and Mesh Resolution

Generalization of the actual error for finite element solutions involve three factors: namely the amplitude (A_0), the frequency and the phase.

There are two main types of error in acoustic problems, these are the interpolation and pollution errors for non-coercive Elliptic type equations (e.g. Helmholtz equation with large wavenumber). The foregoing discussion shows that the deleterious effect of high wave number increases significantly with the increasing dimension of the problem, thus in three dimensions, even $k = 5$ is sometimes considered a high wave number with respect to the size of the computational domain and leads to prohibitive computational effort [183, 293] . The pollution error (phase error) directly affects the frequency and phase of finite element solutions. The scale of the computational domain is highly correlated with the wavenumber, since the number of waves per elements inside the domain dominates the resolution of the numerical solution. If the measure of the wavenumber ka is envisaged where a represents the size of the computational domain (e.g. $area(\Omega)$ or $diameter(\Omega) = D$), then, the numerical comparison can be performed with a fixed number of ka as a measure in advance. In most cases, $a = D$ represents the diameter of the spherical domain.

The linear approximation of the acoustic potential Φ requires the mesh size to be of order $\lambda/10$ and suffers from the pollution error and dispersion effects for high wavenumbers (Ihlenburg and Babuska [182, 183]). In general, in order to reach a satisfactory accuracy, the required number of grid points are 20-30 per wavelength [252]. There is a well known a "rule of thumb" for linear shape functions:

$$k^3h^2 = \text{constant} \tag{5.17}$$

where h denotes $h = max_{i\subset N}h_i$, which means that the accuracy of the numerical solution depends on the number of elements per wavelength. To achieve a sufficient amount of elements, intuitively speaking, $k^2h \ll 1$ is preferable for the pre-asymptotic range. Although the dispersion can be eliminated by modifying the classic Galerkin method in one dimension, it is still unavoidable in higher dimensional problems [45] [51]. Throughout this Chapter, we will use the ideal mesh

resolution $\tau = \frac{\lambda}{h} \approx 10$ as a criterion for the mesh resolution with respect to the wavelength [182, 183]. In three-dimensional problems, we average the maximum edges of each element to formulate the physical resolution measure as:

$$\tau = \frac{c}{h_{max} f_{max}} \tag{5.18}$$

where the maximum frequency f_{max} allowed for specific mesh is related to the maximum element size $h_{max} = \frac{\sum_{i=1}^{N} h_i^{max}}{N}$, N is the total number of elements on domain. In case of higher order approximation basis, the number of degrees of freedom for an edge element are $np + 1$ where n is the total number of discretized parts. Thus, the number of degrees of freedom per wavelength is $\frac{(np+1)\lambda}{nh}$. When $n \to \infty$, asymptotically, we have:

$$\tau_l = \frac{cp}{h_{max} f_{max}} \tag{5.19}$$

such that the number of DOFs per wavelength becomes $D_\lambda = \frac{\lambda p}{h}$. The mesh resolution τ_l provides us a simple measure for selecting mesh and frequency. The wavelength that satisfies the mesh resolution measure guarantees that the current mesh can capture the important features of the problem. Subsequently, a theoretical optimal element size design for higher order FE can be achieved:

$$h_{max} = \frac{p2\pi}{kD_\lambda} \tag{5.20}$$

.

As previously mentioned, there is a simple constraint condition applied to the size of the linear element h given as $k^2 h \ll 1$, for any relatively large k (criterion depends on specific problem). Since the exact error is bounded by the product of the derivatives of the exact solution: $|u - u_{fem}| \leq \left[\overline{C_1}\left(\frac{h}{2p}\right)^p + \overline{C_2} k \left(\frac{hk^{\frac{1}{2}}}{2p}\right)^{2p}\right] |u|_{p+1}$. Hence, *a priori* error bound for the global relative error in H^1 semi-norm is defined as:

$$\frac{|u - u_{fem}|}{|u|} \leq C_1 \left(\frac{kh}{2p}\right)^p + C_2 k \left(\frac{kh}{2p}\right)^{2p} \tag{5.21}$$

where p denotes the polynomial order here, and the constants C_1, C_2 are independent of wave number and mesh size [156, 180].

Asymptotically, the relative error bounded in the H_1-seminorm consists of two parts: the first term reflecting the error of the best approximation (interpolation error) and the second term indicating the phase difference between exact and finite element solutions (pollution error and dispersion effect). The pollution error is caused by the difference between the theoretical k and $\bar{k}$ as it appears in the numerical simulation. The above equation relates to h & p adaptivity and states that p enrichment leads to much faster convergence (exponentially) than the h refinement (sub-linear). In general, the error will remain at the same level as long as $\xi = \left(\frac{kh}{2p}\right)$ is kept constant.

There is no doubt p adaptivity ($p \geq 2$) can reduce the pollution error, relative to the interpolation error, for sufficiently small h (i.e. $\frac{kh}{2p} < 1$). In situations

of high resolution with small values of kh, the convergence rate is dominated by the interpolation error. The relative error converges asymptotically at a rate of $\mathcal{O}(kh/2p)^p$. Consequently, if we have sufficient mesh resolution conditions, the results error obtained from subtracting the finite element solution from the best approximation solution will be the pollution error itself.

In [9], Anisworth provided the explicit form of the pollution error occurring in h & p finite elements. Especially for the well-resolved model which satisfies the simple constraint condition $k^2h \ll 1$, its relative pollution error can be given as

$$\frac{k_h - k}{k} = -\frac{1}{2}\left[\frac{p!}{(2p)!}\right]^2 \frac{(kh)^{2p}}{2p+1} + \mathcal{O}((kh)^{2p+2}) \tag{5.22}$$

where k_h is the discrete wavenumber. Eqn. (5.22) dedicated to the analysis such that the pollution error decreases significantly faster than the interpolation error, though it is only a local effect since it indicates the error occurring in a single wavelength. In contrast, a single wave will travel through many wavelengths in the computational domain for many physical problems, particularly when solving multiple high frequencies sweep acoustic problems. These accumulated errors are known as dispersive effect in the global sense, it is denoted by an additional k in the second term of Eqn. (5.21).

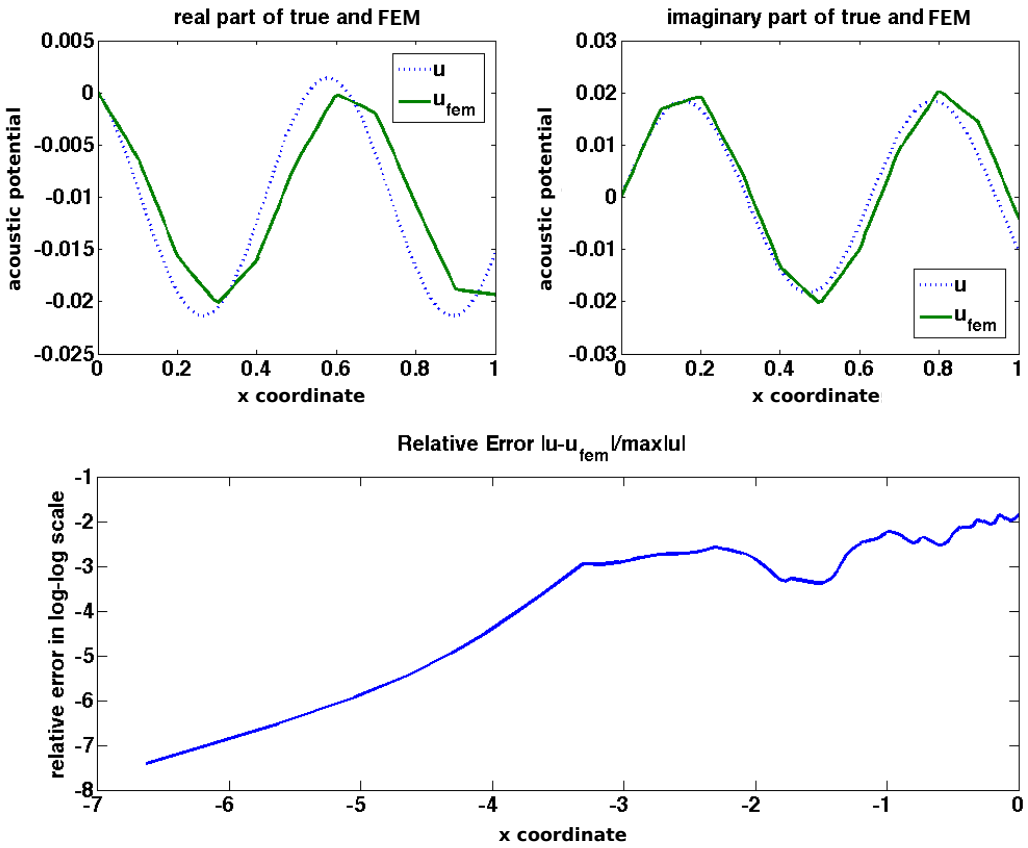

Figure 5.3: Visualisation of pollution error and relative error in L_∞ norm, Helmholtz problem in 1D with $k = 10$, $h = 0.1$, $x = [0, 1]$

In what follows, the Helmholtz problem in Eqn. (A.40) from Appendix A is solved on a unity edge element, in both Figures 5.3 and 5.4.

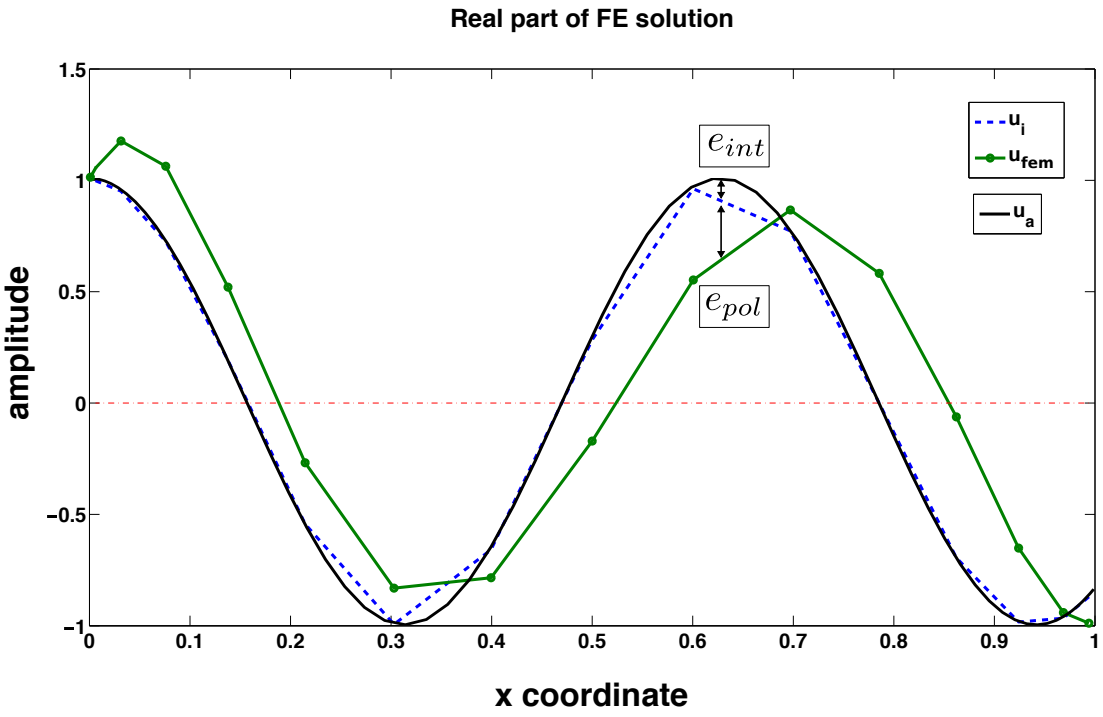

Figure 5.4: Visualisation of pollution error in real FE solution, Helmholtz problem in 1D with $k = 10$, $e_{int} = u_a - u_i$, $e_{pol} = u_i - u_{fem}$

Pertaining to Figure 5.3, we can see a phase shift for both real and imaginary part of the numerical solution. This is a vivid realization of the deleterious effects of high wave number on approximation error. In order to explain the concept of pollution error, in Figure 5.4, the real part of the FE solution is presented with the additional linear interpolated solution denoted as u_i. It is mainly the wavelength dispersion within the FE solution that results in the pollution error and the difference from the exact solution. Again here, the shift in wavelength is seen to accentuate along the propagation direction. We will see this effect in higher dimensional problems as well.

In [256], the authors proved the asymptotically superior properties of the Lobatto shape functions over the other types of shape functions (Hermite, Lagrange and Bernstein) by examining their condition number, number of non-zero entries and number of degrees of freedom related to L_2 error in 1D applications. Moreover, Bernstein type basis functions perform sub-optimally compared to all other shape functions and matrix assemblies, but it is not hierarchic and well conditioned and so is inadequate for frequent frequency sweeps. However, the performance of the proposed method in three-dimensional problems with larger frequencies were not included in their assessments.

5.2.3 Relative Error in Sobolev Space Norms

To determine the accuracy and efficiency of our finite element method, an accurate error estimation technique is required. The typical error level required for conventional engineering applications is 1% [342, 131]. Recall that the L_2 and H^1 norms are widely used in finite element literature [83], these norms are sufficient enough to measure the error itself once the analytical solution is known. Nevertheless, the total error itself is meaningless without a reference contrast. Hence, we define the global relative error as the percentage of error in the domain of interest with respect to the exact solution [116].

$$\eta_{L_2} = \frac{\|u_{fem} - u_{ref}\|_{L_2(\Omega)}}{\|u_{ref}\|_{L_2(\Omega)}} \tag{5.23}$$

is the global relative error in L_2 norm. Consequently, η_{H^1} is the relative error in H^1 norm by replacing the norms,

$$\eta_{H^1} = \frac{\|u_{fem} - u_{ref}\|_{H^1(\Omega)}}{\|u_{ref}\|_{H^1(\Omega)}} \tag{5.24}$$

for global error is the sum of errors contributed from all elements in domain: $\|u_\epsilon\|_\Omega = \|u_{fem} - u_{ref}\|_\Omega = \sum_{i=1}^{N} \|u_{fem} - u_{ref}\|_{\Omega_e}$. In addition, the error in H^1 norm is equal to the error of the numerical solution plus the error in the gradient of the solution: $\|u_{fem} - u_{ref}\|_{H^1(\Omega)} = \sqrt{\|u_{fem} - u_{ref}\|^2_{L_2(\Omega)} + \left\|u'_{fem} - u'_{ref}\right\|^2_{L_2(\Omega)}}$. The norm of the solution in each element is expressed as:

$$\|u_\epsilon\|_{\Omega_e} = \left[\int_{\Omega_e} u_\epsilon \cdot u_\epsilon d\Omega_e\right]^{\frac{1}{2}} \tag{5.25}$$

If we elaborate the best approximation of the exact solution $u = \Phi$ to be $u_{BA} = \Phi_{BA}$ in $H^1(\Omega)$, the best approximation error in space $V = H^1(\Omega)$ with respect to the finite element solution space V_h can be recognised as:

$$\|u - u_{BA}\| = \inf_{u_{fem,} \in V_h} \|u - u_{fem,}\| . \tag{5.26}$$

The above equation can be minimised by computing $u_{BA} \in V_h$ as following:

$$\int_\Omega N^T N u_{BA} d\Omega = \int_\Omega N^T u d\Omega \tag{5.27}$$

Solving for u_{BA}, we have the best approximation of the exact solution of the Helmholtz problem. For sufficiently rich p, the best approximation denoted as $u^{(p)}_{BA}$, we have

$$\kappa = \left\|u^{(p)}_{BA} - u^{(p)}_{fem}\right\| \tag{5.28}$$

which represents the error of the dispersion effect with optimal p, where the norm can be any norm of desired quantity [249]. In other words, for the best approximation solution with optimal h and p, denoted as $u^{(hp)}_{BA}$, we have

$$\|u - u_{fem}\| \approx \left\|u^{(hp)}_{BA} - u_{fem}\right\| \tag{5.29}$$

In addition, if there exists a constant $\eta \propto k$ (η is proportional to k) and independent of h, for sufficiently small k^2h

$$\|u - u_{fem}\| \leq \eta \|u - u_{BA}\| \tag{5.30}$$

defines an upper bound for the finite element approximation error (contains dispersion effect).

5.3 Monochromatic Wave Problems with Analytical Solutions

Monochromatic waves have a single frequency f and time dependent phase, hence they have a single wave number $k(\mathbf{r})$ that may depend on the position of the material but not on time. The monochromatic wave Helmholtz equation is regarded as a steady state version of the wave equation. Before we apply our acoustic solver on time-dependent high frequency applications , it is important to assess both the accuracy (error and convergence rate) and efficiency (computational time, memory, speedup, efficiency) of the codes using numerical tests.

In this section, we restrict our attention to low frequency problems to establish key properties of the proposed method. Several three-dimensional benchmark examples are studied and results are verified with reference to analytical solutions. In particular, the problem of a plane wave impinged on the sound hard surface of a sphere [180] is shown, where solution convergence, for both geometry and physical fields is analysed in detail. Moreover, error estimates and numerical efficiency of *hp*-adaptivity in context of the Helmholtz equation is investigated.

5.3.1 Wave Guide Problem

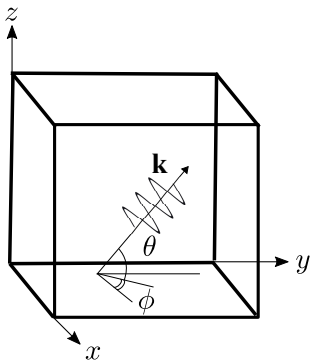

Figure 5.5: 3D wave guide

Suppose there is a three dimensional square domain $\Omega = (0, 2) \times (0, 2) \times (0, 2)$ as shown in Figure 5.5, with mesh resolution h_{max}. The problem is formulated

as in equation (5.13) such that the function g_i is chosen specifically to satisfy the condition for the analytical solution to be a plane wave

$$\Phi = e^{\mathbf{ik}\cdot\mathbf{r}} \tag{5.31}$$

with $\mathbf{k} = k\{cos(\theta)cos(\phi), cos(\theta)sin(\phi), sin(\theta)\}$, where $\theta \in [0, \pi]$ is the polar plane wave propagating angle, while $\phi \in [0, 2\pi]$ is the azimuthal angle of the wave.

5.3.2 Impinging Spherical and Cylindrical Scatterer

Consider an exterior boundary value problem like equation (5.12). We are seeking a solution $\Phi(r, \theta, \phi)$ with spherical coordinate system as shown in Appendix A.5. Assuming the acoustic scatterer is a sphere with radius a, through the derivation stated in many text books (e.g. [180]), we arrive at the analytical solution

$$\Phi_S(r, \theta, \phi) = \sum_{n=0}^{\infty} \sum_{m=0}^{n} h_n(kr) P_n^m(cos\theta)(A_{nm} \cos(m\phi) + B_{nm} \sin(m\phi)) \tag{5.32}$$

where h_n is the spherical Hankel function of the first kind, and P_n^m denotes the Legendre function (see Abramowitz [4] for details, it explicitly explains numerous types of mathematical functions with oscillating properties). Suppose Φ_S is a radiating solution of the Helmholtz problem in the exterior domain $|\mathbf{x}| \geq a$, thus the series solution (5.32) converges uniformly and absolutely to the exact result in every such closed and bounded domain.

Our computational domain is "truncated" to the hollow sphere with $\Omega = \{\mathbf{r} \in \mathbb{R}^3$ $: a < |\mathbf{r}| < \gamma\}$ where γ should be as far as possible. In spherical coordinates, the incident wave can be written as

$$\Phi_I(r, \theta) = \Phi_0 \sum_{n=0}^{\infty} (2n + 1) \mathrm{i}^n P_n(\cos\theta) j_n(kr) \tag{5.33}$$

where j_n is the spherical Bessel function of the first kind. Or equivalently, $\Phi_I(r, \theta) = \Phi_0 e^{\mathrm{i}kr\cos\theta}$ as an incident wave travelling in the z direction. Moreover, the coordinate transformations are:

$$x = r \sin\theta \, cos\phi \tag{5.34a}$$
$$y = r \sin\theta \, sin\phi \tag{5.34b}$$
$$z = r \cos\theta \tag{5.34c}$$

where radius $r \in [0, \infty)$, inclination $\theta \in [0, \pi]$ and azimuth $\phi \in [0, 2\pi]$ for a Cartesian coordinate transformed from spherical coordinate system as illustrated in Appendix A.5. We will use these analytical forms throughout the following chapters. Since the impinging hard cylinder example is just a 2D extension from the above equations by changing the spherical Bessel and Hankel function to cylindrical form, it will not be repeated here for simplicity. Details can be found in [180].

In the case of a rigid obstacle, we have the Neumann BC as in equation (5.12b)

$$\left.\frac{\partial \Phi_I}{\partial r}\right|_{r=a} = \Phi_0 \sum_{n=0}^{\infty} (2n+1)\mathrm{i}^n P_n(\cos\theta) \left.\frac{\partial j_n(kr)}{\partial r}\right|_{r=a} \tag{5.35}$$

Hence, our scattered field of acoustic potential is obtained by setting

$$B_{nm} = 0 \ \forall n, m \tag{5.36a}$$

$$A_{nm} = 0 \ \forall m \geq 1 \tag{5.36b}$$

$$A_{n0} = A_n = \frac{\Phi_0 (2n+1)\mathrm{i}^n \left.\frac{\partial j_n(kr)}{\partial r}\right|_{r=a}}{\left.\frac{\partial h_n(kr)}{\partial r}\right|_{r=a}} \ \forall n \geq 1. \tag{5.36c}$$

Therefore, equation (5.32) is altered to:

$$\Phi_S = \sum_{n=0}^{\infty} h_n(kr) P_n^m(\cos\theta) A_n \tag{5.37}$$

Analogously, the expression of member functions for a sound-soft scatterer is:

$$B_{nm} = 0 \ \forall n, m \tag{5.38a}$$

$$A_{nm} = 0 \ \forall m \geq 1 \tag{5.38b}$$

$$A_{n0} = A_n = \frac{\Phi_0 (2n+1)\mathrm{i}^n \left. j_n(kr)\right|_{r=a}}{\left. h_n(kr)\right|_{r=a}} \ \forall n \geq 1 \tag{5.38c}$$

5.4 Polychromatic Wave Problem

Problems with acoustic waves propagating from one medium to another medium are very important in a variety of micro - fluidic engineering applications, as mentioned in the first chapter of this report. In the hypothesis of wave propagation in both temporal and spatial domains, the problem of waves propagating through different media with multiple time scales demand a time dependent acoustic solver whose input signal can be of arbitrary shape and length.

In the preceding sections, we have explained the formulation and solver for the time harmonic Helmholtz equation. In this section we will introduce the Fourier transformed wave equation based on the fundamental procedure of solving the time harmonic Helmholtz equation.

Polychromatic (transient) waves are non-monochromatic. They can be seen as a superposition integral of time harmonic waves with different frequencies, amplitudes, and phases by the nature of Euler's formula and identity. Thanks to the Discrete Fourier transformation, the polychromatic wave coming from an arbitrary signal can be decomposed into a series of monochromatic waves of different frequencies within each time step [281]. The brief concept of acoustic problems are presented in tree view in Flowchart 5.6.

Regarding the monochromatic property of the Helmholtz equation, they are required to be solved for polychromatic wave problems n times dependent on the temporal resolution during the computational process where n equals the number of time steps and the related $\mathbf{F}_n(k)$ (right hand side vector) after the forward Fourier transformation. Meanwhile, the robustness of the Helmholtz equation is preserved in each time step. Nevertheless, in solving for the polychromatic wave problem through the Helmholtz equation, the amount of effort is still less than solving the wave equation directly from both a computational and theoretical perspective. 1) we have a 3D instead of 4D problem, we avoid solving the additional system of linear equation (please see Appendix C: time dependent Thermal problem for references) 2) we may enable a small interval between time steps without adopting time integration techniques, 3) it is easy to set an input signal as BCs in the time domain instead of periodic BCs for the Wave equation. Alternatively, the wave equation needs periodic boundary condition to represents a time varying signal [138].

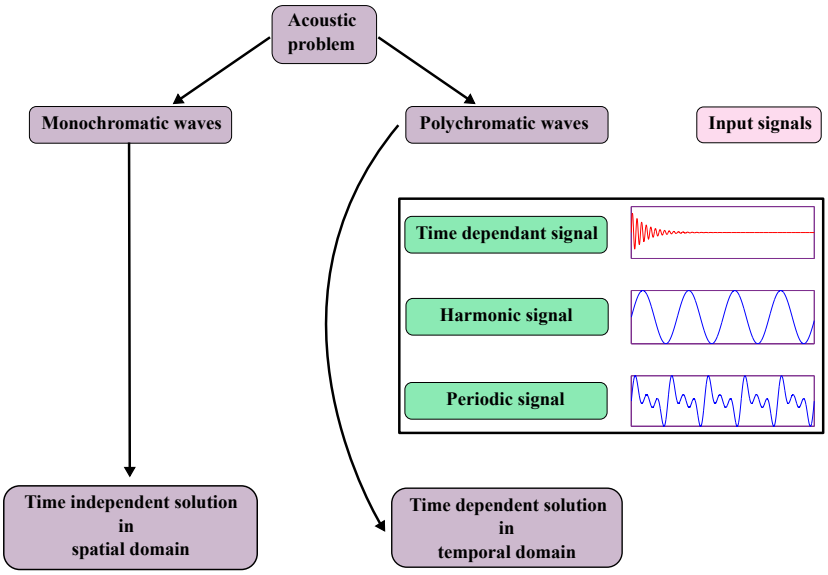

Figure 5.6: Concept of acoustic problems

In addition to the wave number k and the material coefficients (e.g. velocity of waves, density of substrate), when solving an acoustic finite element model one should have extra parameters for time dependent waves: (1) Signal duration, $T = \frac{1}{f^P} = M\Delta t$ is the duration of the signal profile over the full time period. Since T is a constant that is defined at the beginning of a calculation, we can change the time resolution by changing M to N i.e. the number of time steps. (2) Signal length, $\lambda = \frac{c}{f^P}$ is the length of the signal periodically (note that f^P is the frequency of input signal, it should be distinguished from the series of frequencies after Fourier transformation).

5.4.1 Implementation Procedures

A considerable amount of the relevant literature emphasises the importance of the Fourier transformation family, such as discrete FT, fast FT, Fourier Series, etc. Hence, this section will be dedicated to the procedure of implementing the

polychromatic wave with the Helmholtz equation through finite element calculation [228]. Since the continuous Fourier transformation converts a signal from the time domain with infinite duration into frequency domain with infinite sinusoidal waves, we will adopt the feasible discrete Fourier transformation in subsequent texts.

1) Firstly, an arbitrary wave profile (signal) is provided in the time domain. We apply the discrete Fourier transformation (forward FFT) to this profile, which results in a spectrum in the frequency domain. As depicted in Figure 5.7, the series of waves in the frequency domain are represented by a spectrum. Thanks to the theory of Euler's equation, the wave profile has been decomposed into M monochromatic waves (sine and cosine) with M envelopes and frequencies corresponding to the Discrete Fourier transformation with M points. (e.g. a cosine wave in time domain transferred into frequency domain will be denoted by a single peak) Henceforth, we can consider each monochromatic wave as an incident wave impinging on the boundary of the obstacle as shown in Figure 5.8. For instance, a series of wave profiles $a(t_m)$ for $m \in [0, \dots M-1]$ through the forward Discrete Fourier transformation.

$$A_0(f_n) = \sum_{m=0}^{M-1} a(t_m) e^{-\mathrm{i}2\pi f_n t_m/M} \text{ for } n \in 0,1,2,3,\dots,N-1 \; m \in 0,1,2,3,\dots,M-1 \tag{5.39}$$

where we have the envelope $A_0(f_n)$ and $k_n = \frac{2\pi f_n}{c}$, for $M = N$.

2) Secondly, evaluate the incident wave for each frequency f_n, position vector $\mathbf{r}$, amplitude A_0 and direction $\mathbf{d}$,

$$\Phi_I^P(t_n) = \frac{1}{N} \sum_{m=0}^{min(M-1,N-1)} A_0(f_n) e^{\mathrm{i}k_n \mathbf{d}\cdot\mathbf{r} + \mathrm{i}\varphi} = \frac{1}{N} \sum_{m=0}^{min(M-1,N-1)} \Phi_I(t_n) e^{\mathrm{i}\varphi} \tag{5.40}$$

where φ is the phase of the incident wave defined inductively as:

$$\varphi = 2\pi f_m \frac{c\ \Delta t\ t_n}{\lambda} \tag{5.41}$$

for $\Delta t = \frac{T}{N}$, N can be either $0 < N \leq M$ or $N > M$, and $\Phi_I(t_n)$ is the incident wave type chosen (plane wave, spherical wave, etc.). Thereafter, we project the incident wave field into the computational domain, such that now the incident wave field is defined in both space and time $\Phi_I^P(\mathbf{r}, t_m)$.

3) In the third stage, we impose the required boundary condition on the artificial boundary and the boundary of the scatterer with respect to each time step within N. The corresponding boundary conditions in (5.1a) and (5.12b), (5.12c) can be modified to the Neumann (Dirichlet) BC:

$$\left(\frac{\partial \Phi_S}{\partial n} + \sigma \Phi_S\right)\Big|_{\Gamma_D} = \Phi_I \text{ for } \sigma \to \infty \tag{5.42}$$

$$\left(\frac{\partial \Phi_S}{\partial n} + \mathrm{i}\sigma \Phi_S\right)\Big|_{\Gamma_N} = \frac{\partial \Phi_I}{\partial r}, \text{ for } \sigma \to 0 \tag{5.43}$$

The boundary conditions on the surface of an obstacle are calculated for a series of k_n with respect to frequency (f_n), it gives us the right hand side vector $\mathbf{F}_n(k)$ for our linear system of equations. In addition, the non-reflecting boundary conditions of equation (5.12d) are also calculated and stored into a system matrix (in case of exterior boundary value problems).

4) Finally, the series of right hand side $\mathbf{F}_m(k)$ is transferred to the frequency domain through the forward DFT. The left hand side stiffness and mass matrices are evaluated for various k_n. In the final step, after solving the system of linear equations, the inverse Fourier transformation will be applied to the solution vectors of $\Phi(k_n, \mathbf{r})$, and then projected to each meshes corresponding to t_n. To be elaborated, the weak formulation of the polychromatic wave Helmholtz problem in the frequency domain will be fully addressed in the following section.

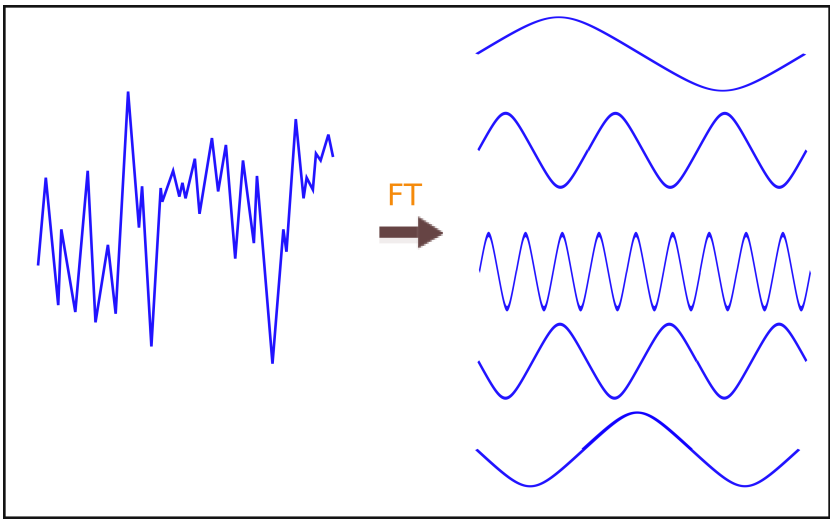

Figure 5.7: Fourier transformation decomposing the wave profile into spectrum

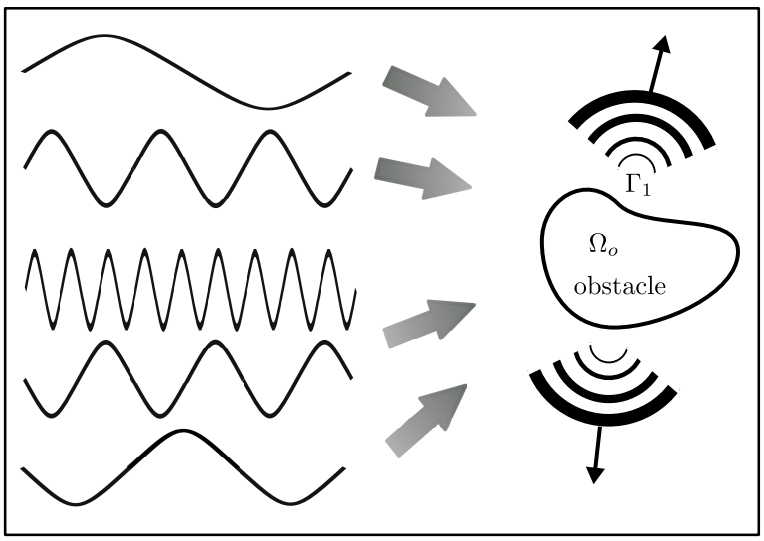

Figure 5.8: Multiple incident waves impinging on the scatterer and radiation waves, in spatial domain

5.4.2 Weak Variational Formulation of the Governing Equation

Following the discussion in section 5.1.2, the variational formulation for the polychromatic wave acoustic problem is described as:

$$\begin{cases} \text{Find } u \in H^1(\Omega), & \text{such that} \\ \mathfrak{a}(u_{k_n}, v_{k_n}) = \mathfrak{f}(v_{k_n}) & \forall v_{k_n} \in H^1(\Omega) \end{cases}$$

where $\mathfrak{a}(\cdot,\cdot)$ is the symmetric bilinear form based on $H^1(\Omega) \times H^1(\Omega)$, ($u_{k_n}$ is the finite element solution of $\Phi_S(k_n)$ from trial spaces for consistency) expressed as:

$$\mathfrak{a}(u_{k_n}, v_{k_n}) = \int_\Omega \nabla u_{k_n} \cdot \nabla v_{k_n} d\Omega - k^2 \int_\Omega u_{k_n} v_{k_n} d\Omega \tag{5.44a}$$

$$+ \sigma_1 \int_{\Gamma_1} u_{k_n} v_{k_n} d\Gamma + \sigma_2 \int_{\Gamma_\infty} u_{k_n} v_{k_n} d\Gamma \tag{5.44b}$$

$$\mathfrak{f}(v_{k_n}) = \int_\Omega f v_{k_n} d\Omega + \left(\Phi_I(k_n) + \frac{\partial \Phi_I(k_n)}{\partial r} \right) \int_{\Gamma_1} v_{k_n} d\Gamma \tag{5.44c}$$

where $\sigma_2 = \mathrm{i}k_n - \frac{1}{2r}$ is the BGT like BC applied on a non-reflecting boundary. Generally, σ_1 and σ_2 are admittance coefficients corresponding to the material of surfaces Γ_1, Γ_∞. The linear system of equations required to be solved is:

$$\mathbf{K}_n \mathbf{U}_n = \mathbf{F}_n(k) \tag{5.45}$$

where the above equation set is solved for $n = N$ frequencies considered here. Once the results are computed, we then apply the inverse Fourier transformation to transfer the radiation potential as well as the incident potential (if required by the specific problem) back to the time domain. With that at hand, the various physical fields based on the acoustic potential can be calculated and stored as a series of tensors and projected on the mesh. For example, we can calculate Reynolds' stress and acoustic radiation pressure based on particle velocities for which they drive the fluid into motion at the slow time scale. The Reynolds stress is calculated from the acoustic potential by averaging velocities [216] in the final chapter. The detailed procedure devised to treat the case of polychromatic waves is shown in Diagram 5.9 as well.

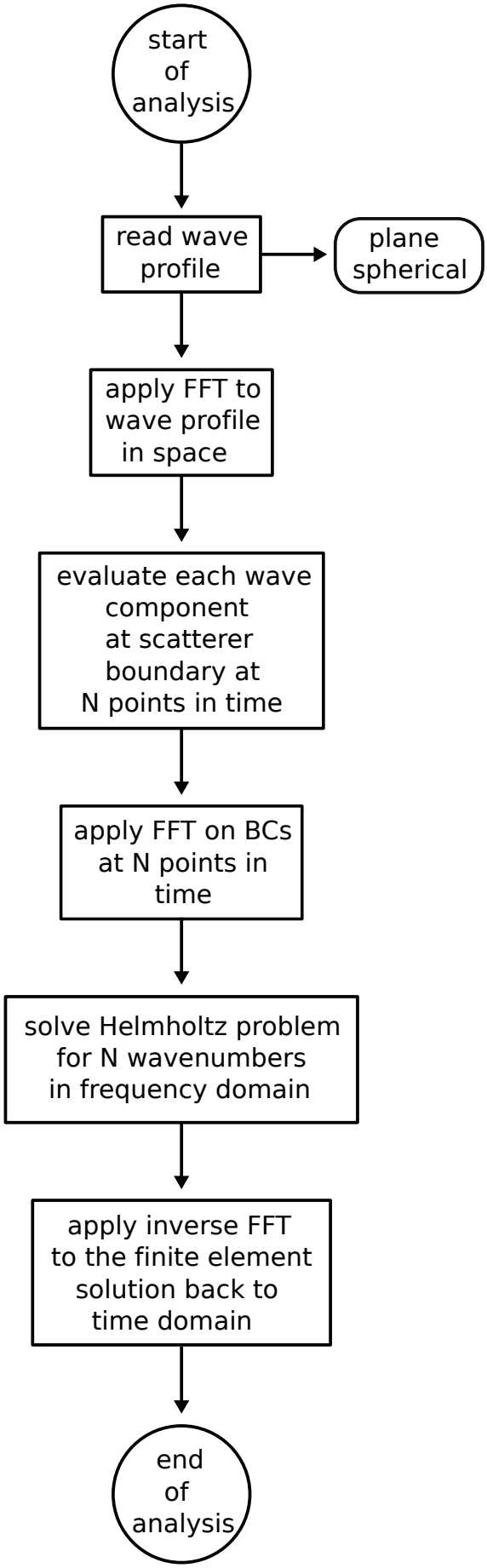

Figure 5.9: Flowchart of polychromatic wave problem solved by Helmholtz equation

5.5 Numerical Analysis and Error Estimation Assessments

5.5.1 Computational Procedure

In the pre-processor, a parameterised geometry with unstructured mesh containing tetrahedrons is required. The computational domain is discretized into either structured or unstructured meshes with simplexes with the unstructured conformal (no overlapping zones) meshes are preferred when subject to complex or curved geometries. The discretized mesh is then saved with proper boundary conditions assigned to the corresponding entities (e.g. surfaces). The mesh data could be easily generated by either Gmesh [157], Salome [68], Cubit [78] (the mesh generation software developed by Sandia National Laboratories) or other mesh generation software available on the market, such that 10 nodes tetrahedron is preferable.

The problem is solved using the Flexible Generalised Minimal Residual method (GMRES) as the main solver for the system of linear equations, and LU (iLU) factorisation as the pre-conditioner. Alternatively, we apply the MUltifrontal Massively Parallel sparse (MUMPS) direct Solver developed by Patrick *et al.* [21] to solve the problem with higher order approximation basis. All computational tools adopted, including the pre-conditioner, are tested to be the best combination of solvers for the Helmholtz equation and which will not be addressed here. In this work, hierarchical Legendre type shape functions are used to further increase the convergence speed of finite element solution [10, 296, 277]. Finally, Paraview is used to visualise the results.

The performance of the higher order FEM is often dependent on the specific types of application, geometry, wave directions, etc. For the sake of robustness, we will assess several benchmark problems including that of a wave-guide problem, and of plane and spherical waves impinging on hard/soft obstacles [169] in order to demonstrate the effectiveness of the acoustic solver. Hence, we can apply the acoustic solver to tackle the practical engineering application in the last Chapter.

In the numerical results below, we will neglect the numerical integration error as it can be eliminated by taking a sufficient number of gaussian points on each element (Grundmann-Moeller quadrature rule) [52].

All simulations are performed on the high speed multiple cores server built in the University of Glasgow (Intel Xeon hyper threading CPU E7- 4830 (2.13 GHz) with a maximum of 32 cores and two threads per core).

5.5.2 Numerical Results of Benchmark Problems

First of all, the plane wave guide problem is discussed. Figure 5.10 depicts the desired direction and distribution pattern of the plane waves inside a wave guide. Figure 5.11 exhibits the absolute acoustic potential distribution of a plane wave

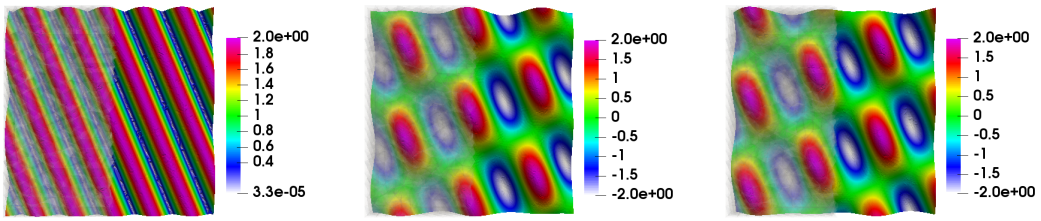

(a) Absolute potential (b) Real potential (c) Imaginary potential

Figure 5.10: Plane wave guide on 2×2 cube, total acoustic potential field $\Phi = \Phi_S + \Phi_I$, where $\theta = 45^o$, $\phi = 0^o$, $k = 10$, number of DOFs is 259778, and approximation order $p = 5$

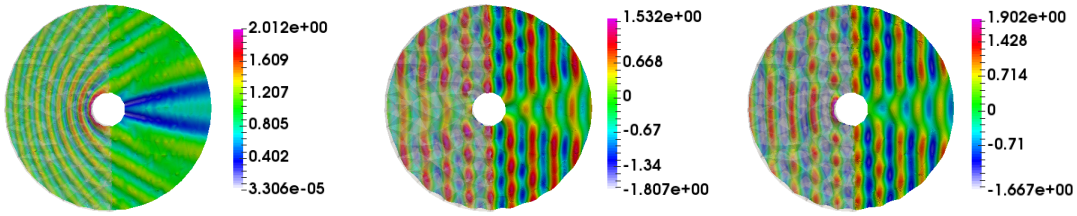

(a) Absolute potential (b) Real potential (c) Imaginary potential

Figure 5.11: Plane wave impinging a hard cylinder, total acoustic potential field $\Phi = \Phi_S + \Phi_I$, where $\theta = 180^o$, $\phi = 0^o$, $k = 10$, number of $DOFs$ is 21446, and approximation order $p = 3$, $r = 4, a = 0.5$

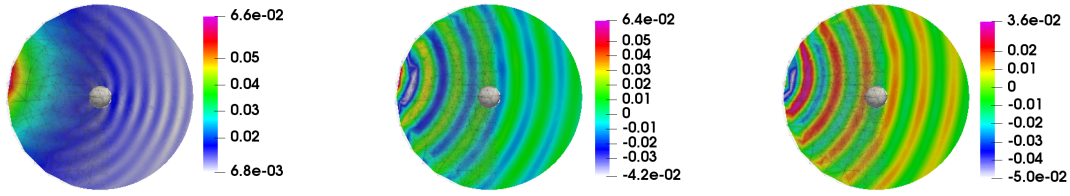

(a) Absolute potential (b) Real potential (c) Imaginary potential

Figure 5.12: Spherical waves from a point source impinging on a sound hard spherical scatterer, total potential Φ, where $a = 0.5$, $r = 3$, $k = 10$, number of $DOFs$ is 243337, and approximation order $p = 5$

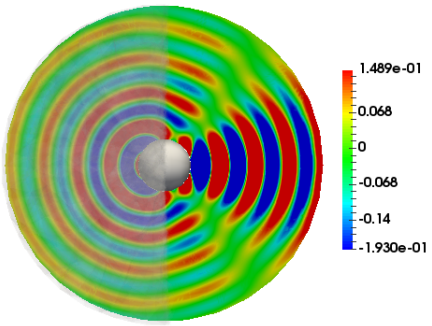

(a) Real potential

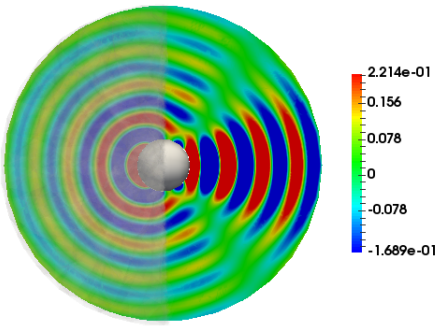

(b) Imaginary potential

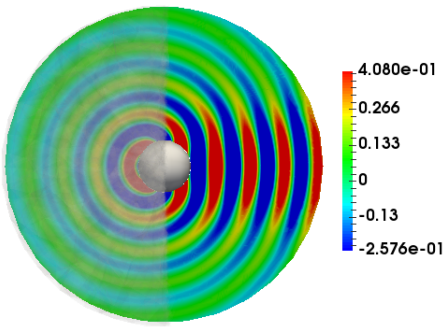

(c) Real potential

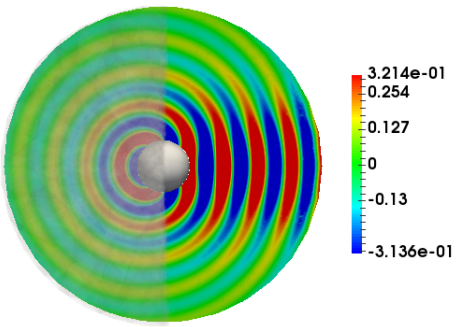

(d) Imaginary potential

Figure 5.13: Plane wave impinging on sound hard (a) - (b) and soft sphere (c) - (d), scattered potential Φ_S, where $a = 0.5$, $r = 3$, $k = 10$, number of $DOFs$ is 243337, approximation order $p = 5$

incident on the surface of an infinitely sound hard cylinder, where $a = 0.5$, $r = 4$ are radii of the cylinder and of the computational domain, respectively.

In Figure 5.12, the real and imaginary parts of the absolute potentials are shown, such that the absolute potential is the combination of incident waves from a point source $[-4.5, 1.0, 0.0]$ and the reflected waves from the sound hard scatterer. From Graphs 5.13, We can distinguish the sound hard and soft scatterers by looking at the scattering wave around the spherical obstacle, a rigid scatterer tends to deflect the wave from its original track while the absolute soft scatterer is penetrated by incident waves. Further to that, in Figure 5.14, the exact solution (EX) and FEM solution plotted against the positive x axis are shown, we can see good agreement between the solutions even with a coarse mesh and a few nodes per wavelength.

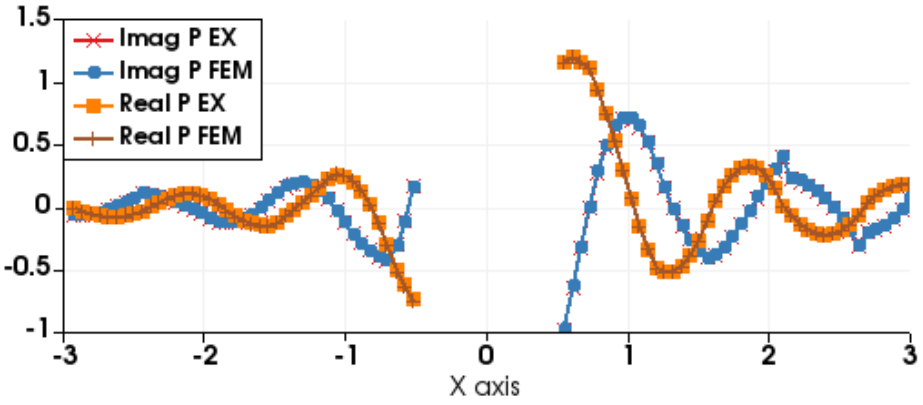

Figure 5.14: Central line plot over x axis for plane wave impinging on a sound soft scatterer. Acoustic potential exact solution (EX) and FEM solution against x coordinate, a = 0.5, r = 3

5.5.3 Numerical Results of Sound Hard Sphere Immersed in Water

In Figure 5.15 below, a sound hard spherical scatterer is immersed in water (density $= 998 kg/m^3$). A polychromatic signal with spherical pulse wave is generated in the temporal domain, where the total duration for one circle of signal (period) is approximately 423.38 μs. We discretized the continuous time duration into 8 steps. As shown in Figure 5.15, the non-symmetric acoustic pressure surrounding the spherical obstacle will be the primary driving force that moves the obstacle from left to right.

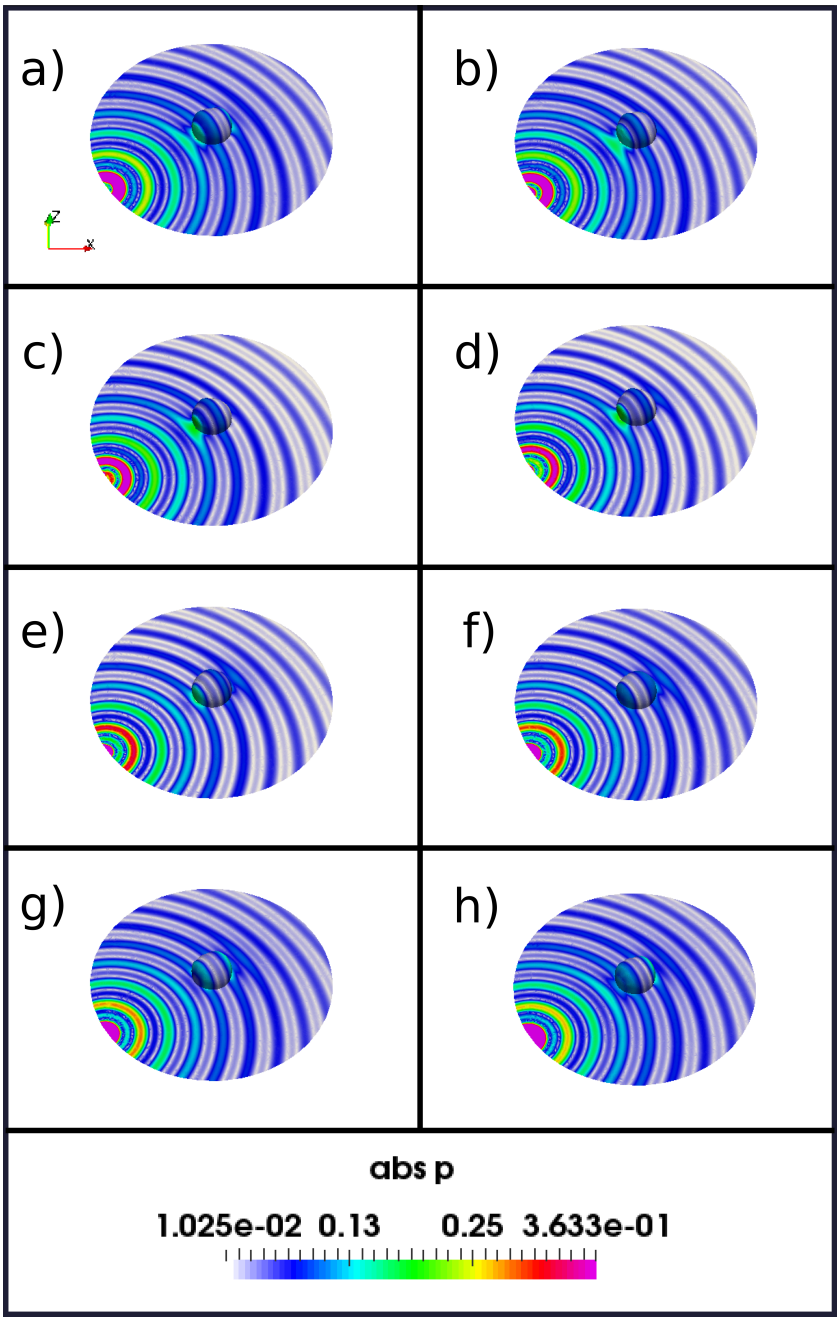

Figure 5.15: Polychromatic spherical wave impinging on a sound hard sphere immersed in water, total absolute potential (magnitude), $k = 12$, $a = 0.5$, $R = 4$, $A_0 = 1$. Pulse signal $[0, 1, 0]$, source $(-2.5, -1.80, 0.15)$, 8 discretized time steps

5.5.4 Numerical Results of Acoustic Problem by Submarine-like Shape in Deep Sea

The aim of this section is to demonstrate that the acoustic solver used in this thesis has the ability to analyse arbitrary signals in frequency space by applying Fourier transformations. This is a fundamental aspect for solving acoustic problems in industrial applications with unsteady arbitrary waves as input signal. The proposed practical problem presented in this section can be easily found in [316] and [312].

In this section, we apply the Neumann (Dirichlet) BC on the surface of the submarine, and BGT BC on the artificial boundary. As seen in Figure 5.17, since the geometry of the submarine is complicated, we are not able to obtain an analytical solution for the problem. Nevertheless, we can employ a simple *a posteriori* error estimator for the sake of numerical analysis of convergence, such as:

$$\frac{\Phi_{ref} - \Phi_{fem}}{\Phi_{ref}} \approx \frac{\Phi_{fem}^{h+m,p+n} - \Phi_{fem}}{\Phi_{fem}^{h+m,p+n}} \tag{5.46}$$

where $m, n \geq 1$. The refinement can take place where the errors are significant whilst keep the rest of the areas invariant. This process can be repeated until the estimated error is below the predefined error tolerance. For instance, the *a posteriori* p adaptivity scheme works as follows: increase the order +1 everywhere for the whole domain, calculate the estimated error on each element, and then keep the order +1 on 1/3 elements with the highest estimated error, and for the rest of the elements keep the original orders. Repeat the operation again by increasing the element orders by 1.

We run a small test with a single pulse wave [0,1,0] as input. The test model problem is identical to that published in [312], except that the geometry of the submarine was designed based on the "red October" as shown in Figure 5.16. The monochromatic wave problem is solved on the right hand side of Figure 5.17. From Figure 5.18, we can see the incident wave is propagating through the truncated spherical domain. Moreover, when the wave is impinged on the body of the submarine, it scattered radiating waves that are immediately diffracted by the incident waves.

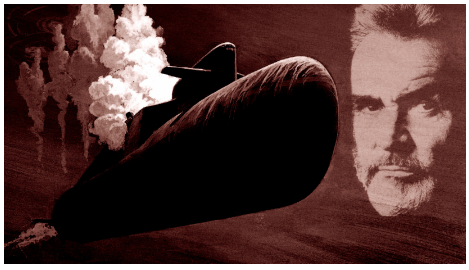

Figure 5.16: Red October submarine model

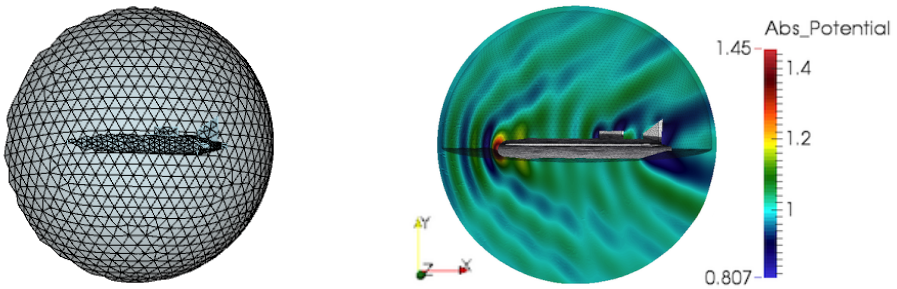

Figure 5.17: Geometry of exterior boundary value problem of pulse wave impinging on sound hard submarine and its numerical result. Absolute total potential Φ_{Abs}, where $R = 5$, $k = 6$, number of DOFs is 371422, and approximation order $p = 4$

5.5.5 Numerical Analysis of Wave Guide Problem

Preliminary numerical tests for this problem have been performed in [158] by Gillman. They have demonstrated that the relative error of this numerical example is highly affected by the propagation angle chosen, with the peak of the error being reached when the angle $\theta = 95^o$. Thus, we will assess the relative error in L_2 norm with three wavenumbers, via both h refinement and p enrichment, setting $\theta = 95^o$.

Firstly, we select a $2 \times 2 \times 2$ sides square cube. Then we fix its maximum mesh size $h_{max} = 0.25$, which generates a coarse mesh as depicted in Figure (5.19), and progressively increase the approximation order p from 1 - 6 with various k values (2, 5, 10). Thus, the classical mesh resolutions are $\tau = 12.5664$, 5.0264, 2.5132 respectively corresponding to Eqn. (5.18), which means we have very poor resolution for high wavenumebrs ($k > 5$) with $p = 1$ in this case. And the mesh resolution τ_l depicted in Table 5.1.

k	τ_l					
$k = 2$	12.5664	25.1327	37.6991	50.2655	62.8319	75.3982
$k = 5$	5.0265	10.0531	15.0796	20.1062	25.1327	30.1593
$k = 10$	2.5133	5.0265	7.5398	10.0531	12.5664	15.0796

Table 5.1: The mesh resolution τ_l for p enrichment, for the wave guide problem

Secondly, we run another test with p fixed at 2 (quadratic element), and slightly decreasing h_{max} in the sequence of $[0.5, 0.25, 0.2, 0.14, 0.0870, 0.0667]$. Finally, we can compare the rate of convergence between h and p refinements. For additional information of classical resolution τ are for $k = 2$: [6.2832, 12.5664, 15.7080, 22.4399, 36.1103, 47.1003]. For $k = 5$: [2.5133, 5.0265, 6.2832, 8.9760, 14.4441, 18.8401], and for $k = 10$: [1.2566, 2.5133, 3.1416, 4.4880, 7.2221, 9.4201]. The modified mesh resolution for h refinement is shown in Table 5.2.

The results in Figure 5.20a illustrate that even with high wavenumber ($k = 10$),

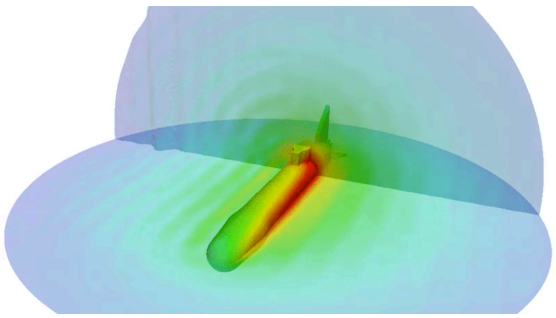

(a) 1st time step

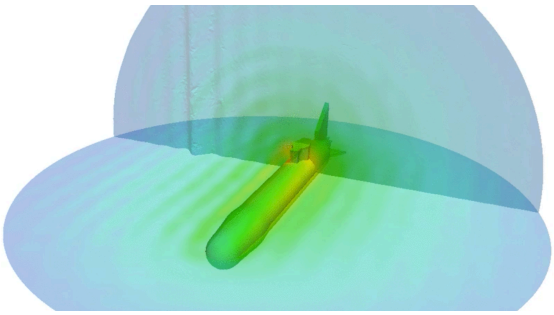

(b) 2nd time step

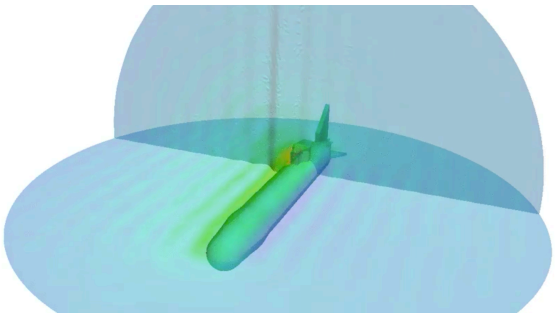

(c) 3rd time step

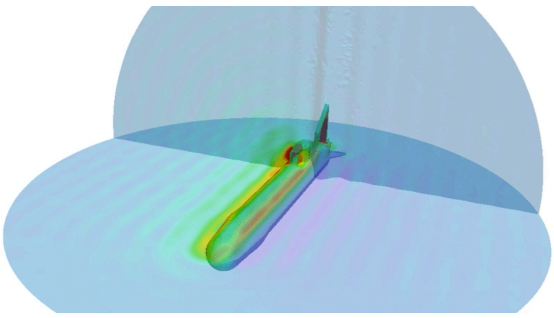

(d) 4th time step

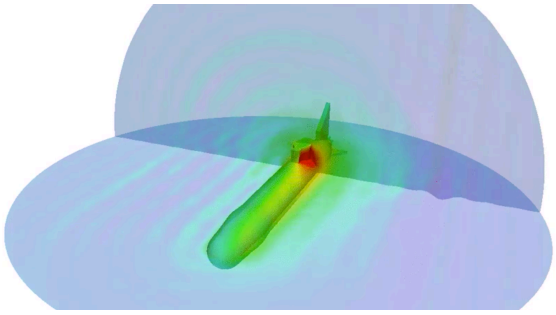

(e) 5th time step

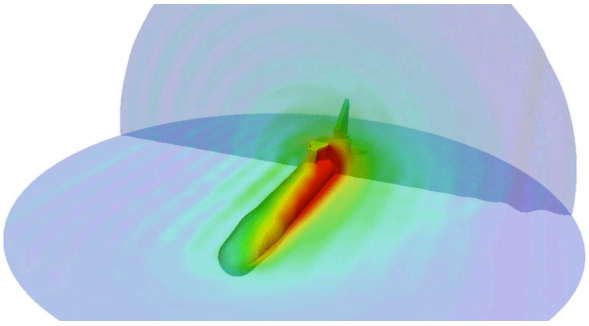

(f) 6th time step

Figure 5.18: Polychromatic wave signal incident on sound hard surface of a submarine, absolute acoustic potential Φ_{Abs}, where $a = 0.5$, $k = 10$, approximation order $p = 5$

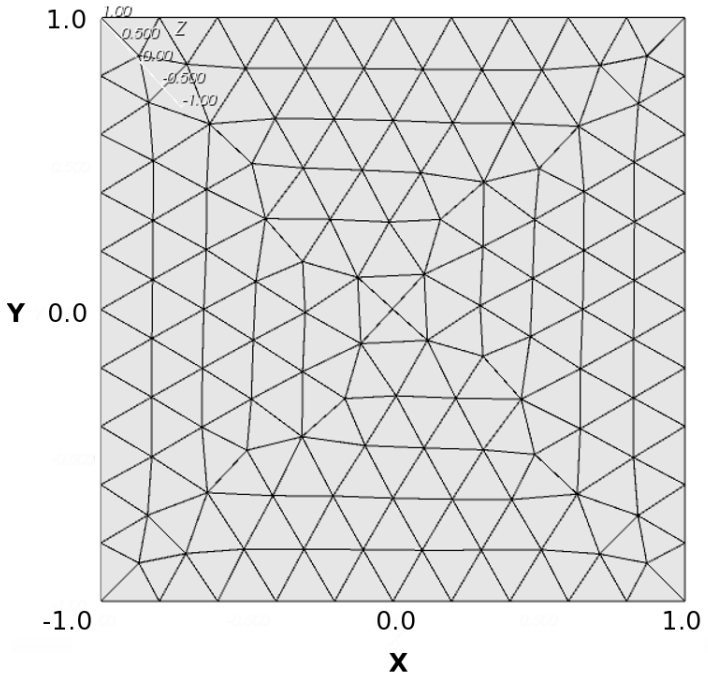

Figure 5.19: Unstructured coarse mesh for p convergence test

k	τ_l					
$k=2$	12.5664	25.1327	31.4159	44.8799	72.2205	94.2007
$k=5$	5.0265	10.0531	12.5664	17.9520	28.8882	37.6803
$k=10$	2.5133	5.0265	6.2832	8.9760	14.4441	18.8401

Table 5.2: The mesh resolution τ_l for h refinement ($p = 2$), for the wave guide problem

our FE solution exhibits monotonic exponential convergence with p enrichment. In contrast, Figure 5.20b shows linear convergence even with $p = 2$ at the earlier stage, and oscillatory behaviour of L_2 error in the pre-asymptotic range due to low mesh resolution. This discrepancy is natural and proves the finite element solutions are correct. The results L_2 error is low even for low τ and τ_l, at high k, which indicates the rule of thumb ($\tau \approx 10$) is no longer applicable for higher order elements.

Despite the fact we omitted the computational time table here, we can conclude that p enrichment converges faster than h refinement with the same number of DOFs in the Figure due to higher order elements. Roughly speaking, when log number of DOFs equals 4.4, the corresponding log relative L_2 error is approximately twice smaller when comparing p enrichment to h refinement due to higher order elements, this observation has practical importance when dealing with large computational domains. During the numerical analysis, we find that three elements per wave length are required to reach a 10% L_2 relative error for solving the acoustic wave guide problem with hierarchical shape functions, and mesh resolution of only 2.5 is required to achieve a error below 0.5% with cubic p. Overall, the p enrichment

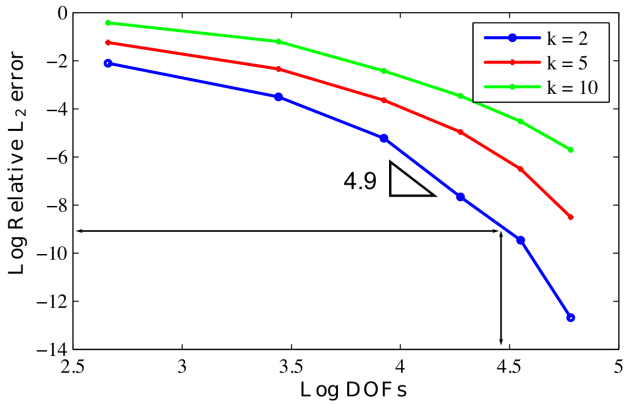

(a) p enrichment, $h_{max} = 0.25$

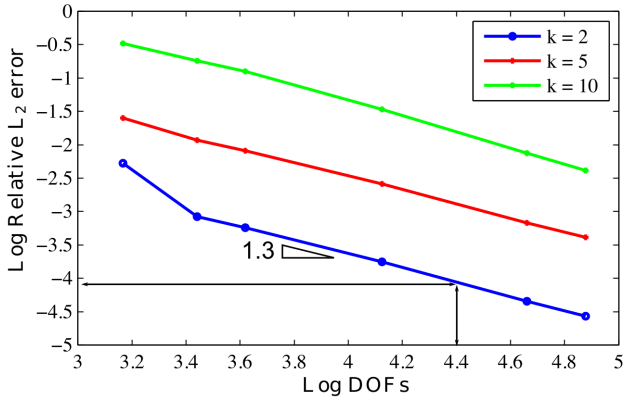

(b) h refinement, $p = 2$

Figure 5.20: Convergence test with plane wave-guide problem, relative error in L_2 norm for $2 \times 2 \times 2$ square cube

approach is found to be superior for the Helmholtz equation wave guide problem, such that p enrichment exhibits exponential convergence, whereas h refinement exhibits algebraic convergence [304, 180].

5.5.6 Numerical Analysis of Impinging Hard Cylinder problem

Figures 5.21 and 5.22 presents the convergence of the relative error in L_2 and H^1 norms versus the number of DOFs. In 5.21(b) and 5.22(b) the polynomial order p is fixed to 2 (quadratic element), and the mesh size h is gradually decreased ($h_{max} =$ [1.1587, 0.3478, 0.2032, 0.1330, 0.1067, 0.0895, 0.0742]). Subsequently, the defined mesh resolutions are: $\tau_{h,k=3}=$ [1.8075, 6.0226, 10.3060, 15.7431, 19.6361, 23.3936, 28.2286], $\tau_{h,k=5}$ = [1.0845, 3.6135, 6.1836, 9.4459, 11.7817, 14.0362, 16.9372], and $\tau_{h,k=10}$ = [0.5422, 1.8068, 3.0918, 4.7229, 5.8908, 7.0181, 8.4686], which contains adequate resolution for high wavenumbers ($kr \geq 40$). On the other hand, in Figures 5.21 (a) and 5.22 (a) we increase the hierarchical basis p order from 1 to 7 whilst keeping the mesh density constant (1439 elements, $h_{max} = 0.3478m$). The mesh resolutions are $\tau_{h,k=3} = 6.0226$, $\tau_{h,k=5} = 3.6135$ and $\tau_{h,k=10} = 1.8068$ respectively.

In case of $k = 10$ we have approximately 2 element per wave length. The resolution τ_l of h and p adaptivities are shown in Tables 5.3 and 5.4, h refinement has the highest mesh resolution when compared to p enrichment.

k	τ_l						
$k = 3$	6.0218	12.0437	18.0655	24.0874	30.1092	36.1310	42.1529
$k = 5$	3.6131	7.2262	10.8393	14.4524	18.0655	21.6786	25.2917
$k = 10$	1.8066	3.6131	5.4197	7.2262	9.0328	10.8393	12.6459

Table 5.3: The mesh resolution τ_l for p enrichment, for the sound hard cylinder problem

k	τ_l						
$k = 3$	3.6151	12.0437	20.6141	31.4947	39.2576	46.8021	56.4527
$k = 5$	2.1690	7.2262	12.3685	18.8968	23.5546	28.0813	33.8716
$k = 10$	1.0845	3.6131	6.1842	9.4484	11.7773	14.0406	16.9358

Table 5.4: The mesh resolution τ_l for h refinement ($p = 2$), for the sound hard cylinder problem

As can be seen from the plot 5.21(a), the error drops substantially when p reaches 3, especially for $k = 3, 5$ when compared to h adaptivity in Figure 5.21 (b). Notably, the convergence speed of the relative error in both plots started to decrease up (represented by plateau area in graphs) to certain percentages (k = 3, 5, 10. corresponding to relative errors of $0.44\%, 0.32\%, 0.26\%$ respectively). This implies that the remaining error is mainly due to the first order BGT BC, geometry description and dispersion effects, which comprise effects of the mesh discretization and domain size . The former sort of error can be minimised by increasing the domain of computation or implementing exact BCs. However, either of these methods will produce more computations in element-wise, so there is a trade-off between accuracy and efficiency. Furthermore, in 5.21a) we can observe that the convergence for the high frequency problem (k = 10) has a super-linear rate. In contrast, the converging rate for $k = 10$ in 5.21b) is sub-linear, owning to the fact that the solution on a fine mesh but with low (p=2) approximation order generally leads to imperfect solutions at high frequency.

We now move our attention to Figures 5.22 (a) and 5.22 (b), where there is identical behaviour for relative error between two type of norms. As expected, the convergence speed of the relative error in the H^1 norm is slower than the L_2 norm, by its nature. This is because the gradient of a finite element solution has less accuracy compared to solution itself, although this can be improved by *a posteriori* techniques such as the "super-convergent patch recovery" method once the super-convergent points can be determined [341]. However, p enrichment still retains its

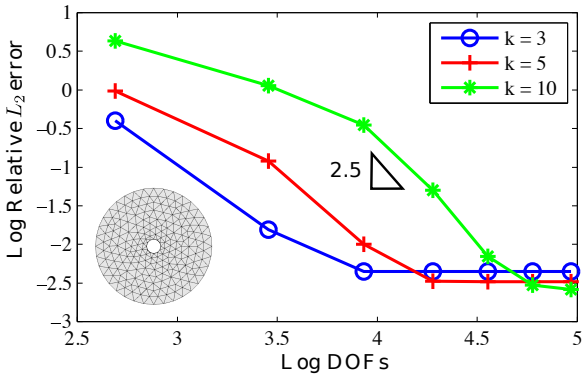

(a) L_2 relative error with p enrichment

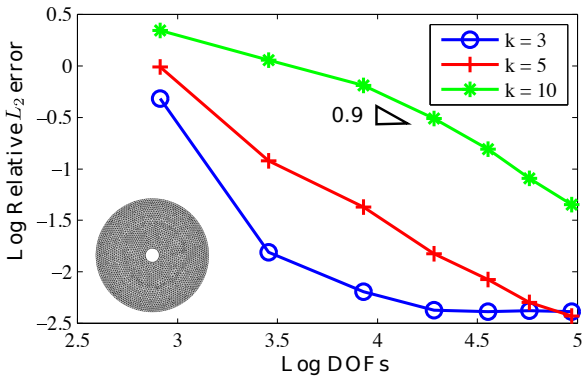

(b) L_2 relative error with h refinement

Figure 5.21: Convergence test for impinging hard cylinder problem, relative error in L_2 norm k=3, 5, 10, $r = 4$, $a = 0.5$. (a) $h_{max} = 0.3478m$, (b) $p = 2$

robustness for the relative error in the H^1 norm with high wavenumber (kD=80, D is the characteristic length of the computational domain) and poor resolution ($\tau = 1.8$). In conclusion, the convergence rate of p enrichment is nearly two times faster than h refinement. In addition, the convergence rate for relative error in H^1 norm is slower than error in L_2 norm.

Therefore, we can conclude that the increment of p is vital when appropriate mesh resolution is low and a relatively simple form of non-reflection BC is used. Furthermore, the performance of h refinement alone tends to converge sub-linearly with high wave number ($k = 10$). However, both adaptivity schemes are performed well with exponential convergence rate when $k = 3$.

5.5.7 Domain Length Analysis and Dispersion Error

In this section, the same incident wave impinging a sound hard cylinder problem is solved with $k = 3, 5$ and 10, while the domain length r is changed from 3 to 5. In doing so, we intend to identify the pollution error and the BGT like boundary conditions applied on the exterior boundary. The polynomial order is varied from 1 to 7.

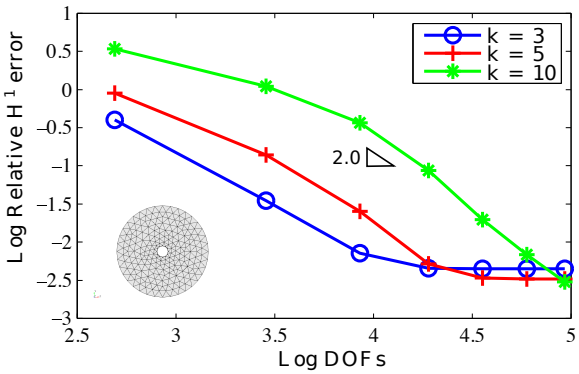

(a) H^1 relative error with p enrichment

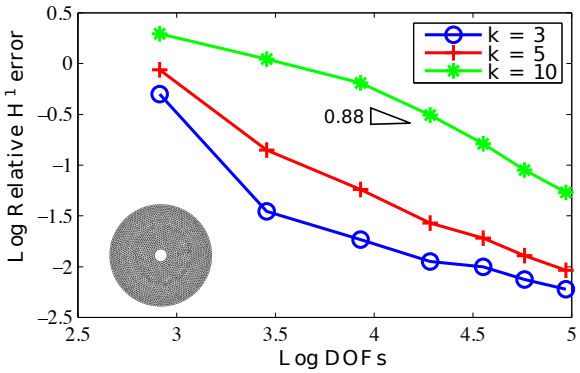

(b) H^1 relative error with h refinement

Figure 5.22: Convergence test for impinging hard cylinder problem, relative error in H^1 norm k=3, 5, 10, $r = 4$, $a = 0.5$. (a) $h_{max} = 0.3478m$, (b) $p = 2$

From Figures 5.23 and 5.24, where the radius of the computational domain is varied from 3 - 5, we highlight that the asymptotic remaining global relative errors for r = 5 are significantly smaller than that of results with smaller radius (r = 3, 4). It should be noticed that in the case of a larger computational domain (r = 5), the number of DOFs associated with the test problem is expected to significantly increase (not to mention the pollution errors are enlarged with increasing domain length). This means that the contribution to the total relative error from local error in each element appears to be numerically smaller on each node. This reveals the fact that increasing the computational domain reduces the effects caused by the approximate non-reflection boundary conditions. Moreover, the higher order elements sufficiently controlled the pollution error on each element with increasing domain length. It is noteworthy that in case of high wavenumbers ($kD = 100$), the non-plateau area occurred in the asymptotic range might due to plain dispersion effects which delay the convergence speed. Furthermore, the increased wavenumber adds more wavelengths between the obstacle and the truncated exterior boundary, this might reduce the additional error caused by the approximate BGT BC.

This observation is consistent for problems with different frequencies (k) in both H^1 and L_2 norms. Therefore, we can conclude that steadily increasing the computational domain with a coarse mesh and a high approximation order can effectively reduce the error caused by the non-reflection property on the boundary. Since the sophisticated boundary condition itself delays the efficiency of the acoustic solver, in some circumstances, additional calculations on extra matrices are required [301].

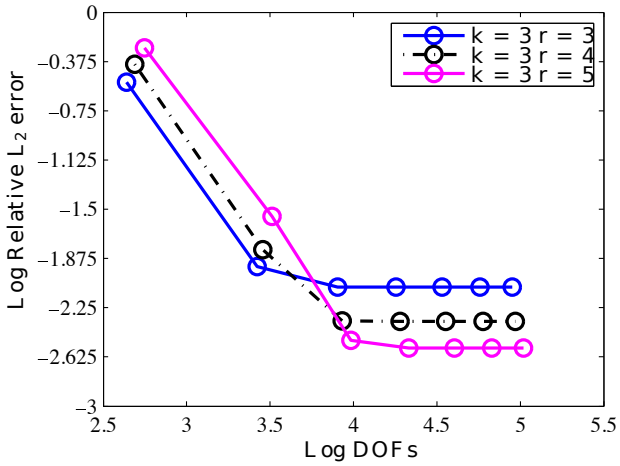

(a) k = 3

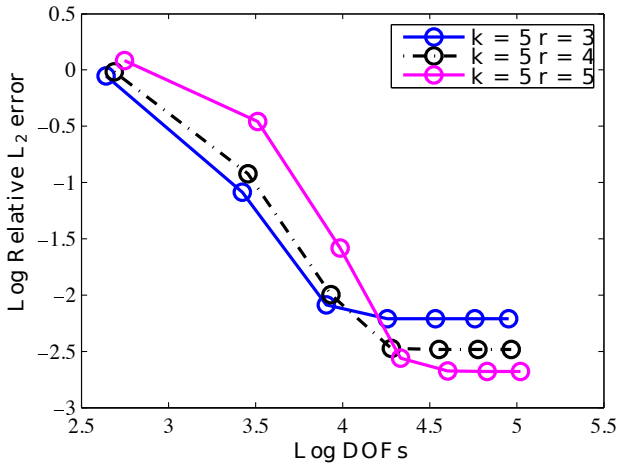

(b) k = 5

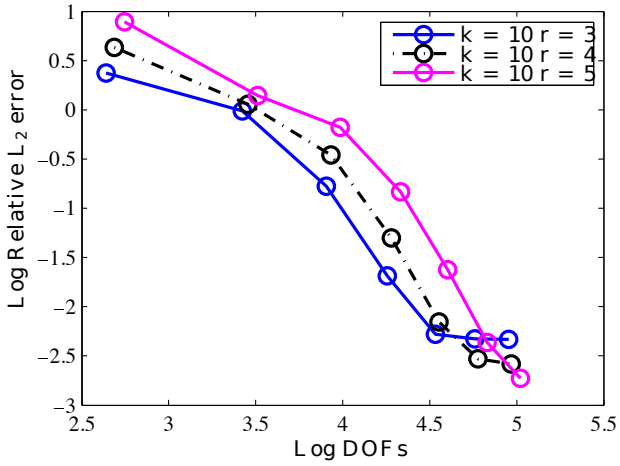

(c) k = 10

Figure 5.23: Convergence test for the impinging hard cylinder problem, relative error in L_2 norm for r=3, 4, 5. a = 0.5

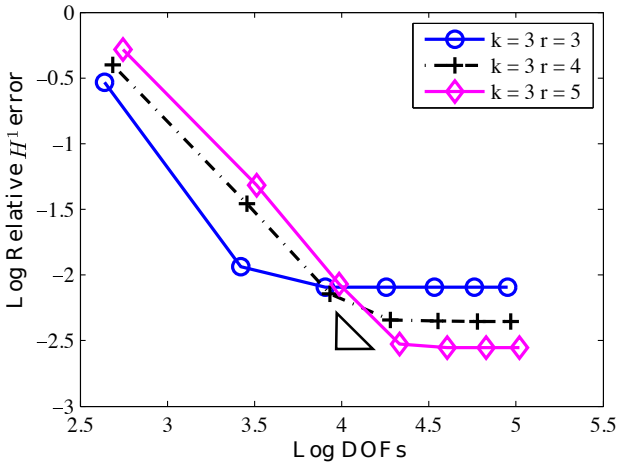

(a) k = 3

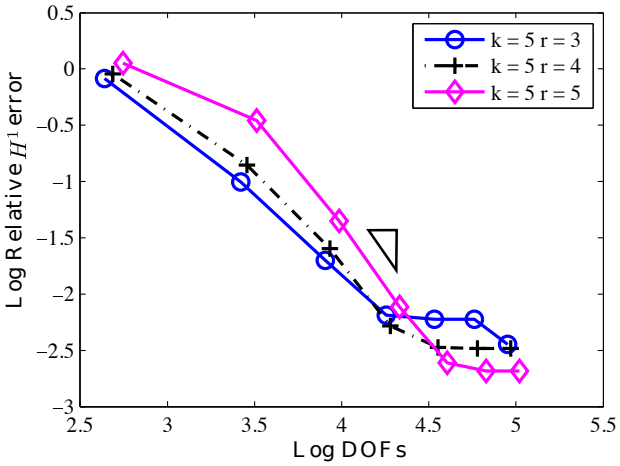

(b) k = 5

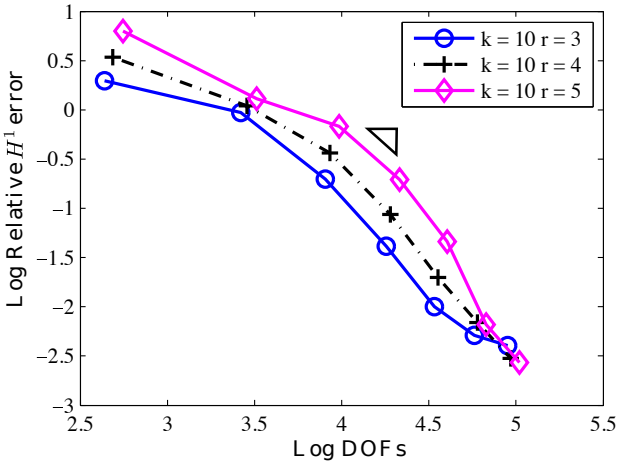

(c) k = 10

Figure 5.24: Convergence test for the impinging hard cylinder problem, relative error in H^1 norm for r=3, 4, 5. a = 0.5

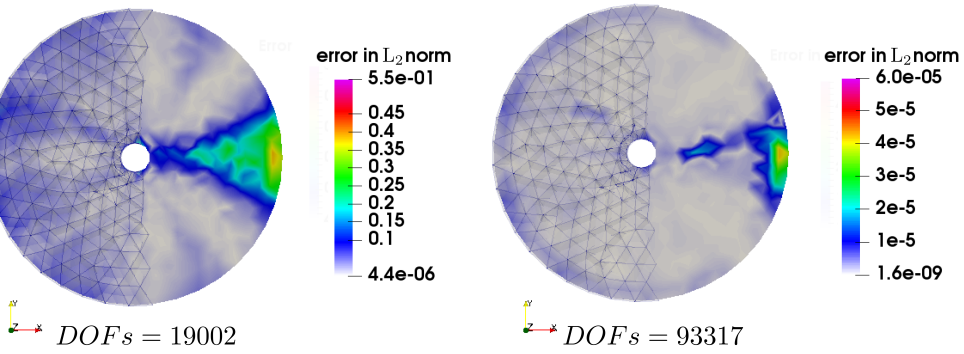

(a) L_2 exact error with p enrichment

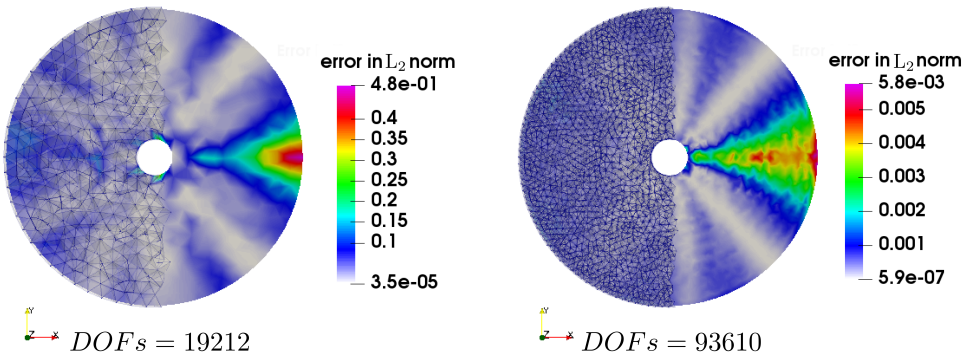

(b) L_2 exact error with h refinement

Figure 5.25: Distribution of exact element-wise error for impinging hard cylinder problem, L_2 norm $k = 10$, $r = 5$, $a = 0.5$

In Figure 5.25, the distribution of the exact error in the L_2 norm is plotted, and the overview of pollution error is illustrated. As expected, the error is asymmetric and greater in the space around the boundary of the cylinder and along the axis of propagation direction, which is the positive x direction. The distribution of the exact error is not symmetric. This observation is consistent with the dispersion effect in 1D, as Figure 5.4 exhibited. Moreover, the L_2 error also steadily increases from left to right along the computational domain with distance travelled. These additional errors account for the dispersion effect. We can also determine that the maximum value of element-wise error (L_∞) for p enrichment is smaller than h refinement (5.973e-05 versus 5.759e-03). In contrast, h refinement ($p = 2$) requires more DOFs than p enrichment to achieve the same result quality (e.g. error and convergence rate). To summarise, both h and p adaptivities show significantly good agreement on the position of the highest error, so one can partly refine the mesh along the propagation direction near the boundary of the far-field domain. In other words, this observation can serve as a rough error indicator for any acoustic problem with specific prescribed propagation direction, special care such as mesh refinement should be taken along the propagation path in order to minimise the errors with less effort. Overall, uniform p enrichment provides better control of the pollution errors over h refinements in a local sense. It should be noticed that the asymmetric error distribution between the north and south directions in Figure 5.25 (a) is due to unstructured mesh with various element sizes.

5.5.8 Numerical Analysis of Impinging Hard Sphere problem

The last section of this chapter is devoted to the analysis of the relationship between global relative error and the total computational cost. A benchmark problem consisting of a plane incident wave impinging on sound hard sphere is solved with both analytical and numerical methods. Uniform h and p adaptivities are applied to demonstrate the effectiveness of the current solver.

First of all, we created a coarse mesh with $h_{max} = 2.337$, and varied the approximation order from 1 to 8. Then, we fixed our approximation order $p = 2$, and manipulated the mesh size from 2.613 to $7.776e-01$. The numerical test is assessed with an available analytical solution. The cost measures, such as the global relative H^1 error, computational time, and memory are retrieved at the end of the calculation and plotted against the number of DOFs per wavelength D_λ. The reason for choosing D_λ is because this measure takes the higher order polynomials into account. Comparisons are made in Figure 5.26. Although the range of number of DOFs per wavelength for h and p adaptivities are not identical, we can still observe the difference in computational cost between the two schemes, in case they lead to similar D_λ level. Overall, p adaptivity performs better than h version in point of views of error. However, p adaptivity does require more time and memory consumption for relatively small problems (less D_λ, memory versus number of DOFs per wavelength) due to smaller matrix and wider bandwidth compared to h adaptivity. This is due to the fact that DOFs ordering before matrix factorization is not optimised for p hierarchical approximation. That causes increasing factored

matrix filling, thus additional memory demand. This fact inspires the adoption of more advanced computational tools in order to compensate the memory cost of using higher order elements.

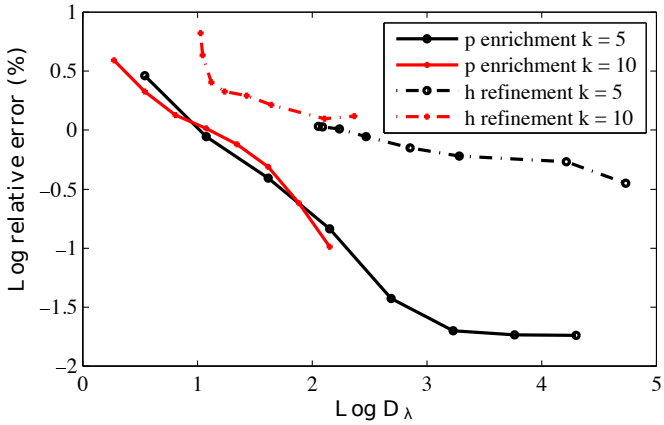

(a) global relative error (H^1 norm)

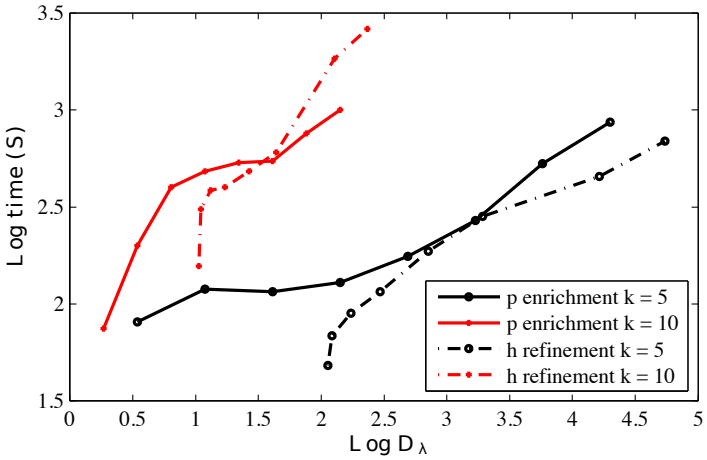

(b) total computational time

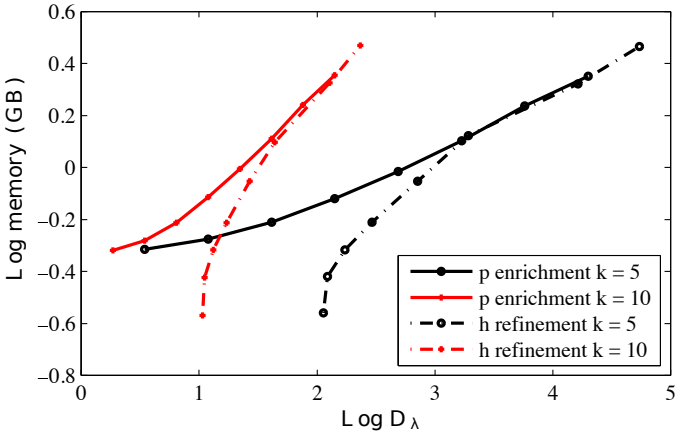

(c) total memory consumption

Figure 5.26: Uniform h & p adaptivity, benchmark problem of impinging hard sphere, $R = 4$, a $= 0.5$, $k = 5$, 10. Measures versus D_λ, solid lines: p adaptivity, $p = 1 \sim 8$, $h_{max} = 2.337$, dashed line: h adaptivity, $p = 2$, $h = 2.613$ to $7.776e-01$

In Figures 5.27 and 5.28, ten spherical meshes are created with the size of

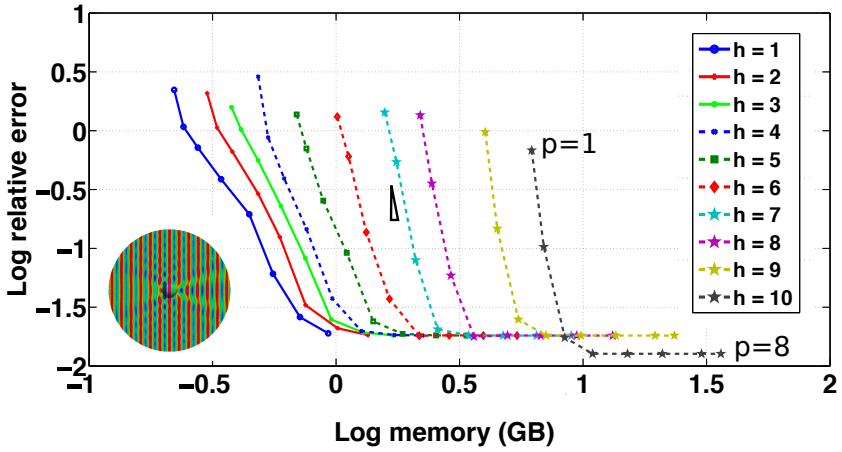

(a) p enrichment

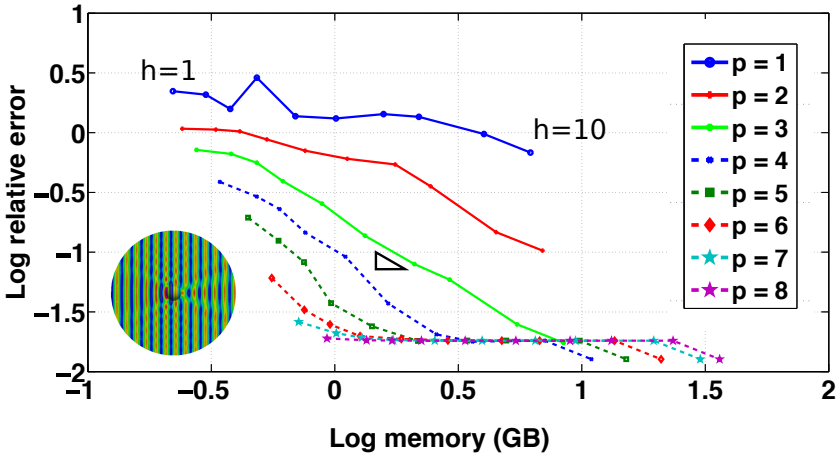

(b) h refinement

Figure 5.27: Convergence test for impinging hard sphere problem, global H^1 relative error versus total memory. Uniform h & p adaptivity, $R = 4$, $a = 0.5$, $k = 5$

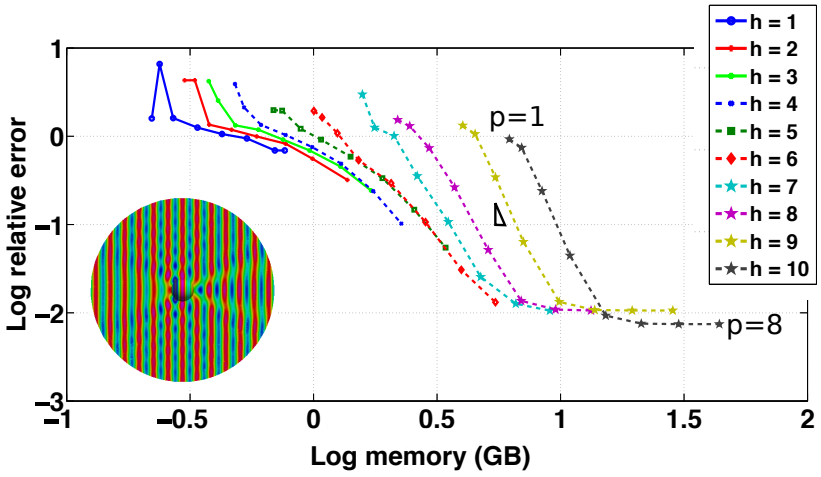

(a) p enrichment

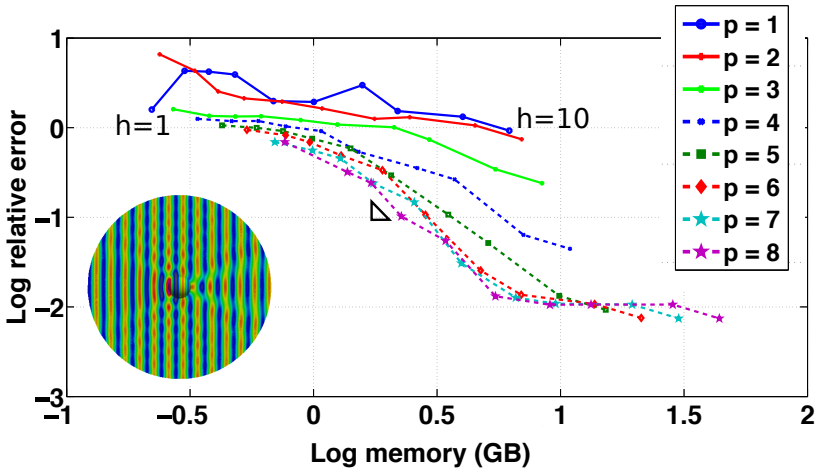

(b) h refinement

Figure 5.28: Convergence test for impinging hard sphere problem, global H^1 relative error versus total memory. Uniform h & p adaptivity, $R = 4$, $a = 0.5$, $k = 10$

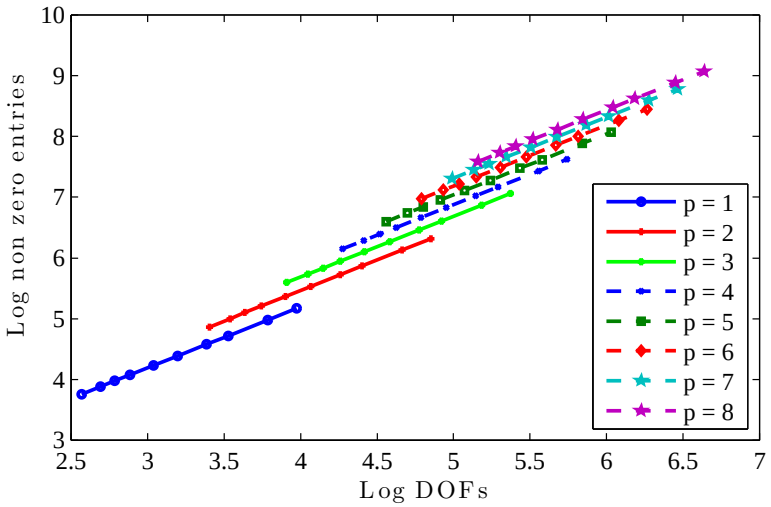

Figure 5.29: Total number of non-zero entries versus total number of DOFs. Uniform h adaptivity with p range from 1 to 8, convergence test for impinging hard sphere problem, $R = 4$, $a = 0.5$, $k = 5$, 10.

h_{max} ranging from indices $h = 1$ to $h = 10$ (with mesh resolutions $\tau_l(k = 5) = [0.8063, 0.9495, 0.9618, 1.0754, 1.1230, 1.6225, 1.9758, 2.1969, 2.9687, 3.2321]$). On the other hand, the hierarchical approximation order is varied progressively from 1 to 8. All global relative errors are measured in H^1 norm space with summation over the whole computational domain (results of relative error in L_2 norm give the same conclusion and will not be repeated here for brevity). The chosen wavenumbers are $kD = 40$ and $kD = 80$ respectively.

The memory costs is a more reliable quantitative measure than the computational times in case of parallel computations with limited computing resources (e.g. personal computers). From both Figures, we can intuitively see that the convergence speed deteriorates as the wavenumber is increased from 5 to 10. Secondly, the overall conclusion is that, the uniform p adaptivities proved to exhibit an exponential convergence rate 5.27 (a) while the h adaptivity shows approximately linear or sub-linear convergence. The remaining errors in the plateau area are due to the application of non-exact exterior boundary conditions. At this stage, in Figure 5.27 (b) h adaptivity did not deliver much refinement with higher order elements ($p = 6, 7, 8$). On the other hand, in 5.28 (b), h adaptivity together with increasing approximation orders successfully reduced the relative error to a minimum. We observe a satisfactory error level of around 1% when the approximation order reaches 8, although with $kD = 80$ the pollution error dominates in the pre-asymptotic range. Another important observation is that increasing p order demands less total memory than reducing the size of h while retaining the same level of accuracy, this is illustrated by the shifted curves in Figures 5.27 and 5.28 (b). For instance, to achieve a relative error of 2.51%, 7.94 Gigabytes (GB) of memory are needed with $p = 3$, where as $p = 8$, only 0.79 GB of memory are required which is almost an order of magnitude less than the former. In other words, since the mesh resolution τ_l corresponding to $p = 8$ is bigger than $p = 2$, it requires less memory and CPU time to solve the identical problem with $p = 8$ than $p = 2$. It is noteworthy, that

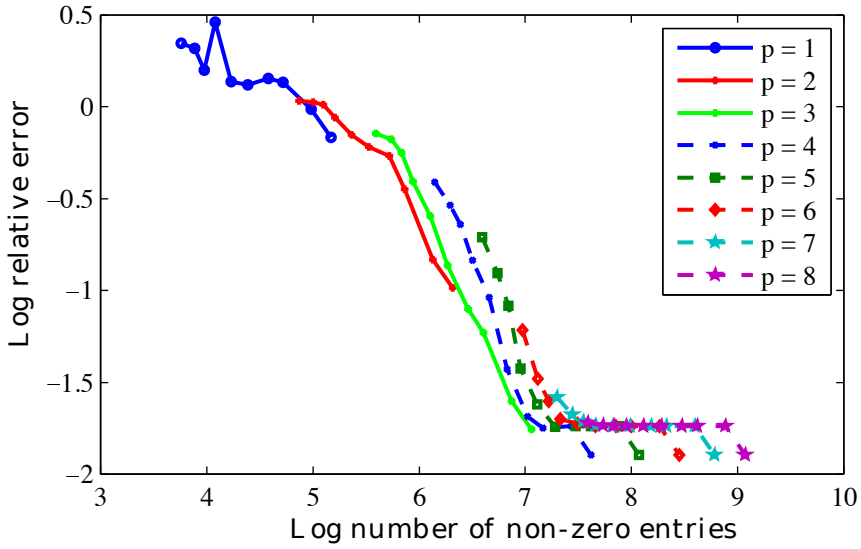

(a) k = 5

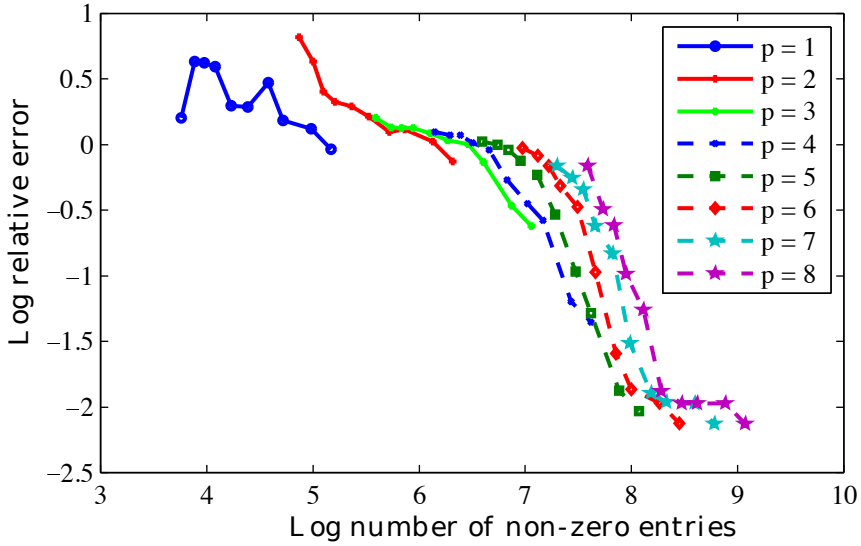

(b) k = 10

Figure 5.30: Global H^1 relative error versus total number of non-zero entries. Uniform h adaptivity with p range from 1 to 8, convergence test for impinging hard sphere problem, $R = 4$, $a = 0.5$, $k = 5$, 10.

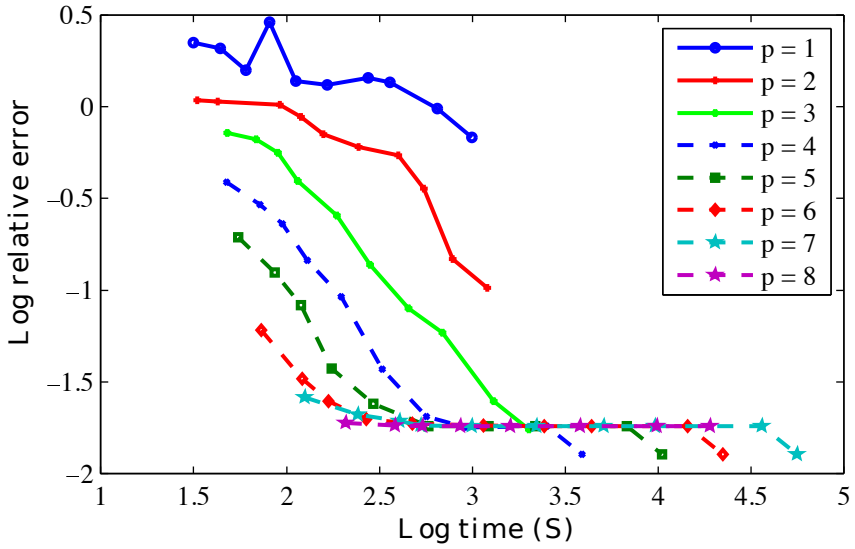

(a) k = 5

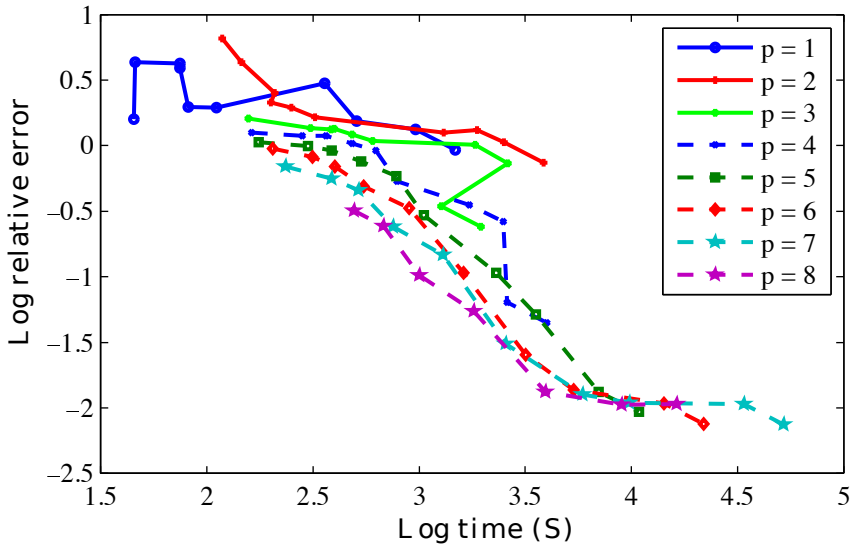

(b) k = 10

Figure 5.31: Global H^1 relative error versus total computational time. Convergence test for impinging hard sphere problem. Uniform h adaptivity with p range from 1 to 8, $R = 4$, $a = 0.5$, $k = 5$, 10.

in Figure 5.27 and 5.28 (a), the extreme coarse mesh (h = 1) cannot capture the geometry of the problem accurately even with $p = 8$. This observation shows the measure D_λ might not be a suitable measure for computational costs.

In Figure 5.29, the number of non-zero entries versus the number of DOFs for $k = 5$ and 10 are identical. They both exhibit that increasing p order results in more number of non-zero entries than number of DOFs. Similar conclusion can be drawn from Figure 5.30 as well, with a relative error of 1% in Figure 5.30 (a), 123.026 million number of non-zero entries are required for $p = 5$, where as $p = 8$ this amount increased to 501.187 million. However, the deleterious effects of the number of non-zero entries should not be unduly estimated. It might be diminished by the benefits of accuracy and convergence rate. In other words, there is no direct link between the computational cost and the number of non-zero entries. As depicted in Figure 5.31 (a), for a given accuracy (1.7%), the total computational time is greatly reduced when increasing the approximation order from 3 (approximately 2238.7 seconds) to 8 (approximately 223.8 seconds). Finally, it should be noticed that the ill-alignment of lines in the above Figures is caused by a narrow range of refinement, due to current basic computer recourses. The maximum solvable number of DOFs is limited to around 2.2 million (without parallel computation and partitioned mesh). Overall, drastic improvements can be obtained with p enrichment in both time and memory for a given fixed level of accuracy. Similar conclusions have been reported in [72], such that a plane wave guide problem is solved and compared with the analytical solution. This found to be especially beneficial for practical applications with prescribed engineering accuracy.

5.6 Concluding Remarks

In this Chapter, we assessed the performance of the finite element h and p adaptivities with hierarchical shape function for solving Helmholtz equation with polychromatic and monochromatic wave solvers. Measures such as L_2 and H^1 relative errors, computational time and memory, number of degrees of freedom per wavelength, mesh resolution τ_l, etc. are evaluated. The accuracy and efficiency of both adaptivity schemes have been verified by three benchmark problems with analytical solutions. The finite element solutions from both h and p adaptivities schemes are in very good agreement with the reference solutions computed. Furthermore, the numerical results suggest that p adaptivity is more adequate than h adaptivity when solving acoustic problem with short wavelength and multiple frequencies.

Chapter 6

Assessment of Advanced Computational Techniques

In this Chapter, we will focus on the the development of advanced computational techniques in order to further mitigate the computational costs associated with the current proposed acoustic solver.

6.1 Factorization Memory Alleviation Scheme

The natural complexity of the Helmholtz operator deserves extra attention. In order to simplify the solution process, we require a simple transformation procedure called the complex and real transformation to build the complex system of linear equations [143]. Further to that, the field split / block solver pre-conditioning with iterative method is implemented to further reduce the memory requirements for solving such systems with parallel computation [55].

It is worth noting that all element level integrations applied in this chapter are performed by a generalized Duffy transformation with Gaussian quadrature rule. Its robustness and accuracy on dealing with higher order polynomials is discussed in Appendix A in detail.

6.1.1 Complex-Real Valued Transformation

In finite element analysis, a complex-valued linear system of equation $(\mathbf{A} + \mathrm{i} * \mathbf{C}) * (\boldsymbol{x}_R + \mathrm{i} * \boldsymbol{x}_I) = (\boldsymbol{b}_R + \mathrm{i} * \boldsymbol{b}_I)$ can be re-written in the form of a real-valued linear system of equation:

$$\mathbf{K}\bar{\mathbf{x}} = \begin{pmatrix} \mathbf{A} & \mathbf{C}^* \\ \mathbf{C} & \mathbf{A}^* \end{pmatrix} \begin{pmatrix} \boldsymbol{x}_R \\ \boldsymbol{x}_I \end{pmatrix} = \begin{pmatrix} \boldsymbol{b}_R \\ \boldsymbol{b}_I \end{pmatrix} \tag{6.1}$$

the above algorithm is implemented [190] in such a way that even with twice the size of the matrix, the computational time demanded for solving the real system is still faster than to directly solve a complex valued linear system of equations. It should be noted that $\mathbf{A}^*$ means the complex conjugate of the matrix $\mathbf{A}$. We yet require fewer entries, instead of calculating and inserting the values of a 2 by 2 matrix. The acoustic solver in MoFEM [199] calculates two small matrices, $\mathbf{A}$ and $\mathbf{C}$. Thereafter, it projects the values into matrices $\mathbf{A}^* = \mathbf{A}$ and $\mathbf{C}^* = -\mathbf{C}$ based on previous results from the indices retrieved. This further reduces the computational time by half. Thanks to the orthogonality of Legendre (Lobatto) type shape functions used in our hierarchical basis, an optimal condition number and sparsity of stiffness matrix are guaranteed for the Helmholtz operator at this stage. In Figure 6.1 below, the sketch of the complex real valued (C-R) transformation is provided.

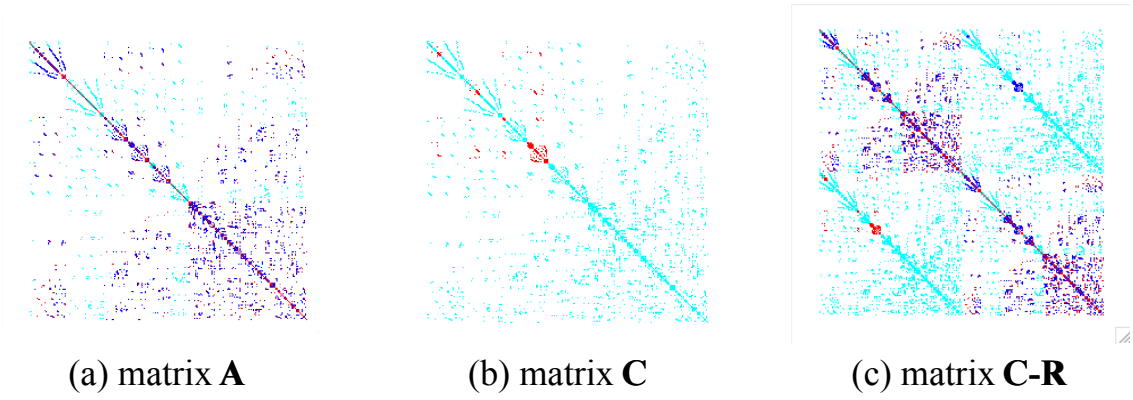

(a) matrix **A** (b) matrix **C** (c) matrix **C-R**

Figure 6.1: Illustration of global stiffness matrix $\mathbf{K}$ by C-R transformation

6.1.2 Field Split and Block Solver Preconditioning Method

In order to solve high wavenumber problems, the system matrix is treated as a 2 by 2 block matrix rather than solving the system of equations without exploiting the structure of the matrix, which allows efficient, iterative solvers to be exploited. The field split / block solver preconditioner requires that the partitioned mesh and the distributed sub-block matrices are stored sequentially in each processor. Through MPI-based parallelisation, the mesh domain is partitioned into n processors. Instead of creating and storing the values of a 2 by 2 matrix in memory, the nest matrix $\mathbf{B}$ will access the calculated two smaller block matrices $\mathbf{A}$ and $\mathbf{C}$ separately.

$$\mathbf{B} = \begin{bmatrix} \mathbf{A} & -\mathbf{C} \\ \mathbf{C} & \mathbf{A} \end{bmatrix} \tag{6.2}$$

here we drop the complex conjugate sign * for simplicity. Hence, the actual matrices in storage are matrices $\mathbf{A}$ and $\mathbf{C}$. The system matrix for acoustic problems can be classified as a combination of nested matrices, and it can be solved by four types of field split / block solver pre-conditionings both available in PETSC [55]. These

are: Block Jacobi, block Gauss-Seidel, symmetric block Gauss-Seidel and Schur Complement respectively.

The Schur complement is proven to be the most efficient and accurate solver combined with LU factorization for acoustic problems with a moderate number of DOFs by numerical tests [337]. The approximate Schur Complement for matrix $\mathbf{A}$ is defined as

$$\mathbf{S} = \mathbf{A} - \mathbf{C}\, ksp\,(\mathbf{A})\, \mathbf{C}^{*} \tag{6.3}$$

where $ksp(\mathbf{A}) = \mathbf{A}^{-1}$ in general if $\mathbf{A}$ is invertible and the ksp is an abstract PETSC abbreviation term representing "scalable linear equations solvers" which can be defined specifically by user [55]. In this way, the factorization process is only executed once for matrix sizes identical to $\mathbf{A}$ instead of the original 2 by 2 matrix.

In numerical analysis, the pre-conditioner Block Jacobi combined with a composite multiplicative scheme would cause the computational time to double compared with using LU factorisation combined with Schur complement preconditioning. The main reason for adopting block Jacobi in problems with massive number of DOFs is because of the less restrictive memory requirements compared with other methods (identical benchmark problem solved with Schur complement combined with LU factorization). To conclude, a 56.92% reduction in total memory requirements (Gigabytes) is obtained when using the field split / block solver preconditioning methods compared to conventional preconditioning schemes (without field split and block solver), in case of solving incident wave impinging on sound hard sphere benchmark problem.

In Figure 6.2, the global stiffness matrix by C-R transformation with multiple processors is plotted (blue = −, red = +, cyan = 0). Figure (6.2a) is generated from direct solver with a single processor, and (6.2b) is the system matrix before field split / block solver preconditioning with partitioned mesh between two processors. We can observe that the global stiffness matrix is sparse. Moreover, the calculation time is reduced more than one half by the one additional number of processor involved in the calculation, and the total memory usage is increased approximately by a factor of three (2.8331) when using a single processor only.

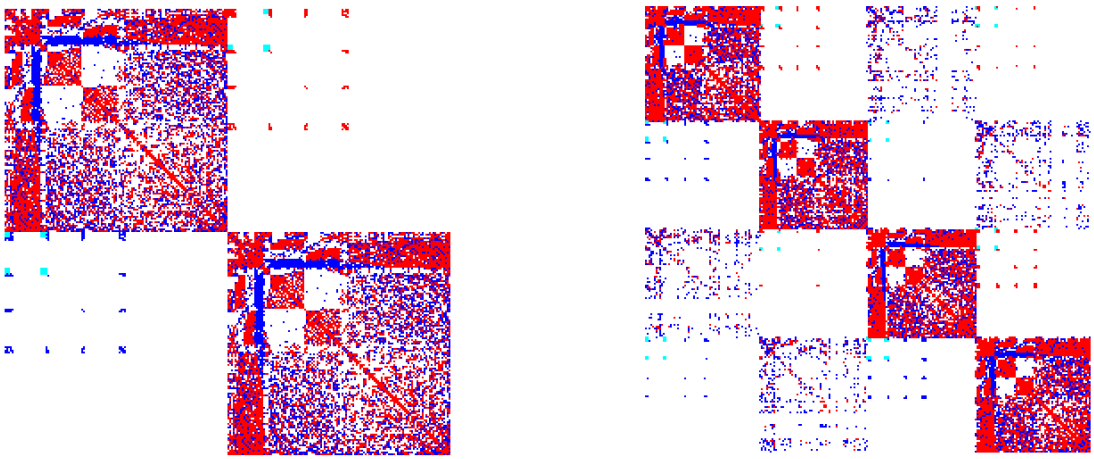

(a) no.of processor:1 (b) no.of processor:2

Figure 6.2: Comparison of global stiffness matrix by C-R transformation with problem number of DOFs equal to 6970, $p = 2$, $k = 10$. (a) Number of processors = 1, calculation time: 10.933453 s, memory usage: 0.209240 Gigabytes (GBs). (b) Number of processors = 2, calculation time: 5.792701 s, memory usage: 0.073856 GBs

6.2 Performance of the Parallel Computations

6.2.1 Introduction

The main difficulties that arise in computational mechanics are the complexity and sizes of physical problems. Conventional sequential computers are limited by large and complicated problems due to computational power and memory requirements. Finite element analysis using parallel computing was first addressed in the book 'Programming the Finite Element Method' in 1995 by Mike Pettipher [57]. The basic strategy is to divide a large physical problem into relative small subproblems and then assign them to separate computer resources, information is exchanged and the problem solved in parallel. It is well known that the total computational cost of FEM is directly related to the number of DOFs, hence, parallel computations are essential for FEM [65, 94, 101, 112]. The accuracy of FE solution is important only when the efficiency is taken into account. To solve finite element problems with large computational domains and a fine discretised mesh, we need highly efficient resources. Due to the rapid development of multi-core processors in modern high performance computing, not only the number of CPUs used, but also the ability to parallel calculating matrices and combine them together is vital [189]. In other words, the ability to perform parallel computation is limited by the methodologies and not only the hardware. In [93], the author suggests that the increment of polynomial order in 3D problems results in better outcomes than in 2D. In this section, we use MOAB (The mesh oriented data base) to partition our mesh into m parts, and then allocate each to a core (up to m processors (functional

units) can be called). The inter-processor communication is provided by the MPI (Message Passing Interface) library, which is based on C++ and implemented in MoFEM. The computation is executed simultaneously in each core. The example of unstructured mesh is partitioned as shown in Figure 6.4 and the memory is distributed as shown in 6.3. The whole calculation processes are performed simultaneously in each core with the maximum number of processors equal to the number of partitioned areas.

6.2.2 Measurements of Efficiency and Accuracy

In order to give a full picture of performance for parallel programs, we need measures of accuracy and total calculation time, as well as speedup and efficiency for the benchmark numerical example. All data is recorded based on an average over ten runs with identical input. This is to account for variation in run time due to variation in the local execution environment due to, for example, the presence of other jobs simultaneously running on the cluster. The total calculation time encompasses assembling of the element matrices, applying quadrature rules, as well as solving the final system of linear equations by direct solvers and saving the result file with mesh information [317]. We now introduce the following measures: C_n is the total calculation time (s) spent from n processors contribute from each processor (parallel run time). It is the time between the start of the program and the end of the execution on the last participating processor. The cost of parallel computation $T_n = nC_n$ is also known as work or processor-runtime product (s) [267, 98]. Hence,

$$S_n = \frac{C_1}{C_n} \tag{6.4}$$

where S_n is the ratio between the time spent executing on one processor and n processors with the same example problem. This measure is termed the speedup. The measure C_1 here denotes the calculation time spent by the parallel program on one processor for solving the same problem. speedup is an indicator of efficiency gain in parallelizing the computation on n processors. Ideally, $S_n = n$ in a perfect situation, but in practice, $S_n \leq n$ due to other works carried out by the parallel program, it is well known as overhead (overheads inherent to the parallelization itself). Examples of overhead include communication between the processors, synchronisation, etc. Moreover, it is impossible to fully parallelise a program, because of its sequential parts, inputs and outputs.

The best performance we can expect is that the work distributed to each core is equally divided, and that there is no extra work for our cores. If we run our program on n cores, and allocate a single process on each core, then the parallel program will work n times faster than the original program. In this case, we will have $C_n = \frac{C_1}{n}$, which is known as linear speedup. Furthermore,

$$E_n = \frac{C_1}{nC_n} = \frac{S_n}{n} \tag{6.5}$$

The above equation defines the parallel efficiency measure E_n, which is defined as the per processor speedup. Equivalently, it is the ratio of speedup to the total number of processors. Ideally, $E_n = 1$, but practically, $E_n \leq 1$.

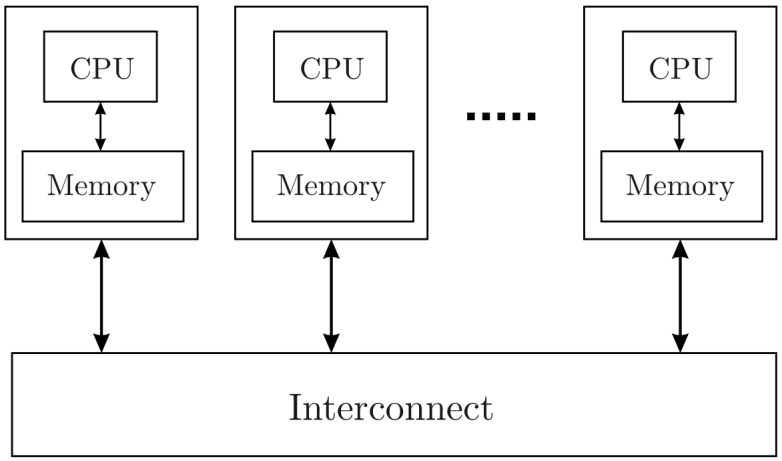

Figure 6.3: Diagram of the distributed memory system architecture [317]

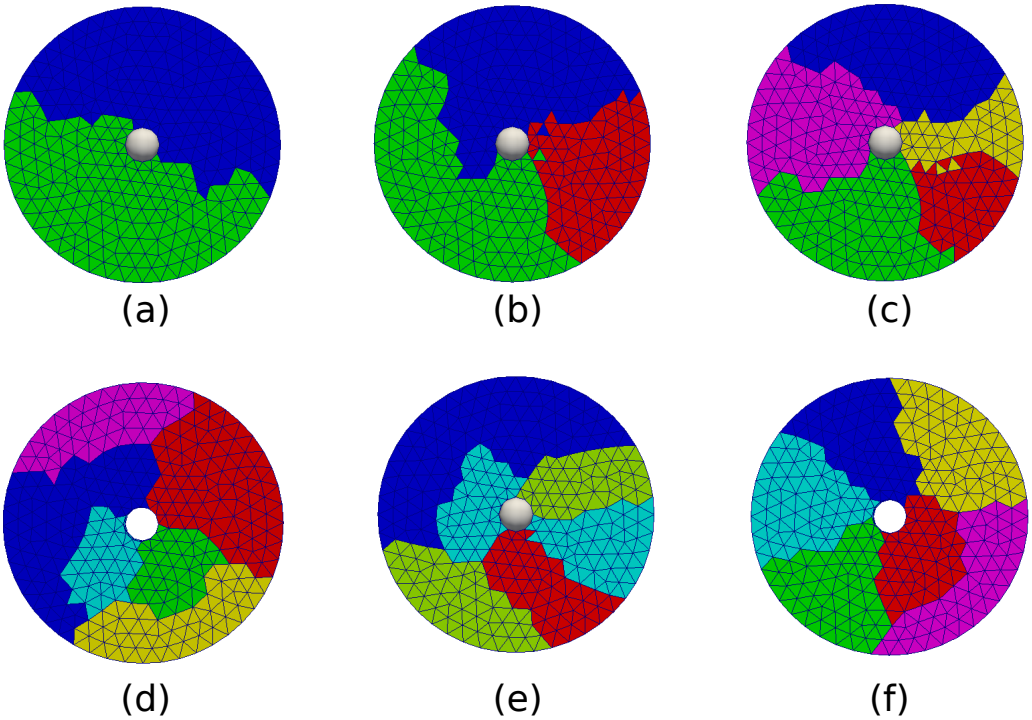

Figure 6.4: Selective partitions for the distribution of discretization with 2684 elements, impinging cylinder scatterer problems. As illustrated by the colouring, $r = 4$, $a = 0.5$. (a) - (f) 2 processors to multiple processors with partitioned meshes

6.2.3 Numerical Analysis of Parallel Computations

In this section, we dedicate work to test the efficiency and speed of a parallel computation finite element program on a specific acoustic problem. The selected test problem is the incident wave impinging on sound hard cylinder problem in section 5.3.2. Please see Appendix C.2 for details about the implementation procedure of the parallel computations.

p enrichment				h refinement			
$T_{n=1}$ (s)	$T_{n=5}$ (s)	#dof	η_{L_2}	$T_{n=1}$ (s)	$T_{n=5}$ (s)	#dof	η_{L_2}
3.5717	1.4364	487	1.967523	2.233890	0.8302	818	2.201882
7.8602	2.4175	2857	0.936548	7.7789	2.1313	2857	1.138935
23.9310	5.8719	8549	0.198971	27.6345	6.6802	8530	0.644591
55.6274	14.4329	19002	0.041398	69.0533	16.8921	19212	0.309405
125.8126	33.5363	35655	0.007010	142.5170	38.6093	35710	0.155090
251.9785	53.7954	58947	0.002955	264.2900	75.6542	57661	0.080991

Table 6.1: Performance of impinging hard cylinder problem with $k = 10$ with sequential computing and parallel computing with 5 processors, relative error in L_2 norm with pure h refinement and p enrichment. From top to bottom, p increases from 1 to 6. η_{L_2} is relative error in L_2 norm

If we first compare the h and p adaptivities in Table 6.1, the total calculation time for solving the acoustic problem is nearly 4 times faster if we increase the number of processors from 1 (the traditional sequential algorithm) to 5 (as well as the mesh is partitioned to 5 parts) for $p = 6$, but only 2.5 times faster for the case $p = 1$. Additionally, p adaptivity is approximately 5 times faster in speed for higher order approximation basis ($p = 6$), but merely 3 times faster exactly for $p = 1$ with an identical coarse mesh. On the other hand, from coarse discretisation to fine discretisation ($p = 2$), h adaptivity requires less calculation time for problems with less DOFs and a single processor, but raises rapidly for multiple processors.

The important result is that with a similar number of DOFs and identical number of processors, p adaptivity with a hierarchical approximation basis can solve larger problems with much smaller error and less calculation time. This fact can be seen from Figure 6.6 as well. We can see from the graphs that the logarithm of the relative error from p adaptivity drops to -2.6 with total calculation time below 2.5 under the black diagonal line. By contrast, the logarithm of the relative error for h adaptivity remains at -1.4 but with log total calculation time exceeding 2.5 for the number of processors n in the range from $1 - 6$.

In Figures 6.7, the straight line called ideal represents the optimal linear speedup and serves as a standard to compare to the actual obtained numerical speedup. The values of h & p in the associated legends indicate the level of refinement by pure

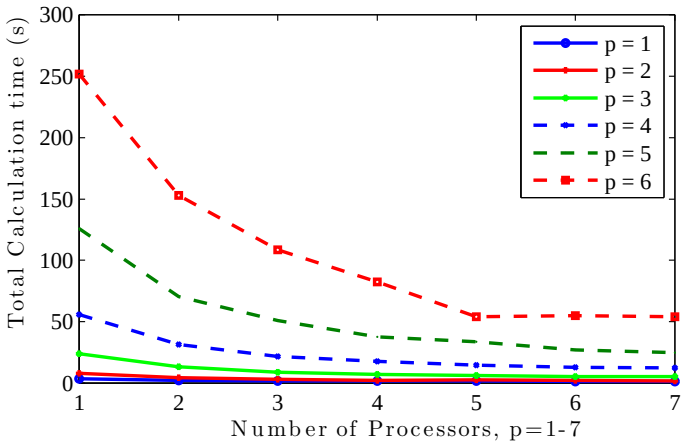

(a) p adaptivity

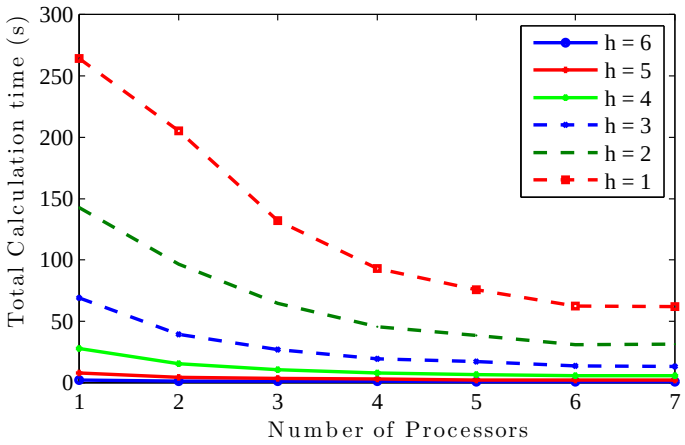

(b) h adaptivity

Figure 6.5: Total calculation time versus number of processors adopted for impinging hard cylinder problem, $k = 10$, $r = 5$, $a = 0.5$, $h = 6$ - 1 indicates the size of element is decreased (mesh density increased from coarse to dense)

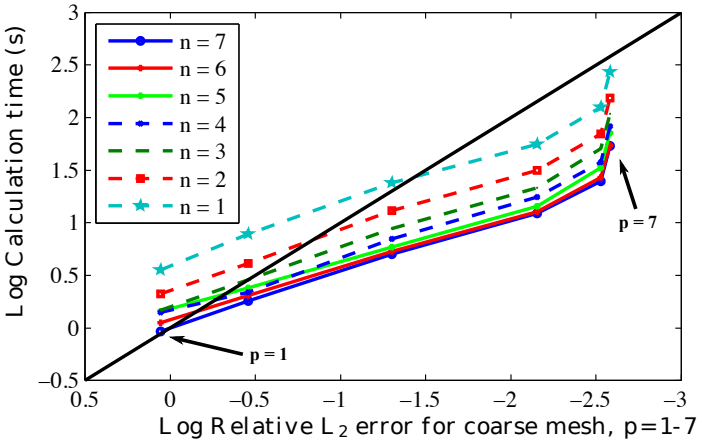

(a) p adaptivity

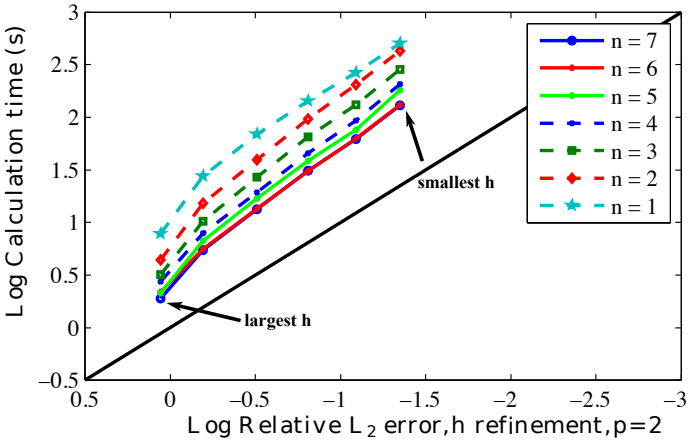

(b) h adaptivity

Figure 6.6: η_{L_2} versus total calculation time for impinging hard cylinder problem, $k = 10$, $r = 5$, $a = 0.5$, $n =$ number of processors used in parallel computation

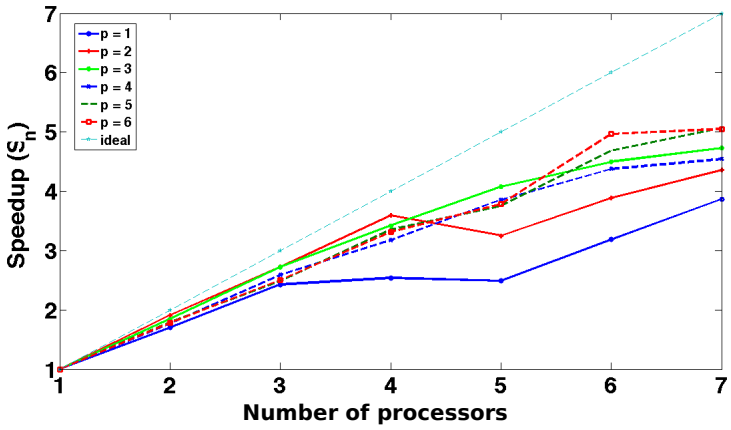

(a) p adaptivity

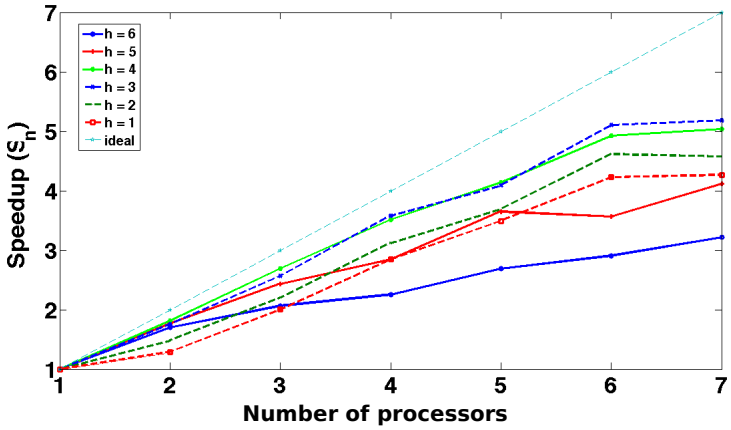

(b) h adaptivity

Figure 6.7: speedup S_n versus number of processors for impinging hard cylinder problem, $k = 10$, $r = 5$, $a = 0.5$

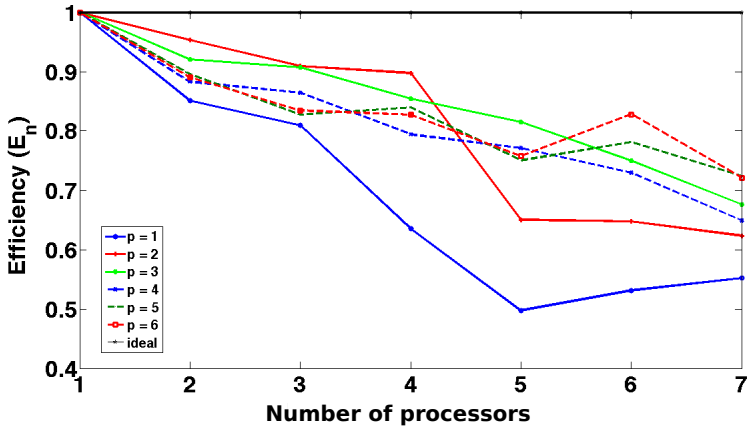

(a) p adaptivity

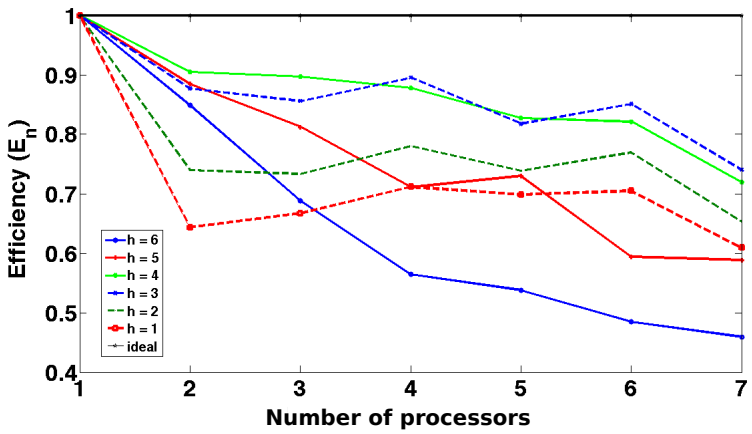

(b) h adaptivity

Figure 6.8: efficiency E_n versus number of processors for impinging hard cylinder problem, $k = 10$, $r = 5$, $a = 0.5$, ideal line equal to 1

h or p adaptivity (h decreases equivalent to increase of p). The speedup of $p = 6$ with 7 processors is 5.0474, where for $h = 1$ with 7 processors is 4.2645. This reveals that with an identical number of DOFs, parallel computation with the same number of processors has higher speedup for p enrichment than h refinement with higher order finite element. Moreover, there is a clear tendency towards the highest speedup occurs with $p = 6$ ($S_n^p = 5.0474$) for increased approximation basis, but the peak of the speedup ($S_n^h = 5.0340$) is at $h = 3$ for mesh refinement (e.g. $h = 3$ represents the level of mesh refinement). The reason behind this might be the fact that increasing p order does not generated additional physical nodes compared to h refinement.

The scalability is a measure which describes whether the efficiency of parallel computation can be kept constant if both the problem size and the number of processors n are increased. In other words, a larger problem can be solved in the same time as the smaller problem with sufficient number of processors.

Albeit there is no linear speedup for our acoustic solver with p adaptivity, we are still able to say that the solver is scalable if the efficiency remains within a certain range (constant) as the number of processors/threads is increased with the problem size within a certain range. From Figure 6.8, the efficiency oscillates from $n = 2 \sim 6$ (number of processors). However, the efficiency measure for $p = 6$ (number of DOFs is 58947) sustains a similar level (6.26% floating), this revealed the fact that p adaptivity in our current parallel solver can be said to be strongly scalable. In addition, $p = 6$ (number of DOFs is 58947) preserves its highest efficiency with the number of processors $n = 7$. Simultaneously, the same scalability condition can be observed (up to 7 processors) with mesh refinement levels at $h = 1, 2, 3$ on the right hand side of Figure 6.8 (b). It is a remarkable result, since for $h = 1$ (number of DOFs is 57661), its efficiency increases from $c = 2 \sim 6$. Notwithstanding the good scalability of h adaptivity, its efficiency tends to reach the peak (0.7115) with finest mesh $h = 1$, on the contrary, $p = 6$ has its peak at 0.8905 which is the maximum. Nonetheless, the scalability condition is only maintained up to 8 processors for the tested benchmark problem, additional processors will consume more time due to costs of information exchange when the size of the problem is retained at the same level [189]. This is also due to limited scalability of the direct solver applied.

In conclusion, the parallel processing computation algorithm in MoFEM performs well for higher order finite elements when solving acoustic problem with high wave number ($kD = 100$, $k = 10m^{-1}$, $D = 10m$) in the sense of efficiency and accuracy.

6.2.4 Performance of Field Split and Block Solver Preconditioning Scheme

In this section, the problem of a plane wave impinging on a sound hard sphere is solved on five different spherical meshes, from dense to coarse as shown in Figure 6.9. The metrics of total computational time and memory consumption are recorded with the averages of ten runs. This is intended to demonstrate the efficiency of the field split preconditioning in a concise manner.

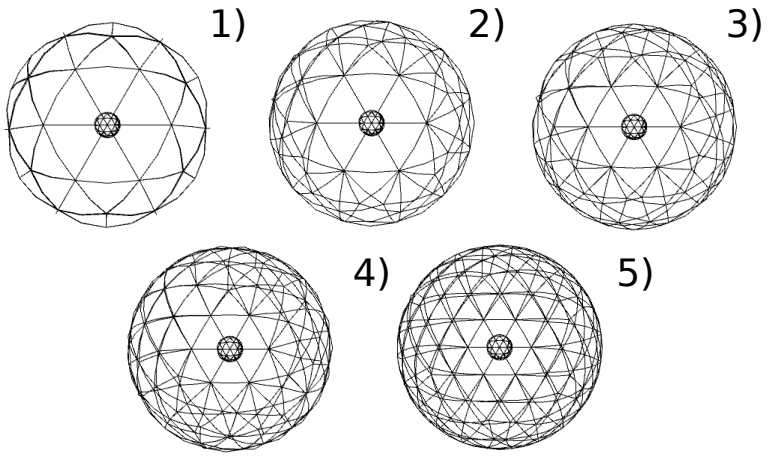

Figure 6.9: Example of five spherical meshes, refined from coarse to dense

In Figure 6.10, the time and memory consumption are plotted against the total number of nonzero entries (NNZ) in the sparse system matrix . The impact of field split preconditioning is demonstrated by the comparison of computational time and memory consumption when compared to conventional parallel computation. A rapid reduction of computational cost can be observed by using field split preconditioning, this is mainly because the size of the system matrix required to be factorized is approximately halved.

As one would expect, the memory usage tends to increase with well resolved models, and the size of the particular problem has a direct effect on the computational costs with the mesh refined in five steps. On the other hand, increasing p order does not result in a proportional growth in memory usage. There is barely any difference in global relative errors between the results from field split preconditioning and conventional parallel computation, therefore, we will omit the relative error plot here. To summarise, the field split preconditioning achieved a lower memory cost with less computational time while maintaining the same level of error as conventional parallel computations without a partitioned mesh due to partitioned smaller block matrices. However, the conclusion is only valid up to certain number of processors ($n = 8$) for the tested problem due to excessive number of processors used, this result can be changed by solving a larger problem with more number of DOFs. Moreover, the efficiency of the solver could be further improved by running a more scalable iterative solver on sub-blocks.

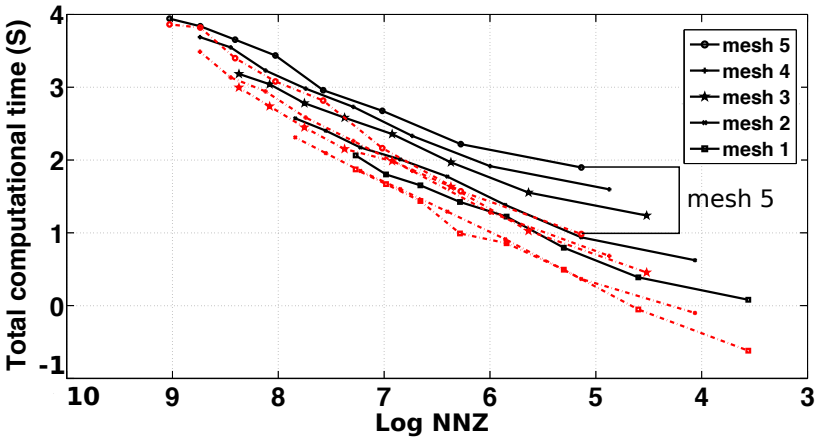

(a) total computational time versus NNZ

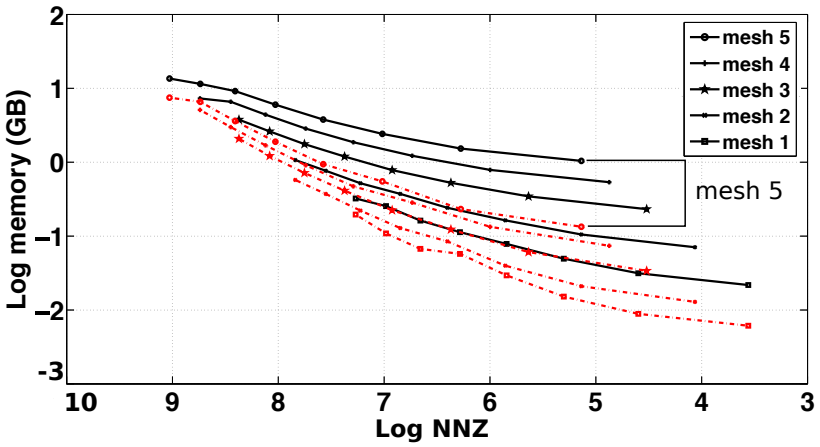

(b) total memory versus NNZ

Figure 6.10: Field split / Block solver preconditioning versus conventional parallel computation. Black solid line: conventional parallel computation with multiple processors. Red dashed line: field split / block solver preconditioning parallel computations with partitioned mesh. NNZ = number of non-zero entries

6.3 Conditioning Property of the Legendre Type Approximation Basis

The difficulty that arises in acoustic problems is that increasing the frequency results in the growth of the condition number of the system matrix. In other words, there will be more eigenvalues with negative real parts in the spectrum, which raises the indefiniteness of the system matrix. The amount of memory required to store and factorize the system matrix is also related to the conditioning of the matrix. The reason for keeping the condition number relatively low is to maintain a stable and rigorous solution, particularly for complex problems with a large, dense system matrix when using iterative solvers. For a system of linear equations $\mathbf{Ax} = \mathbf{b}$, the condition number measures how sensitive of the solution $\mathbf{x}$ is with respect to $\mathbf{A}$ and $\mathbf{b}$ such that is given as:

$$\kappa = \|\mathbf{A}\| \cdot \left\|\mathbf{A}^{-1}\right\| \tag{6.6}$$

where $\|\mathbf{A}\|$ can be specified to any desired norm. And the inverse of $\mathbf{A}$ is approximated:

$$\frac{\|\mathbf{x}\|}{\|\mathbf{b}\|} \leq \left\|\mathbf{A}^{-1}\right\| \tag{6.7}$$

The alternative way to define the L_2 conditioning number for matrix A is:

$$\kappa = \frac{\sigma_{max}(A)}{\sigma_{min}(A)} \tag{6.8}$$

where $\sigma_{max}(A)$ and $\sigma_{min}(A)$ is the maximum and minimal singular values of matrix $\mathbf{A}$ respectively. The method above is relatively accurate for converged solutions [55].

Linear systems of equations with poor condition number generally lead to longer calculation times for iterative solvers and yields results with larger round off errors for direct solvers. The magnitude of round off errors is correlated to the condition number. The type of finite element shape functions also has a strong effect on operator conditioning. In [31], the author suggests that ill shaped elements have a deleterious effect on an operator's condition number as well, since the condition number is proportional to the largest edge over the smallest volume of elements in the domain ($\kappa \subset \mathcal{O}(\frac{l_{max}}{V_{min}})$) [144]. In the case of high wavenumbers ($kD \geq 80$), the condition number directly affects the accuracy and convergence speed (iteration steps) of finite element solutions with iterative solvers [213].

The comparison was made between Lobatto and Legendre basis integrated by generalized Duffy transformation with optimal number of Gaussian integration points ($2p + 1$) (sufficient to integrate the polynomials exactly) [333] and well suited iterative solver with pre-conditioner.

The condition number of the Helmholtz operator versus the total number of DOFs, number of non-zero entries, the H^1 relative error and frequencies are illustrated to demonstrate the special property of the orthogonal polynomial basis coupled with the Duffy transformation. It is not surprising that the evolution of the conditioning number for the system matrix shows a complex trend. In Figures 6.11

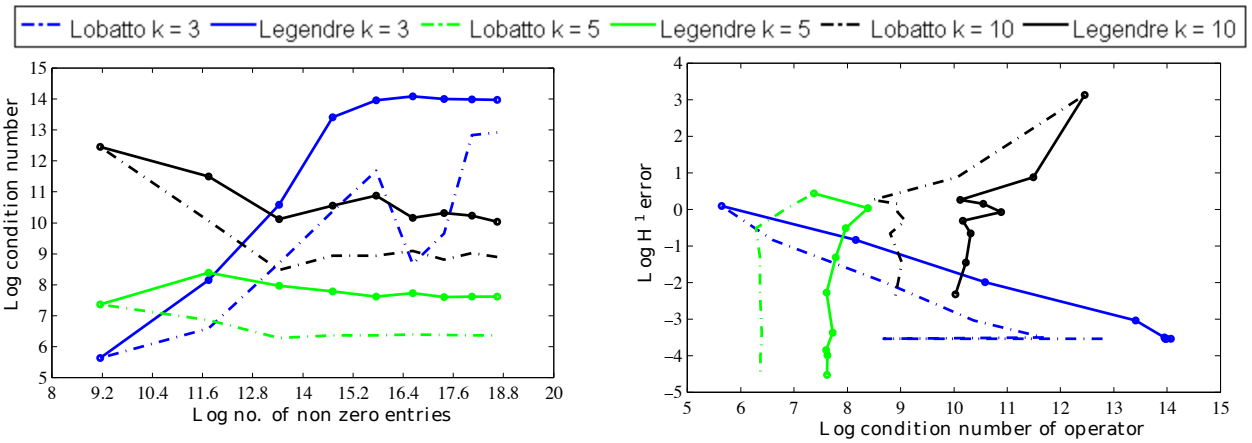

(a) condition number against number of non-zero entries

(b) condition number against relative H1 error

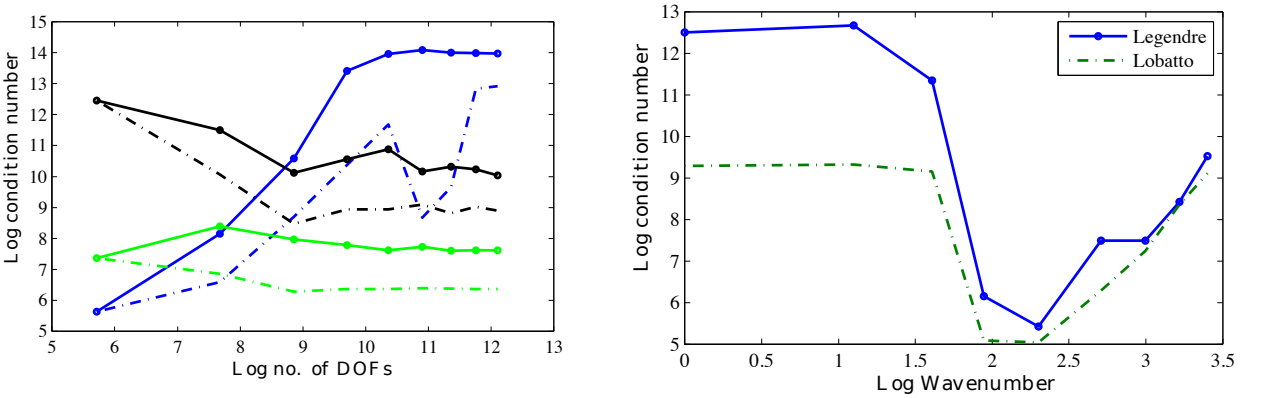

(c) condition number against number of DOFs

(d) conditioning number versus frequency in logarithm scale

Figure 6.11: Conditioning of system matrix (without preconditioning) of the Helmholtz operator, Lobatto basis versus Legendre basis coupled with Duffy transformation. Impinging sound hard sphere with $r = 4$, $a = 0.5$. (a) Condition number against number of non-zero entries, (b) Condition number against relative H^1 error. (c) Condition number against number of DOFs, (d) Conditioning number versus frequency in logarithm scale

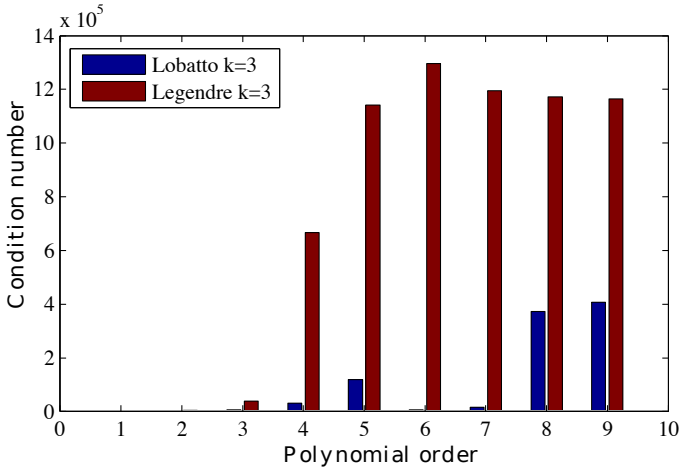

(a) k = 3

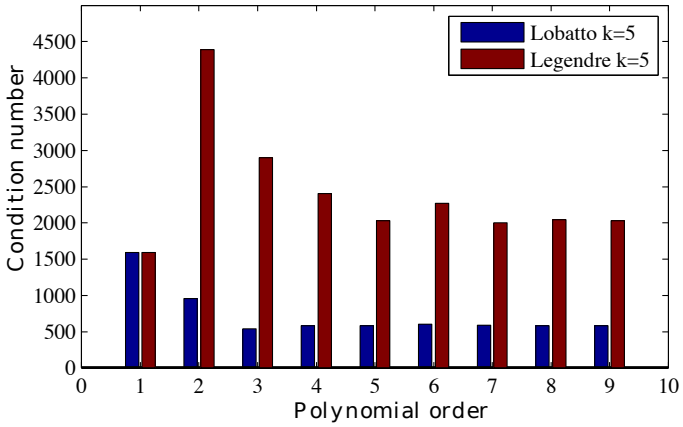

(b) k = 5

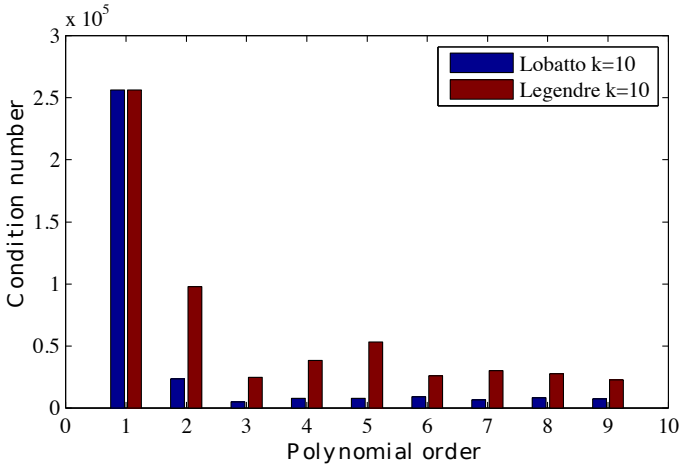

(c) k = 10

Figure 6.12: Conditioning of system matrix of the Helmholtz operator, Lobatto basis (navy) versus Legendre basis (brown) coupled with Duffy transformation, condition number against number of polynomial orders. Impinging sound hard sphere with $R = 4$, $a = 0.5$, $k = 3$, 5, 10.

the polynomial orders are increased from 1 to 9. Noticeably, the condition number versus the number of non-zero entries and DOFs for the Lobatto and Legendre basis coupled with generalized Duffy transformation appear to have identical behaviour for the test case.

On the other hand, in Figure 6.11 (b), a decreasing trend of H^1 error can be observed along with increasing of the condition number for the Legendre basis with small wavenumbers. It is worth noting that the error drops significantly when the polynomial order is increased with large wavenumber, ($k = 5, 10$) while maintaining the condition number around the same order of magnitude (in Figure 6.12 as well). The Lobatto basis is better conditioned than the Legendre basis, especially for high frequency cases (Figure 6.11 (d) , even though there are tiny differences between the H^1 relative error delivered by the Lobatto and Legendre basis (the error of the former is smaller than the latter in small decimal places). Nonetheless, both Lobatto and Legendre basis satisfied the convergence property asymptotically like $\mathcal{O}(D_\lambda^{-p-1})$, as proposed by Ainsworth in [9].

Theoretically, the conditioning of the system operator is expected to deteriorate progressively with the increase of both wavenumber (sign-indefinite of Helmholtz operator) and p order. Despite this, uniform p adaptivity maintains the condition number at the same order of magnitude, especially for the Lobatto basis, and there is no tendency of the condition number to deteriorate with p enrichment. In Figure 6.11 (d). The condition number has a maximum in excess of 1e6 when the highest polynomial orders are reached and at low frequency, and oscillatory region has been observed for small wavenumber. Nonetheless, the condition number tends to decrease with increasing polynomial order for relatively high frequencies ($k = 5, 10$) with both the Lobatto and Legendre basis. This observation demonstrates the effectiveness of these two basis when dealing with high frequency sweep acoustic applications. Similar observations have been demonstrated in [72]. The reason the conditioning number behaves differently with large wavenumber ($k = 10$) might be because of the coercivity of the Helmholtz equation has been deteriorated due to the high wavenumber [235]. This issue has been mitigated by using higher order shape functions ($p > 2$). The orthogonality condition of the Legendre type basis might also be responsible for the dramatical drop in conditioning number [180]. Theoretically, the orthogonality of shape functions can reduce the round-off errors in large problem when using direct solvers [43]. Overall, both the Lobatto and Legendre basis have negative relationship between condition number and wavenumber, which is one of the reasons that an efficient error estimator must take the wavenumber into account. To conclude, the Lobatto basis outperforms the Legendre basis in almost every aspects.

An important indicator of the efficiency of an algorithm is the amount of memory required, as here this is directly related to the process of factorizing and storing the stiffness matrix. The sparsity of the matrix depends on the number of non-zero entries. Subsequently, the number of non-zero entries affects the amount of memory required to store such matrix as well as factorization. In addition, the amount of memory consumed by the factoraziation process is also correlated with the p orders adopted.

It is a well known fact that the direct solver delivers faster calculation for small to medium scale problems. In contrast, Krylov subspace iterative methods and

pre-conditioners are far more efficient for large-scale problems as they require less memory, especially for partitioned mesh computational problems with multiple processors. There are many articles in the literature that test the relationship between operator conditioning and Krylov solver adopted to the operator in which the accuracy of the solution is shown to be significantly affected by the coupling of iterative solver and polynomial basis ([227, 130, 324, 253]). In [253], comparison was made between different iterative solvers on acoustic problems together with incomplete LU decomposition as pre-conditioner. Results indicate that the TFQMR solver with Bernstein basis is the most efficient combination to solve acoustic cavity problems. However, Bernstein has been shown to have a larger condition number than Lobatto basis by Prinn in [256]. Moreover, the condition number of Bernstein basis increases with increasing polynomial orders, which is the foremost defect since in order to solve a large system with high wavenumber ($kD \geq 80$), p adaptivity is compulsory to maintain efficiency. Also, it is not hierarchical based. The conclusion has been made that Legendre type basis are better conditioned than Bernstein, Hermite and spherical basis [77, 348]. Despite the asymptotic condition number, Bernstein results in similar convergence rates as the Lobatto basis within identical total calculation time [256]. Alternatively, CG (conjugate gradient) and GMRES (generalized minimum residual) [280] with pre-conditioner ILUTP and PCG are shown to deliver more stable solutions than direct solvers for solving large-scale problems with triangular shape functions [197].

6.4 Concluding Remarks

Advanced parallel computation algorithms were developed in this chapter for hierarchical higher order finite element with h and p adaptivities. Two and three dimensional benchmark problems, i.e. incident wave impinging on a sound hard cylinder / sphere are solved to show the accuracy and speed of the proposed algorithm. The performance of the distributed memory parallel computation is assessed with measures: computational time, memory consumption, efficiency, speedup and different mesh densities.

The complex-real valued transformation together with the field split and block solver preconditioning method for system of equations are introduced, this implementation can sufficiently reduce the overall computational costs (i.e. factorization memory, computational time) when compared to the conventional parallel computation, and mitigate the complexity of FE codes. The numerical results identified that the parallel computation algorithms perform faster with p adaptivity than h adaptivity scheme when their error levels are identical. Furthermore, the capability of FE codes to handle problems with fine to coarse discretizations with various k values is also demonstrated. In addition, the condition number of the Helmholtz operator is analysed between Lobatto and Legendre shape functions, the result demonstrated the hierarchical Lobatto basis can deliver better condition number than Legendre basis with increasing wavenumber and p adaptivity.

Chapter 7

Automatic Adaptivity Schemes

7.1 Preliminary Notions

Nowadays, efficient and low cost error estimation techniques are active areas of research in finite element analysis. In previous chapter 6, the advanced methods on how to solve a large acoustic problem with distributed memory and parallel computation are expounded in details. In this Chapter, following the discussions of *a priori* and *a posteriori* estimators in previous contexts, the origin and development of *a priori* error estimator for acoustic problems are first presented. The superior property of p enrichment over h refinement has been tested in previous chapters. However, p FEM tends to create large matrix bandwidth compared to pure h refinement, which results in more factorisation memories. Therefore, non-uniform p adaptivity with targeted order and predefined accuracy is vital, in order to minimize the overall computational effort. With the use of automatic p adaptivity scheme, the size of the original problem would be mitigated whilst maintaining the desired accuracy.

First, the *a priori* error estimator adopted in acoustic solvers is introduced and examined in one and higher dimensions with benchmark problems. Then, the encountered error and computational costs are measured through various assessments. The effectiveness of the proposed error estimator on controlling the pollution error in a global sense is demonstrated at various frequencies with increasing domain lengths. In order to identify the accuracy and efficiency of the error estimator, an automatic p adaptivity scheme is assessed together with uniform p and h adaptivities. Finally, conclusions are drawn on the basis of numerical tests with pronounced results.

7.2 A Simple Object Oriented Error Estimate

7.2.1 Introduction

Error estimators were first discussed in 1978 by Babuška, *et al.* [47] , and the study of error estimation techniques has been well established over the past 30 years. A simple *a priori* local error estimator enables a prescribed accuracy as introduced in [343] such that the optimal polynomial order / mesh resolution can be selected automatically prior to the solution. The *a posteriori* error estimators are generally expensive, either requiring interpolation or extrapolation techniques (ZZ like estimators) [343, 340], or solving additional linear system of equations (element residual based estimator) [12, 200, 47, 58]. Most of all, they are not as effective in three dimensions as they are in lower dimensions (e.g. the super-convergent points are non-existent inside 3D elements) [14]. In addition, Ainsworth assessed that *a posteriori* error estimators are only reliable in the asymptotic range, such that they commonly fail to account for the pollution effect [8, 179]. On the other hand, the overhead cost of *a priori* error estimators is extremely small when compared to *a posteriori* error estimators.

Despite the computational efficiency of *a priori* error estimators, the criterion of how to judge the effectiveness of a particular error estimator is vital, since its heuristic nature demands numerical tests on specific problems to affirm its correctness. Moreover, the local error indicator does not account for the pollution effect, which is included in the global relative error. Three automatic adaptive strategies for acoustic wave-guide problems were illustrated in detail in [72], such that their merits, defects and limitation are presented. The *a priori* error estimator produced reliable outcomes on controlling the pollution error, thus the adaptivity strategy based on it proved to be efficient. In [71], the authors concluded about the superior properties of p adaptivity FEM applied on one and two dimensional benchmark wave-guide problems and exponential p convergence is confirmed in their analysis.

Alternatively, the impact of p adaptivity on the efficient mitigation of the pollution error is proved with the wave-guide benchmark problems. A comparison between the Trefftz method and a higher order polynomial adaptivity scheme is performed on four distinguished 2D Helmholtz problems in [214]. The authors summarised that both methods satisfied different metrics used to measure the performances (error, condition number, memory). The general argument is that the time dependant Helmholtz equation requires the Trefftz method for calculating and assembling the element matrix in each time step, due to the frequency dependence of wave based shape functions. In [13], the authors argued that traditional element residual based methods were unable to capture the pollution error, since the desired errors are accumulated outside of the subdomain of interest. Meanwhile, the error estimators measured the local error from local residuals within the subdomain, where as pollution error generated from remote residuals which are outside of the subdomain, hence it can not be detected by this type of error estimators. The authors also concludes that any refinement taken based on such *a posteriori* error estimators would not necessarily reduce the actual error.

7.2.1.1 Asymptotic Error Estimator

The convergence process of finite element solutions can be divided into pre-asymptotic and asymptotic ranges. The pollution error dominates the pre-asymptotic range, whereas the interpolation error becomes dominant in the asymptotic range. The existing error estimator makes use of the parameter kh as a criterion to adjust the polynomial orders of each element present on the mesh.

In order to prejudge the suitable polynomial order for a specific element, the *a priori* error estimator takes the element size (domain size) and frequency as mandatory input parameters. Thus, the Babuska's (asymptotic) estimator in Eqn. (5.16) of [183]) can be rewritten as:

$$p_{opt} = \frac{1}{2}\exp\left\{W_0\left[\frac{2}{kh}\left(2\pi\mathrm{i} + log\frac{C_1 + \sqrt{C_1^2 + 4C_2\Phi_\epsilon k}}{2\Phi_\epsilon}\right)\right]\right\} kh \tag{7.1}$$

where W_0 is called the Lambert function in principal branch in the form of $W(z)e^{W(z)} = z$, $z \subset \mathbb{C}$. In essence, one can select the desired error level Φ_ϵ prior to deciding the optimal polynomial order required.

7.2.1.2 Ainsworth Error Estimator

Apart from the *a priori* upper bound indicator (5.21) addressed previously based on the H^1 semi-norm, according to [9], another *a priori* model for guiding selection of the polynomial order is also proposed. This is again based on the fundamental parameters k and h of the acoustic problem. The basic premise of this guideline is that the final solution neglects the dispersion effects.

$$2p + 1 > kh + C_3(kh)^{\frac{1}{3}} \tag{7.2}$$

where C_3 is a problem specific constant that is equal to unity in practice for simplicity. The above inequality (7.2) [9] can be modified to yield the required polynomial order as:

$$p_{opt} = \frac{kh + C_3(kh)^{\frac{1}{3}} - 1}{2} + \Phi_\epsilon \tag{7.3}$$

Various values of C_n can be tested in the above estimators to determine the optimal response for a given frequency (e.g. $C_1 = 33, C_2 = 6.28, C_3 = 4.45$ are considered as optimal in [256]).

7.2.2 Formulation of an *A Priori* Error Estimator

Here it is assumed that there is a relationship between the 1D edge element and higher dimensional elements for solving the same problem, such as when the error incurred in higher order element can be estimated from the errors incurred in their lower dimensional images. In other words, the numerical errors occurring in the lower dimensional element can serve as an indicator for the higher dimensional element. In essence, the error estimator estimates the average of the error occurring

in each element from a given mesh. By solving a one dimensional Helmholtz problem and obtaining a certain predicted error with input kh, one can determine the optimal p order required to achieve a certain level of accuracy. The element length is defined by taking the average on six edges of the tetrahedron element: $h_a = \sum_i^{N^e} \frac{\bar{h_i}}{N_e}$.

The concise process of adopting *a priori* error estimator is as follows: First, retrieve the characteristic length (e.g. h_a in context) and wavenumber of a specific element in the computational domain, and then assess the algorithm of specific error estimator using a linear element, obtain the actual error associated with the chosen error estimator. Secondly, compare the actual error with a predefined error (or desired error), if the actual error is greater than the predefined error, it is necessary to increase the polynomial order by one, and assess the algorithm of the specific error estimator again. This procedure is executed repeatedly until the actual error is smaller than or equal to the predefined error level, which means the actual error met the criterion, and the predefined error level is achieved. Finally, the sufficient polynomial order p is stored in that specific element. This same loop is carried out repeatedly for every element in the domain until all elements have been assigned a proper p order. Theoretically, this procedure accounts for the local medium property k, and hence the difference between discrete wavenumber k_h and initial theoretical k as previously shown in Eqn. (5.22). However, a parameter that includes the distance is needed.

The adaptivity scheme prescribed can be further optimised by pre-calculating and tabulating the criterion of problem dependant χ_{kh} value corresponding to the best polynomial order p in the premise of predefined error level. Consequently, the value of kh in each element is compared with the criterion value χ_{kh}, if actual $kh < \chi_{kh}$, the best p corresponding to χ_{kh} is employed. Hence, this procedure saves the repeated calculation effort for each element. The execution procedure expressed in pseudo code is depicted in Chart Algorithm 1. In Figure 7.1, the acoustic problem is solved on each edge of a tetrahedron and the actual error is retrieved to represent the higher dimensional error.

7.2.3 One Dimensional *A Priori* Error Estimator

Here in this section we present three one-dimensional Helmholtz problems, which will be used as *a priori* error estimator to predict the actual error on higher dimension elements.

One Dimensional Coercive Elliptic Type Boundary Value Problems

The following problems are solved using Legendre type shape functions on single element with the order varying from 1 to 10.

Once again, on the domain $x \in [0, l]$, one dimensional Helmholtz problems with Dirichlet and Robin BCs are resolved, with various kh values. The first example is an inhomogeneous Helmholtz equation:

$$u'' - k^2 u = 1, x \in [0, l], u(0) = 0, u'(l) - \mathrm{i}ku(l) = 0 \tag{7.4}$$

with analytical solution : $u_a = e^{\mathrm{i}kx} - 1 - \mathrm{i}e^{\mathrm{i}k} \frac{\sin(kx)}{k^2}$, we call it *a priori* error estimator 1 (referred to the author A. Prinn firstly applied this idea of error estimation on

Algorithm 1 *A Priori* Error Estimator-Pseudo Code:

procedure EVERY ELEMENT IN COMPUTATIONAL DOMAIN
    $h_a = \frac{\sum_i^6 h_i}{6} \leftarrow$ average length of *edges*
    $k \leftarrow$ *wavenumber*
    set : $p_{node} = 1$
    set : error $= 0$
    set : $p_{max} = 10$
loop
for $ii = 1; ii < p_{max}; ii++$
    solve 1D acoustic problem based on h_a and k
    set : new error
    if *error* $>$ *expected error level* (ii) **then**
        increase p_{edge}, p_{face}, $p_{interior}$
    else
        break loop;
end
    store p for each entities, and set the polynomial orders.
start *calculation.*

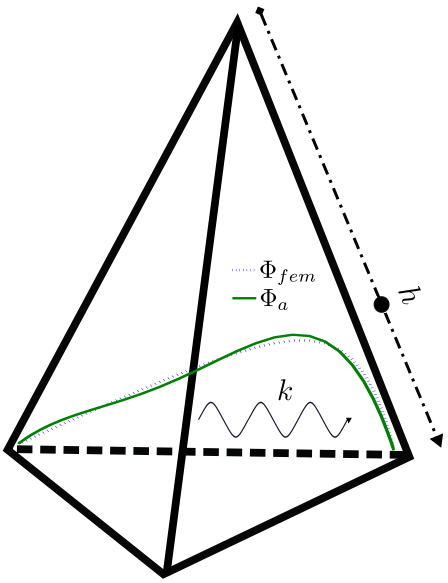

Figure 7.1: Example of one-dimensional acoustic problem solved on the edge of tetrahedron, Φ_{fem} numerical solution, Φ_a analytical solution

wave guide problem in [256]). The second example is as follows:

$$u'' + k^2 u = -k^2 sin(x), x \in [0,1], u(0) = 0, u(1) = 0 \tag{7.5}$$

with analytical solution : $u_a = (e^{-kx} - e^{kx})\frac{sin(1)}{(1+\frac{1}{k^2})(e^k - e^{-k})} + \frac{sin(x)}{1+\frac{1}{k^2}}$. The third example is the homogeneous Helmholtz equation with Dirichlet BC representing a soft boundary impinged by an incident wave, and Robin BC applied at right end point stand for non-reflection boundary.

$$u'' - k^2 u = 0, x \in [0,l], u(0) = 1, u'(l) - \mathrm{i}ku(l) = 0 \tag{7.6}$$

with analytical solution : $u_a = e^{\mathrm{i}kx}$. The following Figures are examples of Helmholtz problems that can be solved on edge elements.

Figures 7.2 to 7.4 show the numerical and analytical solutions of the three example problems as well as the L_∞ errors on a 1D edge element with $p = 3, 4$. From Figures, we can observe that example problems 1 and 2 tend to underestimate the error with higher order element $p \geq 3$.

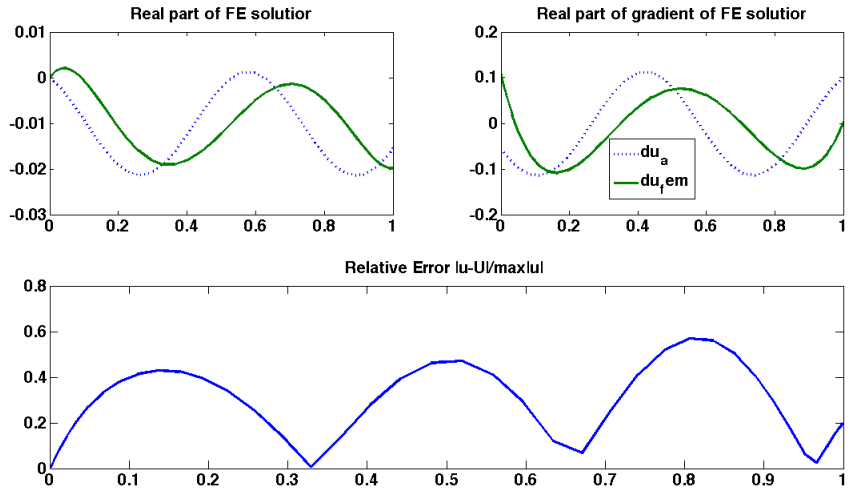

(a) p=3

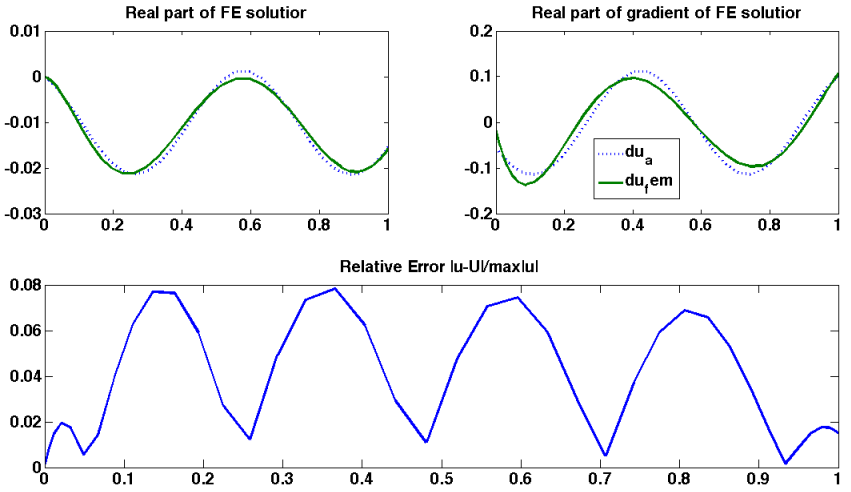

(b) p=4

Figure 7.2: Single edge element Helmholtz problem 1, $p = 3 - 4$

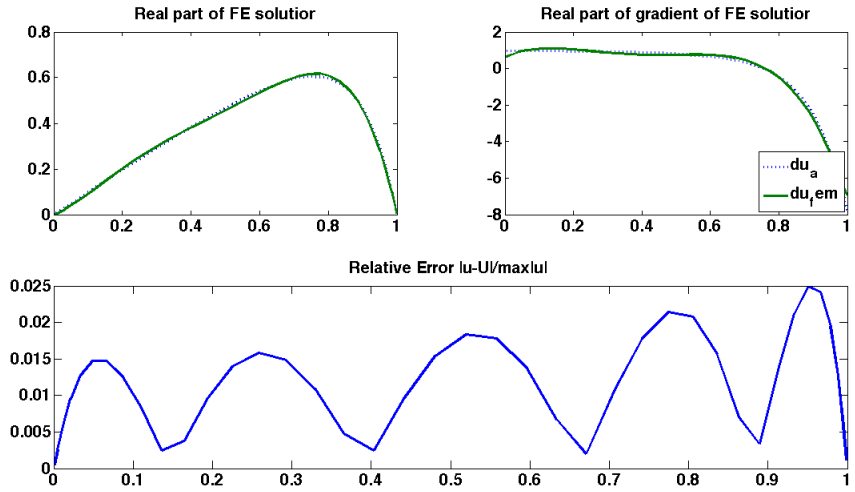

(a) p=3

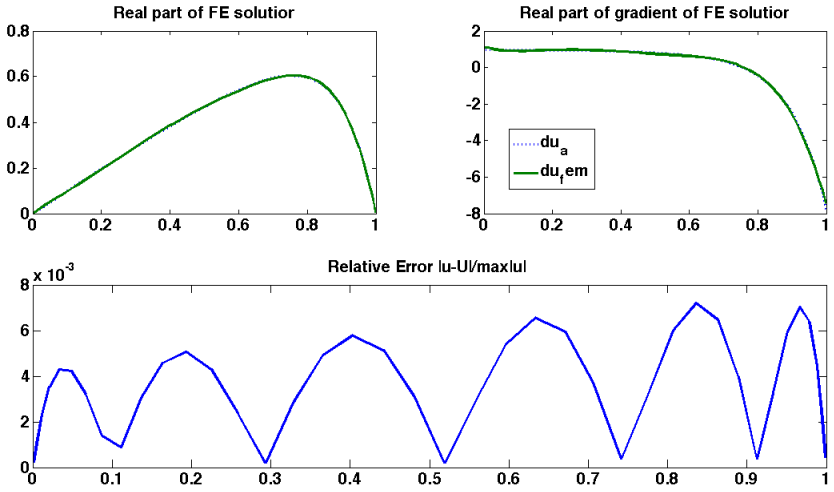

(b) p=4

Figure 7.3: Single edge element Helmholtz problem 2, $p = 3 - 4$

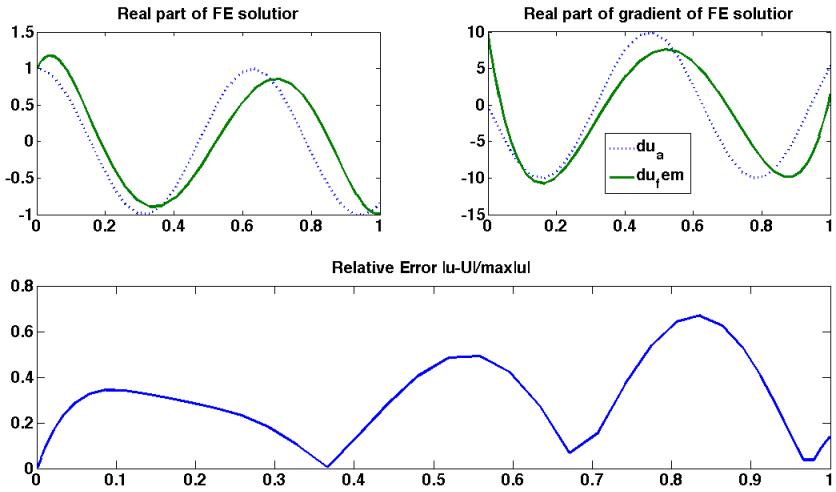

(a) p=3

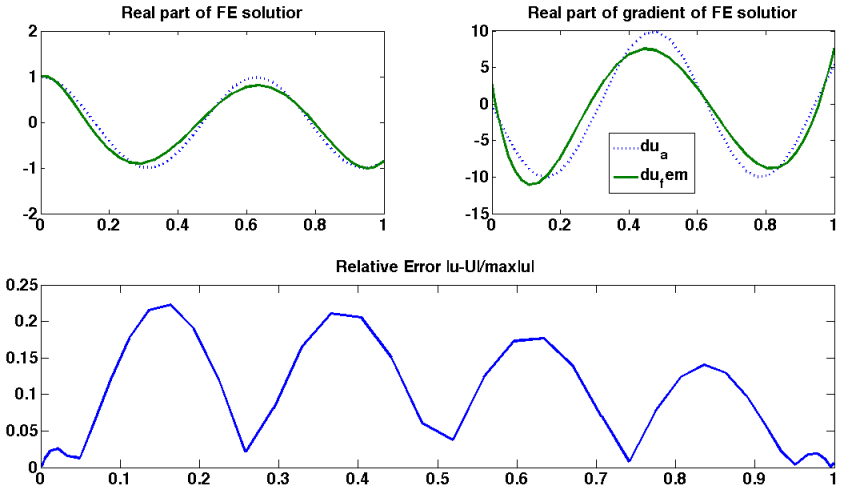

(b) p=4

Figure 7.4: Single edge element Helmholtz problem 3, $p = 3 - 4$

7.3 Performance of Error Estimators in One Dimension

Previously, the basic idea and framework of *a priori* estimator was established. Five possible estimators were proposed based on the assumption of the time harmonic Helmholtz equation. However, the link between kh value and polynomial order p still remains undiscovered. This might be the key factor in efficient error estimation, and the tradeoff mechanism between accuracy and computational cost.

7.3.1 Error Versus Number of Degrees of Freedom per Wavelength

In the following section, we will present the analysis for *a priori* error estimators in 1D linear elements, such that the relative error versus the number of DOFs per wavelength will be drawn for comparison. The aim of this section is to investigate the relationship between errors on edge element and the kD values. In one dimension, the diameter of the computational domain is equal to the length of the edge h, and the wavenumber depends on the angular frequency ω with $c = 1$.

In the first and last set of Figure 7.5, the number of DOFs will be fixed in ranges, where $p = 1 \sim 10$ are applied. In the first set of ten orders (denoted by line style o), the frequencies will be varied from $\omega = 1 \rightarrow 150$. In the second set of ten lines (denoted by the marker $-.$), the angular frequency (ω) will be fixed at 100, while the size of the linear element h is gradually reduced in order to maintain the constant number of DOFs per wavelength. Thus, the connection between k and h can be investigated.

From Figure 7.5 *a*) and *b*) we can see that the L_2 and H^1 error versus $D_\lambda = \frac{2\pi p}{kh}$ respectively. The black straight line in each graph denotes the desired relative error level of 15%. In order to see a notable reduction of errors due to refinements, a relatively higher level of 15% error threshold is chosen. As expected, there are two main observations.

Firstly, different frequencies do not change the L_2 error of the solution as long as kh (D_λ) is kept constant. This is because the main source of the finite element error comes from the interpolation in a single element, this is an artefact reflecting the nature of polynomial interpolation. This observation allows us to manipulate the error by adjusting the frequency and fixed element size. Moreover, in higher dimensional problems, using this fact, a hard coded error table can be generated and a corresponding p can be directly selected based on a pre-calculated value of kh that is correlated to a predefined error level. Thus, additional loop of calculation is saved for every element in the domain. In the situation for which $p = 10$ and $kh < 1$, fluctuation occurs due to machine precision limitation ($error \ll 1.0000e - 12$). However, in some cases, an unchanged error corresponding to increasing DOFs does not necessarily mean the solution has converged.

Secondly, in Figure 7.5b), the number of DOFs per wavelength is increasing due to the variation of element size h while kh is kept constant. The H^1 relative error with smaller frequency (line o) tends to converge faster than reducing the element size but keeping $\omega = 100$ (marker $-$.). Moreover, the difference between H^1 relative errors with the same order and identical kh is mitigated with higher order elements, but rather become significant for linear and quadratic elements. Further tests have been conducted with more DOFs, and complete overlapping is observed in the asymptotic range. It is therefore reasonable for H^1 error convergence plots to exhibit a long pre-asymptotic range during which the interpolation error is not yet dominant [302].

Overall, the values of L_2 and H^1 relative errors in both Figures expound that, even with D_λ kept constant, the error convergence speed is delayed by high wavenumber when the gradient of the solution is involved. It reveals that purely decreasing h while keeping k unchanged is not sufficient enough to include all the errors. It further affirms the necessary choice of kh as input parameters for construction of the *a priori* error estimator. Consequently, the current result also suggests that different weight functions for k and h might be sufficient. Furthermore, the relative errors for low polynomial order case (e.g. $p = 1$) in relatively low discretisation regions (pre-asymptotic region) remain at the same level when the element size h is reduced. Contrarily, the relative error with higher order element (e.g. $p > 2$) decreases dramatically as h is decreased. It proves the fact that even with kh kept constant, higher order elements behave better than low order elements with mesh refinement.

7.3.2 Optimal Polynomial Orders Versus Number of Degrees of Freedom per Wavelength

In this section, the examples of Helmholtz equations (A.38), (A.39) and (A.40) are solved in one dimension. Next, the optimal p order assigned is retrieved and plotted against the number of degrees of freedom per wavelength, the optimal p orders obtained are compared with the predicted p values from the asymptotic error estimator in Eqn.(7.1) and the Ainsworth error estimator in Eqn.(7.3).

The plots 7.6 and 7.7 shown are for the optimal p order against D_λ required to achieve a predefined error level bound of 0.5%, 5% and 15% respectively. The number of elements per wavelength from 0.5 to 15 generated is plotted against the p order, while the input parameter kh is kept constant during the calculation of the *a priori* error estimator.

The predicted p orders from asymptotic Babuska's error estimator and Ainsworth's estimator have been rounded off to integers for visualisation convenience. In plot 7.6, the asymptotic error estimator generates reasonably decreasing p order when the number of elements per wavelength is increasing. On the other hand, the Ainsworth estimator behaves differently such that with the same D_λ, less p order is required to achieve a lower error bound. Intuitively speaking, it is too conservative. Furthermore, the asymptotic error estimator tends to give pessimistic results, which can serve as an upper bound for the optimal order predicted. However, there is no

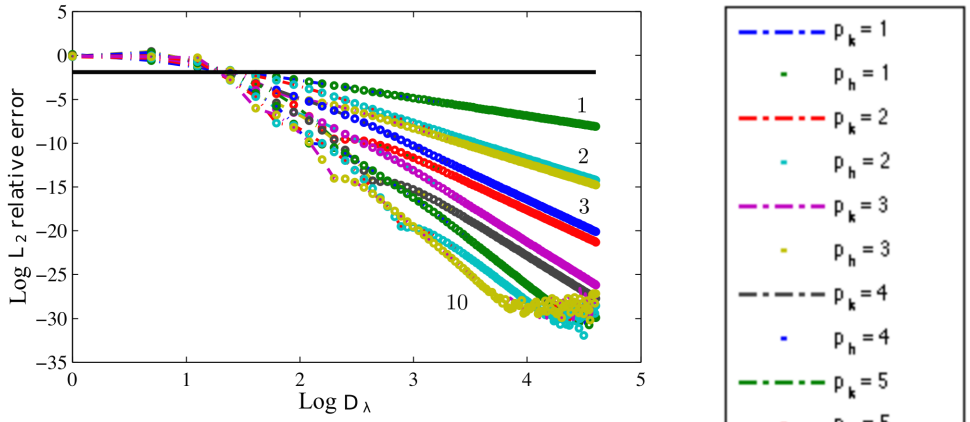

(a) L_2 global relative error

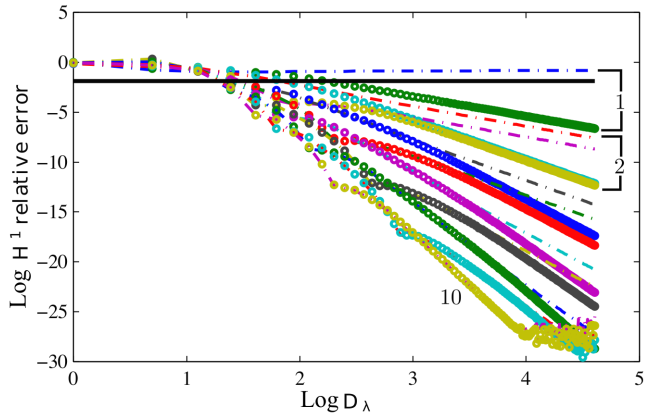

(b) H^1 global relative error

Figure 7.5: Single element predicted error by *a priori* error estimator example problem 3 versus number of DOFs per wavelength, in logarithm scale, start from 100%. Black straight line represents error level of 15%

marked difference between the range of orders. In order to have an efficient adaptivity algorithm adopting these two error estimators, specifically defined problem dependant constants (C_n) will be required in practice. In other words, the shifting process of different predefined error levels will be computationally expensive.

Analogously, in plot 7.7 (c) - (d) the p order predicted by the 1D test problem 2 is underestimated, and the range of p is short. In the context of [324], the authors proved that the longer the range of p order provided by the error estimator, the more accurate the calculated adaptivity solution will be. It is reasonable since in practice, an unstructured mesh with various element sizes is expected. Conversely, The distribution of p order ranges are 10-2 and 10-1 for test problem 1 and 3 respectively. And the range for test problem 2 is 7-2. Theoretically, test problem 3 is more preferable as *a priori* estimator for higher dimensional acoustic applications. Nonetheless, higher dimensional numerical analysis is still mandatory in order to perceive the sufficient p order without wasting excessive memory and calculation times. The reason behind this might be because of the exact solution of test problem 3 is a general solution of the Helmholtz equation, thus it naturally provides better functionality compared to other types.

Table 7.1: Table of χ_{kh} values oriented *a priori* error estimator with three predefined error levels

p **order**	**1**	**2**	**3**	**4**	**5**	**6**	**7**	**8**	**9**	**10**
$\chi^{L_2}_{15\%}$	0.5	2.900	4.8	7.5	7.97	12.33	12.54	14.6	15.2	19.43
$\chi^{H^1}_{15\%}$	0.2	2.3	3.88	6.8	7.1	11	11.17	14.54	15.28	19.023
$\chi^{L_2}_{5\%}$	0.1	1.85	3.67	6.6	6.76	8.96	10.3	13.43	13.7	17
$\chi^{H^1}_{5\%}$	0.05	1.85	3.25	5.5	5.6	8.4	9.67	12.74	12.75	15.04
$\chi^{L_2}_{0.5\%}$	0.05	1	1.33	3.6	4.6	7.05	7.35	9.4	10.76	13.625
$\chi^{H^1}_{0.5\%}$	0.02	0.41	0.83	2.35	3.64	6.25	6.28	8.46	9.83	12.62

The optimal p orders with relevant kh values are retrieved by solving a series of one dimensional Helmholtz problems, and then hardcoded into the program as the example shown in Table 7.1.

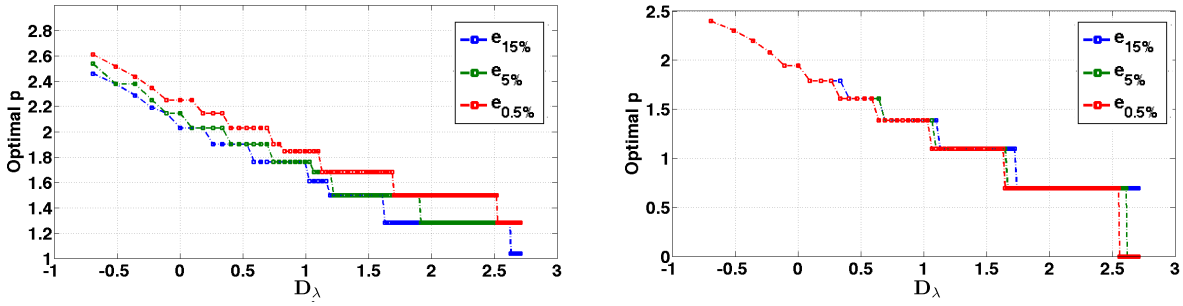

(a) Asymptotic error estimator

(b) Ainsworth error estimator

Figure 7.6: Single element optimal p order predicted by Asymptotic and Ainsworth error estimators versus D_λ in log scale

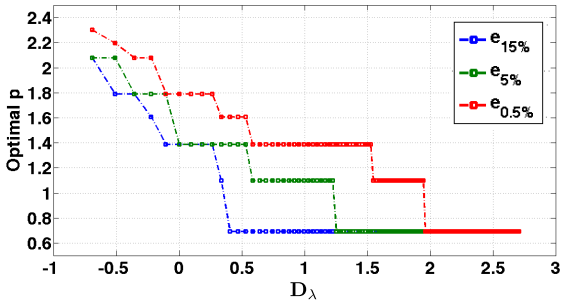

(a) indicator 1 - L2 error

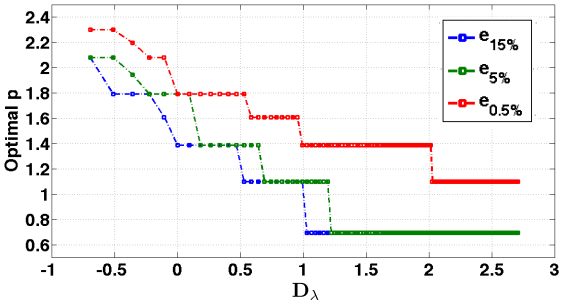

(b) indicator 1 - H1 error

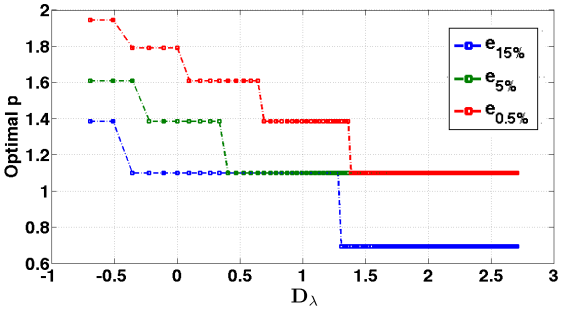

(c) indicator 2 - L2 error

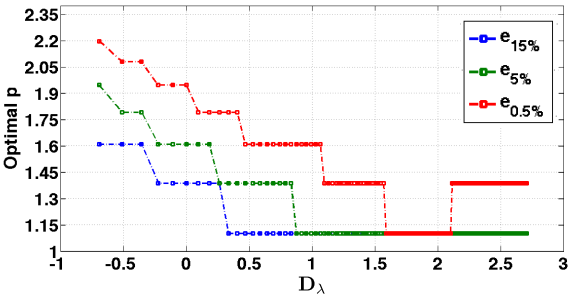

(d) indicator 2 - H1 error

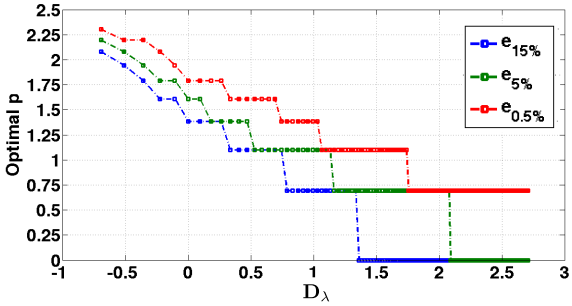

(e) indicator 3 - L2 error

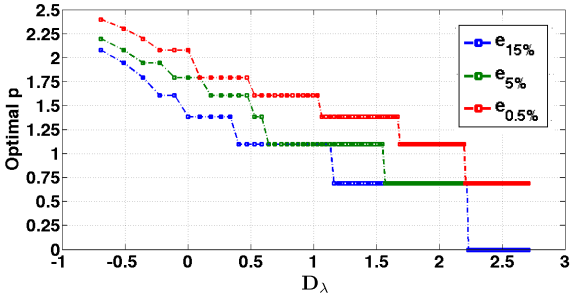

(f) indicator 3 - H1 error

Figure 7.7: Single element optimal p order predicted by *a priori* error estimators with three test problems, against D_λ in logarithm scale

7.4 Analysis of Performance of *A Priori* Estimator in Three Dimensions

7.4.1 Visualization of Performance on Computational Domain

In this section, the adopted *a priori* error estimator will be tested with benchmark problems, and the local errors will be visualized.

As depicted in Figure 7.8, the finite element defined based on p adaptivity indication of Table 7.1 is compared with the analytical solution. The $\chi(kh)$ values in Table 7.1 are obtained from solving Helmholtz equations in one dimensional edge elements with various predefined kh values and corresponding error levels. The benchmark problem of a plane incident wave impinging on a sound hard cylinder is presented in two dimensions. The piecewise H^1 actual error is calculated on the computational domain. The local dispersion error caused by phase shifting is a global effect that builds up over the whole computational domain [180]. Such a measure is useful as, other than the p adaptivity table defined above (with predefined error levels), we could equally well use another intuitive refinement criterion, such that element K needs to be refined whenever the local error in element K is within seventy percent of the largest estimated error group: $\epsilon_K^e \geq 30\% \times \max_{K_j \in \Omega} \epsilon_{K_j}^e$.

As shown, the largest part of the error occurs around the boundaries of the scatterer and the exterior boundary, as well as along the propagation direction. The former can be sufficiently eliminated through the p adaptivity algorithm as shown in 7.8 (b), whereas the latter contribution by the dispersion error can only be alleviated.

Nevertheless, these dispersion errors can be minimised by hierarchical shape functions of the Lobatto basis through automatic p adaptivity, in such a way that the phase accuracy of higher order elements is greater than that of lower order elements with the same number of DOFs. The total relative H^1 error after the p adaptivity scheme is approximately 0.2496% when the predefined error level is 0.5%. In addition, the p adaptivity algorithm has successfully spotted the errors around 34% in Figure 7.8(a), which are indicated by the red coloured regions ($p = 6$) in Figure 7.8 (c). Noticeably, the range of scalar values in Figure 7.8(a) is much wider than 7.8 (b), e.g. the pressure value in the pink region in Figure 7.8 (b) is approximately 319 times smaller than in (a).

It should be noted that the polynomial orders projected on the computational domain in Figure 7.8 (c) are the maximum order between each entities. For instance, if two adjacent elements have different orders for their edges, the highest order among all edges will be selected. Moreover, Figure 7.9 shows the p order map created by the automatic p adaptivity scheme for impinging hard sphere problem with initial non-uniform unstructured mesh.

The dispersion error caused by phase shift (e.g. inconsistence of wavelength)

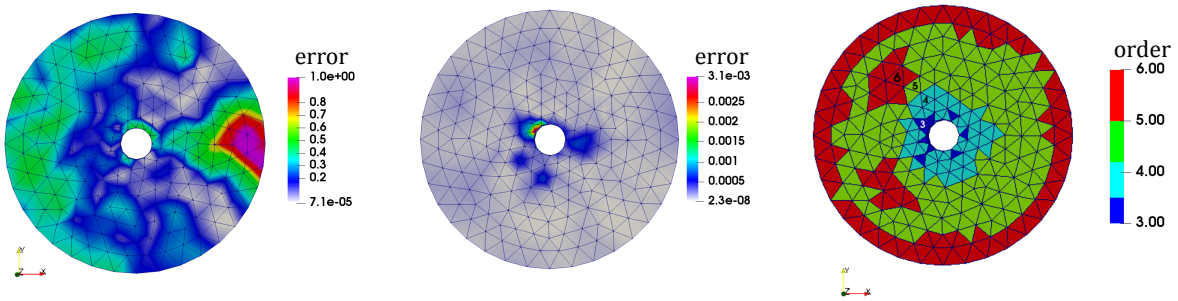

(a) before p adaptivity (b) after p adaptivity (c) predicted optimal p order

Figure 7.8: H^1 global relative error, p adaptivity algorithm for rigid cylinder problem with $k = 10$, $a = 0.5$ and $R = 4$, predefined error level $\eta = 0.5\%$, number of elements = 1439 in total. Before p adaptivity, $p = 1$

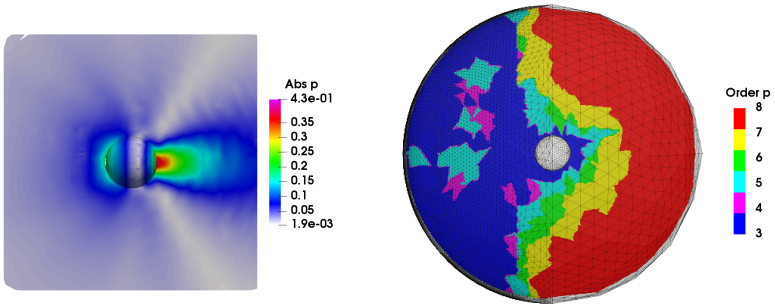

(a) absolute potential (b) predicted p order

Figure 7.9: Automatic p adaptivity, p adaptivity algorithm for rigid sphere problem with $k = 10$, $a = 0.5$ and $R = 4$, predefined error level $\eta = 0.5\%$

is a global effect that builds up itself over the whole computational domain [180]. In Figures 7.10, it is noteworthy that the error drops down significantly after p adaptivity. Especially with non-uniform kh oriented adaptivity scheme, local error decreasing rapidly around the end of x axis where the dispersion error accumulated to its maximum value.

In this Chapter, all the tests assessed, including time and memory recorded, are performed on a Intel Xeon CPU E7- 4830 (2.13 GHz) with maximum of 32 cores and two threads per core. All numerical tests are executed without parallel computation with partitioned mesh and field split / block solver preconditioning, this is done in order to demonstrate the plain and authentic efficiency of a particular method.

7.4.2 Measurement of the Accuracy and Flexibility of Proposed Error Estimator

Since the performance of the *a priori* error estimator is dependent on how well the single element acoustic problem can mimic a three dimensional element, several comparisons will be made based on different criterions. In order to assess this, an unstructured mesh will be discretized by second order tetrahedrons (nodes in the middle of each edge). The hierarchical shape functions of Lobatto type will then be employed together with the generalized Duffy transformation to assure the rigorousness and robustness of our acoustic solver. Thanks to the assessments on element size definitions in [256], the average of element edges has been proven to be the most sufficient measure, of which others measures include the maximum and minimum edge lengths. Three predefined error levels are chosen; they represent fine (0.5%), normal (5%), and coarse (15%) resolutions respectively.

A criterion can be derived from Eqn. (5.19), such that the upper bound for the discretized element size can be defined as:

$$h_{max} < C_E \frac{c}{f_{max}} \tag{7.7}$$

where the constant C_E is set to be the value of $\frac{\chi_{kh}}{2\pi}$, χ_{kh} related to the required predefined error E_p. For example, in Table 7.1 χ_{kh} value of 9.4 corresponds to a predefined desired L_2 error of 0.5% with optimal $p = 8$, hence, $C_E = \frac{9.4}{2\pi}$. Therefore, the maximum frequency limitation is: $f_{max} \approx C_E \frac{c}{h_{max}}$.

7.4.2.1 Unstructured Spherical Meshes

Here we present four different spherical meshes specially designed for the benchmark problem to investigate the application of the *a priori* error estimator. The first two meshes are each composed of roughly uniformly sized elements with the first, coarse, mesh having larger elements than the second, dense, mesh. The third and fourth meshes are non-uniformly h refined along the wave propagation direction. The description of meshes are as follows:

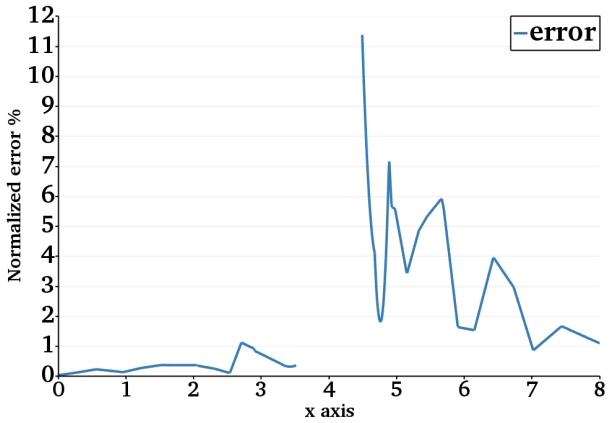

(a) relative error before p adaptivity (linear element)

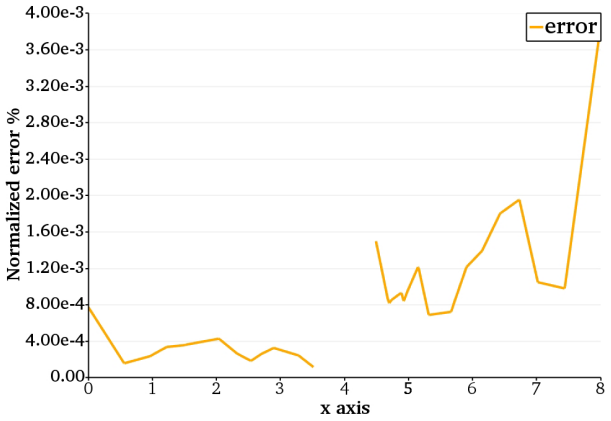

(b) relative error after uniform p adaptivity

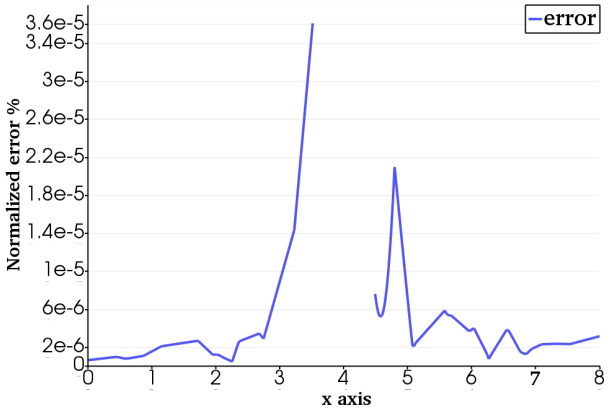

(c) relative error after kh oriented p adaptivity

Figure 7.10: Plot of local L_2 error over central line along x axis, relative error versus diameter of cylinder. p adaptivity algorithm for impinging rigid cylinder problem with $k = 10$, $a = 0.5$ and $R = 4$. $\eta = 0.5\%$, number of elements = 1439 in total. Note: (b) uniform p adaptivity with order 2 (normalized).

1. uniform mesh 1 with 1219 elements, and average element size of 0.7779 (mesh resolution ranges from $\tau = 86.5202 - 0.3624$) with frequency limitation:
    - $\omega_{max}15\%$: 70.7388
    - $\omega_{max}5\%$: 65.0700
    - $\omega_{max}0.5\%$: 45.5442
2. uniform mesh 2 with 9000 elements, and average element size of 0.1827 (mesh resolution ranges from $\tau = 273.6727 - 1.1464$) with frequency limitation:
    - $\omega_{max}15\%$: 138.8114
    - $\omega_{max}5\%$: 127.6875
    - $\omega_{max}0.5\%$: 89.3717
3. non-uniform mesh 3 with 5180 elements, the size ratio of smallest elements versus largest elements is 1:5. And average element size of 0.3463 (mesh resolution ranges from $\tau = 144.3835 - 0.6048$) with frequency limitation:
    - $\omega_{max}15\%$: 98.3733
    - $\omega_{max}5\%$: 90.4899
    - $\omega_{max}0.5\%$: 63.3362
4. non-uniform mesh 4 with 7558 elements, the size ratio of smallest elements versus largest elements is 1:10. And average element size of 0.3317 (mesh resolution ranges from $\tau = 160.4107 - 0.6719$) with frequency limitation:
    - $\omega_{max}15\%$: 102.7032
    - $\omega_{max}5\%$: 94.4729
    - $\omega_{max}0.5\%$: 66.1240

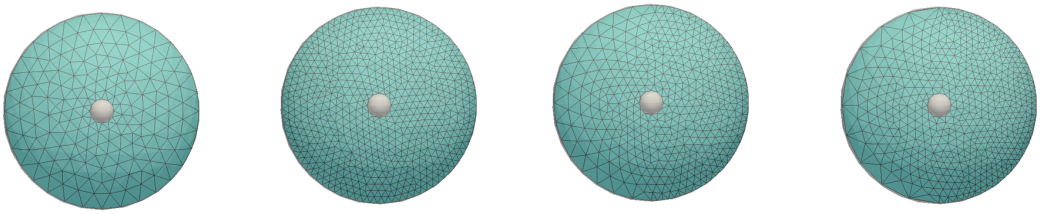

(a) Coarse **(b)** Dense **(c)** 1:5 **(d)** 1:10

Figure 7.11: Sound hard sphere with inner radius a = 0.5 and outer radius r = 4, uniform and non-uniform unstructured mesh grids

7.4.2.2 The Global Relative Error and Effectivity Index Versus Frequency

The benchmark problem of a plane wave impinging a sound hard sphere is solved both numerically and analytically on four spherical meshes. The global relative errors and cost of measures are calculated and recorded with an average of 10 times run on the basis of the automatic p adaptivity scheme prescribed.

The actual errors as a function of frequency are given in Figure 7.12, it is clear that the steady and lowest actual error occurs when mesh 4 is adopted (flat pattern). Mesh 3 is seen to perform sub-optimally with more dips than mesh 4. In contrast, mesh 1 performs less well with small dips incurred by the sudden jump of the

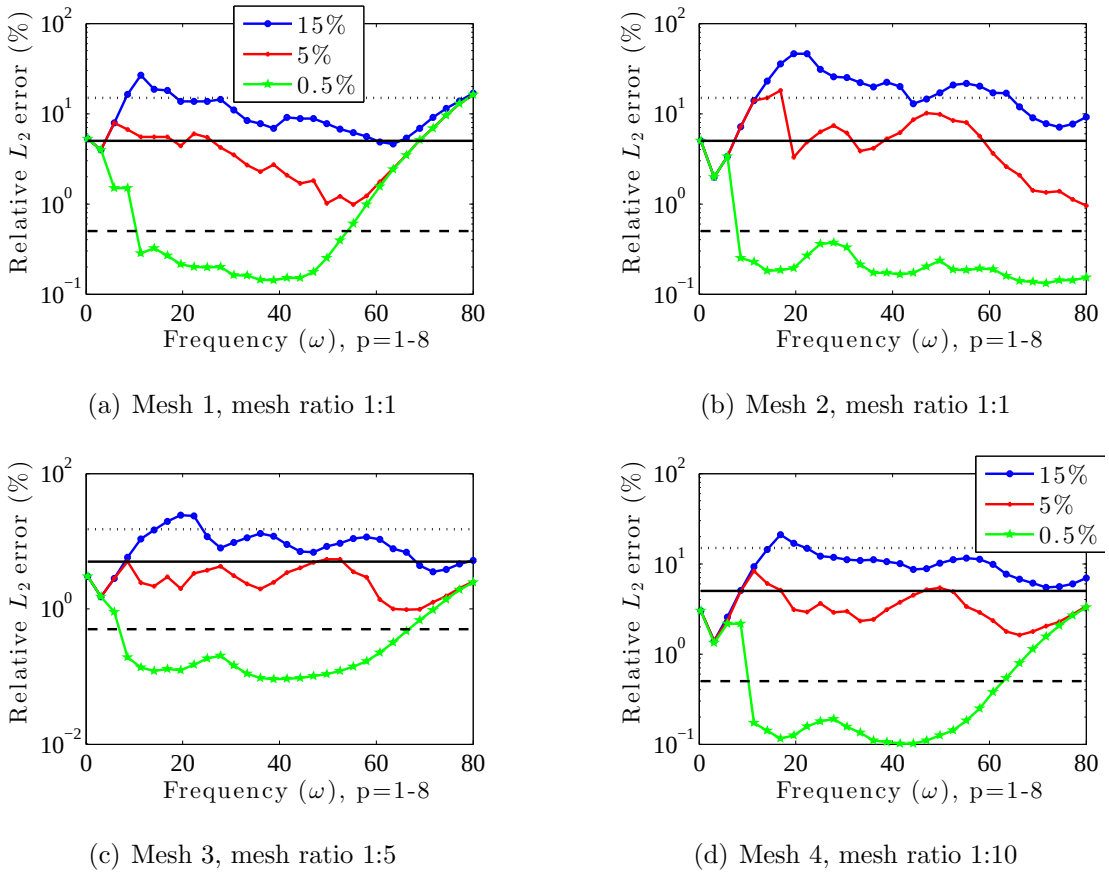

(a) Mesh 1, mesh ratio 1:1

(b) Mesh 2, mesh ratio 1:1

(c) Mesh 3, mesh ratio 1:5

(d) Mesh 4, mesh ratio 1:10

Figure 7.12: Global relative error versus frequency with three predefined errors, 15% (blue line), 5% (red line), 0.5% (green line). The exact values of these three error levels are denoted by black straight lines

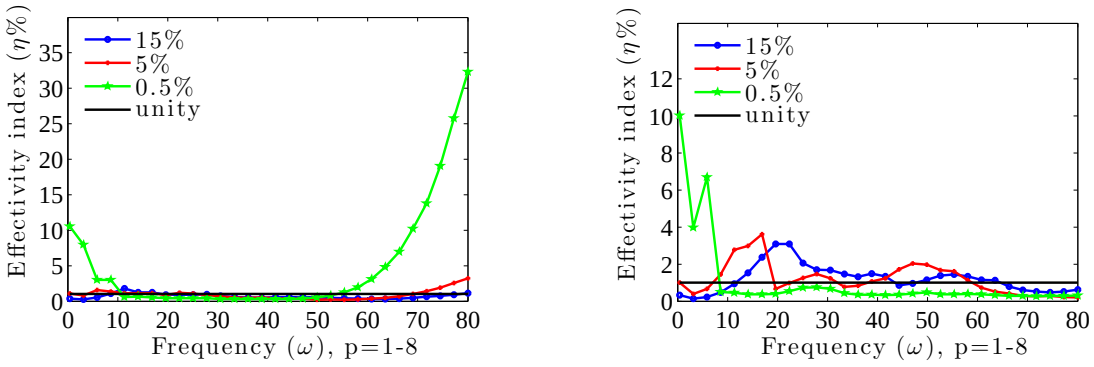

(a) Mesh 1, mesh ratio 1:1

(b) Mesh 2, mesh ratio 1:1

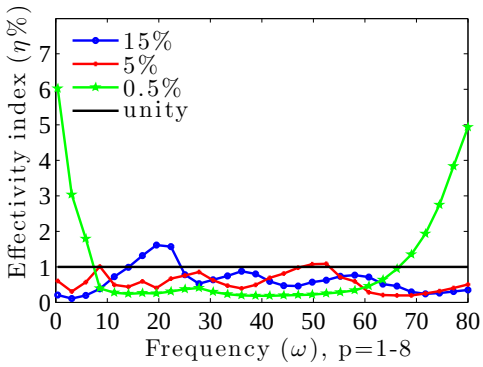

(c) Mesh 3, mesh ratio 1:5

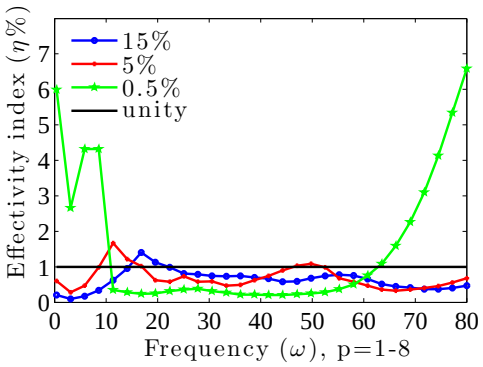

(d) Mesh 4, mesh ratio 1:10

Figure 7.13: Global effectivity index versus frequency with three predefined error levels, 15% (blue line), 5% (red line), 0.5% (green line). The unity value is denoted by black straight lines

element orders. This is due to similar element sizes resulting in the p orders for each element to increase in union. Also the accuracy is limited to short range of frequency because of the maximum p order available in this analysis is 8. In the case of coarse mesh 1, the error estimator requires more high order elements than for the dense mesh to sustain the same level of accuracy. Moreover, dense mesh 2 fails to control the actual error with low and medium predefined error levels (15% and 5%) within the frequency range, which is seen as an instability manifesting as the presence of sudden peaks. Further to this, the error dips and peaks along the plots of relative error have been alleviated with h refinement (meshes 1-2), as well as the additional smaller elements (meshes 3-4).

We now move our attention to Figure 7.13. The specific effectivity index is defined $\eta = \frac{e_a}{e_p}$ (actual error over predicted error) such that in an ideal situation its value approximately approaches to 1. A unity value of η represents the actual error is identical to the predefined error level, or even better with $\eta < 1$ which means the actual error is smaller than predefined error. However, it also introduces additional computational costs with conservative prediction in some cases. Nonetheless, the effectivity indices of mesh 1 are the closest to 1, which means non-uniform meshes tend to overestimate the relative error. Except for dense mesh 2, the effectivity indices exceed one. In addition, all the actual relative errors exceed the frequency limitation derived from the Eqn. 7.7 except for dense mesh 2. The phenomenal growths of effectivity indices in both Figures 7.13 (a) - (d) for relative low and high frequencies might be caused by the approximate non-reflection BGT1 BC. This type of error can be sufficiently reduced by implementing the analytical solution on the exterior boundary of spherical domain [206].

The error estimator behaves unsatisfactorily for the three meshes with both low ($\omega \leq 20$) and high frequencies ($\omega > 60$), which appears as large error in Figure 7.12 and effectivity index $\eta >> 1$ in Figure 7.13. In the former case ($\omega \leq 20$), it is because of the effect of pollution error and the approximate BGT - 1 BC with insufficient number of wavelengths per element between the obstacle and the exterior boundary, which appears as a sudden change in the actual error. On the other hand, once the frequency reaches a certain level, in extreme cases $\omega > 60$, the highest polynomial order available with the current computational resources is exceeded ($p = 8$). Thereafter, any further p enrichments are not executed and consequently the desired error level is no longer maintained. Theoretically, we can implement arbitrary higher order hierarchical shape functions with appropriate computer resources.

Overall, and surprisingly, on the basis of actual error, the unstructured coarse mesh 1 delivers the most stable and cheapest solutions for the spherical geometry problem with mixed BCs. The reason for this is because unstructured mesh 1 has the biggest average element sizes among all the meshes. However, the error tolerance (frequency limitation) associated with mesh 1 is lower than the other three meshes. The non-uniform meshes 3 and 4 guaranteed accuracy and maintained the error level while the frequency exceeded the frequency limitation level.

7.4.2.3 Optimal Polynomial Orders Versus Frequency

To take full advantage of the p adaptivity scheme, adequate assignment of the polynomial order to each element is vital. If we move our attention to the maximum, average and minimum orders applied to each element of meshes with predefined error levels, a positive relationship can be obtained between range of orders and smoothness of actual relative errors. In other words, as the mesh ratio increases, the maximum frequency limitation is improved, as well as the performance of the error estimator. Admittedly, this fact expounds that the *a priori* error estimator is more sensitive and functional for unstructured meshes with various element sizes. As depicted in Figure 7.14, the largest difference of polynomial orders was incurred by the most non-uniform unstructured mesh with ratio 1 : 10 (mesh 4).

Since all the meshes presented here consist of unstructured tetrahedrons, even with uniform meshes (ratio 1:1), the tiny size difference in each meshes will still cause the variation of order selection process. In case of mesh 4 (ratio 1:10), we can see that the maximum order available ($p = 8$) has been reached at a lower frequency than the others, this reveals the fact that the biggest elements in the mesh have been enriched sufficiently during earlier stage of calculation. Here we omitted the plots for error levels 15% and 0.5% since identical conclusion can be drawn.

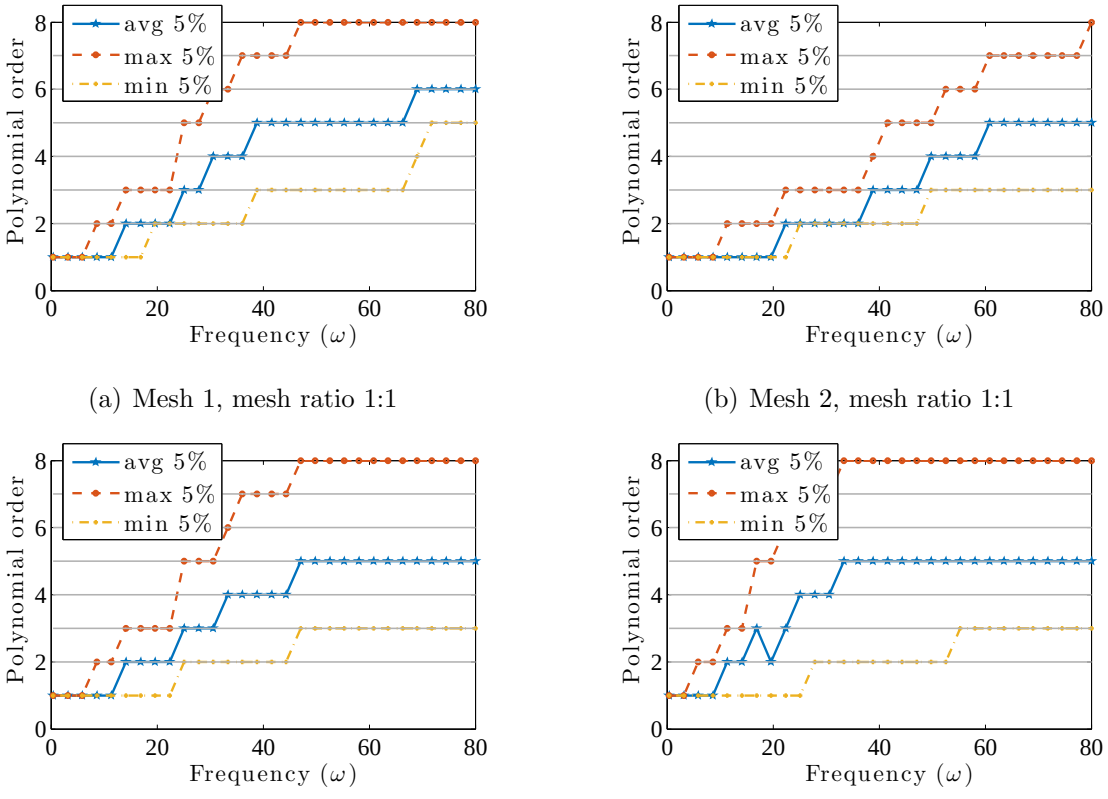

(a) Mesh 1, mesh ratio 1:1

(b) Mesh 2, mesh ratio 1:1

(c) Mesh 3, mesh ratio 1:5

(d) Mesh 4, mesh ratio 1:10

Figure 7.14: Polynomial orders versus frequency with predefined error level: 5%. Maximum (red line), average (blue line), and minimum (yellow line) polynomial orders assigned

7.4.2.4 Total Number of DOFs and Non-zero Entries Versus Frequency

The number of non-zero entries for the sparse system matrix can be crucial measurement on the cost. The memory occupied to store the matrix is related to NNZ (number of non-zero entries). In addition, the total factorization memory is an important measure since it is the major consumer of memory and is dominated by the problem size.

It is not surprising that the number of non-zero entries(NNZ) and DOFs against frequency follows the same trend in Figures 7.15 and 7.16 as all previous results. On the other hand, the ratio of NNZs versus DOFs provides an indicator for the average number of filled in terms in each row of the matrix. In this example, the zero values are also counted. In Figures 7.17, the results affirmed that adding more higher order elements led to huge reduction in the global number of non-zero entries and number of DOFs. The sub Figure 7.17 (a) for mesh 1 has the lowest DOFs versus NNZs, since it contains bigger elements than the other three meshes, though the sparsity of the system matrix is decreased with increasing number of polynomial orders for both cases in Figure 7.16.

Surprisingly, The number of non zero entries against DOFs required to achieve three different predefined error levels are almost identical for mesh 1, it is quite an encouragement for one to use a coarse unstructured mesh with pure non-uniform p adaptivity.

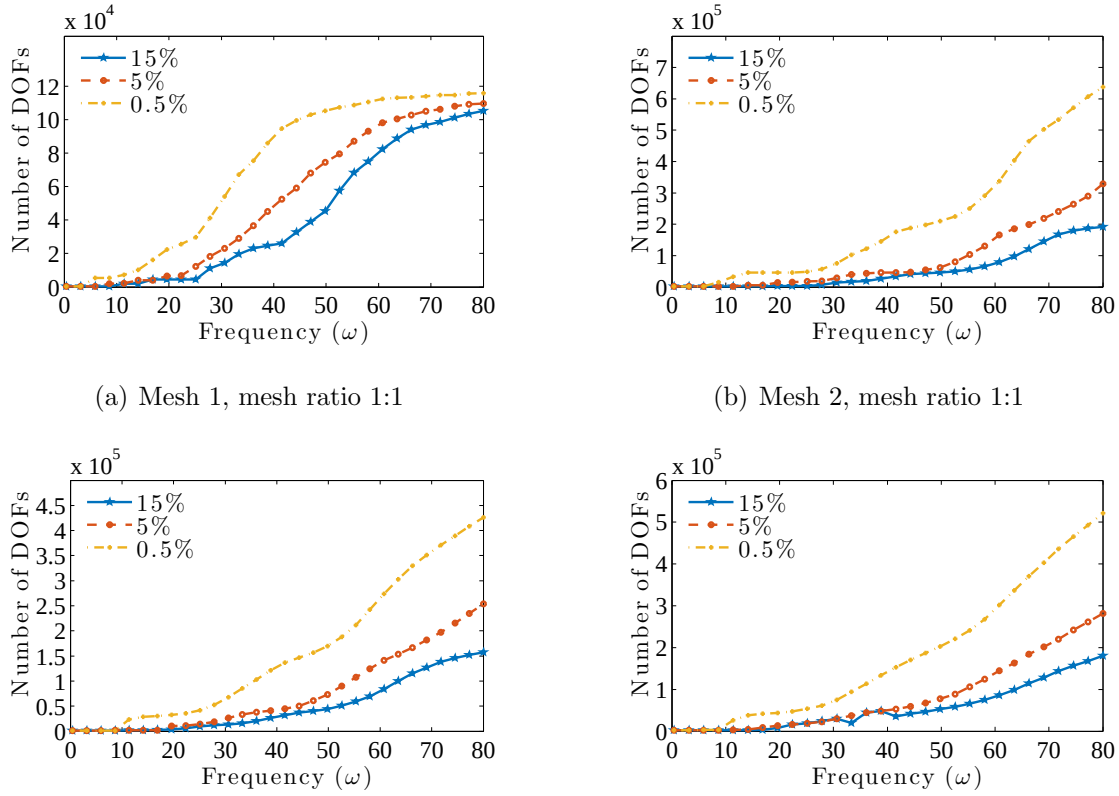

(a) Mesh 1, mesh ratio 1:1

(b) Mesh 2, mesh ratio 1:1

(c) Mesh 3, mesh ratio 1:5

(d) Mesh 4, mesh ratio 1:10

Figure 7.15: Total number of degrees of freedom versus frequency with three predefined error levels: 15% (blue line), 5% (red line), 0.5% (yellow line)

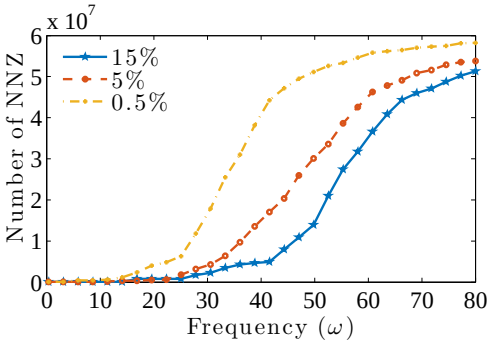

(a) Mesh 1, mesh ratio 1:1

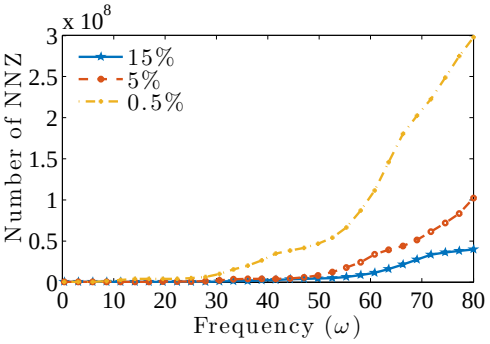

(b) Mesh 2, mesh ratio 1:1

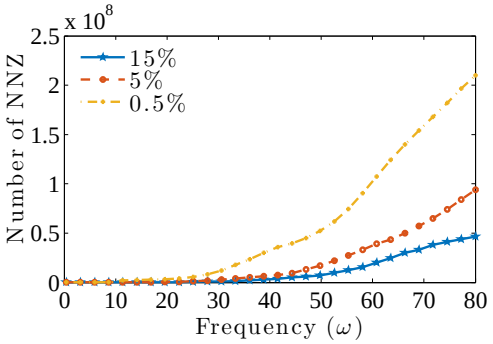

(c) Mesh 3, mesh ratio 1:5

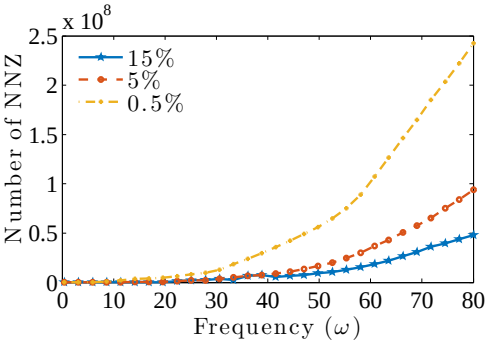

(d) Mesh 4, mesh ratio 1:10

Figure 7.16: Total number of non-zero entries versus frequency with three predefined error levels: 15% (blue line), 5% (red line), 0.5% (yellow line)

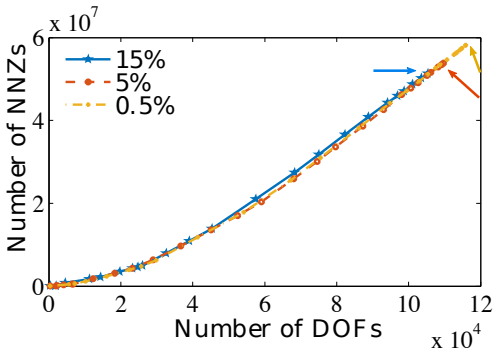

(a) Mesh 1, mesh ratio 1:1

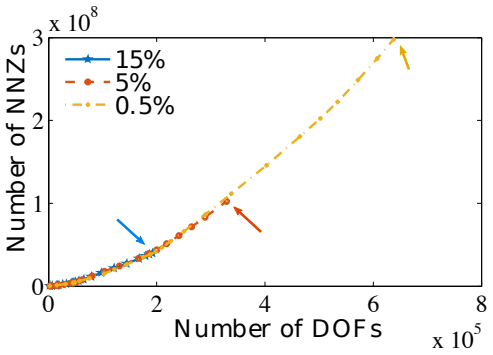

(b) Mesh 2, mesh ratio 1:1

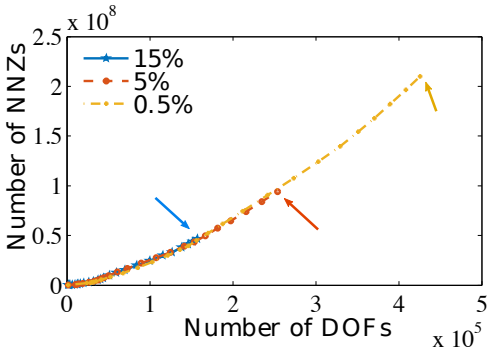

(c) Mesh 3, mesh ratio 1:5

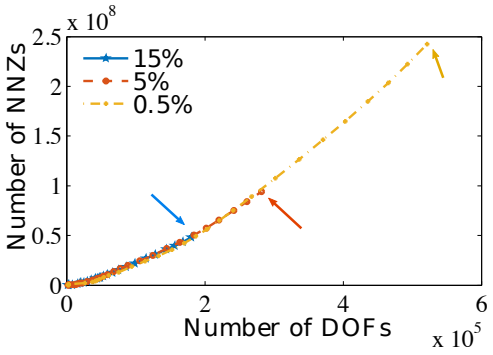

(d) Mesh 4, mesh ratio 1:10

Figure 7.17: Total number of non-zero entries versus number of DOFs with three predefined error levels: 15% (blue line), 5% (red line), 0.5% (yellow line)

7.4.2.5 Total Computational Times Versus Frequency

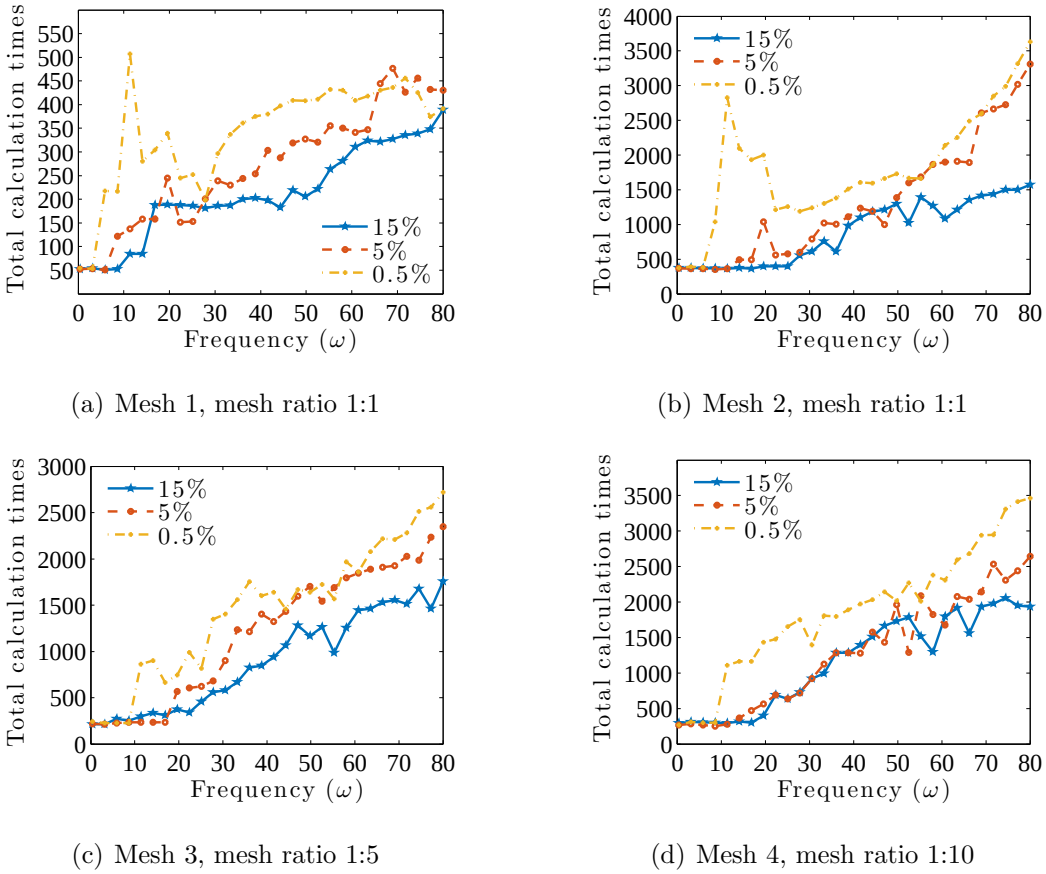

(a) Mesh 1, mesh ratio 1:1

(b) Mesh 2, mesh ratio 1:1

(c) Mesh 3, mesh ratio 1:5

(d) Mesh 4, mesh ratio 1:10

Figure 7.18: Global computational time in second versus frequency with three predefined error levels: 15% (blue line), 5% (red line), 0.5% (yellow line)

If we combine the Figures of the total computational times versus frequencies 7.18(c) and (d) with Figures 7.12(c) and (d) previously exhibited, a combination of optimal choices can be decided. Although dense uniform mesh 2 maintains its accuracy at the high frequencies limit, the computational times suggest massive computational costs are added if we choose mesh 2 as our initial mesh for calculations with frequency sweep. As shown earlier in Figure 7.12(a) and (b), the additional computational costs appear as frequent error dips exhibited by approximately uniform meshes 1 and 2 (the dips in global relative error is related to dips in computational times). Thus, a non-uniform coarse mesh would guarantee the minimum computational cost while keeping the actual error under control within the frequency limit. Nonetheless, computational time by itself is sometimes not a pronounced and unbiased measure to quantify the efficiency. Thus, the total memory consumption against frequency is presented in next section.

7.4.2.6 Memory Consumption Versus Frequency

The same conclusion can be drawn in relation to computational time. In Figures 7.19 and 7.20, since the memory required to do matrix factorisation is reduced by adopting more higher order polynomials with less total number of elements. The

plateau area occurring in mesh 1 around the tail is due to the mesh limitation and highest available order ($p = 8$) have been reached for uniform coarse mesh. This stagnation can be changed by simply implementing arbitrary order polynomials given larger computational resources.

As expected, the coarse mesh 1 requires the lowest factorization memory, since it has lowest amount of elements, such that it is efficient for the least amount of higher order elements implemented. The mesh limitation is breached at high frequencies, which is depicted by the plateau area in 7.18(a). In contrast, dense mesh 2 occupies almost 5 times more memory than mesh 1. To summarise, the total amount of small elements in the mesh denominated the amount of factorization memory required to solve the particular problem, and it is a more optimal strategy to use large elements with higher order p hierarchical shape functions. The results of total memory in Figure 7.20 have a similar trend as factorization memory against frequency. It should be noted that increasing p order or adding more elements both result in additional computational costs and factorization memory. However, In this particular case, increasing p order requires less factorization memory than the latter case at the same level of accuracy.

The discussions for Figures of CPU times and the number of floating point operations required to factorized the matrix are omitted, since they are in good agreement with all previous analysis and consist conclusion can be obtained.

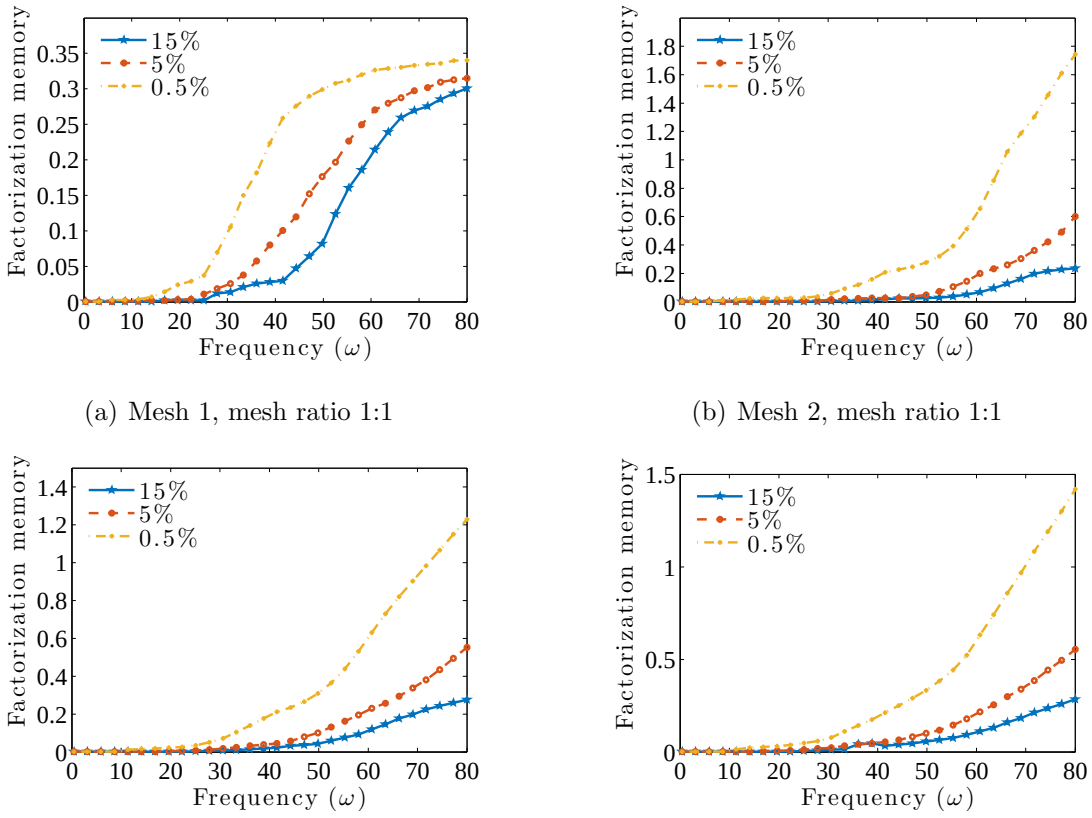

(a) Mesh 1, mesh ratio 1:1

(b) Mesh 2, mesh ratio 1:1

(c) Mesh 3, mesh ratio 1:5

(d) Mesh 4, mesh ratio 1:10

Figure 7.19: Factorization memory in GB versus frequency with three predefined error levels: 15% (blue line), 5% (red line), 0.5% (yellow line)

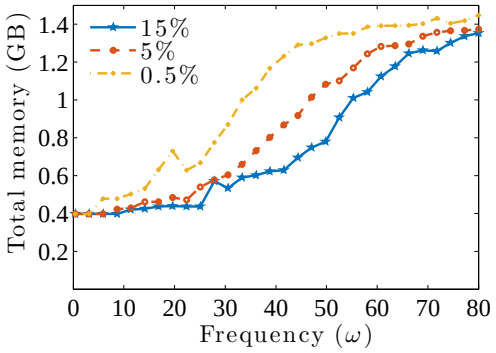

(a) Mesh 1, mesh ratio 1:1

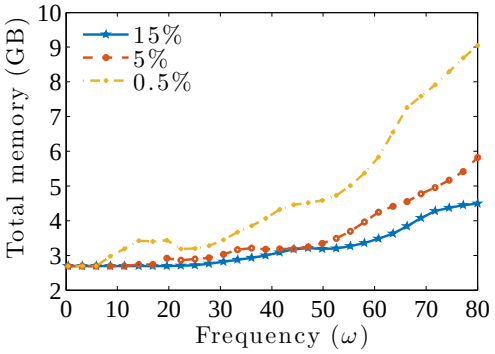

(b) Mesh 2, mesh ratio 1:1

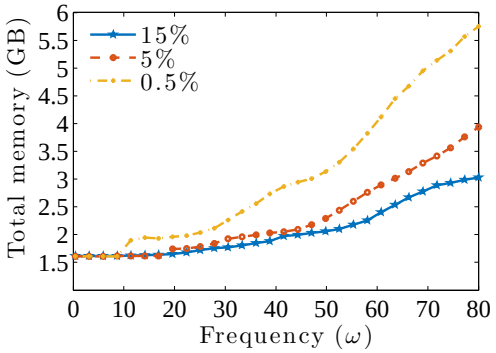

(c) Mesh 3, mesh ratio 1:5

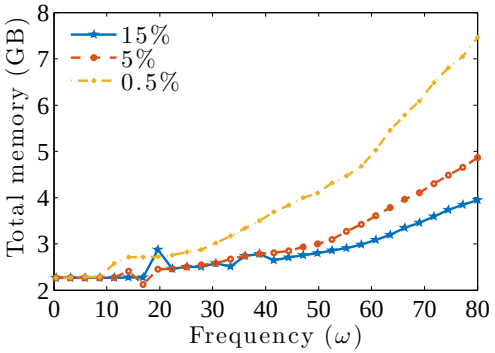

(d) Mesh 4, mesh ratio 1:10

Figure 7.20: Total memory in GB versus frequency with three predefined error levels: 15% (blue line), 5% (red line), 0.5% (yellow line)

7.4.2.7 Upper and Lower Bounds of Proposed *A Priori* Error Estimator

In this section, we demonstrate that the *a priori* error estimator provides rigorous upper and lower bounds for estimated relative errors, as indicated by Figure 7.21. The maximum, minimum and average of the predicted errors are drawn against the frequency. The black dotted line indicates ideal predefined error level. The global relative error predicted by the error estimator maintained its error level at 0.05% within the frequency limit whilst bounded by the maximum and minimum predicted errors. As stated in section 4.4.2 of Chapter 4, the *a priori* error estimator satisfies one of the major features of a good error estimator, since it yields guaranteed sharp upper and lower bounds. The results are rather satisfactory, except in case of low frequencies, where predicted L_2 error might dominated by error of geometry approximation in the pre-asymptotic range with low mesh resolution (insufficient refinement). In other words, the number of DOFs per wavelength is not adequate in case of both low and high frequencies. In addition, the approximate BGT1 boundary condition introduces errors in low frequencies, in term of wavelength distance between obstacle and exterior boundary.

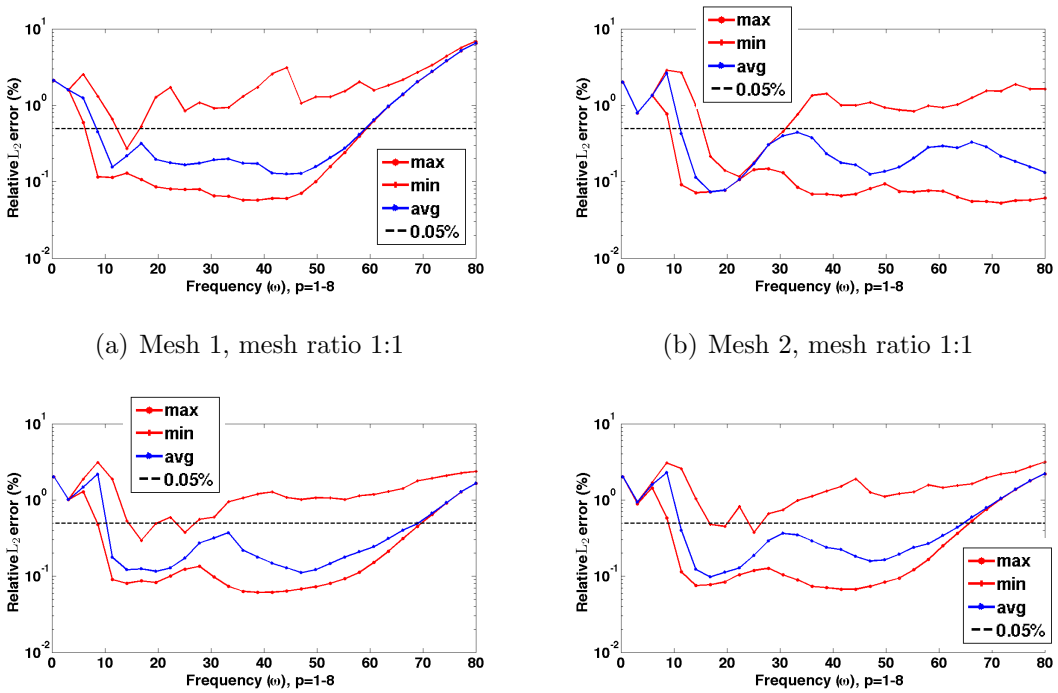

(a) Mesh 1, mesh ratio 1:1

(b) Mesh 2, mesh ratio 1:1

(c) Mesh 3, mesh ratio 1:5

(d) Mesh 4, mesh ratio 1:10

Figure 7.21: Indication of upper and lower bounds for *a priori* error estimator. Global relative error versus frequency with predefined error level, 0.05%. Maximum, minimum (red lines) and average (blue line) global relative error in L_2 norm

7.4.2.8 Summary

In spite of the L_2 relative error from mesh 2 being larger than other meshes, the difference between the highest and lowest p order assigned by *a priori* error

estimator for mesh 2 is small (see Figure 7.14 (b)). Thus, it further confirms the presumption that the range of p orders have direct effects on the actual error of finite element solutions.

It is noteworthy that the errors drop with increasing non-uniformity on the spherical mesh. This is due to the p enrichment being more efficient than h refinement, which has been shown in previous analyses, thus the more higher order elements and wider range of p order, the more accurate and stable the resulting solution. In future work, on account of the pollution effect, wave propagation direction and computational domain size for the design of error estimator (relevantly different weights) would be compulsory.

Albeit the *a priori* error estimator for H^1 relative error is not shown here, similar results have been observed for the performance of the estimator with H^1 error. The only difference is that the H^1 relative error estimator tends to be pessimistic on the predefined error level.

7.4.3 Efficiency Analysis on Adaptivity Schemes

In the following numerical tests, we have assessed pure uniform h refinement (p=2), uniform p enrichment and the error oriented p adaptivity algorithm, whilst fixing the mesh resolution in descending order as: [8.6820, 5.7880, 5.2092, 4.9612, 4.3410, 3.4728, 3.0387, 2.7782] ($\omega = [2, 6, 10, 14, 20, 30, 40, 50]$) based on Eqn. (5.19) by varying h_{max} and f for uniform h and p adaptivities respectively. h_{max} denotes the maximum element size in the mesh. As for the automatic p adaptivity, we replace p in Eqn. (5.19) by the average of summation of p orders over the whole computational domain.

The relative error in the H^1 norm, computational time, number of DOFs and total memory consumed by the program against resolution τ are plotted in Figure 7.22. To be concise, the analysis of CPU time, number of non-zero entries, etc are omitted here. From both Figures, automatic p adaptivity asymptotically delivers the lowest error with decreasing resolution, and its efficiency has been guaranteed by less memory occupied compared to h adaptivity in the asymptotic region. However, it requires more memory than uniform p adaptivity in general, since it allocates more higher order elements based on the need of *a priori* local error estimator. Overall, automatic p adaptivity with a partly refined mesh (also called flagging strategy [15]) are more stable than other adaptivity schemes due to its resilience of predefined error level. This fact can be observed from the plateau area of relative error (red solid line) in Figure 7.22 (a). This approach will be even more valuable in high frequency sweep problems.

7.4.4 Domain Length Analysis

To this end, we will now consider the performance of the proposed error estimator under accumulated domain length dependent dispersion effects by increasing the domain length according to benchmark problem 3 in §5.

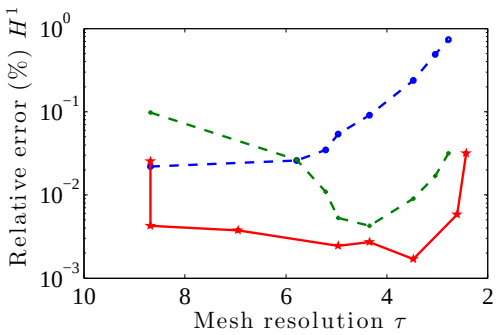

(a) Relative H^1 error versus τ, predefined error level: 0.5%

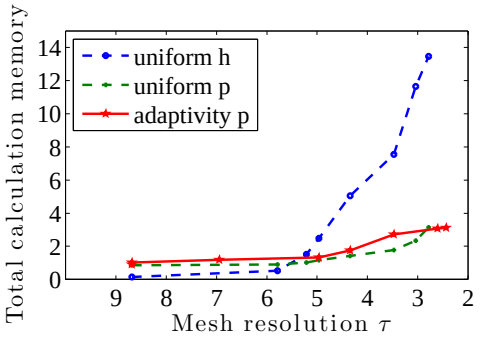

(b) Total memory occupied versus τ

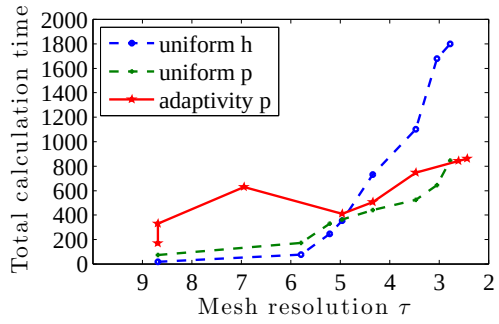

(c) Total calculation time versus τ

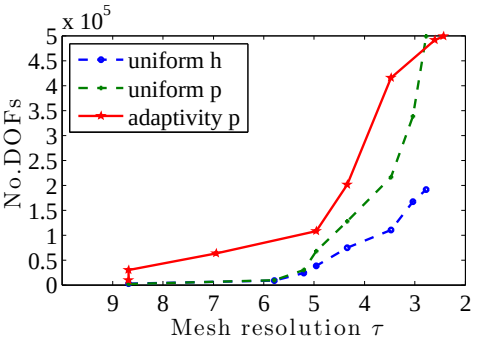

(d) Total number of DOFs versus τ

Figure 7.22: Automatic p adaptivity versus uniform h & p adaptivity based on mesh resolution τ_l, impinging sound hard sphere benchmark problem, $a = 0.5$ and $r = 4$

It should be noted that the current development of an *a priori* error estimator has not yet included the pollution effect in a local sense. This test is carried out for frequencies varied from $\omega = 1$ to 70. A similar mesh is created as of that in Figure 7.11, being partly refined along the propagation direction $(1, 0, 0)$. The diameter of the domain is also progressively increased from 2 to 24. The maximum number of elements and mesh resolution are 8477 and $\tau = 2.7121$ respectively for the maximum frequency $\omega = 70$ and $p = 8$. A direct measure of maximum and minimum k allowed for these meshes are formulated from Eqn. (5.19) as $\frac{2\pi p}{hD_\lambda}$ (in case $p_{max} = 8$), such that maximum and minimum resolvable frequencies are $\omega_{max} = 63.1872$ and $\omega_{min} = 16.2724$ for meshes with different densities (12 meshes in total). The four distinctive sample frequencies ω are $5, 30, 50$ and 70, which are chosen to demonstrate the domain length analysis.

Figure 7.23 shows the evolution of actual relative error in L_2 and H^1 norm against increasing domain lengths. As expected, the global error increases moderately with increased domain length for both norms in high frequencies ($\omega = 50$, 70). This is directly due to the deteriorating effect of the pollution error.

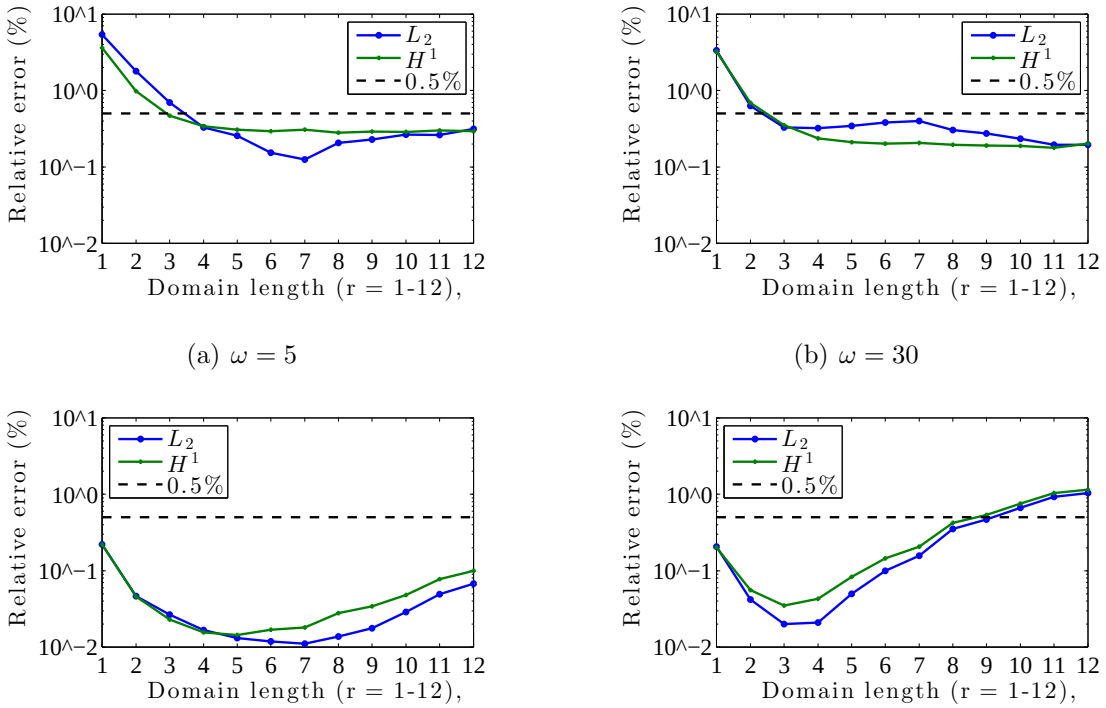

(a) $\omega = 5$

(b) $\omega = 30$

(c) $\omega = 50$

(d) $\omega = 70$

Figure 7.23: Global relative error in L_2 (blue line) and H^1 (green line) norm as a function of radius r (a = 0.5) for various ω with predefined error level 0.5% (dense), the exact value of 0.5% is denoted by the black dashed line

In case of Figure 7.23 (a) and (b), the error exceeds the predefined error level in the pre-asymptotic range as the order assigned to each element is linear due to the insensitive kh value. All other relative errors with higher frequencies are under control via the *a priori* error estimator except for high frequency ($\omega \geq 60$), where the mesh limitation is exceeded, and the error estimator fails. It is a well known fact that the higher order elements can minimise the dispersion effect globally when

compared to the lower order elements [123], and it is exactly what we observe from the error plots with increasing frequency. The polynomial orders distributed among all elements are increased with increasing domain length. Hence, the actual relative error tends to remain in the same level with vastly enlarged domain length but tends to become smaller with largely increased frequency.

To summarise, although the *a priori* error estimator does not account for the pollution effect, it is sufficient to control the pollution error within the frequency limitation through the usage of hierarchical Lobatto shape functions and the Duffy transformation integration technique. In book [28], the authors stated that error indicators do not approximate the magnitude of the actual error, but only indicate where the error is large or small on the computational domain. However, this is not true for the presented *a priori* error estimator. The proposed *a priori* error estimator has the ability to approximate the exact error within certain accuracy and indicates the elements that need to be refined. Thus, it is an estimator and indicator. In case of the *a priori* error estimator, the error tolerance can be adjusted and the refinement criterions are explicit. Ultimately, the features of the proposed *a priori* error estimator are outlined as:

- Inputs:
    1. frequency
    2. initial mesh
    3. prescribed error
- Outputs:
    1. p orders of each elements e_i

And the merits as well as weakness of the *a priori* error estimator are outlined as:

- Merits:
    1. objective (goal) oriented and accurate
    2. error tolerance can be adjusted
    3. error estimator provided upper and lower bounds of actual error
    4. error estimator facilitates a natural adaptivity algorithm
    5. error estimator can be applied to any solution field
    6. cheap
    7. robust
    8. applicable to any acoustic problems
- Defects:
    1. heuristic definition
    2. not general / acoustic problem tailored

7.5 Discussion and Conclusion

In this chapter, an automatic p adaptivity scheme based on heuristic assumptions was implemented with an *a priori* error estimator to achieve a non-uniform local p enrichment with an unstructured coarse mesh. The proposed *a priori* error estimator was first introduced in article [72] and tested on a two-dimensional rectangular wave guide problems. It is rather remarkable that the simplified 1D version of the higher dimensional elements can handle the actual error sufficiently with various range of frequencies.

The two estimators introduced by Ainsworth and Babuska are problem and frequency dependent, thereby strongly rely on the empirical constants chosen. Thus, it is not robust and scalable in the sense that a good error estimator should be. However, they can serve as an upper or lower (conservative) bound to adjust any existing error estimators.

We have not only demonstrated the efficiency and accuracy of a proposed *a priori* error estimator within a three-dimensional spherical domain benchmark problem, but also proved how the partly refined mesh along the propagation direction and automatic non-uniform p adaptivity together can effectively control the dispersion effect accumulated over large distances. Its performance under heavy dispersion effects is assessed. It is evident that *a priori* error estimator can control the pollution error within predefined frequency level, but it unables to eliminate the pollution error. The performance of the proposed *a priori* error estimator is also investigated with measurements such as relative error, effectivity index, run time, frequency changes, computational memory, mesh density, and the variation of characteristic lengths, etc. The robustness and stability of the estimator has been verified by a guaranteed upper and lower bounds over a wide range of frequencies. Finally, the automatic p adaptivity scheme developed based on the *a priori* error estimator is compared with uniform h and p adaptivities by solving acoustic problems with various frequencies, where the mesh resolution is fixed in range. The results suggested that automatic p adaptivity outperforms uniform h and p adaptivities in the sense of efficiency and accuracy. And last but not the least, the automatic p adaptivity scheme is shown to be far more suitable with low mesh resolution (coarse mesh) than the application of plain h and p adaptivities. This fact is particularly beneficial in the case of high frequency sweep acoustic problems.

The major defect of the *a priori* error estimator is that it does not include the pollution error in its framework, an additional criterion might be provided as a measure of the pollution error inside each element and taken into account with the χ_{kh} value. Alternatively, additional weight functions applied on input parameters k and h might improve the accuracy of the error estimator. On the other hand, it is possible to evaluate the dispersion effect as a function of the propagation domain length as well as direction for a specific problem, considering there is strong positive relationship between the propagation distance and pollution error.

Another possible direction of study is that of the investigation of the behaviour of the hierarchical p adaptivity scheme with order greater than 10, in which the robustness and efficiency of the scheme with a higher frequency limit needs to be confirmed. Does the scheme maintain its good conditioning with extreme higher orders? In addition, the performance of the hierarchical p adaptivity scheme to-

gether with the Duffy transformation applied on acoustic problems with singularity points are worth investigating as well.

Considering the choice of approximation example for constructing the *a priori* error estimator, a two-dimensional *a priori* error estimator with a hard-coded table might provide a marked difference on the accuracy of error estimation. For example, an analytical problem is solved on the surface of a 3D element might be more realistic than a solution on an edge. Moreover, problem dependent low dimensional test examples can be specified before the error calculation process, e.g. with an analytical solution analogous to 3D problem. We also need to pay more attention to the discrepancy between pollution error and the numerical error (interpolation error), it is an important fact that the difference between the interpolation solution and the finite element solution with the same order p is closely related to the plain pollution error that appears as phase shifting [123].

In detailed exposition of future studies, a preliminary investigation result suggests that the Rayleigh wave propagating on a SAW device medium can be regard as a plane wave problem [291], which can be resolved with the time dependant Helmholtz equation through Fourier transformation techniques. In a detailed procedure, arbitrary signals can be applied on the medium and analysis can be done in either frequency or time domain. Moreover, Reynolds' stress can be retrieved from the acoustic velocity by taking the average gradient of the acoustic potential multiplied by the density. In the next chapter, a practical problem of high frequency SAW impinging on a semi-spherical droplet in micro-scale level will be presented.

Chapter 8

Acoustic Application of SAW Propagating on $LiNbO_3$ Substrate

8.1 Introduction

In the preceding chapters, a time dependent acoustic solver is built, and its efficiency and accuracy are tested with benchmark problems solved in frequency domain. The time dependant wave equation can be resolved within the frequency domain and easily transferred back to time domain through the use of Fourier transformations. In this chapter, the proposed method is used to predict the acoustic phenomenon in microfluidic applications with high frequency SAW.

The numerical study of a micro-droplet actuated by surface acoustic waves (SAW) generated by interdigital transducer (IDT) from an applied oscillating voltage can inform two separate areas of interest: the acoustic pressure distribution and the acoustic driven fluid streaming inside droplet [274]. The relationship between these two physical fields is generally unknown. Furthermore, the incommensurable time scales between the sound propagating on a solid and propagating in a fluid are of practical importance. In order to have a complete understanding of the physical phenomenon behind the fluid motions inside a droplet cavity, both of the research directions are of importance.

Rheological properties of droplets, studying the acoustic streaming inside a droplet, was first investigated by Shiokawa *et al.* [291] in 1989 to the best of the author's knowledge. The jetting, atomisation and displacement of droplets are obtained by applying SAW at 50 MHz [291, 292]. In their assumptions, the internal reflections of waves inside a droplet are neglected and simplified to an incident wave field. In what follows, the Nyborg's streaming theory was used to provide a driving force for acoustic streaming to happen. Numerical results of the fluid field are calculated in order to quantitatively compare with experimental results [17]. Much of the following research that has since been conducted has been based on the hypothesis developed by Shiokawa and his co-authors [134, 16, 19, 284].

On the acoustic side of studies, Koster *et al.* [197] solved acoustic problems for micro sessile droplets under a single frequency. In this study the radius of semicircular water droplets was fixed to 0.25 mm. The authors pay more attentions to the development of numerical methods rather than explaining the physical phenomena behind the numerical model.

In spite of Shiokawa's frameworks, Brunet *et al.* [87] have simulated micro-droplets actuated by 20.375MHz single frequency SAW. Their numerical result shows a chaotic structure when the droplet material is water. The two dimensional acoustic pressure field was calculated within a micro-drop with various dynamic viscosities. The numerical results were also compared with experimental results in their studies. In their conclusion, they argued that the acoustic radiation pressure causes free-surface oscillations, while the internal flow of droplet is mainly driven by acoustic streaming effects. However, there are experimental results from various sources which do not support this hypothesis [292, 270]. The acoustic radiation pressure is the source of acoustic streaming as well.

In the article [196], a two dimensional SAW application under a single frequency is presented with rectangular and semi-spherical domains. The proposed model considered dimensionless free capillary boundary as boundary conditions. But the applied method is computationally expensive and limited to 2D. Numerical simulation results suggested that the acoustic pressure and streaming fields are non-symmetric inside the droplet cavity.

In 2011, a fluid-solid coupling problem was solved, continuity of velocity field is enforced on the solid-fluid interface. The acoustic field has been calculated inside a micro-liquid with a fixed frequency of 20MHz SAW, such that three time harmonic Helmholtz equations were solved during the process. The results are limited to a single frequency within an non-practical geometric shape (an idealized rectangular domain) in two dimensions. On the other hand, the exponential decay of LSAWs are attenuated in the positive x direction and perpendicular to the droplet at the point of incidence. As expected, the damping of viscosity is not visible due to the small scale of the droplet characteristic length compared to the wavelength [320].

In 2013, a micro-drop and substrate subject to relatively low frequency of 3.5 MHz SAW, was simulated using the finite element method [260]. In this study, the transmitted waves circulating around the interface near the contact line of the droplet are revealed, which are identified as Stoneley waves. The propagation path of Stoneley waves is highly dependent on the difference between material properties of sessile droplets and substrate interfaces, which may either be approximated as hard or soft BCs on the interface in different situations. The complex structures of acoustic pressures inside a droplet are far more complicated than Shiokawa's assumptions. The acoustic streaming in the circumferential direction might be induced by Stoneley waves circling around the contact line of the droplet. Recently, Riaud *et al* not only simulated the acoustic field in a micro-drop, but also coupled the Navier-Stokes equations to derive the flow pattern by input acoustic radiation pressure (Reynolds' stress) as a nonlinear average driving body force for acoustic streaming [274]. Accordingly, a two-dimensional simulation of a sessile droplet subject to a 20 MHz SAW is presented, where the relationship between wave attenuation and acoustic flow pattern inside the droplet is investigated. Subsequently, the authors also singled out the importance of the forcing term act as momentum

source points to generate the flow and streaming. If the force terms are imbalanced inside the droplet cavity, the flow will subsequently be pushed away from the side with strong forces towards the weak side.

8.2 Closed Form of Rayleigh Wave

The propagation of surface acoustic waves in any medium has been thoroughly studied for many years, while the waves transmitted between two different materials have been under sustained development over the past decade [278]. The application of SAW propagating into microfludic droplets is now discussed based on the prescribed acoustic solver and boundary conditions. In this physical problem, we distinguish three time scales:

1). the fast (μs) microsecond time scale of Rayleigh waves on the solid surface beneath the droplet,

2). medium (μs-ms) millisecond time scale of acoustic wave in fluid droplet, and

3). slow (ms-s) time scale of capillary wave propagation on fluid-air surface.

As shown in Figure 1.3 and 8.2, the need of an efficient p adaptivity scheme is of the utmost importance for waves in the fast time scale propagating along the solid surface.

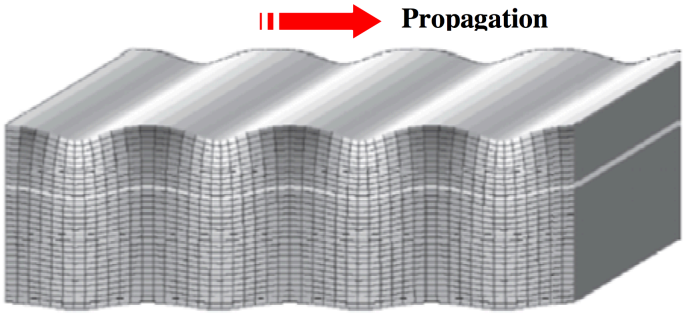

Figure 8.1: Snapshot of Rayleigh wave propagating on the surface of elastic body, wave amplitudes decay both horizontally and vertically [238]

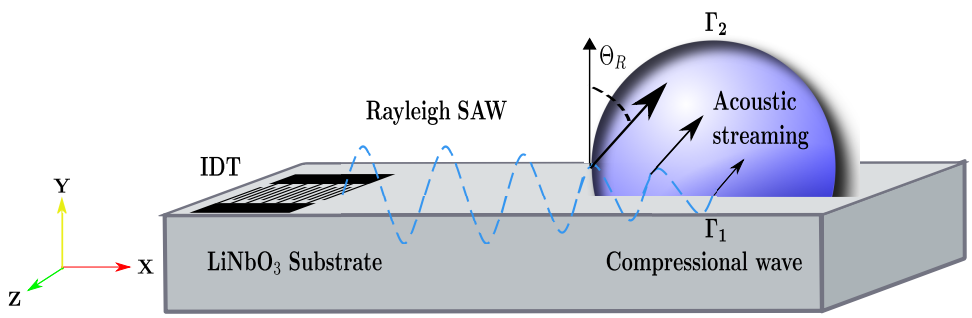

Figure 8.2: SAW actuation of a droplet in 2D view

A closed form of the acoustic potential of Rayleigh waves is derived from the analytical solution of the wave equations with specific boundary conditions [153, 320]. Rayleigh waves are a specific type of surface acoustic waves which describe the surface acoustic motion that was theoretically proposed by Lord Rayleigh's pioneering work in 1887. Rayleigh waves propagate along a free surface and its amplitude decays exponentially away from the surface [126], while the wave particle motion is in the opposite direction of the wave propagation. Thereby it forms an elliptical displacement at any depth as depicted in Figure 8.1. Rayleigh wave consists of two types of SAWs propagating on the piezoelectric surface. Their potentials are: longitudinal (compressional) wave φ and transverse (shear) wave $(0, \psi, 0)$, in this case merely the compressional waves are considered to be propagated into the fluid [17, 89, 269]. Primarily, Rayleigh wave is generated by applying an alternating electric field through coupled with interdigitated transducers (IDTs) on a piezoelectric substrate [279]. We will omit the cumbersome derivations here for the sake of brevity. Thus, the potentials of Rayleigh waves are:

$$\varphi = F(y)e^{\mathrm{i}k\mathbf{d}\cdot\mathbf{r}} \tag{8.1a}$$

$$\psi = G(y)e^{\mathrm{i}k\mathbf{d}\cdot\mathbf{r}} \tag{8.1b}$$

which the functions $F(y)$ and $G(y)$ expressed as:

$$F(y) = A_0 e^{-q|y|} \tag{8.2a}$$

$$G(y) = A_0 e^{-s|y|} \tag{8.2b}$$

for attenuation coefficients, the analytical forms are:

$$q^2 = k^2 - k^2\frac{c_s}{c_l} > 0 \tag{8.3a}$$

$$s^2 = k^2 - k^2\frac{c_s}{c_t} > 0 \tag{8.3b}$$

where $k = \frac{\omega}{c_s}$, and c_s is the phase velocity (speed) of Rayleigh wave propagating in solid ($c_s = c_L$ for leaky Rayleigh wave). In addition, c_l and c_t denote the speed of longitudinal and transverse waves propagating on solid surface respectively. Intuitively speaking, the amplitude of Rayleigh SAW is mitigated with depth and increasing frequency.

8.2.1 Leaky Rayleigh Wave Boundary Conditions

As illustrated in Figure 8.2, when a SAW passes beneath the droplet, it leaks energy into the droplet, this phenomenon is called the leaky SAW [17, 99]. To be more precise, merely the longitudinal waves propagate into the micro-droplet, with a complex wavenumber $k_L = k + \mathrm{i}k_i$ and speed c_L. The motion of particles that collectively form the Rayleigh wave is composed of components parallel and perpendicular to the substrate surface, since the particle motion of Rayleigh wave underneath the droplet is partially parallel to the substrate surface and partially perpendicular to it.

The compressional component (parallel) emits energy into the fluid medium, whilst the tangential component (perpendicular) couples to the adjacent micro-fluid via the liquid viscosity and results in frictional loss such that both mechanisms contribute to the attenuation of Rayleigh wave propagation. The compressional wave is also named the longitudinal wave, and the tangential wave is called the transverse wave.

Owing to the large difference in the density of the liquid droplet, which is smaller than the density of the solid substrate, the speed of sound in the droplet is lower than that of the substrate. Where the droplet is water and the substrate is $LiNbO_3$, the speed of sound in the droplet is approximately 2.6 times slower than in the substrate. Thereby, the simple form proposed for the acoustic admittance coefficient is employed to represent the energy loss with transmitted and reflected waves. In the assumption of constant fluid density, the admittance coefficient is defined as $\sigma = \frac{1}{\rho c} = \frac{1}{Y}$, named after the specific dimensionless admittance coefficient [88].

The leaky SAW forms a Rayleigh angle $\Theta_R = \arcsin(\frac{c_f}{c_s}) < 1$ with the horizontal axis [129], and can be applied as in [285], such that the longitudinal part of the SAW is propagating along the X axis and forms an angle with Y-Z plane. In addition, c_f is the speed of wave inside the fluid. The Rayleigh angle is approximated as 22.05 degrees for a water drop sitting on a 128^o Y-X cut $LiNbO_3$ substrate (ρ_s) [188] and nearly normal to the surface if the liquid is gas. The complex wave number is defined as in literature [274, 18, 188] for $k_i = \alpha$, where α is the attenuation coefficients distinguished by longitudinal and transverse parts of Rayleigh wave:

$$\alpha_t = \frac{\sqrt{\rho_f \xi_f \omega^3}}{4\sqrt{2}\pi^2 \rho_s c_s^2} \tag{8.4}$$

$$\alpha_l = \frac{Y_f}{Y_s \lambda} = \frac{\rho_f c_f}{\rho_s c_s \lambda} \tag{8.5}$$

α_t also denotes as attenuation coefficient of SAW caused by force of viscous frictions, where $\xi_f = b = \frac{4}{3}\mu + \mu'$ is the function of dynamic and bulk viscosity of droplet [170]. On the other hand, in [320] and [282], the measure of leaky SAW (LSAW) number $k_i = 2768m^{-1}$ is provided for substrate made of Y-X $LiNbO_3$. In theory, the amplitude of an LSAW will attenuate exponentially from its original value over a distance of a few wavelengths from the point where energy is emitted into the fluid [129]. The speed of waves:

$$c_l = \sqrt{\frac{\lambda_{lam\acute{e}} + 2\mu_{shear}}{\rho_s}} \tag{8.6}$$

$$c_t = \sqrt{\frac{\mu_{shear}}{\rho_s}} \tag{8.7}$$

where $\lambda_{lam\acute{e}}$ is the Lame constant of the medium, and μ_{shear} is the shear modulus corresponding to the dynamic viscosity in the case of a liquid [262]. For a voltage signal produced by an interdigital transducer (IDT) with a frequency of 10 MHz, $\alpha_l = 199.5968/m$ and $\alpha_t = 0.1470/m$ are calculated respectively [246]. In many studies, the attenuation of transverse waves are typically neglected due to $\alpha_l \gg \alpha_t$ in comparison with the compressional waves [129, 27].

The simulated actuation of a droplet can be achieved by the application of two forms of SAW, spherical and plane waves, that can be freely selected by the user. The appropriate BCs are mandatory on the surface of the droplet in order to represent the material properties of interfaces that waves are passing through, such as surface adjacency to solid substrate, and surface adjacency to air. Ideally, the attenuation length is several times larger than the droplet size in order to reflect the diffractions inside the droplet cavity.

As depicted in Figure 8.2, the system of SAW actuation of a droplet in 2D is shown. The propagation of the Longitudinal part of the Rayleigh wave, with direction angle Θ_R diffracted into the fluid is imposed as a Neumann boundary condition in [240]. Furthermore, a hard boundary condition is employed on the interface of liquid/air in article [87], which contradicts the pressure free assumption used in numerical experiments in [260]. In the current numerical example, we first imposed the hard boundary condition on the surface Γ_2, the interface between water and air of the droplet since $\rho_{air} \approx 1.225 \ll \rho_{water} \approx 998.2 kgm^{-3}$ [88, 165], then the mixed boundary condition in order to clarify the difference . However, the effects of soft and hard BCs applied on droplet/substrate interface have been examined and discussed in [260]. The incident waves will be free from energy loss (without any scattering) if the two materials have exactly the same impedances. Ultimately, we have the following BCs applied on Γ_1 and Γ_2.

In the current configuration, we set the droplet/ambient boundary Γ_1 to absorb BC and hard BC respectively. Then apply the mixed BC on droplet/substrate interface Γ_2.

8.2.2 Transmitted Waves

In the physical problem of acoustic actuation of a droplet, the general setup for Rayleigh SAW incident on the bottom interface of the droplet separates the two half spaces with different admittances. And what is more, the waves exit from the top interface into air as well as reflected from the droplet surface. The transmitted coefficient is given as:

$$T_{\Gamma_1} = \frac{2Y_{liquid}}{Y_{solid} + Y_{liquid}} \tag{8.8}$$

in [111, 287] and [263]. Y is the impedance coefficient as mentioned earlier. The unit of transmission and reflection coefficients is $MRayl$, which is equivalent to $1e + 6\frac{kg}{m^2 \cdot s}$. Thus, the boundary conditions on surface of droplet are defined as:

$$\left(\frac{\partial \Phi}{\partial n} + \mathrm{i}\sigma_1 \Phi\right)\Big|_{\Gamma_1} = T_{\Gamma_1} \frac{\partial \Phi_{LSAW}}{\partial n} \tag{8.9a}$$

$$\left(\frac{\partial \Phi}{\partial n} - \mathrm{i}\sigma_2 \Phi\right)\Big|_{\Gamma_2} = 0 \tag{8.9b}$$

in which $-\omega\rho T_{\Gamma_1}\Phi_{LSAW}$ denotes the amount of transmitted pressure of LSAW into fluids through layer Γ_1. Where Φ_{LSAW} is the longitudinal part of Rayleigh SAW

with complex wave number and form a Rayleigh angle Θ_R. The Rayleigh angle is also known as the refraction angle that obeys the Snellius-Descartes law [87]. The derivation process of a system of linear equations is prescribed in Eqn. (5.44), which will not be addressed here for brevity.

As depicted in Figure 8.3, the leaky Rayleigh waves with wavelength λ_R formed an angle θ with vertical axis whilst propagating beneath the droplet. And the longitudinal part of Rayleigh wave emanated into liquid with wavelength λ_f. The amplitude of the SAW subject to direct effect of RF electrical signal power is carefully chosen based on the literature.

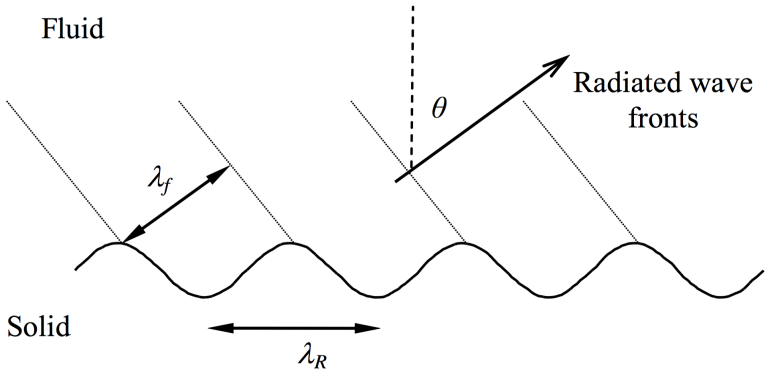

Figure 8.3: Diagram of Rayleigh angle formed between wave propagating through solid-fluid layer [153]

8.2.3 Acoustic Stress and Forces

8.2.3.1 Time Averaged Reynolds' Stress

The frequency domain of wave equation through Fourier transformation is the Helmholtz equation that describes the acoustic pressure and particle velocity fields in any medium. Thanks to the time dependant acoustic velocity vector, one of the important concepts of energy is the mean value of the below quantity associated with the theory of turbulence. It was introduced by Reynolds in 1895 for the first time [273],

$$R_{ij} = \rho v_i v_j \tag{8.10}$$

is the "fluctuating Reynolds stress" tensor from acoustic equation in tensor notation (Einstein notation), also named momentum flux. It describes the amount of pseudo-momentum (mass flux vector ρv_j per unit volume) across the unit area in the x_i direction, which can be employed as a Neumann boundary condition for the fluid mechanical equations such as Euler equation and Navier-Stokes equation. Notation v_i is the velocity vector component in the i_{th} direction, such that notation $\mathbf{r} \equiv [x_1, x_2, x_3] \equiv [x, y, z]$ is used for suffix i and j to represents the Cartesian coordinates [210]. In addition, $\underline{\mathbf{v}} = v_i \underline{\mathbf{e}}_i = v_1 \underline{\mathbf{e}}_1 + v_2 \underline{\mathbf{e}}_2 + v_3 \underline{\mathbf{e}}_3$ is defined, such that $\mathbf{e_i}$ is the basis

vector. In recent publications [215] and [216], the stress components were studied in depth with the theory of waves in fluids. For instance, if $i = j = 3$, then the Reynolds' stress tensor is expressed in matrix form as:

$$R_{3X3} = \begin{bmatrix} \rho v_1^2 & \rho v_1 v_2 & \rho v_1 v_3 \\ \rho v_2 v_1 & \rho v_2^2 & \rho v_2 v_3 \\ \rho v_3 v_1 & \rho v_3 v_2 & \rho v_3^2 \end{bmatrix} \tag{8.11}$$

the component $\rho v_1 v_3 \equiv \rho \frac{\partial \Phi}{\partial x} \frac{\partial \Phi}{\partial z}$, where Φ is the acoustic potential.

In [219], Lighthiill proved that the energy per unit volume of a sound field in a fluid medium generated by flow motion is

$$S_{ij} = \rho v_i v_j + p_{ij} - a_0^2 \rho \delta_{ij} \tag{8.12}$$

where ρ is the total density ($\rho\delta_{ij}$ is the density variation, δ_{ij} is the Kronecker delta function), v_i is the particle velocity, p_{ij} is the compressive stress tensor in Einstein notation, and a_0 is the velocity of sound outside the flow. The Eqn. (8.12) can be approximated to $\rho_0 v_i v_j$ in the absence of hydrostatic pressure and viscous stress. Since the dissipation of acoustic energy into heat due to the contribution of viscosity is very slow [219], merely half of the acoustic energy was lost in the atmosphere during the first mile of propagation process with frequency $4kc/s$ (kilocycles per second) of the top note of pianoforte, the viscous term to the above equation could be neglected in micro-scale for simplicity. In addition, the last term can be omitted if the temperature differences are not of concern [217].

As previously mentioned, $\rho v_i v_j$ is also presented as the 'momentum flux tensor' since it represents the rate of momentum in the v_i direction across the unit surface in the direction of velocity v_j. In other words, in 3D, there is a force equal to inward flux per unit volume produced by the stresses such that

$$F_j^R = \frac{-\partial S_{ij}}{\partial x_i} \tag{8.13}$$

According to the Eqn. (4) in [219], the Eqn. (8.12), Eqn. (8.13) can be written as the mean force acting on a unit volume of fluid in the x_j direction:

$$F_j^R = -\frac{\partial \rho \overline{v_i v_j}}{\partial x_i} \tag{8.14}$$

Here, F_j^R denotes the net rate of change of x_j momentum per unit volume due to a mean flow of such momentum per unit area in the x_i direction. The above equation referred to 'Reynolds' force' where the bar above denotes the mean value of the fluctuating 'Reynolds stress' over a wave period and the repeated suffix i are summation of $[1, 2, 3]$ [273, 54]. This force F_j^R is able to generate a steady streaming motion of fluid.

According to reference [17], the nonlinear acoustic streaming force components F_j^R and R_{ij} can be calculated once the wave particle velocity is known. Consequently, the pattern of acoustic streaming inside any liquid is forced by the mean value of the acoustic momentum flux can be simulated [216]. The droplet on substrate could be moved in the propagation direction by the SAW under the condition

of relative small volume of liquid and certain level of acoustic power [291]. The current development follows the steps of Vanneste & Buhler in [320] and Eckart in [139], the Reynolds' stress is thus formally defined in its matrix form as:

$$\sigma_{ij}^{R} = \rho\overline{v_i v_j} = \rho < v_i v_j > \tag{8.15}$$

with time average over a full oscillation period of tensor products of the velocities.

8.2.3.2 Acoustic Radiation Stress

In many publications, it is argued that the acoustic force derived from the time averaged acoustic stresses can be exploited as a driving force to move the fluid particles and change the motion of the fluid parcel, these forces are calculated based on a previous solution obtained by resolving the acoustic problem in a computational domain. The studies can be traced back to 1994 in [127] from King's results. Further development and application has been proved by Gorkov, such that a small particle is moved by the acoustic forces in an ideal fluid [161]. Despite Reynolds' stress, Bruus introduced a novel second-order stress term that neglected the thermo-viscous effects as:

$$\sigma^{r} = -\frac{1}{2\rho c^2} < p^2 > + \frac{\rho}{2} < \underline{\boldsymbol{\nu}} \cdot \underline{\boldsymbol{\nu}} > \tag{8.16}$$

where the average over $v_i \cdot v_j$ can be decomposed into time integration over the signal duration T, it is named as acoustic radiation stress in [289] and static acoustic pressure in [332].

The acoustic radiation pressure is a second order effect that is exerted from the acoustic waves. It is a unidirectional force / pressure acting on the external surface of the body [160]. The acoustic streaming phenomena, movement and deformation of micro fluid particles subject to acoustic radiation pressure are well studied in the literature [289, 187, 239, 194, 160]. For instance, numerical analysis can be done on the deformation of a spherical body due to acoustic power by solving acoustic impinging sphere problem in advance, then input the stress terms calculated from acoustic potential into mechanics equation for solid. Thus, we employed the method proposed by Sankaranarayanan in [283] to include both the time harmonic part and varying part of the velocities, which the later caused acoustic streaming inside the fluid. Consequently, if the time period T is relatively large enough, the effect of the time harmonic part can be reduced to zero, merely the unsteady part is left in the equation. In Eqn. (8.16), the mean of velocity is taken by the average value over the time integral (period T) such as:

$$\overline{v_i} = \frac{1}{T}\int_{t_0}^{t_0+T} v_i \; dt \tag{8.17}$$

for $i = 1$, 2, and 3, which integral can be approximated by Trapezoidal rule over a chosen time period. The Trapezoidal rule for velocity is described as:

$$\int_{t_0}^{t_n} \boldsymbol{v}(t)dt \approx \frac{t_n - t_0}{2N}(\boldsymbol{v}(t_0) + 2\boldsymbol{v}(t_1) + 2\boldsymbol{v}(t_2) + \ldots + 2\boldsymbol{v}(t_{N-1}) + \boldsymbol{v}(t_N)) \tag{8.18}$$

The pseudo-momentum introduced in this section would be sufficient to provide a driving force to move the molecules inside a fluid, or even as a surface acoustic force incident on the droplet sitting on a substrate [136]. For the sake of brevity, the detailed derivation of acoustic radiation pressure will not be addressed in this article, which can be found in [289] for reference.

8.3 Numerical Experiments Setup

8.3.1 Description of the Problem

The bulk waves inside sessile droplet stimulated by SAW must be throughly studied, in order to aid the efficient design and manipulation of SAW device for Lab-on-chip system. The 3D droplet numerical model has been built with various boundary material properties and parameters, such that the application is resolved with both monochromatic and polychromatic waves accordingly. The same procedures are performed as in Chapter 5, such that the pre-conditioner and solver are chosen to be the most amenable combination for the acoustic problems.

Prior to the calculation, our model geometry and input parameters came from the experiment conducted by Bioelectronics group at the University of Glasgow, the video of a micro-droplet actuation by a periodic sinusoidal voltage wave is captured by a high-speed camera with 250,000 fps sample rate, a total time period of 100 seconds are recorded. In Graph 8.5, the sinusoidal input signal and the micro-droplet actuated by the former is shown. The two cycles sine wave with frequency in MHz range and lasting a few micro seconds are generated by a digital transducer. The short period of the wave pulse circumvents the heat conduction in the system. Figure 8.4 shows the different positions of a droplet placed on a $LiNbO_3$ substrate, which decides the streaming pattern and direction of acoustic waves inside the fluid. The experiments have been conducted in [18] where different volumes of water droplets under SAW are studied. In this work, an Eulerian formulation is adopted (there is no distortion of mesh, opposite to the Lagrange formulation), the RF powers are set to relevantly low, such that no apparent deformation of droplet can be visualised [17]. Thus the destabilization around the free surface is avoided.

A similar experimental set up has been conducted in the literature [270, 225, 271, 258, 76, 331]. There are many attempts on computing the acoustic fields stimulated by dissipated LSAW energy propagating through micro-droplet [274, 188]. Though their problems are limited in two dimensions, the numerical results firmly supported the observation from experiments such that the circulation and streaming of energies inside droplet are revealed. However, the axis-symmetric assumption on SAW beneath the droplet was unable to manipulate the SAW direction generated by the transducer, which follows a different acoustic streaming pattern inside the droplet.

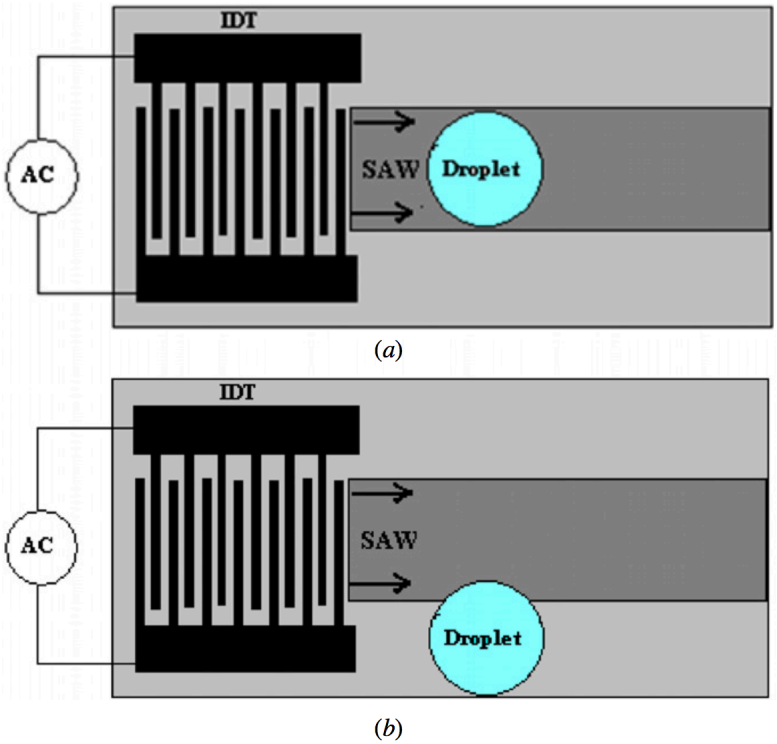

Figure 8.4: Illustration of droplet positioning on the surface of substrate actuated by SAW device,(a) symmetrically, (b) asymmetrically [17]

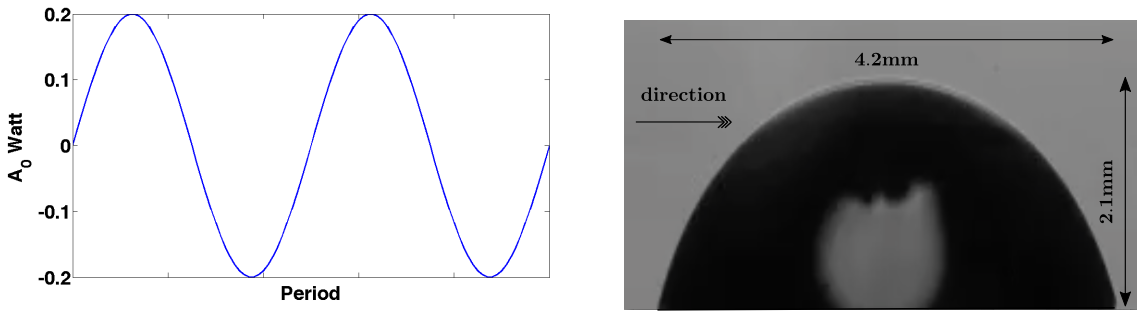

(a) input signal, amplitude versus period, s

(b) micro-droplet

Figure 8.5: Model setup,(a) input signal of two cycles sine wave, amplitude versus period, (b) image of micro-droplet sitting on substrate

8.3.2 Travelling Incident Waves

In physics, the category of surface acoustic waves can be classified as progressive waves and standing waves [245]. Previously, we have demonstrated the accuracy and effectiveness of our acoustic wave solver. When solving the time-harmonic Helmholtz equation, we obtain standing waves and a steady state solution. In this situation, the difference in phase velocity between Rayleigh waves propagating on the substrate and incident into the droplet cavity is not taken into account.

In microfluidic applications, the density between the solid substrate and liquid

droplet are different, such that $\rho_s \neq \rho_f$. Consequently, in the solid substrate we observe the propagation of monochromatic standing waves.

Since the speed of the incoming wave in the solid and the speed of a wave in the fluid are different, the wave propagating in the droplet is progressive. It is a superposition of waves of different frequencies, phases and amplitudes. Notably, when waves of different frequencies interfere, they generate a beating phenomenon, which may be of fundamental importance for an explanation of capillary waves observed on the surface of microfluidic droplets. The problem of the propagation of polychromatic waves was solved in the frequency domain and space domain, by applying the Helmholtz equation for every harmonic wave in truncated Fourier transform. The detailed implementation of the polychromatic wave solver has been explained thoroughly in chapter 5.

The beating phenomenon occurs when two or more waves travel on a medium with slightly different frequencies, then an interference pattern of wave packets is formed called the beating phenomenon. In case of the beating phenomenon, the outgoing and incoming parts of the periodic progressive wave are neither completely in phase nor out of phase. Alternatively, the waves do not require to travel in opposite directions for the beating phenomenon to occur, two waves travelling in the same direction with slightly different phase and frequency could form a succession of progressive waves as well [209]. In the current numerical analysis for droplet application, we take into account that the progressive wave is propagating in a fluid and form a beating phenomenon, hence, we will observe a significant difference in results between the polychromatic wave solution and a monochromatic wave solution. As a result of the beating phenomenon, we can state by hypothesis that capillary waves are created on the droplet surface.

In conclusion, the use of a polychromatic wave solver to simulate the actuation of a droplet by a leaky Rayleigh SAW, rather than a monochromatic solver, would be more physically accurate, since the propagation of the leaky Rayleigh SAW on the interface is also considered. However, the speed and shape of the refracted waves inside the droplet cavity depend on the properties of the droplet. Since the acoustic pressure distribution is dependent upon the reflections from both interfaces (Γ_1, Γ_2), as well as diffracted waves inside the droplet cavity, the solution has a certain level of complexity. In essence, the merits of a polychromatic solver allows us to solve the Helmholtz problems instead of a coupled time dependant large acoustic problem with discontinuities across the droplet / substrate interface.

Figures 8.6 and 8.7 refer to the different behaviours between standing waves and progressive waves in both space and time. The differences in phase and time between each wave are revealed. Firstly, Figure 8.6 depicts a standing wave travelling (as a function of position) in space. In the assumption of time harmonic waves, the incident wave function and radiation wave function contain two parts, the incoming wave and outgoing wave. The red and black solid lines in the Figure indicate that the incoming and outgoing waves are completely out of phase when the waves coincide at the anti-nodes (particles) over sufficiently one period of time T. The two travelling waves have the same wave period and frequencies. In other words, the position of the maxima and minimum of two waves match exactly over time.

If we move our attention to the second set of Figures 8.7, waves in space and

time are shown. The distance traveled with time is c_sT, where c_s is the speed of the wave travelling in medium s, and T is the period (the time for wave particle to complete one cycle). As shown in 8.7 (a), the standing wave does not have an onward motion in the domain. The waves between each period are identical. That means in one period of time, the particle of waves complete one cycle (complete up and down motion) exactly. Consequently, standing waves do not transport energy in any direction. The wave potential function $\Phi(\mathbf{r}, t) = \Phi(\mathbf{r})\mathbf{f}(t)$ is dependent on the coordinate vector (position changes) and the passed time. The function $\Phi(\mathbf{r})$ describes the amplitude distribution of the harmonic vibration in space. $\mathbf{f}(t)$ is the specific time dependent function. The amplitude increases and decreases with time by the same function $\mathbf{f}(t)$. In contrast, the progressive wave in 8.7 (b) is moving through both space and time. Although represented as a sinusoidal wave, it could in general be the superposition of multiple waves as stated in previous context. In one period of time, the particle of waves can complete multiple cycles. In Figure 8.7 (c), The wave potential function is expressed as $\Phi(\mathbf{r}, t) = \sum_{n=0}^{\infty} \Phi_n(\mathbf{r})\mathbf{f}_n(t)$. The amplitude of the progressive wave in 8.7 (c) is attenuated with distance traveled in space. As stated in Eqn. (8.4), the magnitude of attenuation might depend on the property of the medium, the frequency of the wave and the spatial coordinates.

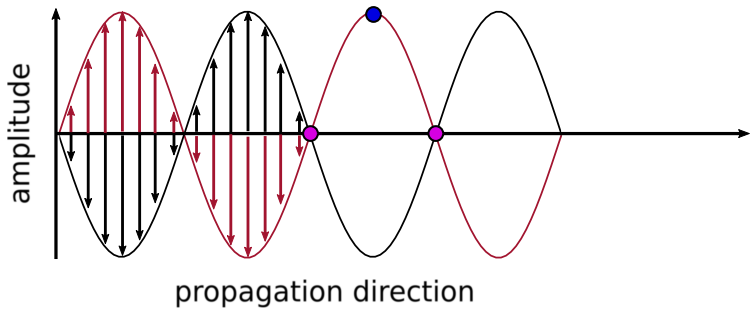

Figure 8.6: Standing incident wave profile for monochromatic wave acoustic solver. The wave profile is moving up and down completely in one period of time [66]. Outgoing waves: in red solid line, incoming waves: in dark solid line. Pink dot: anti-node, navy dot: node

In the following contexts, the density of liquid is set to $\rho_f = 998kg/m^3$, it serves to compute the pressure of acoustic wave by Eqn. (2.21). Further to that, $\rho_s = 4650kg/m^3$. We then set the simulation time to $T = \frac{1}{f}$ s which is exactly the time required to complete the input signal with given frequency. Each time step is: $\Delta t = \frac{T}{N}$ s, where N is the discretized number of time steps.

The other setup parameters for our analysis are assuming a room temperature of approximately 20C, the speed of the Rayleigh SAW is described as $c_s = 4000m/s$ in the solid substrate and $c_f = 1500m/s$ in the micro-droplet, while the frequency of the SAW from experimental devices are 4MHz, 10MHz and 20MHz respectively with an RF power of 200 mW [91]. The droplet has a hemispherical shape with some contact angle of 90 degree for simplicity. The heat energy induced by acoustic dissipation inside the droplet will be omitted since the concentration process is not affected by the bounded rising temperature in experiments [257]. The complete set of parameters adopted in the following numerical examples are listed in Table 8.1 below.

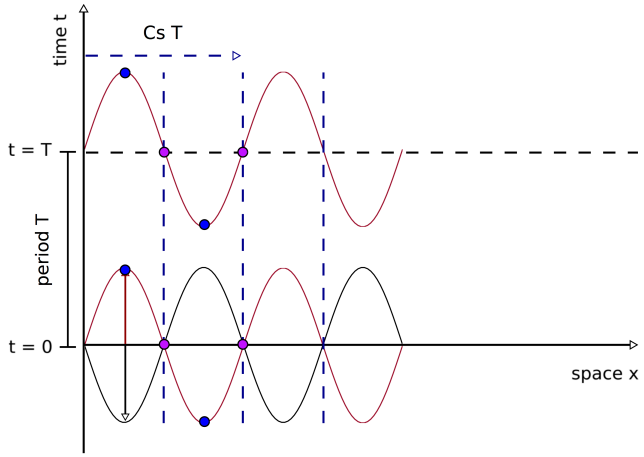

(a) Standing incident wave profile

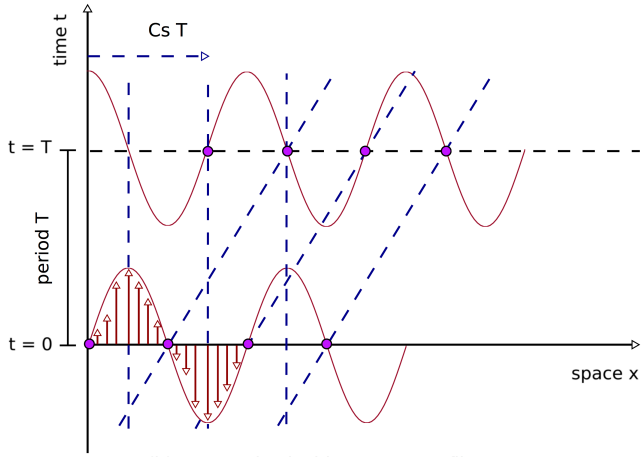

(b) Progressive incident wave profile

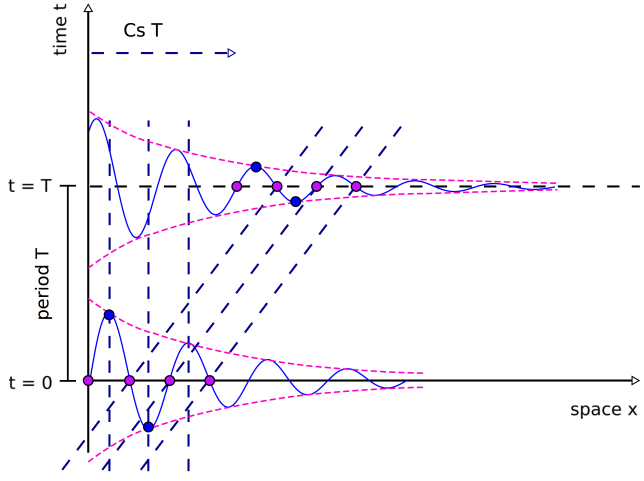

(c) Attenuated progressive incident wave profile

Figure 8.7: Illustration of waves in space and time. (a) standing wave (b) progressive wave (c) attenuated progressive wave. Pink dot: anti-node, navy dot: node. T denotes one period of time

Table 8.1: Properties and parameters of water droplet sitting on an $LiNbO_3$ stimulated by SAW for numerical experiment and simulation

f (MHz)	λ_R (m)	$k \approx (m^{-1})$	$\alpha_l \approx (m^{-1})$	$\alpha_s \approx$
4 MHz	0.001	6283	79.8387	0.0670772
10 MHz	0.0004	15708	199.5968	0.265146
20 MHz	0.0002	31416	399.1935	0.749946

8.3.3 Mesh Generation

The development of boundary refinement methods to capture the mesh geometry remains a challenging research area nowadays. There are many approaches such as NURBS, T-spline [293, 290], and curvilinear meshes [315], which are beyond the scope of this article. Here we use the ten-nodes tetrahedron (curvilinear tetrahedrons) in mesh generator to represent our geometry with smooth boundaries (additional nodes on each edges) [220]. However, the curvilinear tetrahedrons are projected into tetrahedrons with arbitrary and heterogeneous order of hierarchical Legendre polynomials in MoFEM. In fact, the hierarchical polynomials can be applied on the tetrahedrons without adding additional nodes. With regard to the current computational resources (memory, cores), hierarchical Lobatto basis of order 8 is the highest order feasible at the time of writing.

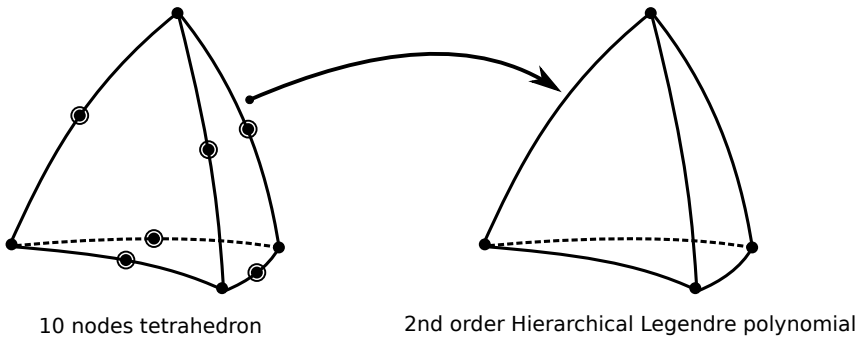

Figure 8.8: Example of curvilinear tetrahedrons with arbitrary and heterogeneous polynomial orders, the curvilinear tetrahedron is projected into hierarchical higher order tetrahedron

In Figure 8.9, the example of hemispherical droplet geometry is shown. From the previous numerical analysis in Chapter 7, we acknowledge that the local error has the tendency to increase along the direction of propagation. Alternatively, the propagation speed of acoustic waves on the surface of the substrate is much faster than the wave speed inside the droplet. Consequently, the mesh is partly refined along the central line of bottom surface Γ_2, where the SAW is propagating with $c_s = 4000m/s$, especially along the propagation direction of waves shown in Figure 8.9. But the mesh remains a relatively coarse mesh in the interior of the droplet.

The diameter of the droplet from meshes in Figure 8.9 is chosen to be 4.2 mm (radius = 2.1 mm), which is approximately 21 times that of the smallest $\lambda_R = 200$

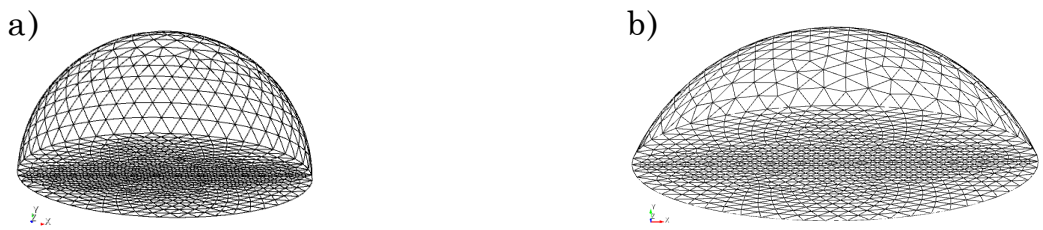

Figure 8.9: Example of the meshes presented for droplet application, frequency range from 4MHz to 20MHz.(a) droplet geometry with 19473 elements, height = radius = 0.0021 m, f = 4, 10, 20 MHz. (b) droplet geometry with 17480 elements, height = 0.0014 m, radius = 0.0021 m, f = 10 MHz

μm (f = 20MHz). The Rayleigh wavelength λ_R is the wavelength on the substrate. In the following sections, we will use mesh 8.9 a) with f = 4, 10, 20 MHz respectively, and mesh 8.9 b) with 10 MHz.

The mesh resolutions for the current geometry ranges from 0.485 to 3.396 (h_{max} = 412.2 μm). Recall that in Eqn. (7.7), the maximum frequency limitation can be obtained: $f_{max} = C_E \frac{c}{h_{max}}$ = 19 MHz for a specific accuracy level of at least 15%. The frequency limitation derived from the rule of thumb for p = 1 is $f_{max} = \frac{c}{10 h_{max}}$ = 0.9704 MHz for a mesh resolution condition of 10 DOFs per wavelength to be fulfilled. In [72], the author and his coworkers suggest that if the chosen model characteristic length of the mesh geometry and the minimum wavelength satisfy the relationship: $l \ll \lambda_{min}$, then one can say that the geometry feature is acoustically compact. Otherwise, if $l \approx \lambda_{min}$, one should refine the mesh until $h \ll l$. It is clear that the characteristic length of our geometry is many times larger than the minimum wavelength. Therefore, theoretically the h_{max} should be much smaller than λ_{min}. In our model geometry setup, the smallest characteristic length $l_{min} = 2.1\ mm$ for mesh 8.9 (a) which is approximately 5.1 times of h_{max}. In [72], h_{max} is set to be smaller than l by a factor of 96. The ratio between maximum and minimum element size is 1 : 5.7338.

8.4 Stimulated Droplet Application

8.4.1 Acoustic Application in Spatial Domain with Monochromatic Waves

In this section, the numerical simulation of droplet application with monochromatic waves as input signal is examined, where frequencies are varied from 4MHz to 20 MHz. And the impact of droplet size as well as material coefficients are identified.

In Figure 8.10(a) and (b), the micro-droplet siting on a near hydrophobic substrate surface with incident plane and spherical waves propagating on full path

(Figure 8.4 (a)) are simulated. Figure 8.11(a) is a droplet with cap shape as depicted in Figure 8.9 (b) impinged by SAW. Where 8.11 (b) is a droplet sitting on a near hydrophobic surface with incident plane wave propagating on its side path as shown in Figure 8.4 (b). Subsequently, in Figure 8.12(a) and (b), hemispherical droplets sitting on a near hydrophilic surfaces, with an incident plane wave propagating on full path (contact angle ≈ 90) are depicted. In addition, in these two Figures, the attenuation of Rayleigh waves caused by viscosity is set to be water and 25 times stronger than water respectively. Lastly, in Figure 8.13, the micro-droplet is actuated by a SAW with various frequencies ranging from 4 MHz to 20 MHz, such that the real acoustic pressure field is presented at steady state.

First of all, in Figure 8.10(a) and (b), the difference between the two wave fronts did not result in distinguished acoustic patterns inside the droplets. Symmetric acoustic pressure structures are observed in steady state position.

It turns out that the shape difference of the two droplets in Figure 8.11 affects the acoustic pressure, as depicted by the chaotic pattern inside 8.11(a). Since the height of the droplets are 3.5 times (in comparison with 5.3 times in Figure 8.11 (b)) bigger than the wavelength, the waves were reflected (radiation pressure) more times inside the bulk of shorter drop than the drop with normal height in Figure 8.10(a). The caustics are separated apart from the centre of the droplet in 8.11(a) which might link the flow pattern to geometrical acoustics. (See Figure 8.14 for graphical interpretation). In this case, we might expect more jumping and free surface oscillation motion of the droplet in experiments [87]. On the other hand, the waves propagating through one side of substrate and leaking energies into the droplet as shown in Figure 8.4 and 8.11 (b). We can intuitively observe that the waves are circulating around the edge of the droplet, and the systematic structure of the acoustic pressure might lead to a mixture of different liquids inside the droplet. Moreover, whispering gallery mode waves are observed in Figure 8.11 (b), the leaky SAW generated by the IDTs circles around the droplet cavity [167, 231]. The Rayleigh whispering-gallery wave occurs in concave surfaces on the X-Z plane due to waves reflected from the surrounding boundaries of the droplet [336].

Since the internal acoustic streaming within the droplets is inductively dominated by the energy dissipation caused by the liquid bulk viscosity ξ_f and shear μ, it tends to be more intense for larger values of viscosities and frequencies. In contrast, the acoustic radiation pressure is proportional to the energies reached at the drop/ambient interface. Thus, the greater the viscosity, the less the acoustic radiation pressure reflected from free-surfaces [79]. Consequently, the acoustic field inside the fluid tends to mimic incident waves with large attenuation. This fact can be evidenced by Figure 8.12 (b) such that the droplet with attenuation (α_l) 25 times stronger than water tends to produce recognisable bulk waves reaching the free-surface. In Figure 8.12 (b), most of the acoustic energy is damped before reaching the top surface, but the bulk waves climbed through the drop surface and along the propagation direction of the SAW. Since there is less reflections inside the droplet, the maximum real pressure is less than in Figure 8.12(a) with a water droplet. In article [284], the authors revealed the acoustic streaming stimulated a force potential towards the propagation direction inside the droplet at high frequencies, which headed to the liquid/ambient interface and caused the droplet deformation.

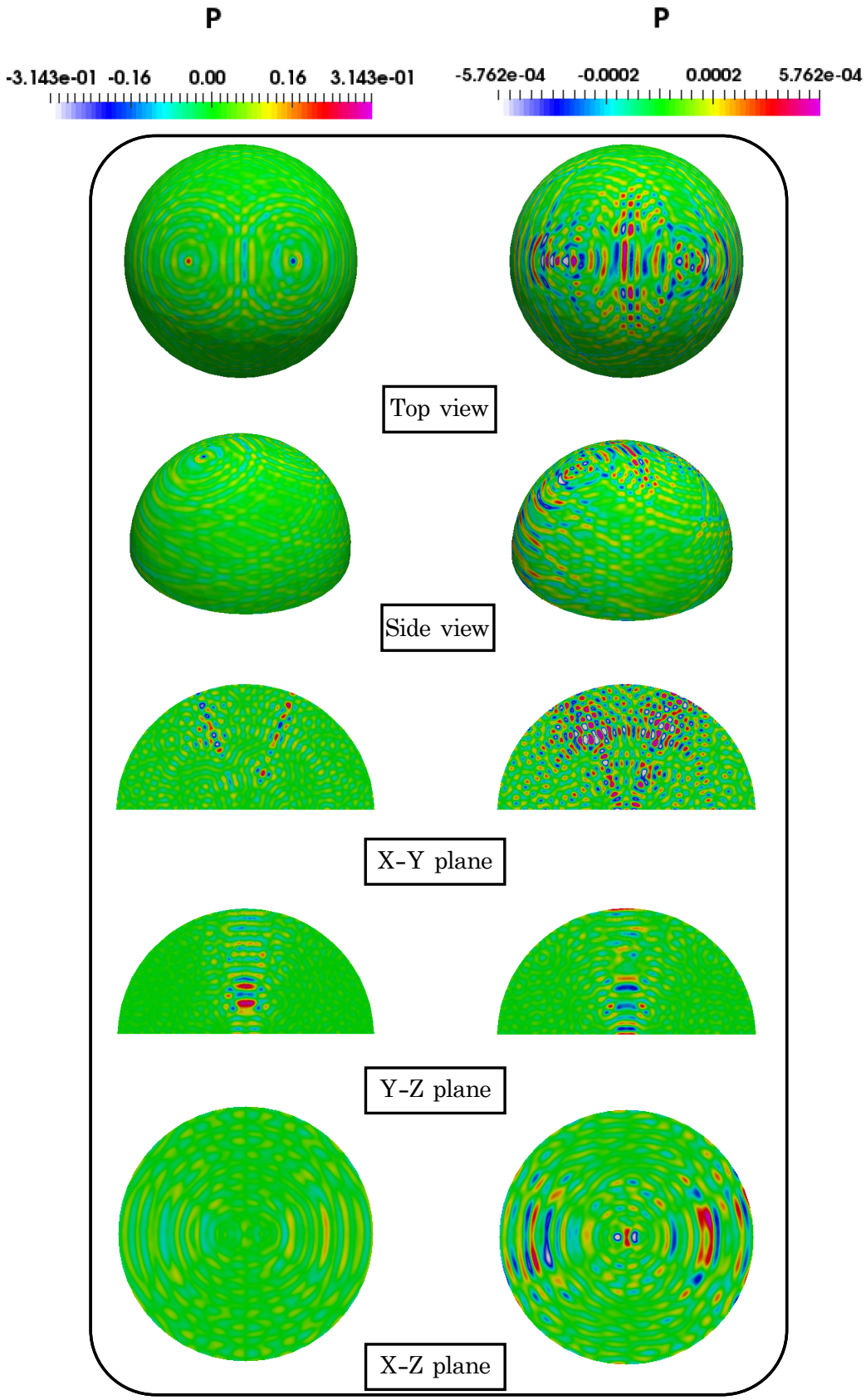

(a) Plane wave (b) Spherical wave

Figure 8.10: Micro-droplet actuated by 10 MHz IDTs, steady state real pressure field. Comparison of wave front forms.(a) plane wave (b) spherical wave

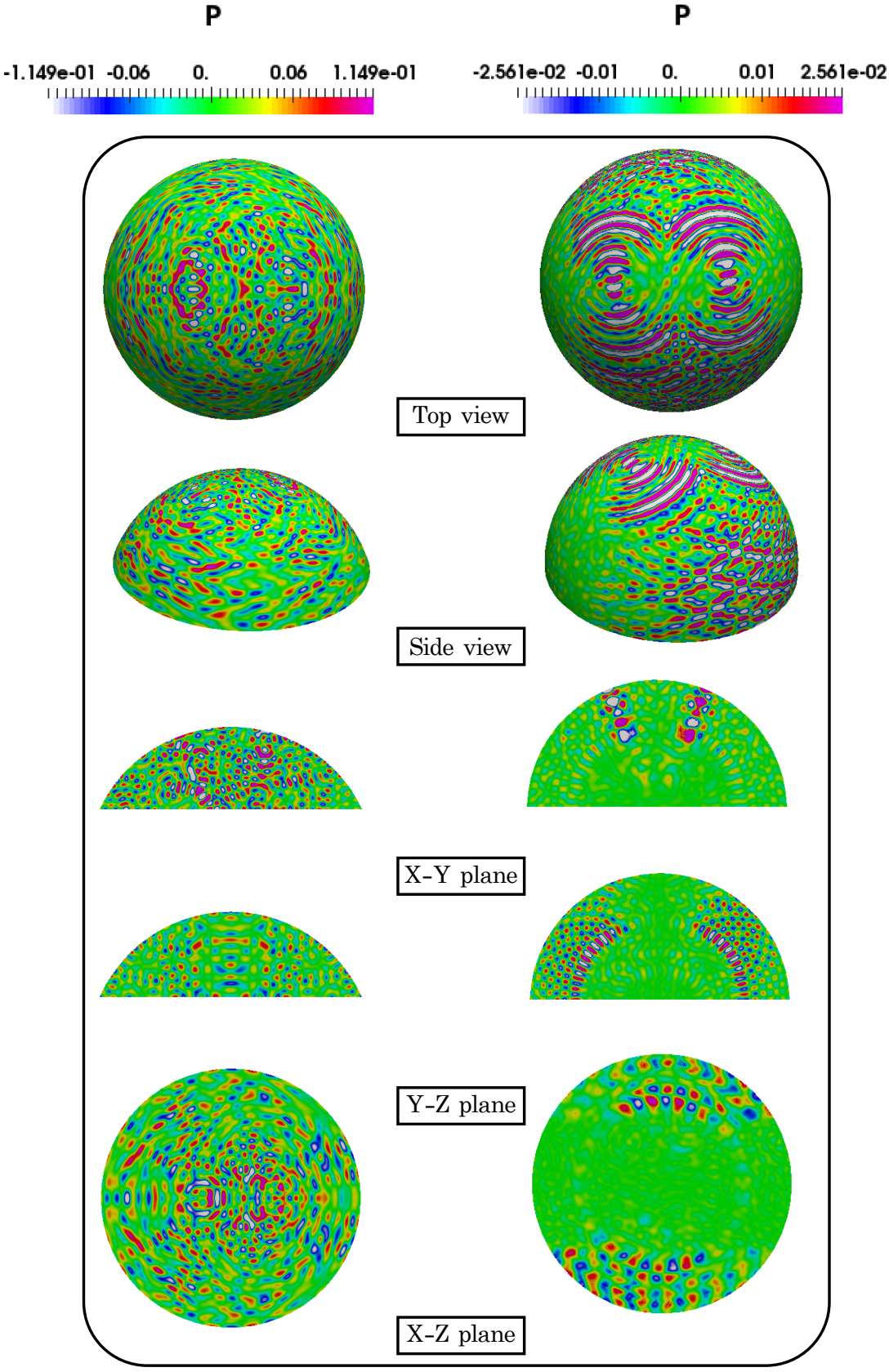

(a) Plane wave & cap shape (b) Plane wave & side path

Figure 8.11: Micro-droplet actuated by 10 MHz IDTs, steady state real pressure field. Comparison of droplet shapes, and propagation path.(a) plane wave and cap shape geometry, (b) plane wave and side propagation path

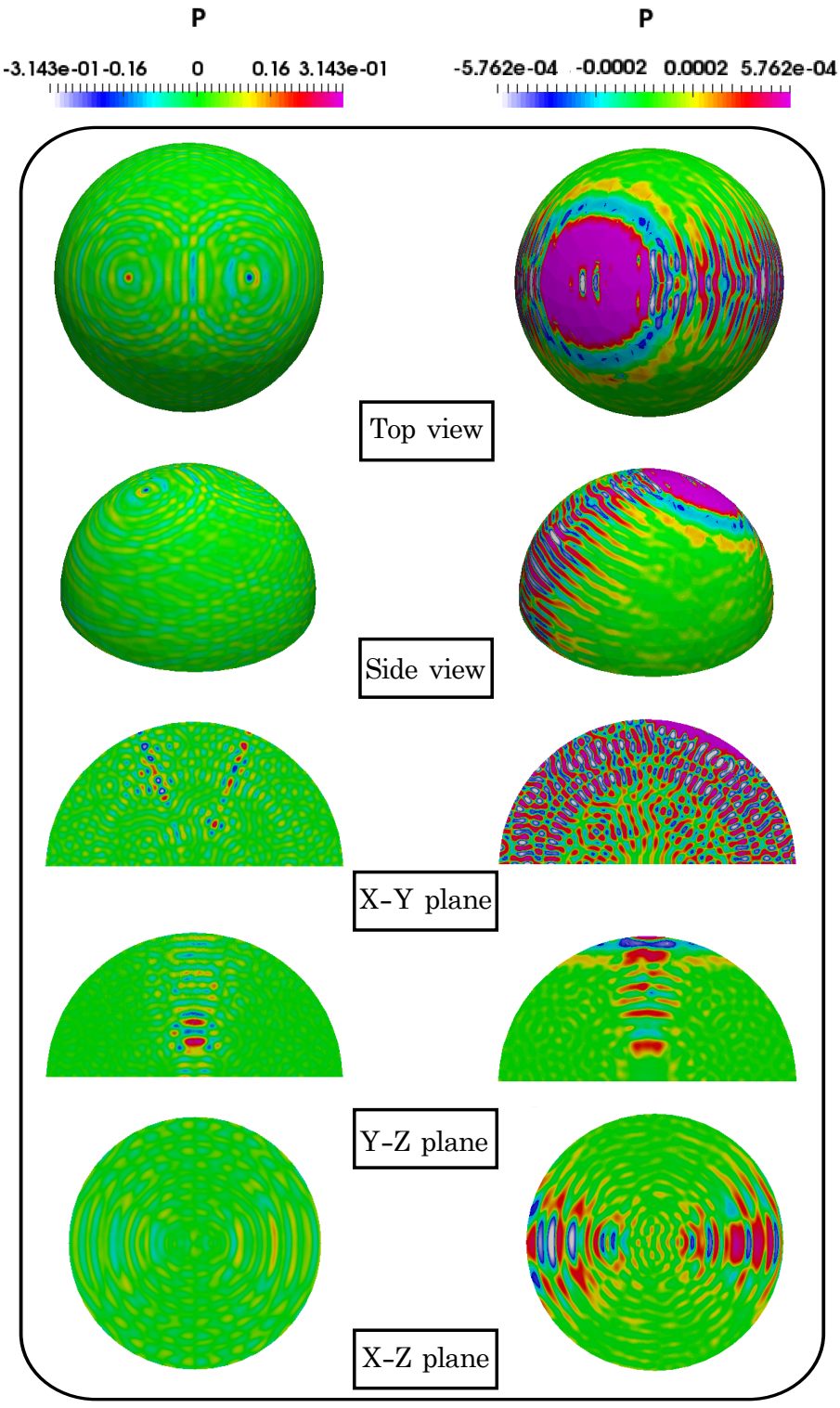

(a) Weak attenuation, water (b) Strong attenuation, 25 times

Figure 8.12: Micro-droplet actuated by 10 MHz IDTs, steady state real pressure field. Comparison of weak and strong attenuations.(a) weak attenuation, water α_l. (b) strong attenuation, 25 times stronger than water

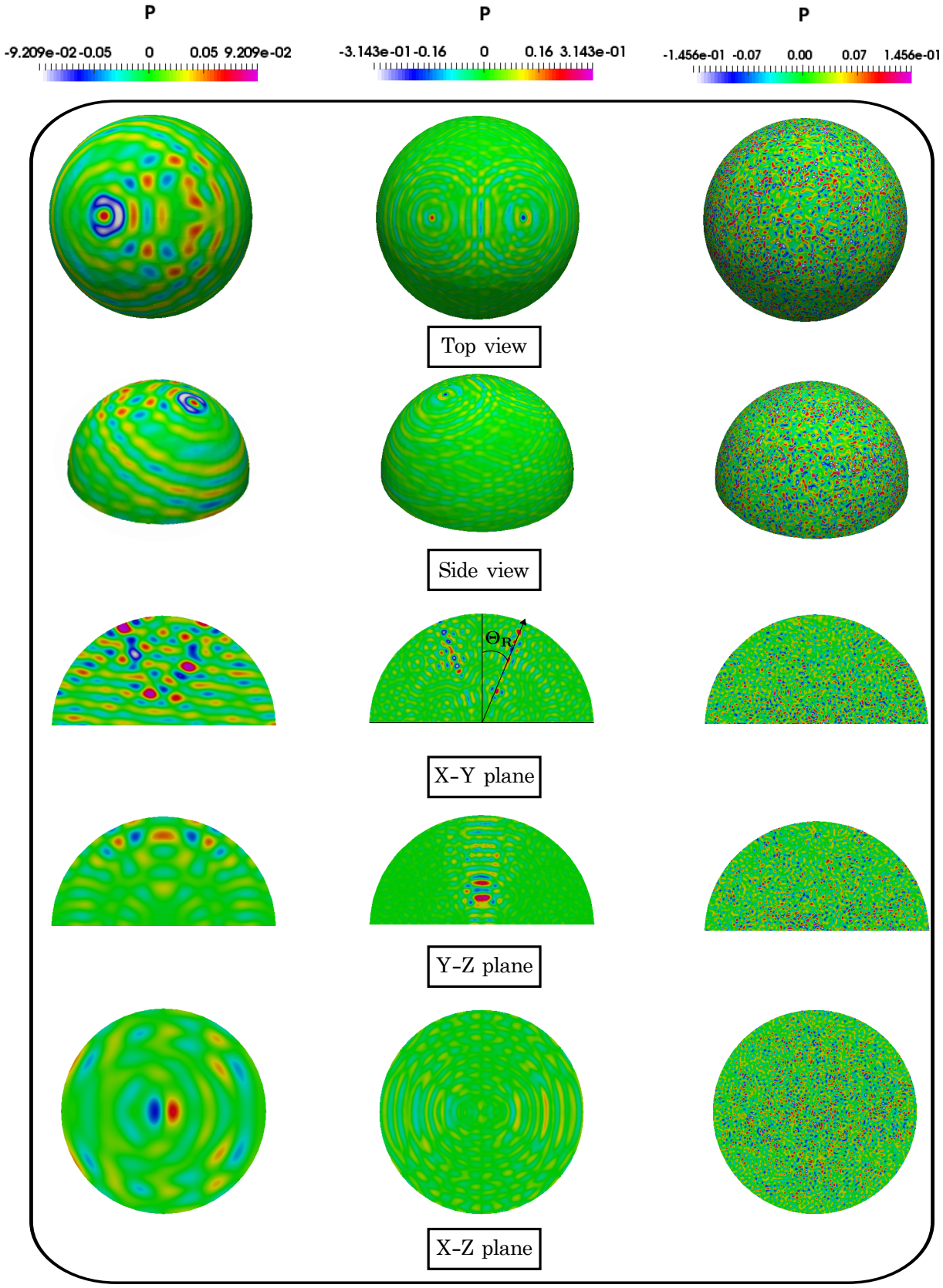

(a) 4MHz (b) 10MHz (c) 20MHz

Figure 8.13: Micro-droplet actuated by 4 MHz, 10 MHz, and 20 MHz IDTs, steady state real pressure field.(a) 4 MHz SAW, (b) 10 MHz SAW, (c) 20 MHz SAW

As displayed in Figure 8.13, when the SAW frequency is increased from 4 MHz to 20 MHz, the droplet cavity has more pronounced chaotic structure (complex standing wave pattern), which is caused by the multiple reflections of waves. The chaotic pattern vanished for smaller f, indeed the acoustic waves with large wavelengths tend to be diffracted with large gap between reflected waves than waves with short wavelength.

In the last set of Figures, the structure of the acoustic pressure field is broken when the frequency reaches 20MHz, which is exactly as described in article [87] for low viscosity fluids. Up to this point, the symmetric pattern of pressure is dictated not only by the size of the drop, but also by the frequency. The chaotic cavity property inside the droplet and the relevant caustics caused by multiple reflections at Γ_1 and Γ_2 can be observed from both Figure 8.13(a), (b) and (c), especially with 10MHz and 20MHz frequencies, resulting in complex intricate wave pattern.

Overall, the caustics superimposed on the chaotic radiation field are more remarkable in the case with 10 MHz frequency than other frequencies. The angle of the caustic lines obeyed the Rayleigh refraction angle ($\Theta_R \approx 22^o$), which matches the results in [274] exactly. The caustics also served as one of the major driving forces to the internal flow motion within the droplet.

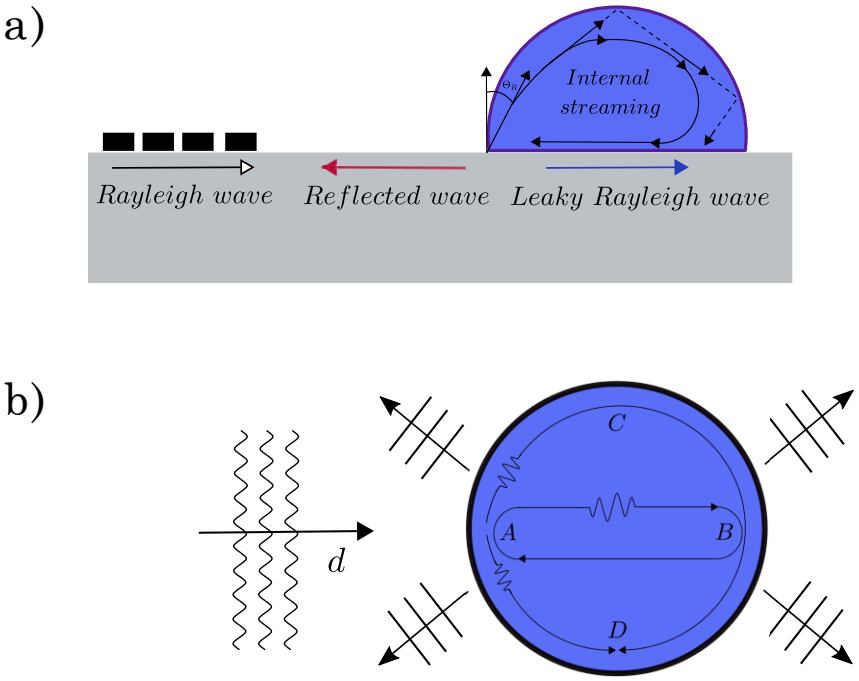

Figure 8.14: The systematic illustration of the circulation of acoustic internal streaming caused by leaky Rayleigh wave.(a) The incident Rayleigh wave changed its form into reflected wave and leaky Rayleigh wave (b) The bulk waves inside droplet pass points A, B, C, and D. **d** represents the wave direction

8.4.2 Performance of Adaptivity Schemes

In this section, the practical simulation of a droplet actuated by SAW is resolved by the developed hierarchical finite element method. In this example, we have a dense mesh (95410 elements) with optimal h value, a coarse mesh (3207 elements) with uniform optimal p order ($p = 8$ as reference solution), and a coarse mesh with automatic p adaptivity scheme respectively. The automatic p adaptivity scheme is activated with a stringent 0.5% target error. At the time of writing, the highest optimal p order allowed with the current computational resource is 8.

The number of non-zero entries represent the sparsity of a matrix, which in theory is related to the computational costs of a specific method. Hence, the total number of non-zero entries is one of the key factors for controlling the computational cost, this fact is reflected by the similar tendency of the three lines in plot 8.15. As we can observe from the plots, uniform $p = 8$ generates the densest matrix compared to the other two methods. Surprisingly, the total computational runtime and memory cost associated with uniform high order 8 are almost identical to the one of the dense mesh with quadratic elements. This observation again confirms that the number of non-zero entries does not necessarily relate to the computational cost. On the other hand, The automatic p adaptivity scheme shows progressively growing computational cost with increased frequency. The memory and time consumed by automatic p adaptivity finally coincided with uniform optimal p order due to current mesh resolvable limitation has been breached by the high frequency. Thus, all elements are assigned to order 8 . In the pre-asymptotic regime, the computational costs of the automatic adaptivity scheme remained low due to the large amount of linear / quadratic orders assigned on the mesh. Figure 8.15(a) and (c) together support the previous arguments discussed in chapters 5 and 6, such that using higher order p elements leading to less memory consumption even with larger amount of number of non-zero entries when compared to pure h adaptivity with increasing frequency. This is mainly because the factorization memory required on solving system of equations is greatly reduced by hierarchical higher order shape functions. In other words, for a fixed NNZ, the amount of factorization memory required as well as the time spent on matrix factorization for solving a particular problem is greatly reduced with increasing p order.

If we move our attention to Figure 8.16, the contour plots of numerical results with 16 contour levels are selected on the cross sectional of X-Y and Y-Z planes, located in the central axis of droplet. Comparison is made between meshes with different densities as described in Figure 8.9(a). From the contour plots, we can see that the real pressure inside the droplet solved by automatic p adaptivity is in good agreement with the uniform optimal p order (reference solution), where there are visible differences between reference solution and the solution obtained by dense mesh with $p = 2$, and it is because the mesh resolution of the dense mesh FEM is lower than the high order FEM. Overall, the automatic p adaptivity scheme performs rather satisfactory in droplet applications.

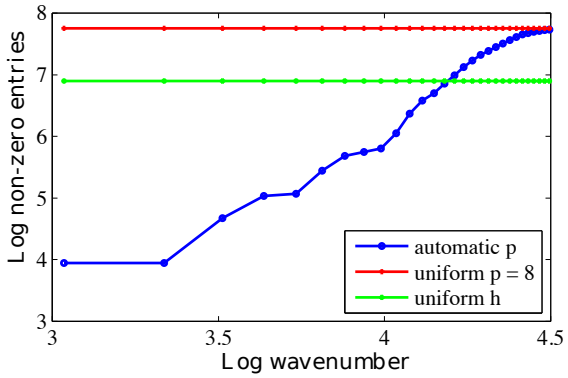

(a) k vs non-zero entries

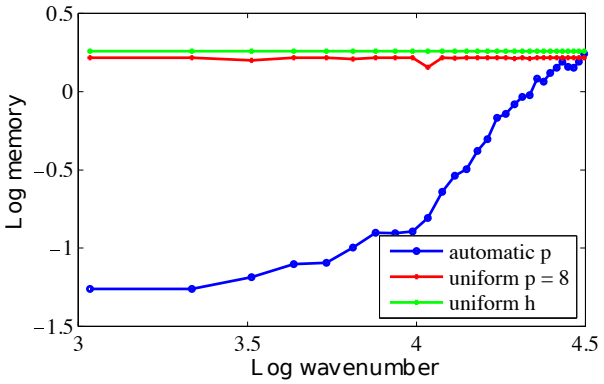

(c) k vs total memory consumption

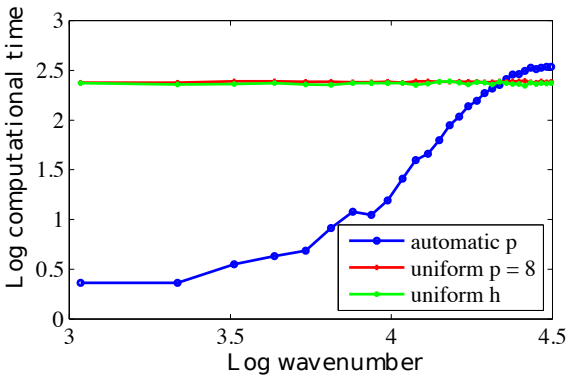

(b) k vs total computational times

Figure 8.15: Micro-droplet actuated by SAW with increasing wavenumbers, computational costs of numerical schemes.(a) k versus number of non-zero entries. (b) k versus total computational times. (c) k versus total memory consumption

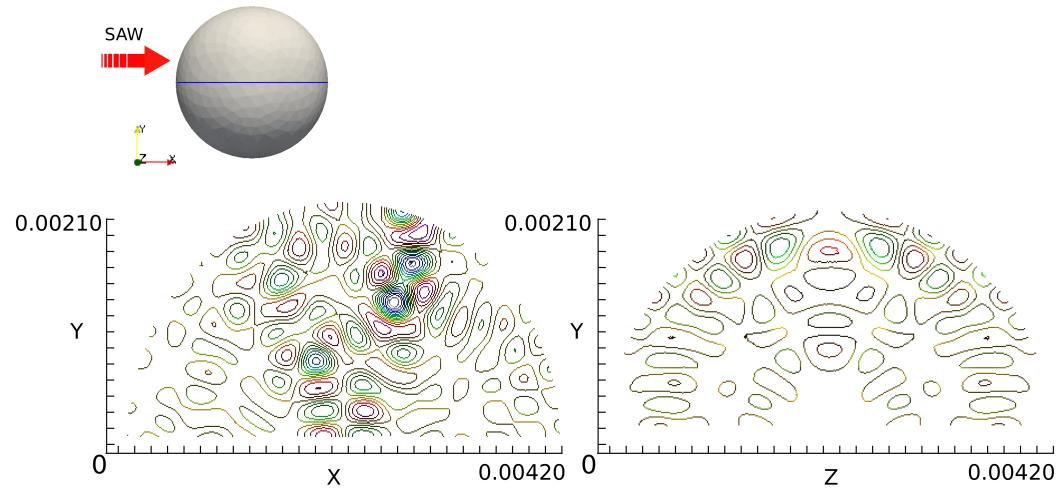

(a) p = 8, reference solution* on coarse mesh

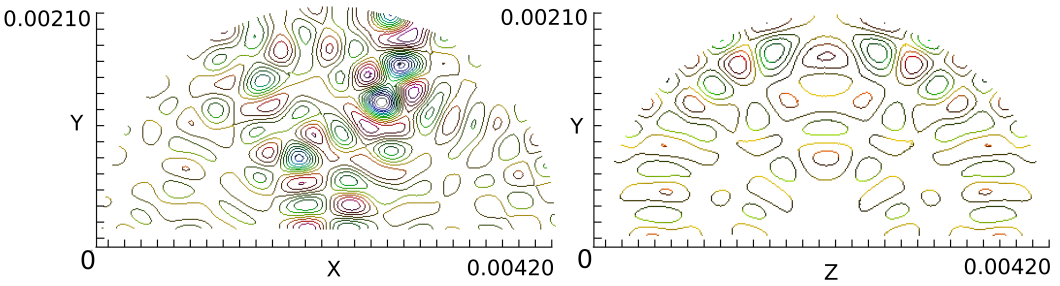

(b) automatic p adaptivity scheme on coarse mesh

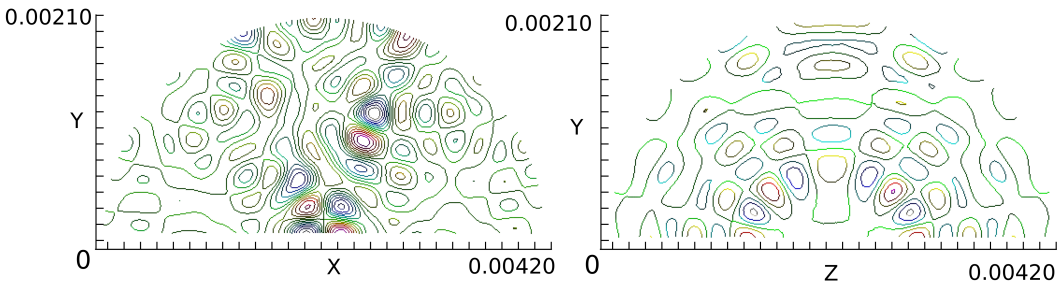

(c) quadratic elements on dense mesh

Figure 8.16: Micro-droplet actuated by SAW, 4MHz. Contour plot of real part of radiation pressure on X-Y and Y-Z planes, 16 contour levels. From top to bottom:(a) coarse mesh with optimal $p = 8$, (b) coarse mesh with automatic p adaptivity scheme, and (c) dense mesh with quadratic element respectively

8.4.3 Acoustic Application in Temporal Domain with Polychromatic Waves

In this section, the application of leaky Rayleigh waves propagating on a $LiNbO_3$ substrate and beneath the micro-droplet interface is simulated. It should be noted that the absolute potentials of the acoustic field in this analysis can have negative numbers due to the input signals are real values instead of complex values. The various acoustic fields including pressure, velocity, and stresses are retrieved based on formulas. The input signals are set to be consecutive sine shape pulses with two cycles in phase, as shown in Graph 8.5 over one time period. In addition, the droplet geometry is discretized by ten nodes tetrahedrons (curvilinear tetrahedrons) with $h_{max} = 0.5587$ mm. Thanks to the construction of a polychromatic wave solver, FEM solutions for each frequency can be solved separately and reassembled in the final step which saves the time and memory of using direct time integration solvers. The proposed time dependent acoustic solver is implemented in MoFEM [190], which has features of full flexibility to adopt any boundary conditions as desired.

The huge discrepancy between time scales of hydrodynamic and acoustic fields mentioned earlier in the beginning of this thesis limited the direct computational ability of acoustic streaming in unstructured three dimensional geometries. In terms of accuracy and realism, the procedure is to firstly compute the second-order acoustic driving force extracted from the numerical solution of the wave equations, and then insert the acoustic driving force as a body force term into the N-S equations and solve for the fluid velocity field [274]. The time averaged property of the body force prevents the tens of seconds required for the acoustic streaming inside the droplet to reach its steady state condition.

The question then arises whether the leaky Rayleigh wave affects the acoustic wave pattern inside the droplet. The difference between mixed, hard and soft boundary conditions applied on the semi spherical surface of the droplet have been examined, the former represents the amount of reflected acoustic energy according to the density of the droplet liquid. The main difference is the length of time that the acoustic energy is trapped inside the droplet. This can be understood from the maximum amount of acoustic pressure remaining within the droplet, as well as that the reflected waves are more visible in the case of mixed and hard BCs, since the soft BC transmitted almost all the acoustic energy into the air. It is important to know that there are stronger radiation pressures inside droplets with bigger horizontal lengths than in small drops with a short radius, since most of the acoustic energy propagates through the solid substrate without leaking into sessile drops with relatively small volumes [260].

Previously, in [260], the phenomenon of Rayleigh wave mode conversion was illustrated in detail. The theory of Rayleigh waves propagating through a fluid-solid interface while changing its mode to a leaky Rayleigh wave is proposed. In case the emission of longitudinal waves into the fluid medium, meanwhile, the frictional losses are generated by the transverse component, which is connected with the adjacent fluid by the viscosity of fluid ξ_f and shear μ. Thus, the transmitted wave inside the droplet will be attenuated along both horizontal and vertical directions [99]. Furthermore, the boundary along the far side of the droplet will reflect the transmitted wave to the opposite direction of the LSAW. These reflections can be

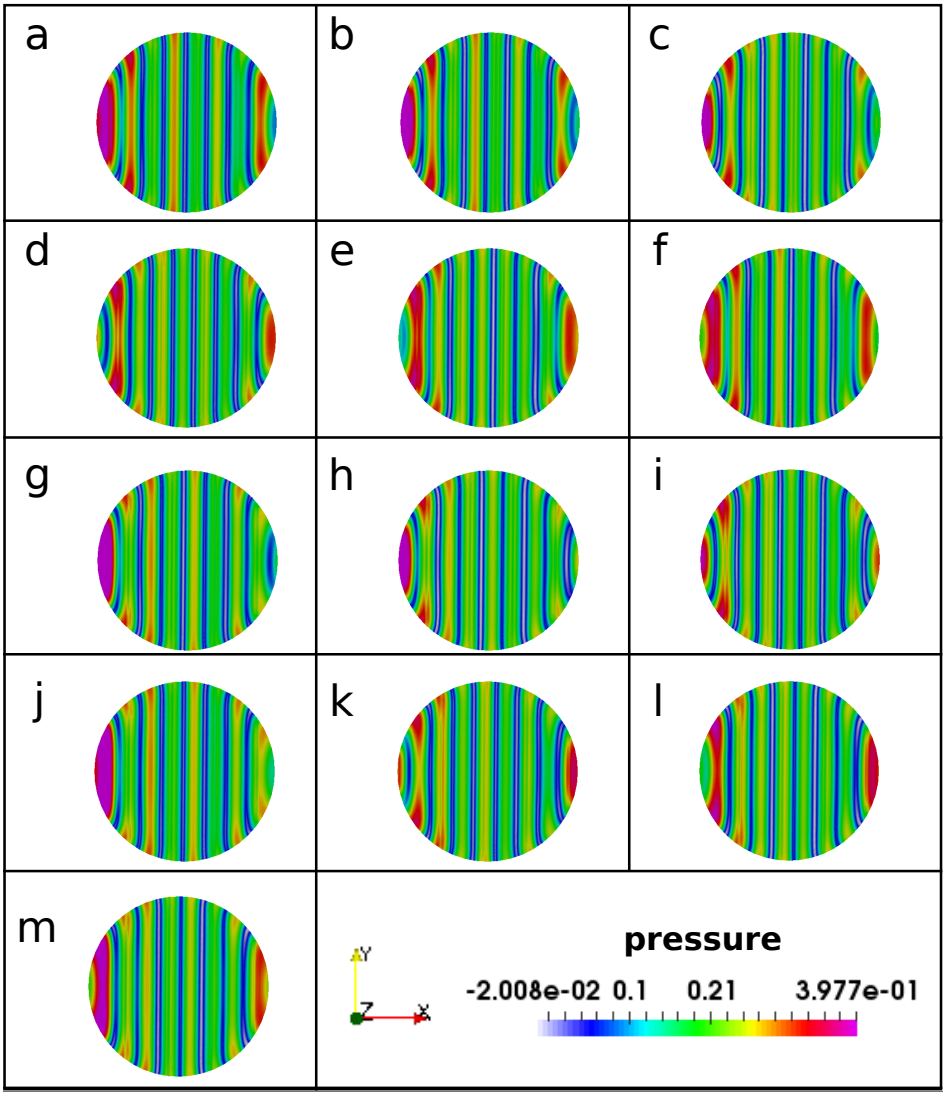

Figure 8.17: Total pressure field, bottom view, propagation of 4MHz SAW beneath the micro droplet, water. Total signal duration = 0.25 μs, pressure = $Re(\Phi_I) + \sqrt{[Re(\Phi_S)]^2 + [Im(\Phi_S)]^2}$

seen from numerical and experimental results in [260], along the top surface of the micro droplet. The circulation of reflections is observed in Figure 8.17 as bulk waves propagating along the contact circle line. Noticeably, the diffracted waves inside the droplet indicate the interference effects of Rayleigh waves reverberated from both sides of the droplet. In Figures 8.18 and 8.20, It is apparent that the transmitted wave is attenuated rapidly in the direction normal to the solid-fluid interface at different frequency levels, it further confirms the analytical theory that the transmitted wave inside the fluid droplet decays with a speed depending on the angular frequency [106]. In 2006, Schindler and his co-authors illustrated that the conservative force generated by acoustic streaming towards the top surface of the droplet along the propagation direction of a high frequency SAW induced deformation of the droplet and movement on the substrate [284], this phenomenon is evidenced by both Figure 8.18 and 8.20 to support the acoustic part of the theory. The fluid motion of droplet could be observed by solving an Euler / Navier stokes

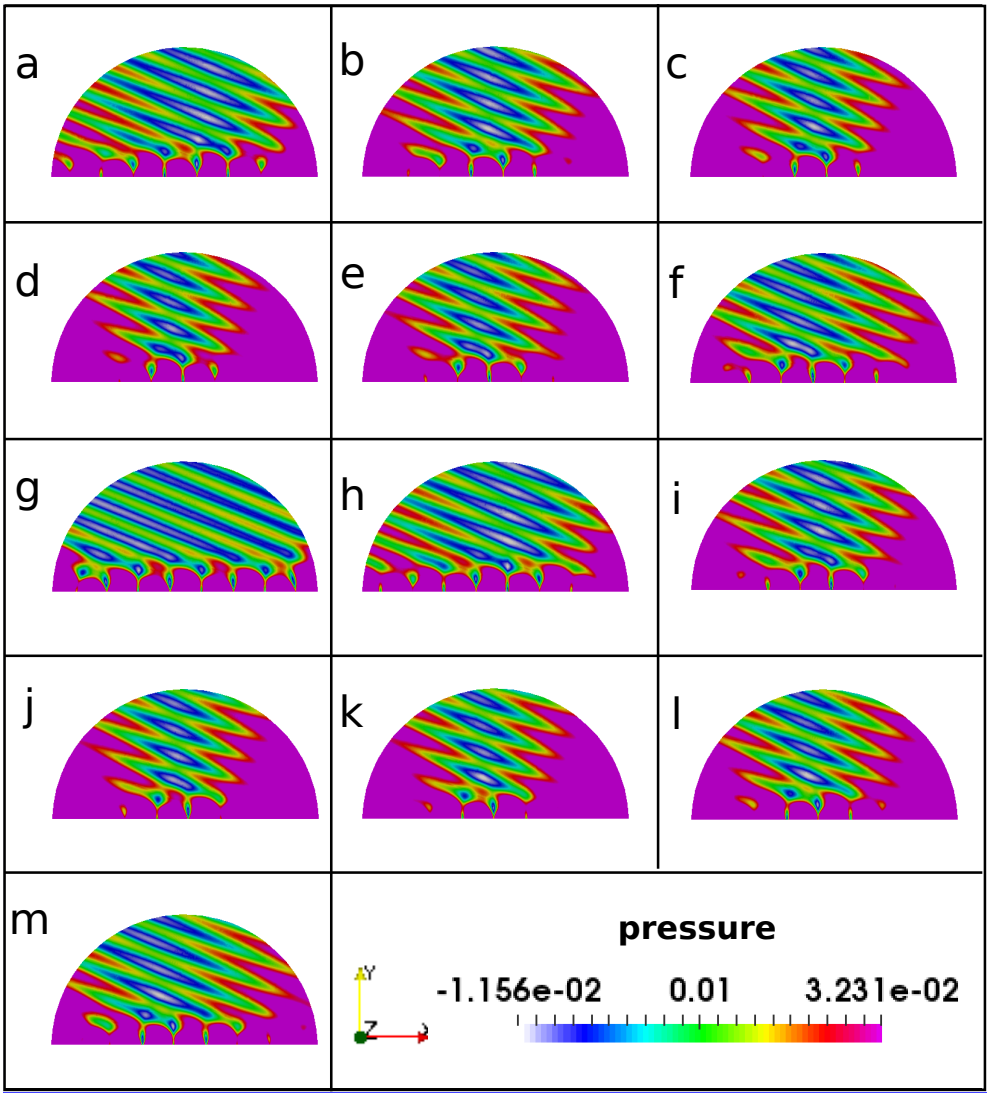

Figure 8.18: Total pressure field, X-Y plane view, propagation of 4MHz SAW beneath the micro droplet. Total signal duration = 0.25 μs

equation with acoustic fields as boundary conditions.

The polychromatic wave solver provides a solution space that contains the sum of waves with different frequencies (wavelengths). The superposition of waves of different frequencies results in a beat like pattern (interference between waves), and the wave amplitude is a function of time and space. Note that for standing waves, the amplitude is constant in time with single frequency f at all positions, and is only function of space. If we move our attention to Figure 8.18 and 8.20, it is salient that in Figure 8.20 the LSAW was attenuated very quickly, within approximately $2\lambda_R$ (the diameter of drop is more than $10\lambda_R$ for 10MHz signal), due to the relatively high frequency of the input sine signal. The shape of the plane SAW wave from the boundary of the droplet has been refracted according to Snell's law which obeys the theory of the leaky Rayleigh wave reported in articles [286] and [320]. Eventually, we can no doubt confirm that at the contact angle of the droplet, the acoustic wave tends to propagate up to the surface of the droplet. This phenomenon might be the explanatory reason for the occurrence of capillary waves on the droplet/ambient

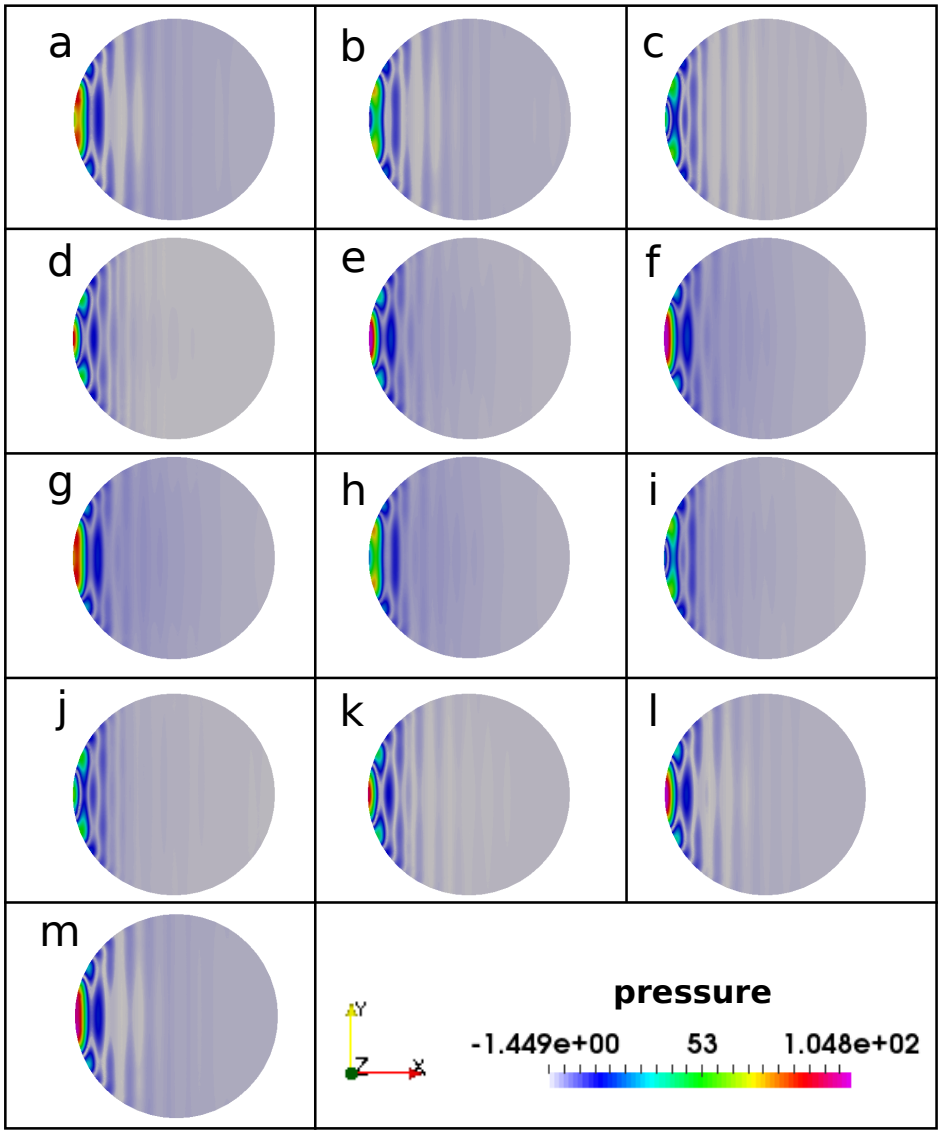

Figure 8.19: Total pressure field, bottom view, propagation of 10MHz SAW beneath the micro droplet, 14 times larger viscosity than water (large α_l value). Total signal duration = 0.1 μs

surface. Alternatively, the changing of contact angle will demonstrate the variation of capillary waves. For different power of amplitudes (RF power) applied through input signals, qualitatively similar behaviours can be found.

Horizontally, high pressure occurs circularly near the fluid-air interface, and reach lowest at the centre of the droplet, such that most likely the LSAW transmitted from interface is converted to evanescent bulk wave inside the fluid away from the bottom surface [153, 229]. The bulk waves are opposite to the surface wave which travels along the interface between two different media. This fact can be visualised from both Figures 8.20 and 8.18. Nevertheless, the acoustic pressure reaches its peak value when the LSAW emerges from the left hand side of the droplet. The momentum imbalance is due to attenuation and reflections of the leaky Rayleigh wave propagating through the droplet/substrate interface. This net momentum

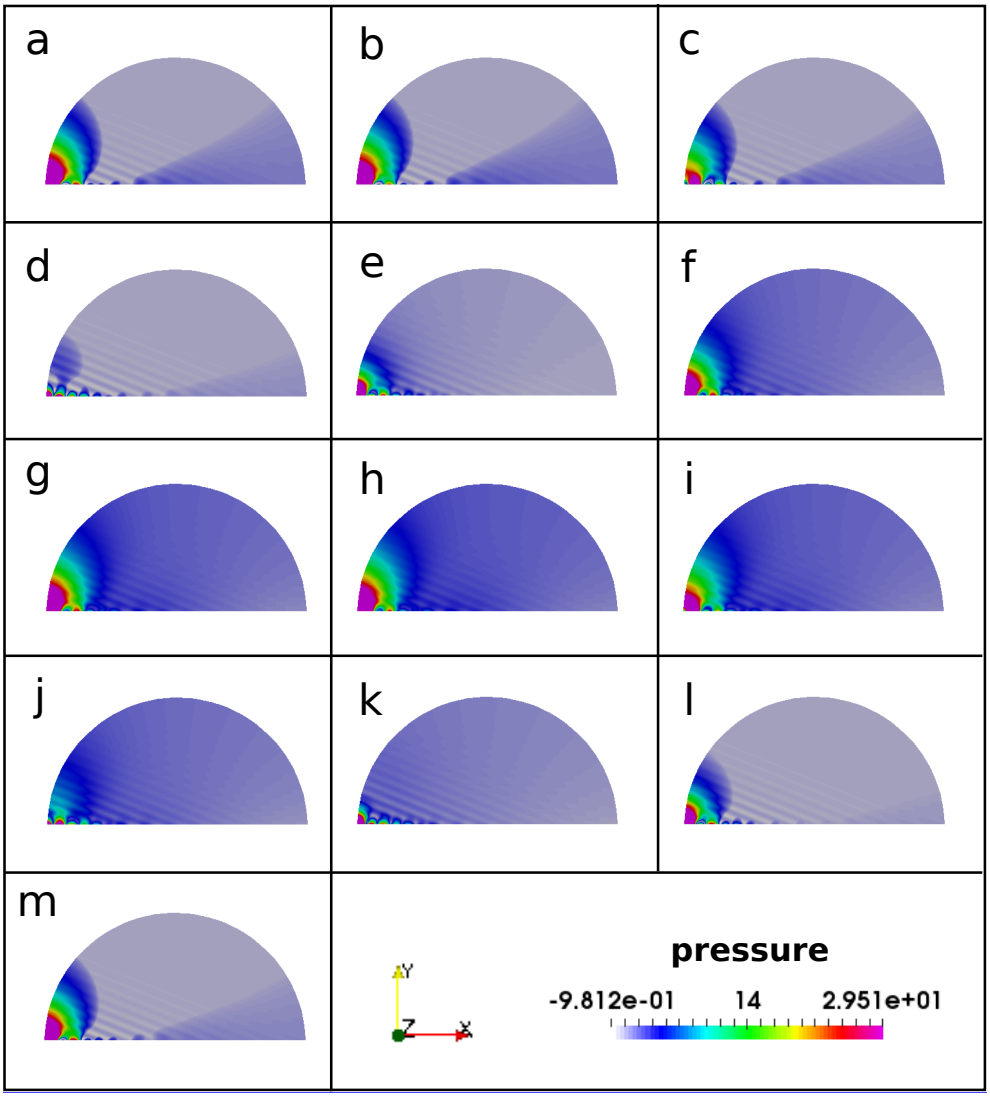

Figure 8.20: Total pressure field, X-Y plane view, propagation of 10MHz SAW beneath the micro droplet, 14 times larger viscosity than water. Total signal duration $= 0.1\ \mu s$

influx can be indicated by the acoustic radiation pressures and stress in Figures 8.27 and 8.26. It is noteworthy that the Rayleigh wave on the bottom interface moves faster than in the fluid, that is why waves propagate at an angle that is not perpendicular to the solid surface (Rayleigh angle). It is well known that the acoustic streaming (Eckart streaming) caused by the force is the spatial variation of the Reynolds' stress [195]. Consequently, the intensity of the driving force optimally depends on the strength of the wave attenuation / absorption power.

It is essential to understand the attenuation that arises as the frequency is increased as well as its relation to the bulk viscosity of the fluid. Consequently, the capillary waves on the droplet interfaces will appear in earlier time steps for Rayleigh waves with a shorter attenuation length, it can be observed as the propagation of acoustic waves to the top surface of the droplet within a certain time intervals. In other words, as the frequency increased, the acoustic energy reached

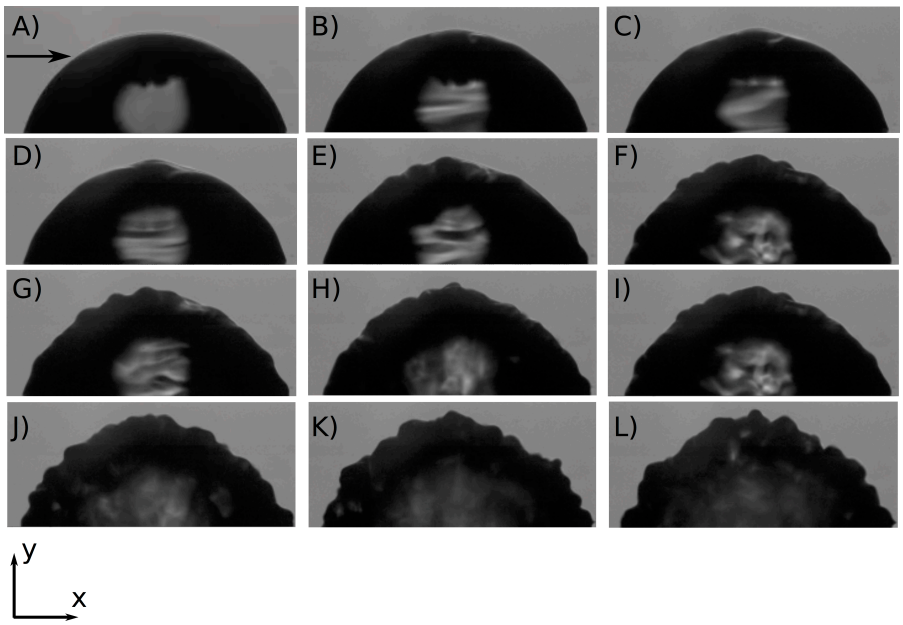

Figure 8.21: Side view of micro droplet sitting on an $LiNbO_3$ substrate impinged by 10MHz SAW generated from sine wave signal. Drop of 2 μL volume, power: 5 mW

the interface between fluid/ambient in earlier time steps and closer spatial position to the point of incidence. The above incidence might be related to the existence of coherent flow patterns inside the droplet. The increasing viscosity (low Reynolds number) of the fluid causes the gradual loss of symmetrical pattern from left to right, this observation corresponds with the experimental results shown in Figure 2 from [274]. Indeed, the increasing of frequency will boost the speed of SAW attenuation beneath the droplet, hence the evanescent bulk waves inside the droplet. The Rayleigh angle settled initially can be observed intuitively by the direction of acoustic radiation waves, it appears that the radiation force drives the flow to move toward one side of the droplet. To summarize, the asymmetric pattern of acoustic pressure might be the main reason to drive the droplet to move / jump (droplet displacement on substrate) in the wave propagation direction.

According to the article postulating the acoustic streaming phenomena incurred by leaky SAW [291], the circulation of acoustic energy inside the micro droplet is depicted in Figure 8.14. Since the material property of $LiNbO_3$ is neither absolutely sound hard nor soft ($\rho_s = 4650 kg/m^3$), its power of absorption attributes to the admittance coefficient in the model. Pertaining to both Figure 8.17 and 8.18, the acoustic pressure is traveling from both sides of the droplet, and inducing an acoustic pressure that constantly changes circularly in both horizontal and vertical directions. The reason that internal circulation occurs is because of the partially reflected waves from the interface between fluid-air and fluid-solid on the far field, the reverberated waves propagating in opposite direction of the leaky SAW such that internal acoustic streaming is formed inside the droplet. In Figure 8.21 the water droplet actuated by 10MHz SAW is shown, with 12 frames. The free surface of the droplet starts to destabilize and oscillate when the acoustic radiation pressures reach the top. In the frame B), capillary wave with large wavelength can be

visualized from the free surface. From Figure 8.21 C) to J), we can observe that the capillary waves are amplified with time until the droplet begins to deform and unpin from the substrate. The phenomenon of capillary waves (capillary frequency) increasing with time supports the fact that confined acoustic energies inside the droplet are streaming and reflected in different directions [305]. The shape of the droplet is deformed by the amount of acoustic radiation pressures reached at the free surface, as well as the bulk wave recirculation (acoustic streaming) within the drop cavity. Taken together, the future goal would be to estimate the exact time needed for capillary waves to reach the free surface of a droplet with specific size, which might coincide with the time required for the acoustic radiation pressure to reach the free-surface in numerical simulation. The contribution of acoustic radiation pressures to the acoustic streaming might exploit the mechanism underlying the physical phenomena of the droplet atomisation and jetting [258].

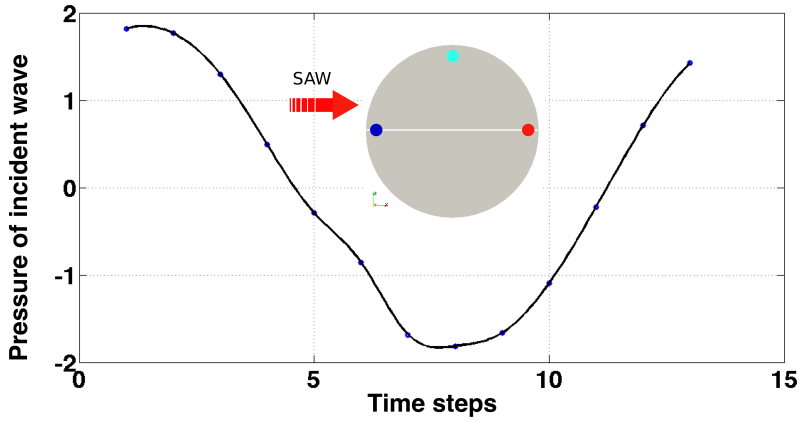

(a) real incident wave pressure on point A

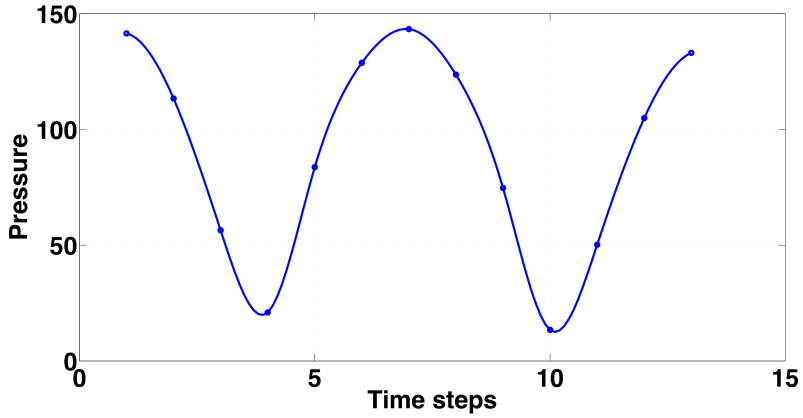

(b) total pressure on point A

Figure 8.22: Pressure of micro-droplet, 10MHz polychromatic sine wave, recorded on point A depicted in Figure 8.14 over 12 time steps. (a) real part of incident wave pressure on point A, (b) total acoustic pressure on point A. point A: blue dot, point B: red, point C: green

To gain further insight to the acoustic waves leaked into the droplet, the acoustic pressure has been recorded at points A, B and C at different discretized time steps.

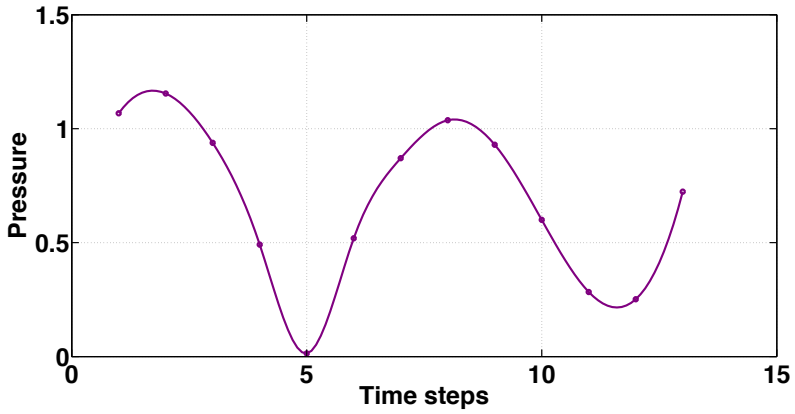

(a) total pressure on point B

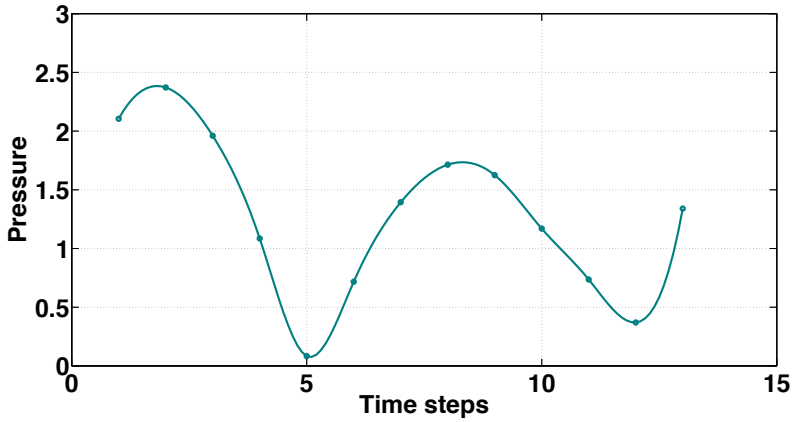

(b) total pressure on point C

Figure 8.23: Pressure of micro-droplet, 10MHz polychromatic sine wave, recorded on points B and C as depicted in Figure 8.14 over 12 time steps. (a) total acoustic pressure on point B, (b) total acoustic pressure on point C

In Figure 8.14, the approximate location of points A, B and C are shown. For simplicity, 12 discretized times steps are recorded within 0.1 μs . The total period of time steps includes one cycle of sine wave signal traveled through the droplet. Since the position of these points are opposite to one another, we expect to see how the reflected and refracted waves affect the propagation waves in terms of asymmetric pattern observed from the acoustic pressure distribution. Two wave pulses arrived one after another at all the observation points. However, at point A, the first pulse wave corresponds to the incident LSAW, and the second pulse wave, which has slightly smaller value, is due to a small amount of reflection from the right end of the drop. In contrast, the wave pulses retrieved at point B have a similar trend but in different phase, such that the first wave pulse on point B arrives later than waves on point A. In addition, the second wave pulse on point B is much smaller compared to point A, this is because of the waves are reverberated twice from both ends of the micro-droplet before arriving at point B. On the other hand, the wave pulses measured at point C exhibit identical behaviour at observation

point B, which indicates part of the transmitted waves travel circularly around the contact edge of the drop. To conclude, a possible explanation is that the internal circumferential streaming of fluid motion inside the droplets are the results of circulation and reverberation of Rayleigh waves.

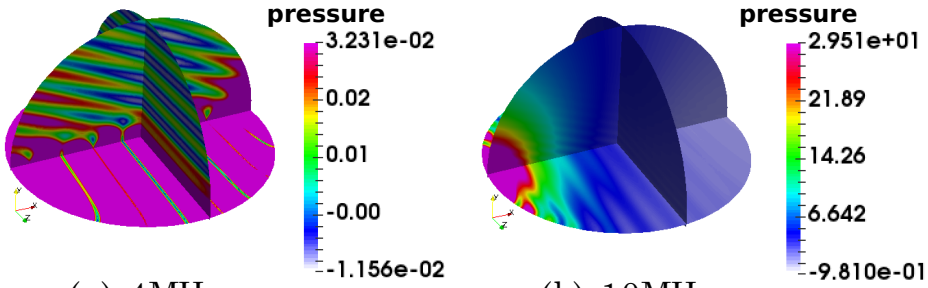

(a) 4MHz (b) 10MHz

Figure 8.24: Pressure of micro-droplet, 4, 10MHz polychromatic sine wave, at time step 1, X-Y, Y-Z, X-Z plane

On the other hand, in Figure 8.24, the cross sectional areas of X-Y, X-Z and Y-Z planes are shown. It is evident the acoustic pressure decays over a short range along the vertical direction from the solid/liquid interface, it coincides with the observation of the attenuation length inside fluids which are much shorter than along the horizontal directions [106]. The amount of acoustic radiation pressure reaching the droplet interface is responsible for the free surface oscillation (tiny deformations along the droplet top surface).

To completely understand the acoustic side of SAW interactions with a droplet, the time averaged acoustic stress is another key quantity. Figure 8.26 and 8.27 present the acoustic stresses derived from particle velocities inside the droplet. We can also see that the stresses from the far end of the droplet are much weaker when compared to the waves generated (reflected) near the interaction region. This imbalance becomes more perceivable with increasing frequency and it indicates that the droplet might be pushed forward in the direction of propagation. Predictably, the ARF and Reynolds' stress have been confined into small regions (within two wavelengths) around the first wave incident point at high frequency (10MHz), due to fast attenuation of sound waves. This phenomenon has been experimentally observed in [122]. According to experimental observations in [274], the increasing velocity of flow leads to asymmetric pattern of streaming, which are positively related to the number of viscosity, hence frequency. On the other hand, the Rayleigh wave with 4MHz appears slightly symmetric like structure due to weak attenuation and low frequency. Since the acoustic radiation stress acting inside the droplet is not symmetric, it explains the reason for the fluid parcel circulation occurring in the droplet. In essence, as pointed out earlier in this section, the acoustic pressure fields monitored at point C along the circumference are diffracted by waves travelling from opposite directions, this might be the cause for internal flow streaming and particle concentration occurring inside the droplet.

From Figure 8.27, we can observe the distribution of Von-Mises scalar of Reynolds' stress and acoustic radiation (AR) stress, such that the magnitude of the former has good agreement with the later in three different angles (X-Y, Y-Z, X-Z). Since

the AR stress is a scalar value, in order to compare it with the Reynolds' stress, we calculate the well known Von-Mises scalar from the six components of Reynolds' stress. The result of AR stress is smaller than Reynolds' stress following the theory of AR stress, such that the unsteady part of AR stress changes its values and direction between at each time step. In future research, the Reynolds' stress derived from acoustic pressures can be further employed as an input source stress term into the separated mechanical equations for microfludics.

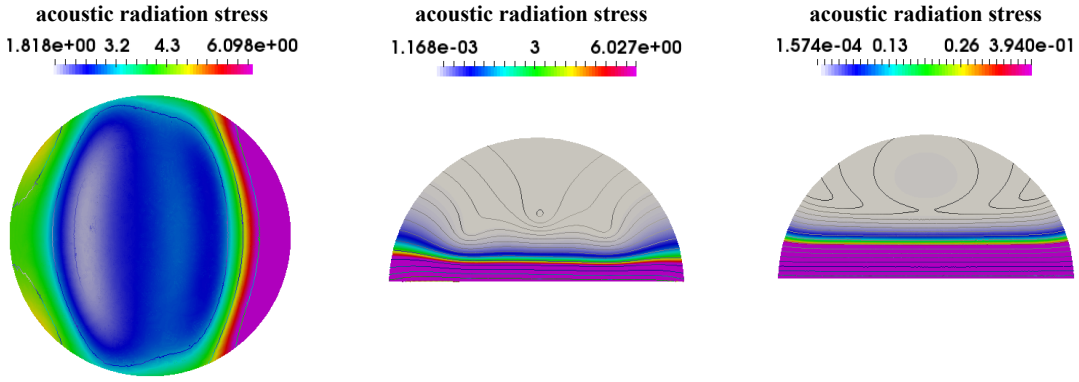

(a) Top view (b) X-Y plane (c) Y-Z plane

Figure 8.25: Acoustic radiation stress of micro-droplet [N], 4MHz polychromatic sine wave. Droplet size - radius = height = 2.1 mm. (a) Top view, (b) X-Y plane, (c) Y-Z plane

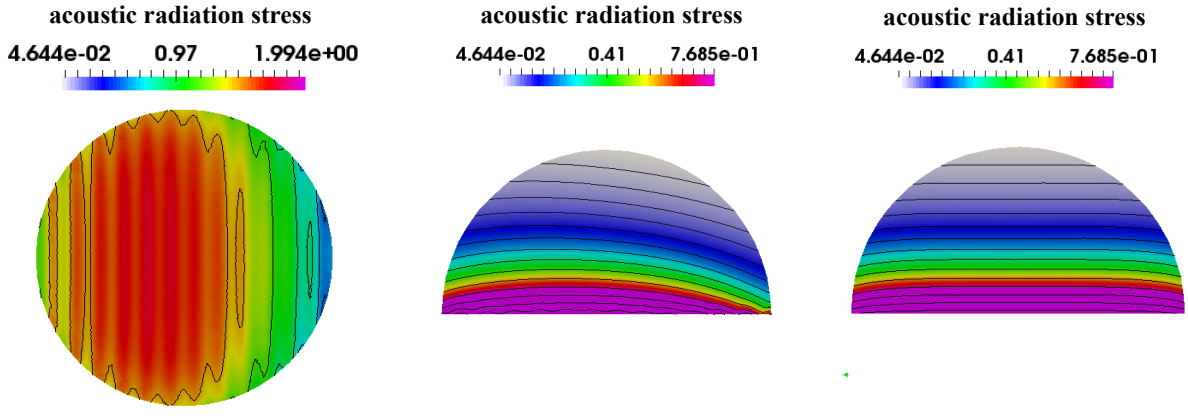

(a) Top view (b) X-Y plane (c) Y-Z plane

Figure 8.26: Acoustic radiation stress of micro-droplet [N], 4MHz polychromatic sine wave. Droplet size - radius = height = 0.525 mm. (a) Top view, (b) X-Y plane, (c) Y-Z plane

Overall, the distribution of acoustic pressure and velocities (stress) inside the droplet have good agreement with physical behaviour as expected.

In future study, the diameter D of the droplet and attenuation coefficient α can be varied, $D\alpha = 0.1, 0.5, 1.0$, etc.. as constants can be tested in order to distinguish

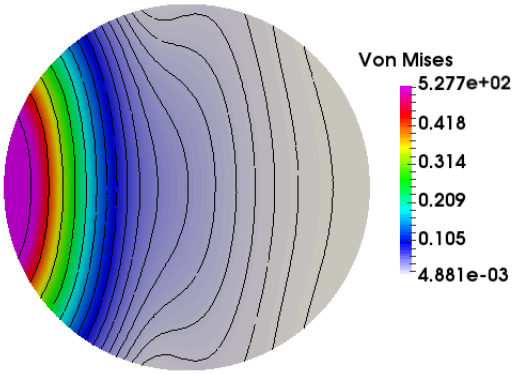

(a) Von Mises of σ_R top view

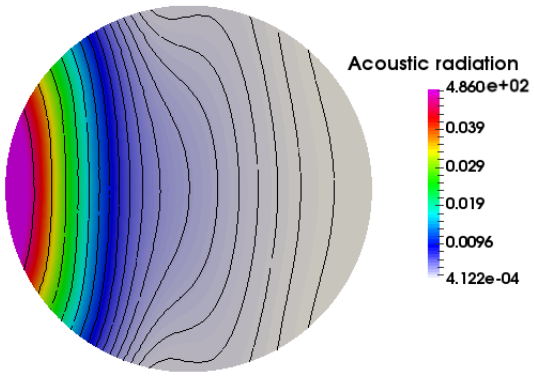

(b) σ_r top view

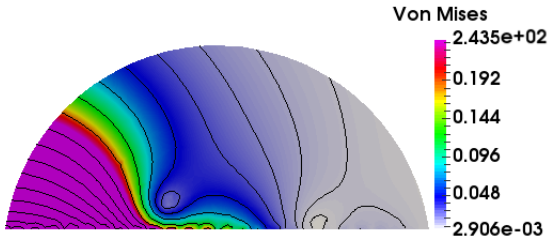

(c) Von Mises of σ_R X-Y plane

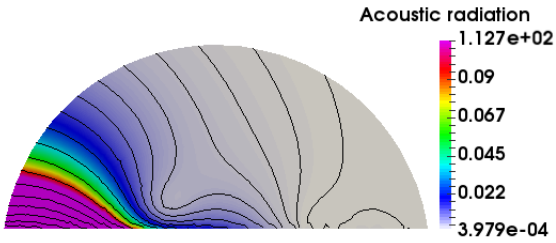

(d) σ_r X-Y plane

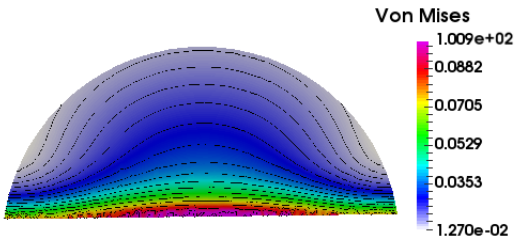

(e) Von Mises of σ_R Y-Z plane

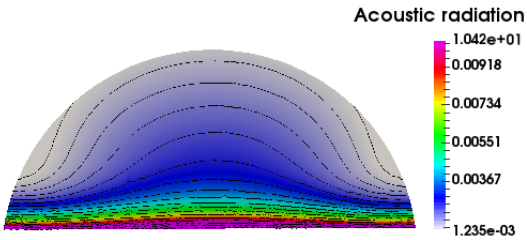

(f) σ_r Y-Z plane

Figure 8.27: Von-Mises of Reynolds' stress and acoustic radiation stress of micro-droplet, 10 MHz polychromatic sine wave [Pa]. (a), (c) and (e) top view, X-Y plane and Y-Z plane of Von-Mises of σ_{ij}^R. (b), (d) and (f) top view, X-Y plane and Y-Z plane of acoustic radiation pressure σ^r

the left-right symmetry of acoustic radiation pressures, and further deduce the relationship between acoustic streaming and droplet motion on substrate. The threshold value of the droplet diameter and the attenuation length might play an important role in the acoustic driving force. The attenuation length is equal to $\frac{1}{\alpha}m$.

8.4.4 SAW Propagating on Solid $LiNbO_3$ Substrate with Droplet

In this section, we will analyse the acoustic field on the substrate where the SAW propagates, both before and after impinging the droplet through Rayleigh angle, and transmitted into leaky SAW. The radius of the droplet is chosen to be always greater than λ_R which is the wavelength of Rayleigh wave subject to frequency as 0.0021m. The dimension of the substrate is adjusted to $2\lambda_{R_{4MHz}} \times 8\lambda_{R_{4MHz}} \times 15\lambda_{R_{4MHz}}$ which represents the height, width and length of a rectangular domain. These configurations assured the accuracy while maintaining computational efficiency. The substrate geometry is meshed with second order tetrahedrons (curvilinear tetrahedrons). The Rayleigh wave is propagating from left to right with IDTs placed at the far end along the positive x direction. The boundary conditions applied on truncated boundaries of the substrate are non-reflection BCs, where mixed boundary BC with leaky Rayleigh wave closed form is applied on the drop/substrate interface (substrate side).

The acoustic fields of the solution merely described the pressure vibration of the droplet despite being the focal point for acoustic streaming within the droplet cavity. The Rayleigh SAW propagating on the solid substrate behaves as a standing wave before it is incident on the liquid drop with some angle [20]. In Figure 8.28 and 8.29, the acoustic shadow region can be observed from the right hand side of the droplet such that the shape of droplet diffracted/absorbed the wave during propagation. This might be considered as one of the factors to placing multiple droplets on substrate in experiments, the second droplet closely behind the first one would not be actuated effectively by a SAW due to this absorption of power [299, 330]. On the other hand, the reflected waves from the left hand side of the droplet weaken the incoming SAW propagating in the x direction, which appears as sudden drop and jump as shown in Figure 8.29 left column(a) around coordinate $(-0.002, 0.001, 0)$ in front of the droplet. This is due to diffraction and absorption of the SAW behind the droplet. The reflected waves have a slightly different frequency from the incident wave, which appears as the beating phenomenon.

Moreover, the increasing frequencies decreased the amount of reflections that the interface of droplet/substrate stimulated. As shown in Figure 8.29 right column (b), most of the acoustic energies are absorbed by the droplet rather than reflected back.

In what follows, two experiments are analysed where mineral oil droplets ($2\mu l$ - $20\mu l$ respectively) were actuated by SAW on a X-Y cut LiNbO3 substrate. The vibration on the surface of the piezoelectric crystal were observed using a laser scanner vibrometer (Polytec UHF, Germany). Polydimethylsiloxane (a soft polymer) was deposited at the boundary of the substrate in order to prevent unnecessary reflections. The viscosity of the mineral oil is approximately 17 times higher than that of water. The IDT was fabricated by staff in the biomedical engineering group to exhibit a resonance at 10 or 20MHz respectively. The speed of SAW generated on the substrate was 4000 m/s, and the power was 15 dBm. Since the density of the oil (838 kg/m^3) is softer than water, the power absorbed by the liquid would be higher in the case of the oil than in that of the liquid, but only slightly so almost non-significantly. Oil was used to prevent evaporation as experiments can take days to complete. Extrapolating from the modelling results (Figures 8.30 and 8.31), al-

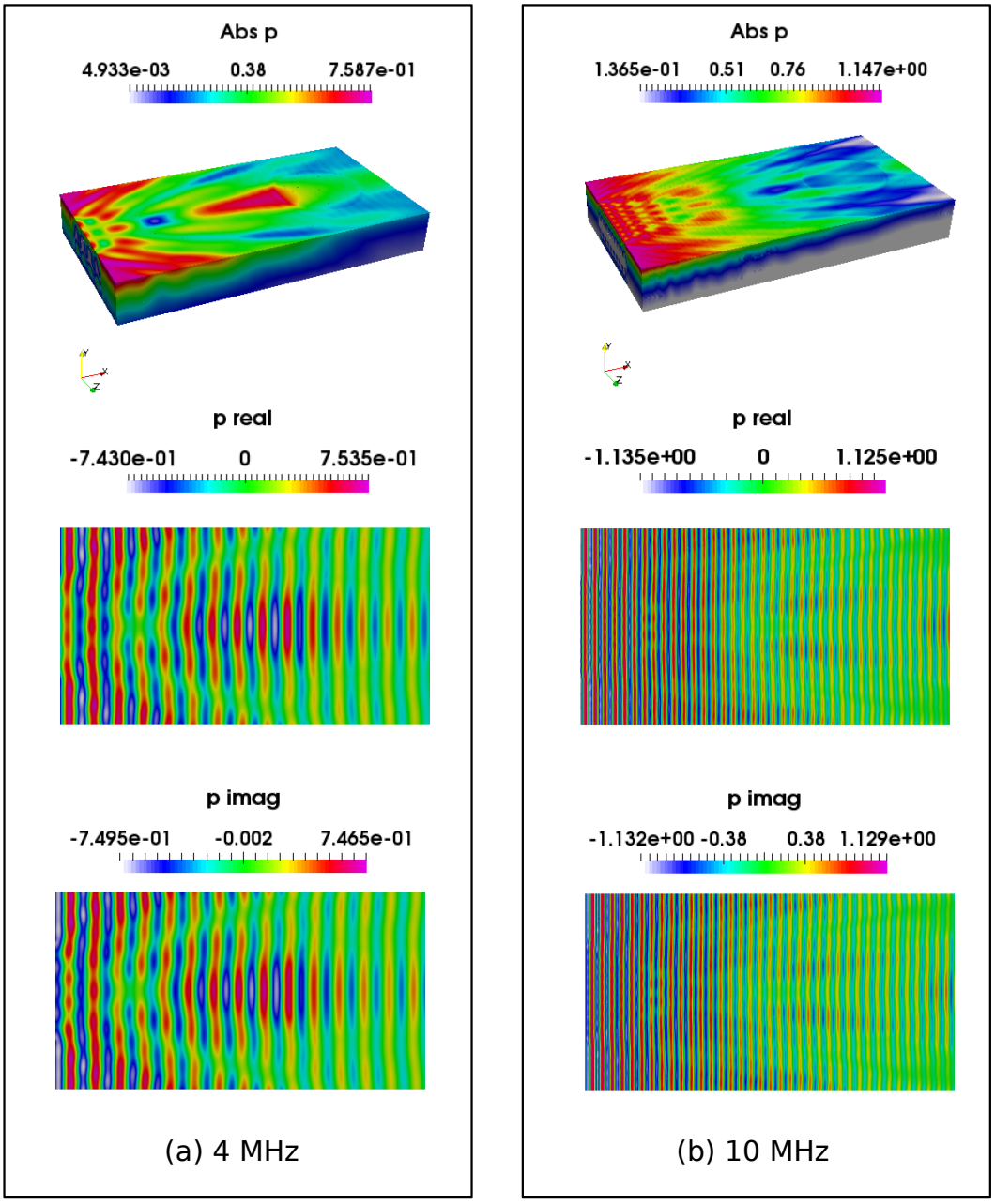

Figure 8.28: Total acoustic pressure fields on $LiNbO_3$ substrate. In(a) 4 MHz and (b) 10 MHz monochromatic incident waves, RF power of 0.2 mW, from side and top views

lows to make the hypothesis that multiple wave reflections should take place at the boundaries of the substrate and droplet as they are absorbing obstacles. As a result, a "shadow" region is expected directly behind the droplet, as an area with weak acoustic pressure. This attenuation of the leaky SAW is more pronounced for the higher frequency, as shown in Figures 8.30 and 8.31. Figure 8.30 shows a darker region, indicative of a lower amplitude of the vibrations. It should be noted that Figure 8.30 has a low resolution for wave signals due to limited amount of mesh points implemented for high frequency of 20MHz.

From Figure 8.31, it could be assumed that part of the Rayleigh waves is refracted

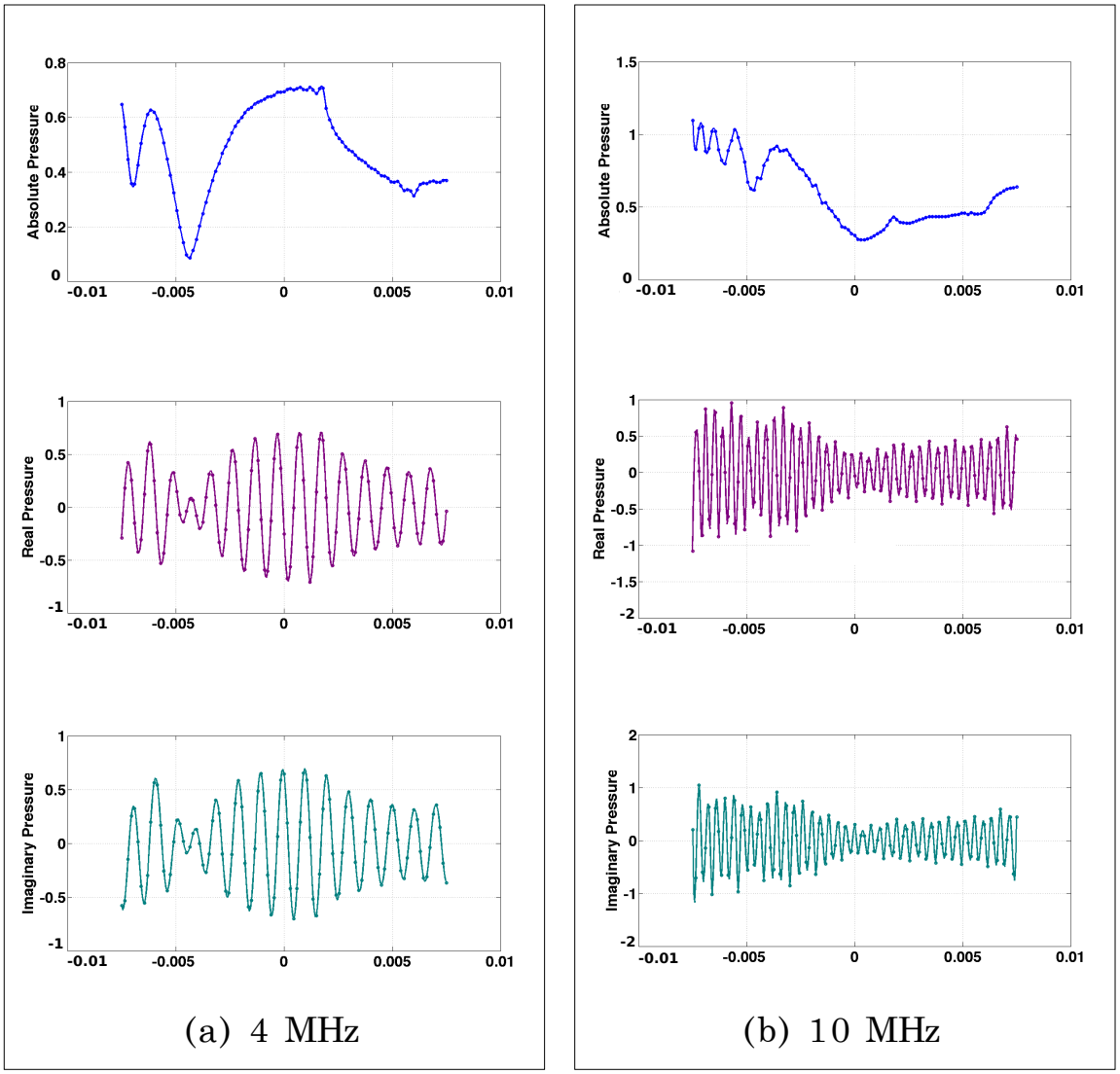

Figure 8.29: Total acoustic pressure fields (kPa) on $LiNbO_3$ substrate. In(a) 4 MHz and (b) 10 MHz monochromatic incident waves, RF power of 0.2 mW. plots over selected line along x axis for central z axis position, in the positive wave directions

into the liquid (with Rayleigh angle) since the waves behind the droplet, which would have travelled through, appear to have a smaller amplitudes. Comparing the results shown in Figure 8.31 (a), (b) and (c), it can be observed that bigger droplets absorb more than smaller ones, as seen from the pressure level behind the droplet on the substrate. Overall, these experimental results provide a qualitative confirmation of the numerical results, since experimental conditions could not be controlled as required.

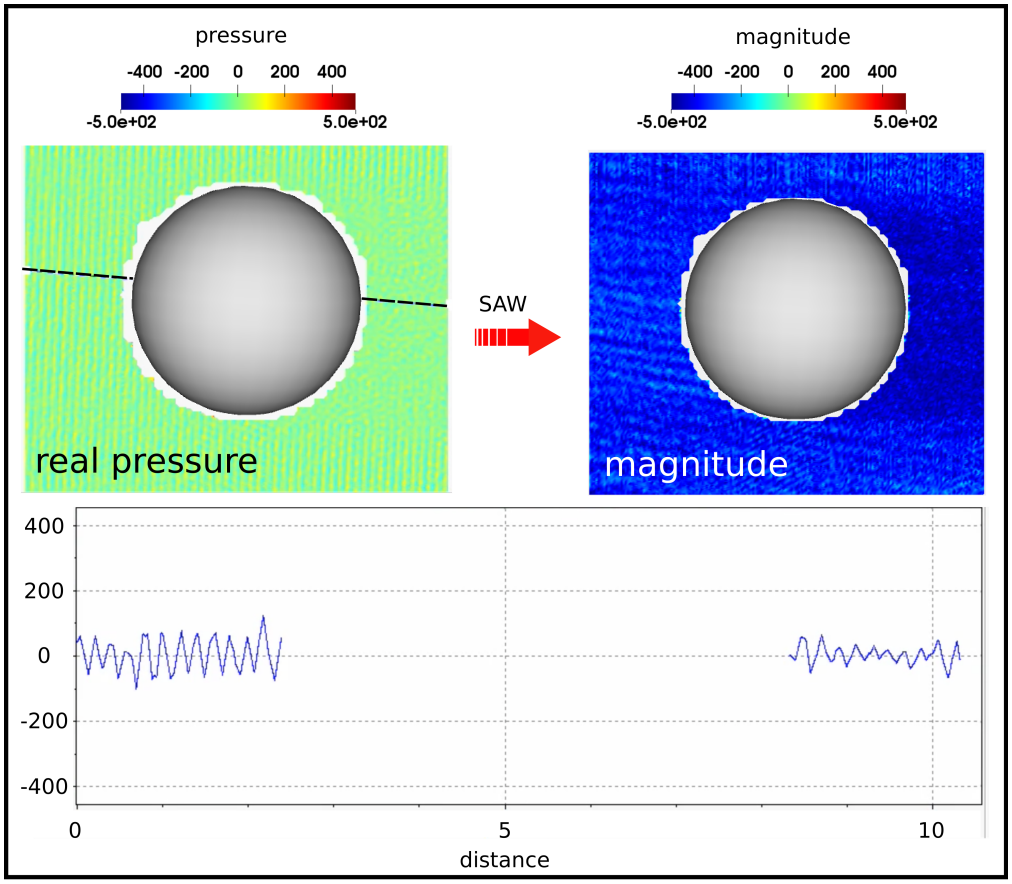

Figure 8.30: Real part of acoustic pressure fields and magnitude (Φ_{Abs}) on $LiNbO_3$ substrate (length of substrate = 0.0104m (10.4 mm)), 10 μl oil droplet. 20MHz SAWs with droplet. Top view, and amplitude along the cross sectional line of X-Z plane

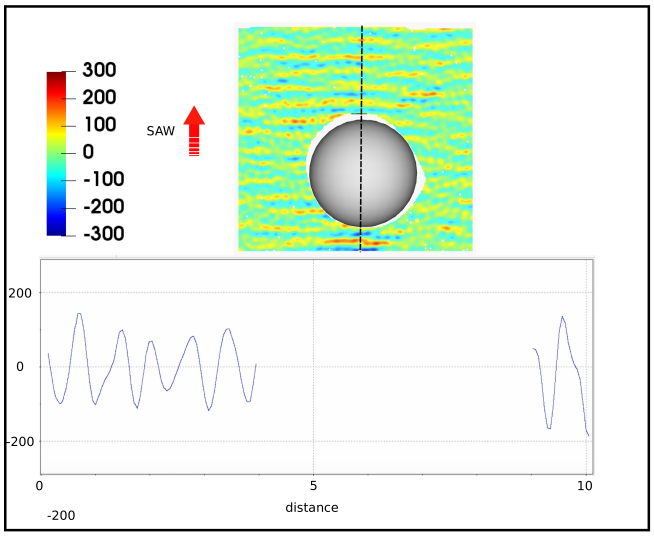

(a) 10MHz SAW, 20ul droplet

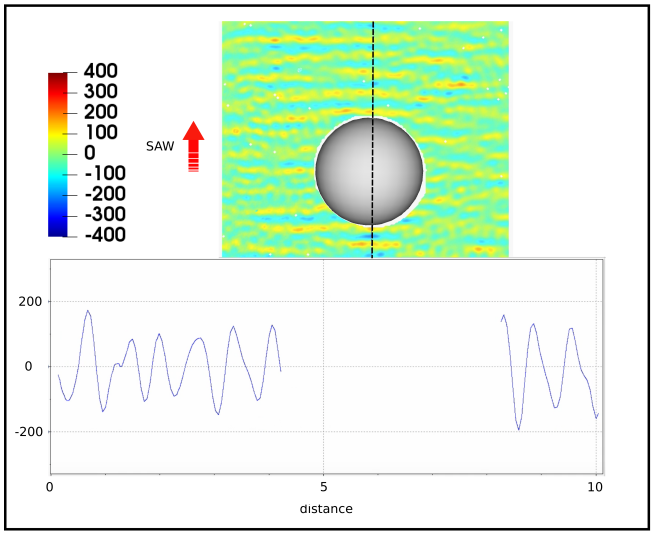

(b) 10MHz SAW, 10ul droplet

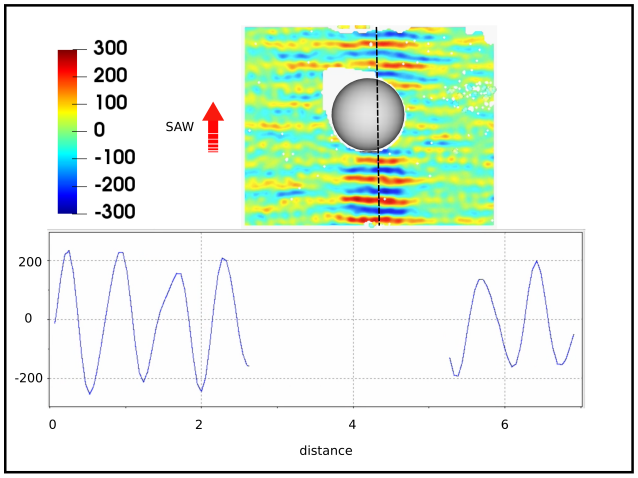

(c) 10MHz SAW, 2ul droplet

Figure 8.31: Real acoustic pressure fields on $LiNbO_3$ substrate (length of substrate = 0.00612m to 0.010m), oil droplet. SAW in positive Z direction. (a) 10MHz SAWs with $20\mu l$ droplet (b) 10MHz SAWs with $10\mu l$ droplet. (c) 10MHz SAWs with $2\mu l$ droplet. Top view, amplitude against distance traveled along the cross sectional line of X-Z plane

8.5 Concluding Remarks

In this chapter, a qualitative study has been conducted on the basis of LSAW driven micro-droplet application. The previously proposed hierarchical finite element method with automatic p adaptivity scheme is used. For the sake of interest, the viscosity, shape of the droplet, frequency and position of the droplet are varied in order to validate the effectiveness of measures on the mechanism of numerical experiments. The physical fields such as pressure and stresses are retrieved. As depicted in the numerical results, the leaky Rayleigh waves enter the bottom of the droplet at the Rayleigh angle while propagating on the solid/liquid interface. The displacement of the LSAW obeys the motion of Rayleigh wave and Snells law as mentioned in the literature [286]. The Rayleigh wave propagating on the solid/liquid interface is an attenuated progressive wave. Attenuation is influenced by wavelength and fluid viscosity. As a consequence, power is a function of space and time. Also, it can be noted that the acoustic streaming phenomenon and particle concentration/mixing process inside the droplet are affected by both the frequency and the shape of the droplet.

The closed solution of the Rayleigh wave for the solid in the time domain is translated to the frequency domain (by applying a Fourier transform), where for each harmonic of the truncated transform, the Helmholtz problem is solved in the micro-fluidic domain. In the post-processing stage, the solution can be converted back to the time domain using the inverse transform, enabling to calculate the unsteady acoustic radiation stress/pressure.

The resulting nonlinear force can be applied into the Navier-Stokes equation. This flow takes place in a much slower time scale as that of the propagation of the acoustic wave and triggers capillary wave propagation on the droplet surface, for example leading to nebulization, mixing processes and other phenomenon important for practical applications.

The flow velocities and particle displacements driven by acoustic radiation pressures (stresses) and vibration of surfaces are not explicitly dealt with within the current work. Additionally, the surface tension and resonance are similarly not taken into account. In future work, these physical quantities can be extended as model inputs and solved numerically. Consequently, the values of these parameters can be manipulated in order to compare the numerical solution with experimental results.

Chapter 9

Conclusion and Discussion

9.1 Summary

The present finite element modelling of acoustic problem on micro-scales with inhomogeneous media remains a challenging area due to its highly oscillatory nature and massive computational cost. The main objective of this research work is to develop a novel computational tool that enables a high frequency sweep acoustic application to be solved with accuracy and efficiency. Especially, it can provide the insight of acoustic applications in micro-fluidics subject to high frequency waves. The feasibility of such an acoustic solver is demonstrated throughout the entire thesis.

To be precise, first of all, a computational framework for monochromatic waves based on the hierarchical finite element method for the Helmholtz equation is described. The proposed computational method is implemented using high performance computing based on the distributed memory computer architecture with partitioned mesh, leading to an efficient code even for the vast amount of computational effort associated with multi-scale and multi-physics problems. The Helmholtz equation is solved on unstructured meshes, where the domain is discretized by the second-order tetrahedrons. The second-order tetrahedrons are then projected into tetrahedrons with arbitrary and heterogeneous order of hierarchical Legendre type polynomials in MoFEM. Hierarchical Legendre and Lobatto approximation basis are derived and implemented with L_2 and H^1 spaces. The accuracy and robustness of the proposed solver is examined by two and three dimensional benchmark problems with different geometries. The global and local relative errors are calculated from analytical solutions in hand. The proposed acoustic solver is then extended its scalability to time dependent polychromatic waves, from which arbitrary waves can be applied as input signals. Fourier transformations are applied to solve acoustic problems in the frequency domain, and projected to the time domain through inverse Fourier transformation. The detailed implementation procedures are explained in the main contexts.

In the current study, two types of hierarchical approximation basis as candidates

are compared, the total and factorisation memories required by the h & p adaptivities as well as the conditioning numbers of the global stiffness matrix have been retrieved and investigated thoroughly. Results show the hierarchical Lobatto basis together with generalized Duffy transformation yields the best conditioned system, and further reduces the assembly time of the global system matrix. In finite element calculation, the increasing of the polynomial order or frequency does not necessarily result in worse problem conditioning or increased factorization memory.

In the preceding chapters we argued that improving the solution quality by increasing the approximation order with hierarchical Lobatto and Legendre basis is more efficient than making the mesh denser in the sense of accuracy and computational resources for acoustic problems. Various numerical assessments are then performed on three benchmark problems, with performance measures such as: number of DOFs, number of non-zero entries, required memory, computational time, relative error in different norms. The results suggested the hierarchical Lobatto approximation basis together with generalized Duffy transformation and Field split / Block solver preconditioning are the best combination in the current solver. This kind of acoustic solver with p adaptivity has practical importance since, in industrial applications, problems with high frequency sweeps are considered and it will be extremely expensive to refine the mesh within each frequency and create a large number of meshes. In contrast, we solve acoustic problems with an initial coarse mesh, and enrich the approximation basis at each frequency and elements individually.

The merits of parallel computation over single processor finite element computation are examined. The features of the partitioned mesh are stored and retrieved between interfaces of MoFEM and MoAB, and the MPI library is employed for inter processor communication. Moreover, the PETSc enables creation, assembly and calculation of both sequential and parallelized system matrix and right hand side vectors. The parallel computation code significantly reduces the computational costs with increasing number of processors (up to 7 processors depend on the current computational resources and the problem size). This fact is validated by various measures like speedup, efficiency and total computational time, etc. on solving benchmark problems. The scalability and flexibility of paralleled computation with partitioned mesh and Field split / Block solver preconditioning are also demonstrated, where Field split / Block solver preconditioning halves the size of the original matrix required to be factorized.

Furthermore, the significance of the pollution error and its measurements are also demonstrated with three-dimensional problems. the pollution error caused by phase shift / lag is accumulated on the computational domain along the propagation direction, which can be partially mitigated through local mesh refinement techniques.

The unified approach of the acoustic solver in MoFEM enables the user to retrieve the acoustic potential, pressure field, velocity fields and acoustic stress simultaneously. In addition, various boundary conditions can be applied based on user's preferences in order to facilitate and construct arbitrary physical applications.

The difference between *a priori* and *a posteriori* error estimates are discussed in detail. Traditionally, the error estimation techniques measure the global error as

a whole. Nevertheless, the error estimates that measured the specific quantity of interest is goal-oriented which allowed the construction of adaptivity schemes with numerous reductions in computational efforts, in particular, when the information of actual error is obtained *a priori* to calculations. Pertaining to the demand of efficient adaptivity scheme for solving high frequency acoustic problems, an object oriented *a priori* error estimator has been derived and implemented with both hierarchical Lobatto basis and generalized Duffy transformation, in order to take the advantages of the computational efficiency from hierarchical approximation basis.

Essentially, this novel type of *a priori* error estimator is derived from solving a lower dimensional acoustic problem with the identical properties as its original problem. In the assumption, the error obtained from solving a higher dimensional acoustic problem is related to the error derived from its lower dimensional images. The predicted error on each element is then exploited as an error estimator to guide the local automatic p adaptivity scheme, assigning an appropriate order to each element entity. This type of *a priori* error estimator is firstly introduced by Prinn in [256]. The accuracy and efficiency of the proposed automatic adaptivity scheme are then tested with numerical examples. It promised to keep the actual error upper and lower bounded, while also controlling the pollution error within satisfied frequency ranges.

Since most of the practical acoustic applications with mixed boundary conditions are resolved in convex-like domains or meshes with curvatures [312, 188], we take our numerical test on three dimensional problems such as plane / spherical wave impinging on a sound hard / soft sphere, both mixed BC and sound hard BC are encompassed in the domain. Although the *a priori* error estimator does not account for pollution effect [123], it enables the control of the pollution effect within the frequency limit when increasing the length of the propagation path. Results have shown the automatic p adaptivity scheme based on the *a priori* error estimator outperforms h and p adaptivity schemes in every aspects, while maintaining the predefined error level within a certain frequency band. This finding is validated by different performance parameters. To summarise, numerical results encouraged the efficient time dependent acoustic solver to be applied in practical physical applications.

Finally, the numerical experiment of actuation of a micro-droplet sitting on an $LiNbO_3$ substrate is solved by the proposed solver, which gives us the required acoustic fields without solving a solid-fluid coupling problem. The speed and performance of the algorithm is optimised through numerical techniques. A computational framework for polychromatic waves and arbitrary signal based on the time harmonic wave equation is described for microfluidic applications. A closed form of Rayleigh wave is imposed as a mixed boundary condition on the boundary of the droplet. Consequently, the acoustic pressure exhibits the desired pattern as expected, the Rayleigh angle and the acoustic driving force can be visualized through numerical simulation. It partly explains the acoustic streaming phenomena occurring in experiments. Moreover we calculated the components of the acoustic stress and radiation forces inside the droplet cavity subject to leaky SAWs. The calculated non-linear body force can be further applied into the Navier-Stokes equation as an input source.

9.2 Original Contributions

- Assessed the performance of parallel computational higher order hierarchical finite element method with acoustic benchmark problems in the frequency domain. The efficiency and conditioning of Lobatto and Legendre type approximation bases are demonstrated. A great reduction of computational cost is detected through using the p adaptivity when compared to h adaptivity, this is proved by measurements like computational memory, factorisation memory, calculation time, and relative errors.

- A polychromatic wave acoustic solver is developed and implemented. The polychromatic wave acoustic solver is designated based on the Helmholtz equation solved in the frequency domain, where an arbitrary shape of wave can be applied as an input signal. The input wave is decomposed into the frequency domain through Fourier transformation and solved by the Helmholtz equation. Then the numerical solutions in each time step are transferred back to time domain through inverse Fourier transformation. The merits of the polychromatic acoustic solver are not only to boost the speed of solving time dependent acoustic problem with accuracy and efficiency, but also enables the unsteady wave solution to be obtained.

- A novel *a priori* error estimator is implemented and extended to three dimensional spherical exterior boundary value benchmark problems. The solution of the Helmholtz equation can then be found with a predefined level of accuracy, and the accuracy is sustained over a wide range of frequencies. In addition, the pollution error has been controlled within the predefined frequency ranges. The automatic non-uniform p adaptivity scheme is thus developed based on the *a priori* error estimator. A significant improvement in terms of accuracy and efficiency of proposed automatic p adaptivity scheme over the uniform h and p adaptivities is demonstrated by comparison of the numerical accuracy and cost.

- Investigated the application of microfludics subject to high frequency surface acoustic waves. Due to the relatively large characteristic length of the computational domain compared to the wavelength associated with MHz range waves, the attempts of solving an acoustic problem in a droplet actuated by high frequency SAWs generally leads to prohibitive computational times and resources. This issue is partly tackled by the implementation of the developed polychromatic wave solver with automatic p adaptivity. In the assumption of a Rayleigh wave propagating on substrate / droplet interface suffers from inconsistency of phase velocities, the speed of wave travelling on substrate is much faster than in the fluid. The leaky Rayleigh wave is characterised as a progressive wave. As well as the assumption on the boundary condition of the droplet, the closed form of the Rayleigh wave can be applied as a mixed boundary condition on the interface. A new formulation of the progressive Rayleigh wave is solved by the polychromatic acoustic wave solver. Hence, the Helmholtz problem is solved instead of a coupled time dependent large acoustic problem with a discontinuity across the droplet / substrate interface. The use of the polychromatic wave acoustic solver enabled an accurate description of the acoustic field inside a microfluidic droplet whilst circumventing the re-meshing associated with uniform adaptivities in each time step.

Consequently, the complex simulation can be performed on a desktop computer. The numerical solution is compared and discussed qualitatively with the experimental results and analysis by other researchers.

9.3 Recommendation for Future Works

The present work can be extended in the future to the following directions:

- In this thesis, the numerical accuracy of benchmark problems implemented and solved depends on the boundary conditions applied. In order to eliminate the minor effects of inexactness caused by numerical non-reflecting boundary conditions (NRBCs), a better conditioned formula than BGT can be incorporated. For example, an exact BC such as Dirichlet to Neumann (DtN) condition can be implemented, it can provide better accuracy than the approximate NRBCs. Alternatively, the analytical solution can be obtained and applied on the exterior boundary as a Robin type BC for the benchmark problems [206]. However, there is always a trade-off between accuracy and efficiency associated with sophisticated BCs. The computational time required for DtN operator are slightly higher than approximate NRBCs, because of its non-local nature. Furthermore, the geometry description of the problem can be improved by implementing subdivision surface, NURBS, or using higher order polynomial to represent geometry, etc. [293].

- Although the generalized Duffy transformation coupled with the Gauss-Legendre quadrature rule are implemented and hardcoded into our acoustic solver, the effectiveness of solving singular Helmholtz operator with this method has not yet been verified.

- Despite the robustness of tetrahedral elements, other type of hierarchical elements are also available with the current acoustic solver in MoFEM. Indeed, investigation on prismatic and pyramid elements along with their performance on acoustic solver are of interest.

- The *a priori* error estimator and automatic p adaptivity scheme are designed for fast frequency sweep problems. The automatic p assignment would allow users to create an initial coarse mesh with *a priori* knowledge in hand, and enrich the mesh separately depending upon the frequency of time steps.

- Hybrid element combined Trefftz method (PUFM) and hierarchical approximation basis might be an enlightened future research direction.

- Demkowicz and Gopalakrishnan [119] exhibited the ultra weak form adopted with DPG method, and proved the optimality of the method applied on Poisson equation. In addition, error estimates in terms of h & p are identified. At last, uniform h refinement, h adaptivity and p adaptivity based on error residual are tested, the element error estimator extracted from element residual delivers exponential convergence rate for 2D Poisson equation. In [82] the authors proposes a simple *a posteriori* error estimator based on the

ultra-weak formulation of linear system of equations, the Raviart-Thomas element in natural pair of space ($H(div, \Omega) \times L_2(\Omega)$) and example function of Elliptic Poisson equation are demonstrated. Proposed error estimator has both upper and lower bounds, its robustness are elucidated analytically in details. Since the nature of the error estimator, it can be parsed in case of Helmholtz equation with Hierarchical basis as well, which will be given in future research. Furthermore, there is also an *a priori* error estimator based on the L_2 projection of right hand side term of conservation equation [128].

Further on this, *a posteriori* error estimator can be derived with two additional terms: the error from the jumps on the inter-element boundaries, and the error of the gradient of solution. The summation of these three terms gives a comprehensive and reliable measurement on the actual error. These types of error estimators have a stringent mathematical foundation and strictly bounded.

- Although the proposed *a priori* error estimator does not include the pollution effect [123], it can no doubt alleviate the dispersion error aliased by increasing the domain length efficiently within the frequency band. In the presence of mesh limitation, the actual relative error converges to the predefined error level. Overall, the *a priori* error estimator assessed in this report is flexible and robust, also simple to implement, while computationally inexpensive. The current configuration for *a priori* error estimate is to predict the error in one dimensional mirror image acoustic problem. However, since the predicted error information are hardcoded without additional computational costs, it is feasible to solve a two dimensional acoustic problem with better similarities to the original problem, and store the p order related to the predicted error with respect to mesh resolution and frequencies. It is believed that it will further improve the accuracy of the solution.

  In past work, there was a vast amount of error estimators with solid and rigorous mathematical backgrounds, some of them have been discussed in the Appendices. It is essential to compare them with the existing error estimators by solving identical benchmark problems, thus the optimal combination can be decided.

- The *a priori* error estimator could encompass the propagation direction as another parameter to adjust the predicted error along the propagation direction. The length of propagation path is one of the crucial facts that affects the pollution error. Hence, this might be a way to actually include the pollution error in the adaptivity scheme.

- This is an ongoing area of research. In our implementation of polychromatic wave Helmholtz equation, there are methods that might work to refine the time steps in temporal domain, such as interpolation of Fourier Transformation with particular window function. The goal is to sustain the computational cost while increasing the frequency resolution.

- Finally, the incompressible Navier-Stokes equation can be solved based on the results of acoustic stresses / radiation forces inside a micro-droplet cavity, its acoustic streaming behaviour under high frequency signals remain to be tackled. The interested quantities include fluid velocity and its associated flow pattern. On the other hand, for the acoustic phenomena occurring inside the

droplet and on the substrate, the relative weight (portion) of contribution from droplet scale (height, radius), signal type and frequency are of interest and remains un-tackled. The asymmetry pattern of radiation force and acoustic velocity inside droplets are one of the key factors required to understand the jumping and jetting motions of droplets. Further studies will be conducted on the fluid topology and shape of movements of droplets affected by these factors mentioned above. Further to that, there is a lack of experimental specimens in order to compare the numerical results with experimental outcomes and data.

The next challenges lie, for instance, in the many variation of combinations with different configurations, including substrates, IDTs, micro-drops. The future goals are to provide further insight on the design of valuable tools for basic science and improving the functions of acoustic diagnostic device committed to human health. The highlighted issues founded during our research required in-depth work and improvement on the methodology.

Appendices

Appendix A

Mathematical Definition

A.1 Spaces and Norms

In this section the important definitions and properties of various spaces and norms will be briefly discussed, we will frequently use them as the measure of error or the solution spaces in the main contexts. For details of the mathematical definitions in finite element approximation, please see "the mathematical theory of finite element method" [83].

A.1.1 $\mathbb{C}^k$ Spaces

The space contains all the functions that are continuous and k times differentiable are denoted as $\mathbb{C}^k$ spaces. In special cases, $\mathbb{C}^0$ denotes all the continuous functions, C^∞ indicates the infinite differentiable smooth functions.

Definition of Norms:

i. $\|v\| \geq 0 \ \forall v \in V \ \|v\| = 0 \longleftrightarrow v = 0$

ii. $\|a \cdot v\| = |a| \, \|v\| \ \forall a \in \mathbb{R}, v \in V$

iii. $\|v + u\| \leq \|v\| + \|u\| \ \ \forall v, u \in V$

A.1.2 Lebesgue Spaces and Relative Norms

The domain Ω is a Lebesgue measurable subset of $\mathbb{R}^n$ with non-empty interior. If a real-valued function $q(x)$ is Lebesgue measurable, then

$$\int_\Omega q(x)dx \tag{A.1}$$

exists, where $\int$ is the Lebesgue integral of function q, and dx is the Lebesgue measure (For details, see Bartle [60]). Assume $1 \leq p < \infty$, we can then defined the L^P space and norm as the following:

$$L^p(\Omega) := \{q : \|q\|_{L^p(\Omega)} \leq \infty\} \tag{A.2}$$

$$\|q\|_{L^p(\Omega)} := \Big(\int_\Omega |q(x)|^p dx \Big)^{1/p} \tag{A.3}$$

for any function ψ belong to the Lebesgue spaces is also denoted as Lebesgue integrable. If $p = 2$, and for $\psi \in L_2(\Omega)$, we have the following scalar product:

$$(\psi, \phi) = \int_\Omega \psi\phi \, d\Omega \leq \infty \tag{A.4}$$

where in special cases $p = 1$ and $p = \infty$, we have:

$$\|q\|_{L_\infty(\Omega)} := ess\, sup\{|q(x)| : x \in \Omega\}^1 \tag{A.5}$$

$$\|q\|_{L^1(\Omega)} := | \int_\Omega |q(x)| dx| \tag{A.6}$$

where *ess sup* indicates the essential supremum. There are several definitions holds for the functions in the L^p space which we will use in the following chapters:

Definition : **(Minkowski's Inequality)** For $1 \leq p \leq \infty$ and $q, f \in L^p(\Omega)$, we can say that:

$$\|q + f\|_{L^p(\Omega)} \leq \|q\|_{L^p(\Omega)} + \|f\|_{L^p(\Omega)}$$

Definition : **(Hölder's Inequality)** For $1 \leq p \; k \leq \infty$ such that $1 = 1/p + 1/k$, in addition, if $q \in L^p(\Omega)$ and $f \in L^k(\Omega)$, we therefore can say that:

$$\|qf\|_{L^1(\Omega)} \leq \|q\|_{L^p(\Omega)} \|f\|_{L^k(\Omega)}$$

Definition : **(Cauchy Schwarz' Inequality)** This is simply the strong version of **Hölder's Inequality**, in the sense that $p = k = 2$, for q, $f \in L_2(\Omega)$ and $qf \in L^1(\Omega)$, we have that:

$$\int_\Omega |q(x)f(x)| dx \leq \|q\|_{L_2(\Omega)} \|f\|_{L_2(\Omega)}$$

[1]The precise definition: $\|q\|_{L_\infty(\Omega)} = inf\{M > 0 : |f(x, y)| \leq M \; a.e. \text{ in } \Omega\}$ except a set of measure zero

A.1.2.1 Banach Space

A normed vector space $(V, \|\cdot\|)$ is called Banach space, if and only if it is complete which means every cauchy sequences in V are converging to an element in V. This space is named after the Polish mathematician Stefan Banach for his contribution works [56]. Here we should noticed that the Cauchy sequence has the property: $\|v_i - v_j\| \to 0$ as $i, j \to \infty$. If V is complete, then there exists $v \in V$ such that $\|v - v_j\| \to 0$ as $j \to \infty$.

Weak Derivatives: Let us define a multi index, say α is an n-tuple of non-negative integers α_i, the length of α is denoted by

$$|\alpha| := \sum_{i=1}^{n} \alpha_i. \tag{A.7}$$

for function $\psi \in \mathbb{C}^p$ the partial derivatives are given by

$$D^\alpha \psi;\ D_x^\alpha \psi;\ D_y^\alpha \psi;\ \frac{\partial}{\partial x}\psi. \tag{A.8}$$

where $|\alpha|$ means the order of the derivatives.

Definition :(Compact Support) Let Ω be a domain in $\mathbb{R}^n$. It is indicated by $D(\Omega)$ or $\mathbb{C}_0^\infty(\Omega)$ the set of $\mathbb{C}^\infty(\Omega)$ functions with compact support in Ω.

Any given function has compact support means its support is a compact set. A "*support*" of a function is given by:

$$Supp(f) := \{x \in X | f(x) \neq 0\}. \tag{A.9}$$

And "*compact set*" is defined as: For an open cover of the subset S, $\{U_j\}_{j\in J}$, we have $S = \underset{j\in J}{\cup} U_j$, there exists a finite subset I of J such that $S = \underset{i\in J}{\cup} U_i$. Further more, we have:

Definition :(Locally Integrable) Given a domain Ω, the set of "locally integrable" functions is defined as:

$$L^1_{loc}(\Omega) := \{q :\ q \in L^1(S)\ \forall \text{ compact set } S \subset \text{interior of } \Omega.\}$$

Definition :(Weak Derivative) There exists a *weak derivative*, $D_\omega^\alpha q$ of a given function $q \in L^1_{loc}(\Omega)$, if and only if there is another function $f \in L^1_{loc}(\Omega)$ defined as:

$$\int_\Omega f(x)\psi(x)dx = (-1)^{|\alpha|} \int_\Omega q(x)\psi^{|\alpha|}(x)dx \text{ for } \forall \psi \in D(\Omega)$$

if such function f exists, then we can say that $D_\omega^\alpha q = f$

Lemma A.1.1 *Suppose α is an arbitrary integer, and function $\phi \in \mathbb{C}^{|\alpha|}(\Omega)$. Thus, the weak derivative $d_\omega^\alpha \phi$ of function ϕ exists, and it is denoted by $D^\alpha \phi$*

A.1.2.2 Sobolev Spaces

Sobolev spaces are named from the Russian mathematician Sergei Sobolev [230], its norm are the combination of the function itself and its derivatives up to a certain order in the L^p norms, we will explain it in details:

Definition : Let k be any non-negative integer, and q be arbitrary function that satisfied $q \in L^1_{loc}(\Omega)$. Let the weak derivatives $D^\alpha_\omega q$ exist for all $|\alpha| \leq k$, then the Sobolev norm is defined as:

$$\|q\|_{W^k_p(\Omega)} := \left(\sum_{|\alpha| \leq k} \|D^\alpha_\omega q\|^p_{L^p(\Omega)} \right)^{1/p} \tag{A.10}$$

for $1 \leq p \leq \infty$, in the special case for $p = \infty$, we have:

$$\|q\|_{W^k_\infty(\Omega)} := \max_{|\alpha| \leq k} \|D^\alpha_\omega q\|_{L_\infty(\Omega)} \tag{A.11}$$

Overall, the definition of Sobolev space is:

$$W^k_\infty(\Omega) := \{q \in L^1_{loc}(\Omega) \ : \ \|q\|_{W^k_\infty(\Omega)} < \infty\} \tag{A.12}$$

Theorem A.1.2 . *The Sobolev space $W^k_\infty(\Omega)$ is also a Banach space.*

Proof : See Brenner, Susanne C and Ridgway Scott [83].

Lemma A.1.3 *Suppose there is an arbitrary domain Ω, for k and n are non-negative integers satisfied $k \leq n$, furthermore, p is any real number such that $1 \leq p \leq \infty$. Then, we can say that: $W^n_p(\Omega) \subset W^k_p(\Omega)$.*

Lemma A.1.4 . *Suppose there is a bounded domain Ω such that k is a non-negative integer, p and g are real numbers satisfied $1 \leq p \leq g \leq \infty$. Hence, we can say that: $W^k_g(\Omega) \subset W^k_p(\Omega)$*

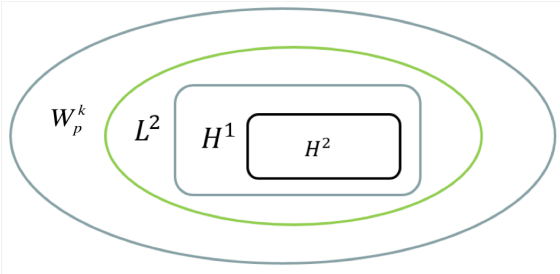

Figure A.1: Relationship between various spaces

The above Figure A.1 gives rigorous relationship between different spaces which will be frequently used in the thesis.

A.1.2.3 Lipschitz Space

Lip$(\Omega) = \{q \in L_\infty(\Omega) : \|q\|_{Lip(\Omega)} \leq \infty\}$ where $Lip(\Omega) = W_\infty^1(\Omega)$ with equivalent norms.

Definition :**(Lipschitz domain)** Let the domain Ω be an open and bounded subset of $\mathbb{R}^n$, it is called *Lipschitz domain* if its boundary $\partial\Omega$ is *Lipschitz boundary*. If there exists a collection of open sets O_i, a parameter $\epsilon > 0$, such that $\forall x \in \partial\Omega$ the ball with radius ϵ centred at x is contained in some O_i. Furthermore, there are no more than M sets of O_i intersect with each other nontrivially. In addition, $O_i \cap \Omega = O_i \cap \Omega_i$ where Ω_i is a domain whose boundary is a graph of the Lipschitz function ϕ_i satisfied $\|\phi_i\|_{Lip(\mathbb{R}^{n-1})} \leq M$, for a finite number M. For instance, $\Omega_i := \{(x, y) \in \mathbb{R}^n : x \in \mathbb{R}^{n-1}, y < \phi_i(x)\}$.

A.1.2.4 Hilbert Space

Definition : Suppose $(V, (\cdot\,, \cdot\,))$ is an inner product space, if its corresponding linear norm space $(V, \|\cdot\|)$ is complete, we can say $(V, (\cdot\,, \cdot\,))$ is a **Hilbert space**. In addition:

$$H^k(\Omega) \stackrel{\text{def}}{=} W_2^k(\Omega) \tag{A.13}$$

which means for example: the space of all Lebesgue integrable functions v defined on the domain Ω with property such that v and all its partial derivatives up to order k are all belong to $L_2(\Omega)$. In particular, the inner product of Hilbert space $(\cdot\,, \cdot\,)_{H^k}$ is equal to the norm of the Sobolev space $\|\cdot\|_{W_2^k(\Omega)}$. For instance, The $H^1(\Omega)$ is a space which are bounded in following norms:

$$\|\psi\|_{H^1(\Omega)}^2 = \|\psi\|_{L_2(\Omega)}^2 + \|\bigtriangledown\psi\|_{L_2(\Omega)}^2 < \infty \tag{A.14}$$

Thus, we have the $H^1(\Omega)$ semi-norm (which means $\|v\| = 0 <\neq> v = 0$) as:

$$|\psi|_{H^1(\Omega)} = \|\bigtriangledown\psi\|_{L_2(\Omega)} \tag{A.15}$$

Energy norm:

$$\|u\|_e = a(u,u) \tag{A.16}$$

where $a(\cdot,\cdot)$ is the bilinear form of the boundary value problem in finite element analysis.

$H(div)$ **Space**: A space is denoted as H_{div} space if and only if

$$H(div,\Omega) = \{q \in L_2(\Omega) | \nabla \cdot (q) \in L_2(\Omega)\} \tag{A.17}$$

$H(curl)$ **Space**: The H_{curl} space is defined as:

$$H(curl,\Omega) = \{q \in L_2(\Omega) | \nabla \times (q) \in L_2(\Omega)\} \tag{A.18}$$

where q represents the shape functions in finite element method.

A.2 Elliptic Type Partial Differential Equation

The Elliptic type partial differential equations are the fundamental type of PDEs which can describes many physical applications.

$$-a(\mathbf{x})\Delta U + b(\mathbf{x})\nabla \cdot U + c(\mathbf{x})U = q(\mathbf{x}) \tag{A.19}$$

for $\mathbf{x} \in \Omega$, $q(\mathbf{x}) \in L_2(\Omega)$. In specific $a(\mathbf{x})$, $b(\mathbf{x})$ and $c(\mathbf{x})$ are material data, $q(\mathbf{x})$ is the load data. These type of problems also have the name: "Sturm-Liouville problem" with coefficient $b(\mathbf{x})$ vanishes, as well as Helmholtz equations are derived (see Ciarlet in [104]). The generic type of Elliptic PDEs comes with the following kind of boundary conditions:

Dirichlet Boundary : it is also known as essential boundary condition: $U_{|\partial\Omega} = u_0$.

Neumann Boundary : it is also known as natural boundary condition: $-a(\mathbf{x})U|\partial\Omega' = u_N$ for $u_N \in L_2$

Robin / Mixed Boundary : it is also known as mixed boundary condition: $-a(\mathbf{x})U|\partial\Omega' + \alpha U_{|\partial\Omega} = \gamma$.

The **regularity conditions** are:

$$\begin{aligned} 0 < a(x)_{min} \leq a(x) \leq a(x)_{max} < \infty \; a(x) \in C^1[\Omega] \\ b(x),\, c(x),\, q(x) \in L_2(\Omega) \end{aligned} \tag{A.20}$$

the theory of ordinary differentiation equation states that the solution exists for $U \in C^2(\Omega) \bigcap C1[\Omega]$, but U may not be unique.

Proposition A.2.1 *We should notice that the L_2, H^1, W_k^p spaces are the spaces which contains our solutions or the load data, these are the regularity conditions the problem must be satisfied, if it admits a unique solution can be solved by the finite element approximation.*

In addition,we could neither impose the Neumann BC on the whole boundary of our domain nor with null boundary conditions. The former would generally leads to singularity of the stiffness matrix in algebraic equation. The later situation would results in non-unique solutions. Nonetheless, there are some special formulations of the pure Neumann boundary value problem which can be solved with unique solutions.

Proof See Oden, J. Tinsley, and Leszek Demkowicz in [248] or any other relevant applied mathematic textbooks.

A.3 Weak Variational Formulation of Elliptic Equation

The weighted residual method is applied by multiplying both sides of the Eqn. (A.19) with arbitrary test function $v(\mathbf{x})$, and integrated them over the domain $\Omega = [0, l]$ on edge element. Hence, results in the following:

$$-\int_0^l a(\mathbf{x})\Delta u v d\mathbf{x} + \int_0^l b(\mathbf{x})\nabla \cdot u v d\mathbf{x} + \int_0^l c(\mathbf{x}) u v d\mathbf{x} = \int_0^l q(\mathbf{x}) v d\mathbf{x} \tag{A.21}$$

where the solution u and test function v both belong to the Sobolev space $w_k^2(\Omega)$. Consequently, we define our test functions in $H_0^k(\Omega)$ to be the subspace of $w_k^2(\Omega)$ which contains all functions in it though with trace zero. Therefore, $v(\partial\Omega) \subset L_2$ (see trace operator in [83]). If we further apply Green's first identity (in 1D "integration by parts") to Eqn. (A.21), we have:

$$\begin{aligned} &\int_0^l a(\mathbf{x})\nabla u \cdot \nabla v d\mathbf{x} - a(\mathbf{x})\nabla u(l) v(l) + a(\mathbf{x}) u(0) v(0) \\ &= \int_0^l a(\mathbf{x})\nabla u \cdot \nabla v d\mathbf{x} - a(\mathbf{x})\nabla u(l) v(l) \end{aligned} \tag{A.22}$$

since $v(0) = 0$. By apply the boundary conditions under Eqn. (A.19), the final system of formulation is given by:

$$\begin{cases} \int_0^l \Big(a(\mathbf{x})u'v' + b(\mathbf{x})u'v + c(\mathbf{x})uv\Big)d\mathbf{x} + \alpha a u(l)v(l) = \int_0^l q(\mathbf{x})vd\mathbf{x} + \gamma v(l) \\ u(0) = u_0 \\ \forall v \in H_0^k(\Omega), v(0) = 0 \end{cases} \tag{A.23}$$

Equation (A.23) is the weak form of Eqn. (A.19). If we set the right hand side of (A.23) as:

$$f(v) = \int_0^l q(\mathbf{x})vd\mathbf{x} + \gamma v(l) \tag{A.24}$$

for $f \in V'$ the dual space of V, in case the solution space is $V \in H_0^k$. Then, the left hand side of (A.21) becomes:

$$a(u, v) = \int_0^l \Big(a(\mathbf{x})u'v' + b(\mathbf{x})u'v + c(x)uv\Big)d\mathbf{x} + \alpha a u(l)v(l). \tag{A.25}$$

Consequently, Eqn. (A.24) is the linear form of the boundary value problem, Eqn. (A.25) is called the bilinear form of the problem. Henceforth, our problem can be defined as:

$$\begin{cases} a(u, v) = f(v), \forall v \in H_0^k(\Omega), v(0) = 0 \\ u(0) = u_0 \end{cases} \tag{A.26}$$

The Eqn. (A.26) admits a unique solution $u \in V\big(\mathbb{C}^2(\Omega) \bigcap \mathbb{C}^1(\Omega)\big)$, if the following conditions are satisfied:

Lemma A.3.1

1. $\big(\mathbb{H}, (.,.)\big)$ *is a Hilbert space.*

2. $a(.,.)$ *is a continuous, symmetric and non-degenerate bilinear form which is also coercive on* V *such that,* $a(u, v) \leq M \|u\| \|v\|$, $\gamma \|v\|^2 \leq a(v, v)$.

3. V *is a closed subspace of Hilbert space* $\mathbb{H}$.

(A.27)

In case of the Dirichlet BC is inhomogeneous, *affine space* is introduced:

$$\tilde{u}_0 + H_0^k = [\tilde{u}_0 + v : v \in H_0^k\ ].$$

We seeking for solution in:

$$\begin{cases} u \in \tilde{u}_0 + H_0^k \\ a(u, v) = f(v)_{new} \end{cases} \tag{A.28}$$

where $f(v)_{new} = f(v) - a(\tilde{u_0}, v)$ is a new linear form which distinct from the original homogeneous Dirichlet BC problem.

Proposition A.3.2 *There are generally three criterions for specific numerical method which will leads the numerical solution to convergence. Firstly, the stability is guaranteed by the well-posedness of the problem with one unique solution as stated previously. Second, the completeness of method depends on whether the order of continuity within each elements is equivalent to the highest order derivatives derived in the variational formulation. Lastly, the compatibility of elements must be satisfied at the element interface by impose the order of continuity is at least one order below the highest order derivative [173].*

Definition : **(Coercivity)** If there exists constant $C_1 > 0$, such that

$$\|a(v,v)\| \geq C_1 \|v\|_\nu^2 \quad \text{for all } v \in \nu$$

A.3.1 Non-symmetric Bilinear Form

In previous section, our bilinear form of the problem is symmetric by assumptions. Then by three constrain conditions from Eqn. (A.27), we have a unique solution for this problem, but what if the bilinear form of the problem is non-symmetric? The situation occurs very often in practical physical problems [104]. In specific cases, The Lax-Milgram lemma together with Céa's theorem guarantees the existence and uniqueness of the solution for such problems.

Theorem A.3.3 ***(Lax-Milgram Lemma)***

Let V be a Hilbert space, and $a(\cdot,\cdot) : V \times V \to \mathbb{R}$ be a continuous V-elliptic bilinear form, moreover, $f : V \to \mathbb{R}$ is a continuous linear form. Thus, for any variational form problems,

$$u \in V \quad \& \quad \forall\, v \in V, \quad a(u,v) = f(v) \tag{A.29}$$

where the finite element solution u is unique and exists.

Proof : Omitted. Referred to Ciarlet, Philippe G [104].

Theorem A.3.4 ***Céa's Theorem***

Suppose conditions (A.27) holds for particular problem except the symmetric part. Furthermore, u is a unique solution solves the problem. Then for this problem, we have:

$$\|u - u_h\|_V \leq \frac{M}{\gamma} \min_{\omega \in V_h} \|u - \omega\|_V \tag{A.30}$$

$$\textit{Equivalently, } \|u - u_h\|_V \propto \frac{M}{\gamma} \min_{\omega \in V_h} \|u - \omega\|_V \tag{A.31}$$

Proof : Omitted. Referred to Ciarlet, Philippe G [104].

Céa's theorem suggests that the error bounded in V space norm is quasi-optimal such that it is proportional to the best approximation in the subspace V_h.

A.3.2 Generalized Duffy Transformation for Simplex

The accurate higher order Gauss points and weights lying within the element domain are extremely difficult to derive for simplex geometry, especially for higher order elements [212, 310, 108, 338]. Many of the quadrature rules developed in literatures either have points outside the element domain or negative weights. There have been many studies looking for quadrature rules on simplex element, both numerically and analytically. The difficulty of searching quadrature rules generally leads to well known problem of finding the zeros or minima of high-order multivariate polynomials.

In [338], Zhang, *et al.* proposed a symmetric quadrature rules for triangles and tetrahedrons of orders up to 21(14), with positive weights and points lying inside integration domain, and the symmetric structure of quadrature points together with symmetric basis functions can hugely alleviates the computational cost in assembling element matrices. However, this fact restricts our polynomial order below 7 in order to achieve an optimal quadrature orders. On the contrary, quadrature rule for hexahedra elements can be derived by taking the tensor products of 1D Gauss-Legendre Jacobi quadrature rules. In addition, the tensor products Gauss quadrature rule is non-symmetric, thereby, lower order quadrature rules can be selected on the direction of variables with less exponents, which in total saving the assembling efforts on each integration domain. Nonetheless, the results of direct apply the tensor product of 1D Gauss quadrature rule on hexahedra element will theoretically leads to more points and weights.

In [266], the numerical integration over standard tetrahedron is by the mathematical transformation that maps the tetrahedron in (x, y, z) spaces into a standard 2-cube with (ζ, η, γ) space. Then classical Gauss Legendre method is performed. This algorithm circumvented the cumbersome process of deriving new sampling points and weight functions within the tetrahedron.

In acoustic applications, numerical solutions are severely depend on the boundary condition applied on the boundary of obstacle, subsequently, their form of complexity highly rely on the specific type of incident wave which based on experimental assumption. For instance, to express acoustic wave propagating from

a point source (dipole), we either have a singular body force or $\frac{1}{r}$ singularity for integration on boundary. The analytical form of point source conditions:

$$\Phi_{ps} = A_0 \frac{e^{-\mathrm{i}k|\mathbf{x}-\mathbf{x}_0|}}{4\pi|\mathbf{x}-\mathbf{x}_0|} \tag{A.32a}$$

$$\frac{\partial \Phi_{ps}}{\partial r} = -A_0 \frac{e^{-\mathrm{i}k|\mathbf{x}-\mathbf{x}_0|}}{4\pi|\mathbf{x}-\mathbf{x}_0|} \cdot \frac{1+\mathrm{i}k|\mathbf{x}-\mathbf{x}_0|}{|\mathbf{x}-\mathbf{x}_0|} \cdot \frac{(\mathbf{x}-\mathbf{x}_0)\cdot\mathbf{n}}{|\mathbf{x}-\mathbf{x}_0|} \tag{A.32b}$$

which causes the uncertainty on the location of source points if user specify the source point lying within the computational domain. These type of waves are frequently used in physical applications like: sound generation in the nonvacuum medium, seismic waves in earthquake, and fluid-structure interaction problems respectively [254].

In 1982, Duffy introduced an integration techniques which can increasing the accuracy of integration while eliminates the integrand with a $\frac{1}{r}$ singularity on vertex [137], Duffy transformation serves to collapse one side of the square into hypotenuse of the triangle as shown in Figure A.2. The original Duffy transformation is:

$$x = u \tag{A.33a}$$

$$y = xv = uv \tag{A.33b}$$

$$z = xw = uw \tag{A.33c}$$

which transform the square $\hat{\mathcal{Q}}^2\square = [0,1]^2$ into triangle $\hat{\mathcal{T}}^2\triangle = 0 \leq x \leq 1 \bigwedge 0 \leq y \leq x$. And the determinant of Jacobian matrix $\mathcal{J} = \frac{\partial(x,y,z)}{\partial(u,v,w)} = uv$. There also exists many different transformation which results in different reference coordinates system such as [140] and [309] proposed reference square elements in range of $[-1,1]^2$. In [237], S. E. Mousavi developed a revised Duffy transformation which adding exponent term on direction u, it changes the transformation to : $\mathcal{Q}^2\square(u,v,w) \rightarrow \mathcal{T}^2 \triangle (x,y,z) : x = u^\beta, y = u^\beta v, z = u^\beta w$. The exponent β is chosen and tested such that with $\beta = 2,3$ the integration error is minimized when compared to the Duffy transformation and other direct quadrature rules, especially for problems with higher order singularity on its dominator. This Generalised Duffy transformation can be extended to three dimensional with pyramid elements. In this paper, we present a special case of generalised Duffy transformation which collapse the hexahedron to tetrahedron directly by the following:

$$x = u^\beta vw \tag{A.34a}$$

$$y = xv(1-z) = u^\beta v(1-w) \tag{A.34b}$$

$$z = x(1-y) = u^\beta(1-v) \tag{A.34c}$$

where the determinant of Jocobian matrix $\mathcal{J}$ is : $\beta u^{3\beta-1}v$, the cube $\hat{\mathcal{Q}}^3\square = [0,1]^3$ is transferred into simplex $\hat{\mathcal{T}}^3\triangle = 0 \leq x,y,z \leq 1 \bigwedge x+y+z \leq 1$. Assume the integrand function is $f(x,y,z)$, we then have

$$\mathcal{I} = \int_0^1 dx \int_0^x dy \int_0^x dz f(x,y,z) = \int_0^1 \int_0^1 \int_0^1 f(u^\beta vw, u^\beta v(1-w), u^\beta(1-v))\mathcal{J} du dv dw \tag{A.35}$$

the choice of $\beta \in \mathbb{Z}^+$ has to ensure the positiveness of exponent in u direction. This conventional scheme guarantees the exactness of integrand with arbitrary polynomial orders.

If the computational domain is discretized into hexahedron (square) elements, one may prefer to subdivide the hexahedron into multiple tetrahedron and Duffy transform each of the tetrahedron into square, products of Gaussian-Jacobi quadrature rule can then be applied. This procedure can be repeated in iteration to improve the accuracy of integration techniques in any dimensions.

The Gauss-legendre quadrature points only need to be generated once for each polynomial orders and stored for future usage. A Gauss-Legendre quadrature can integrates the $(2n-1)$th order polynomial with exactness by placing n Gaussian points, it is generally in the sense of accuracy and efficiency for finite element analysis [62].

In the following contexts, we assess numerical tests to affirm the accuracy as well as the computational time associated with extra transformation. The performance of G-D transformation for highly oscillated acoustic problem is presented to demonstrate the improvements of solution while maintain its efficiency.

The reference solution are solved with optimal p and highest order quadrature rule to assure its correctness extend to as many digits as possible. The FE solutions are calculated using ascending p order and progressively increasing order of Gauss quadrature rule corresponding to p, which the relative error in H^1 norm is expect to capture the errors over the whole computational domain in any sense.

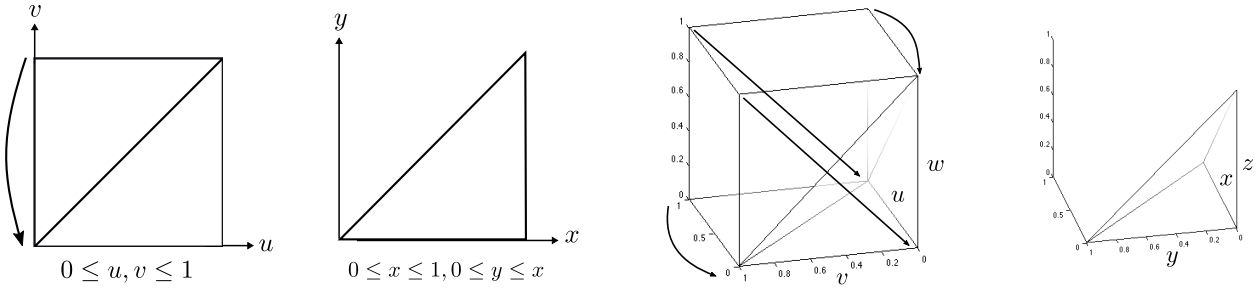

a) Duffy transformation (generalized) in 2D

b) Duffy transformation (generalized) in 3D

Figure A.2: Illustration of Duffy transformation for simplex, (a) 2D (b) 3D

In Figure A.3, a graph of log global relative error in H^1 norm is drawn against increasing p orders from $1-6$, and number of Gauss points from 9 to 121 in order to sufficiently evaluate the polynomials over integral domain. At the time of this test, the available computer resource (limited by memory and cores) can support polynomial orders up to 6. Although we have no singularity point for plane incident wave as Neumann boundary condition, we still observe solution with slightly lower errors when using Duffy transformation to apply our BC on triangular surface. The computational time difference for two transformation is also nearly identical since the number of integration points chosen in advance. In essence, generalized Duffy transformation can provides an integration tools up to arbitrary higher order polynomials while maintain its accuracy. Regardless of computational resources,

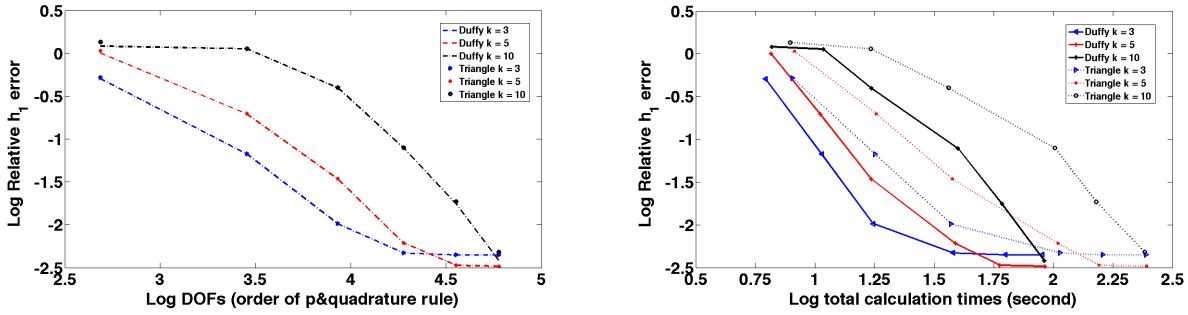

(a) error vs DOFs

(b) error vs time

Figure A.3: Global relative error $\eta\%$ against p (no.of Gauss points $= 2p + 1$) convergence analysis in H^1 norm, impinging sound hard cylinder problem ($a = 0.5$ $r = 4$)

this merit is especially convenient for applying p adaptivity finite element method with hierarchical type polynomial basis. Further numerical tests are required to estimate the improvement of G-D transformation to point source spherical wave acoustic problems with singular solution.

Overall, uniform p adaptivity with Duffy transformation outperforms triangular integration rule in the field of both accuracy and efficiency. Even so, the minor difference of accuracy between two rules only incurs by high frequency ($k \geq 5$) with linear and higher order ($p \geq 4$) elements.

A.4 Acoustic Admittance

The specific acoustic admittance parameter for waves passing through the medium is denoted as $\rho_2 c_2$, since

$$\nabla P_f \cdot \mathbf{n} = \frac{\mathrm{i}\omega\rho_f P_f}{\rho_2 c_2} \tag{A.36}$$

for $P_f = \mathrm{i}\omega\rho_f \Phi_f$, where P_f is the pressure distribution in material f.

A.5 Spherical Coordinates

Consider a spherical or polar coordinate system as shown in figure A.4, we thus have:

$$r = \sqrt{(x^2 + y^2 + z^2)} \tag{A.37a}$$

$$\varphi = arctan(\sqrt{x^2 + y^2}/z) \tag{A.37b}$$

$$\theta = arctan(\frac{y}{x}) \tag{A.37c}$$

where in polar coordinates, we replace φ by z, and remove z from A.37(a) and radius $r \in [0, \infty)$, inclination $\theta \in [0, \pi]$ and azimuth $\phi \in [0, 2\pi]$.

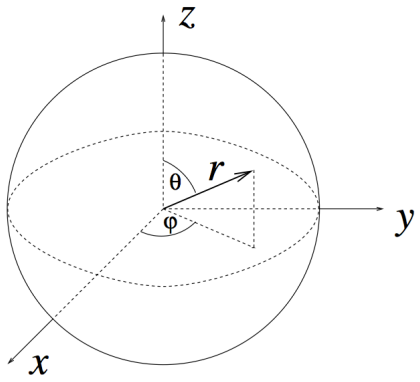

Figure A.4: Spherical coordinates

A.6 One Dimensional Coercive Elliptic Type Boundary Value Problems

The following examples are Helmholtz acoustic problems which can be solved on edge element. The main purpose is to use them as test problems to assess the efficiency of *a priori* error estimator on single element.

$$u'' - k^2 u = 1, x \in [0, l], u(0) = 0, u'(l) - \mathrm{i}ku(l) = 0 \tag{A.38}$$

with analytical solution : $u_a = e^{\mathrm{i}kx} - 1 - ie^{\mathrm{i}k}\frac{\sin(kx)}{k^2}$, we will call it *a priori* error estimator 1. The *a priori* error estimator 2 is as following :

$$u'' + k^2 u = -k^2 sin(x), x \in [0, 1], u(0) = 0, u(1) = 0 \tag{A.39}$$

with analytical solution : $u_a = (e^{-kx} - e^{kx})\frac{sin(1)}{(1+\frac{1}{k^2})(e^k - e^{-k})} + \frac{sin(x)}{1+\frac{1}{k^2}}$. And the third example is homogeneous Helmholtz equation with Dirichlet BC represents soft boundary impinged by incident wave, and Robin BC applied at right end point stand for non-reflection boundary.

$$u'' - k^2 u = 0, x \in [0, l], u(0) = 1, u'(l) - \mathrm{i}ku(l) = 0 \tag{A.40}$$

with analytical solution : $u_a = e^{\mathrm{i}kx}$.

Appendix B

A Posteriori Error Estimates on One Dimensional Elements

The theme of this section of appendices is to study and implement the *a posteriori* error estimators applied on one-dimensional elliptic type benchmark problems solved by Finite Element method. In order to get familiar with the notable arithmetics and basic theory behind the standard FE method from fundamental level.

Firstly, the four types of *a posteriori* error estimator are proposed with derivations. The one dimensional coercive (become sign-indefinite when $c(\mathbf{x}) = k$ is large) Elliptic type benchmark problem 2 given in Chapter 4 is assessed with presented error estimators, their features, merits and defects were identified as reference of the studies on higher dimensional problems.

B.1 Global Effectivity Index

As stated by many articles, a good error estimator should tends to zero at the same rate as the exact error. Hence, the quality of particular error estimator can be measured by the effectivity index.

$$\Theta = \frac{\eta}{\|e\|} \tag{B.1}$$

where $\|\|$ is the arbitrary norm depends on specific error estimator chosen in advance. And the element-wise local effectivity index is written as:

$$\Theta_K = \frac{\eta_K}{\|e\|_K} \tag{B.2}$$

where K is the specific element that we aim to measure its error. A good effectivity index should as close to unity as possible. However, in practice, an error estimator with global effectivity index around $2.0 - 3.0$ or higher numbers are acceptable in many engineering problems [14]. The error estimators we present in the following sections will encompass the variational crimes, the errors generated by solving the linear system of equations using iterative method and the round off errors (Bank and Weiser [58]).

Proposition B.1.1 *(Relative Error)*

$$R_e = \frac{\|e\|}{\|u\|} \tag{B.3}$$

Proposition B.1.2 *(Deviation of Effectivity Index)*

$$D_e = |1 - \Theta| \tag{B.4}$$

for D_e tends to zero when Θ converges to unity. Assume an error estimator is efficient, the deviation should be as small as possible.

B.2 Element Residual Based Methods

B.2.1 A Explicit a Posteriori Error Estimator Based on Element Residual

The explicit error estimator adopts the available data from the specific problem and calculates the error estimator & indicator intuitively. The strength of explicit estimator over the implicit one is that it requires less computational costs. But it is not as accurate and robustness as the implicit error estimator based on its definition. The explicit error estimator in H^1 norm for test problem 2 will be depicted in the following contexts.

B.2.2 Galerkin Orthogonality

First of all, we need the following two basic properties:

$$\begin{gathered} a(u - u_h, v) = a(e, v) = \\ a(u, v) - a(u_h, v) = f(v) - a(u_h, v) \ \ \forall v \in V \in H^k. \end{gathered} \tag{B.5}$$

$$a(e, v_h) = 0 \ \ \forall v_h \in V_h \in V \tag{B.6}$$

where Eqn. (B.5) characterizes the true error e as a solution to the variational formulation of the boundary value problem, and (B.6) is known as the Galerkin orthogonality condition. The Galerkin orthogonality condition is a key for the derivations of *a posteriori* error estimates.

B.2.2.1 Error in Energy Norm

Primarily, Eqn. (B.5) is extended to local element level, in order to reduce the cost of dealing with large problem in global domain. Suppose function u is chosen arbitrarily from solution space V, then, we can take the integral over whole domain as a direct sum of integrals on each element:

$$\begin{aligned} &a(e, v) = f(v) - a(u_h, v) = \\ &\sum_{K \in \mathcal{T}} \Big\{ \int_K f v dx + \int_{\partial K \cap \Gamma_N} u_N v dx - \int_K (a \nabla u_h \cdot \nabla v + c u_h v) dx \Big\}. \end{aligned} \tag{B.7}$$

where Γ_N is the Neumann boundary, and $\mathcal{T}$ is the partition of the domain Ω. If we further apply the Green's first identity to the above equation term by term, it leads to:

$$a(e, v) = \sum_{K \in \mathcal{T}} \Big\{ \int_K r v dx + \int_{\partial K \cap \Gamma_N} R v ds - \int_{\partial K \backslash \Gamma_N} \frac{a \partial u_h}{\partial n_K} v ds \Big\}. \tag{B.8}$$

where $\partial K \backslash \Gamma_N$ denotes the element boundary that belong to K is an interior boundary. Moreover, $\frac{\partial u_h}{\partial n_K}$ is the derivative of u_h in the direction of outward normal to the element boundary ∂K, for n_K is the outward pointing unit normal vector to ∂K. Thus, it is noteworthy that:

Lemma B.2.1 ***Interior Residual:***

$$r = f + \nabla \cdot (a \nabla u_h) - c u_h \ \textit{in} \ K \tag{B.9}$$

where r measures how far is u_h from the exact solution u in the interior of each element.

Boundary Residual:

$$R = u_N - a\frac{\partial u_h}{\partial n_K} \ on \ \partial K \cap \Gamma_N \tag{B.10}$$

In addition, R measures the same quantities instead on the boundary of each element.

Proof : The proof of above Lemma can be found in many literatures (e.g. Verfürth, Rüdiger in [322], Ainsworth M, Oden J T in [14] and Babuška Ivo in [34]).

We should bear in mind that the above two residuals will be widely used in *a posteriori* error analysis which also includes the natural error estimator rooted in Ultra-weak variational formulation. Here we omitted many theorems and proofs merely left the key aspects from now on. The contribution of the last term in Eqn. (B.8) can be reconstructs to a different form, in the presumption that the function u overlaps in an edge belongs to two adjacent elements. Hence, we have that:

$$a(e,v) = \sum_{K\in\mathcal{T}} \Big\{ \int_K rvdx + \int_{\partial K\cap\Gamma_N} Rvds \Big\} - \sum_{\gamma\in\partial\mathcal{T}\setminus\partial\Omega} \int_\gamma \left[\frac{\partial u_h}{\partial n}\right] vds. \tag{B.11}$$

where the summation of the second term in (B.11) only counts all the inter-element edges γ in the interior of the domain. Eqn. (B.11) holds if and only if we derive an inhomogeneous Dirichlet boundary condition to homogeneous condition for:

$$\int_{e\cap\Gamma_D} a\frac{\partial u_h}{\partial n_{e_K}} v = 0 \ \ \forall \ \ e\cap\Gamma_D \tag{B.12}$$

$$\begin{aligned} \left[a\frac{\partial u_h}{\partial n_e}\right]_e &= n_K \cdot (\nabla a u_h)_K + n_{K'} \cdot (\nabla a u_h)_{K'} \\ &= a\frac{\partial u_{h|K_e}}{\partial n_{e_K}} v - a\frac{\partial u_{h|K'_e}}{\partial n_{e_K}} \end{aligned} \tag{B.13}$$

where $K^{'}$ is the element shares the same interface e with K, and n_{e_K} is the outward unit normal vector to the ∂K on edge e. Specifically, Eqn. (B.13) represents the jump discontinuous of the piecewise polynomials $a\frac{\partial u_h}{\partial n_e}$ across e. Thus, we have the following:

$$R|_{e_k} = \begin{cases} \left[a\frac{\partial u_h}{\partial n_e}\right]_e, & \\ 0, & e\subset\Gamma_D \\ u_N - a\frac{\partial u_h}{\partial n}, & e\subset\Gamma_N \end{cases} \tag{B.14}$$

with (B.14), (B.11) becomes:

$$a(e,v) = \sum_{K\in\mathcal{T}_h} \int_K rvdx + \sum_{e\in\partial\mathcal{T}_h} \int_e Rvds \quad \forall v \in V \tag{B.15}$$

where $\partial\mathcal{T}_h$ contains all the edges of the elements partitioned in Ω.

Theorem B.2.2 *let $p \in [1,\infty)$, and for a non-negative integer r assume X be a finite element subspace established on an regular element (triangle or quadrilateral) partition $\mathcal{T}$ of the polygonal domain Ω. Now propose a number $s \in [0,1]$ such that $s \le k \le r+1$. In addition, there exists a bounded linear operator $\mathcal{I}_X : W_p^k(\Omega) \mapsto X$ and for all $u \in W_p^k(\Omega)$, all elements $K \in \mathcal{T}$, we have the following condition holds:*

$$|u - \mathcal{I}_X u|_{W_p^k(K)} \le C h_K^{k-s} |u|_{W_p^k(\tilde{K})} \tag{B.16}$$

and

$$|u - \mathcal{I}_X u|_{W_p^k(e_K)} \le C h_K^{k-s-1/p} \|u\|_{W_p^k(\tilde{K})} \tag{B.17}$$

for a constant C that independent of h but depends on the regularity of the elements (refer to Ainsworth M, Oden J T. page.9-14 [14]), and $\tilde{K}$ is the patch of elements associated with K.

Proof : See theorem 1.7, Ainsworth M, Oden J T in [14]. Theorem 4.4, remark 8 in Bernardi and Girault [73] for detail proofs.

Suppose the element K (in [14], triangle elements) is surrounded by an element patch such that:

$$\tilde{K} = \{K_l \in \mathcal{T} \,:\, K_l \cap K \neq \emptyset\} \tag{B.18}$$

where $\tilde{K}$ is a group of elements in partition $\mathcal{T}$ that shares at least a single point with element K. Let $v \in V$, and $\mathcal{I}_X v$ be an interpolation approximated solution as v from subspace described in Theorem B.2.2. Subsequently, by Galerkin orthogonality condition (B.5) and error in Bilinear form (B.15) the following holds:

$$a(e, \mathcal{I}_X v) = \sum_{K \in \mathcal{T}} \int_K r \mathcal{I}_X v dx + \sum_{e \in \partial \mathcal{T}} \int_e R \mathcal{I}_X v ds \tag{B.19}$$

therefore, we have

$$a(e, v) = a(e, v - \mathcal{I}_X v), \tag{B.20}$$

together with (B.16), we can deduce that:

Theorem B.2.3

$$\|e\|_K \leq C \sum_{K \in \mathcal{T}} \left\{ h_K^2 \|r\|_{L_2(K)}^2 + \frac{1}{2} h_K \|R\|_{L_2(\partial K)}^2 \right\}^{\frac{1}{2}} \tag{B.21}$$

Proof : According to theorem B.2.2, we have:

$$|u - \mathcal{I}_X u|_{W_2^0(K)} \leq C h_K \|u\|_{W_2^1(\tilde{K})} \tag{B.22}$$

and

$$|u - \mathcal{I}_X u|_{W_2^0(e_K)} \leq C h_K^{1/2} \|u\|_{W_2^1(\tilde{K})} \tag{B.23}$$

where W_2^0 equivalent to L_2 space here, and the constant C is independent of u and h_K - the diameter of K. Thus, from Eqn. (B.19), we have that:

$$\begin{aligned} a(e, v) &= \textstyle\sum_{K \in \mathcal{T}} \int_K r(v - \mathcal{I}_X v) dx + \sum_{e \in \partial \mathcal{T}} \int_e R(v - \mathcal{I}_X v) ds \\ &\leq \textstyle\sum_{K \in \mathcal{T}} \|r\|_{L_2(K)} \|v - \mathcal{I}_X v\|_{L_2(K)} + \sum_{e \in \partial \mathcal{T}} \|R\|_{L_2(e)} \|v - \mathcal{I}_X v\|_{L_2(e)} \end{aligned}$$

by applying Cauchy-Schwarz inequality for integral, we arrived

$$a(e, v) \leq C \|v\|_{H^1(\Omega)} \left\{ \textstyle\sum_{K \in \mathcal{T}} h_K^2 \|r\|_{L_2(K)}^2 + \sum_{e \in \partial \mathcal{T}} h_K \|R\|_{L_2(e)}^2 \right\}$$

by (B.22), (B.23) and $\sum_{K\in\tilde{\mathcal{K}}} \|v\|^2_{H^1(\tilde{K})} + \sum_{e\in\partial K} \|v\|^2_{H^1(\tilde{K}_e)} \leq C \sum_{K\in\tilde{\mathcal{K}}} \|v\|^2_{H^1(K)} = C \|v\|^2_{H^1(\Omega)}$, we have:

$$C \leq \left\{ \sum_{K\in\mathcal{T}} h_K^2 \|r\|^2_{L_2(K)} + \sum_{e\in\partial\mathcal{T}} \frac{1}{2} h_K \|R\|^2_{L_2(e)} \right\}^{\frac{1}{2}}$$

since $a(e,e) = \|e\|_e$ and $\|v\|_{H^1(\Omega)} \leq C \|v\|_e$, where $\|\|_e$ is the energy norm. Thanks to the coercivity of the bilinear form over space V, as well as the fact that most of the edges are belong to two elements (in 1D is point), the desired results follows.

Consequently, by Theorem (B.2.3), we can derive a local error indicator for each element in the energy norm as following:

$$\eta_K^2 = h_K^2 \|r\|^2_{L_2(K)} + \frac{1}{2} h_K \|R\|^2_{L_2(\partial K)} \tag{B.24}$$

The explicit *a posteriori* error estimator is given by:

$$\|e\|_e^2 \leq C \sum_{K\in\mathcal{T}} \eta_K^2 \tag{B.25}$$

which provides an upper bound for the actual error derived from the finite element approximation solution. The persuasive argument of the error provided in H^1 norm is equivalent to the energy norm in benchmark problem 2.

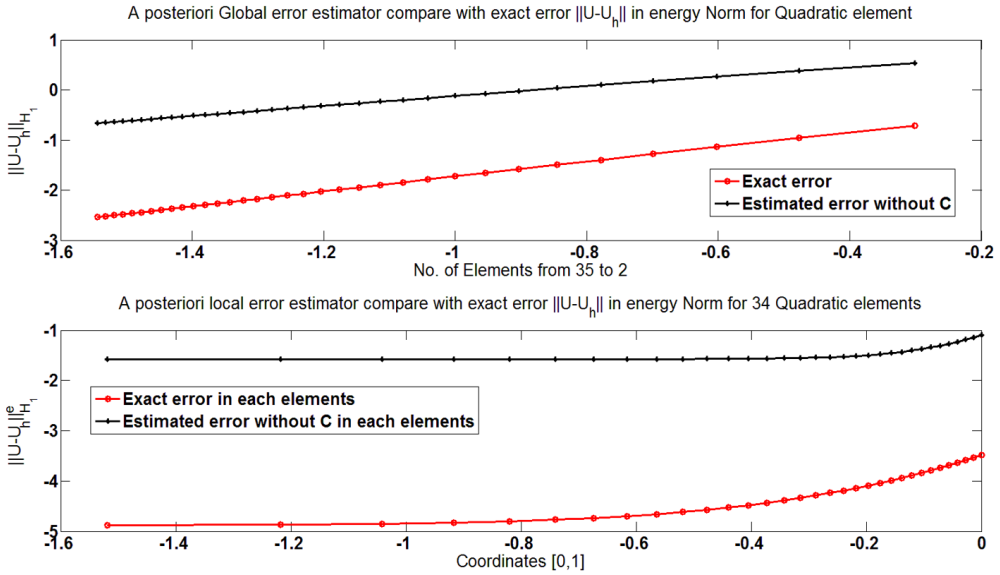

Figure B.1: A posteriori explicit error estimator based on residual for problem 2 with quadratic elements, upper part - global error with h refinement, bottom part - local error in element domain

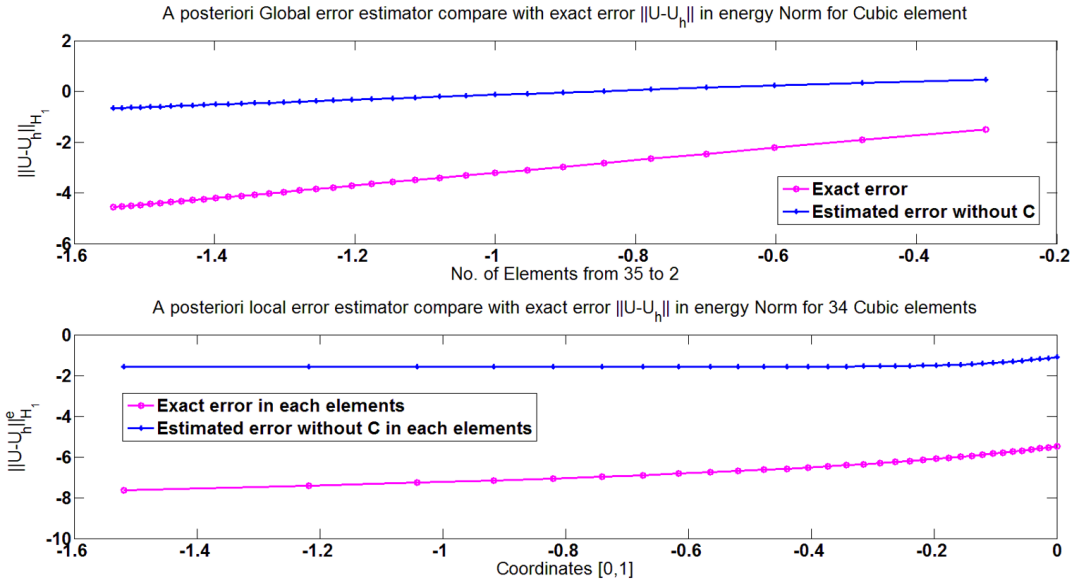

Figure B.2: A posteriori explicit error estimator based on residual for problem 2 with cubic elements, upper part - global error with h refinement, bottom part - local error in element domain

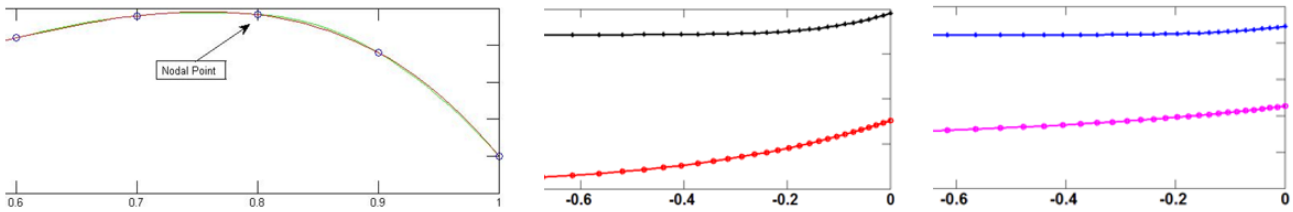

Figure B.3: Comparison of explicit error estimators on element curvature

It can be seen from figure B.1 - B.3 with finite element solution obtained by quadratic and cubic elements respectively, the estimated error decreases with increasing approximation order from quadratic to cubic. This fact is reflected by both the estimated error and the actual error in energy norm. However, the error estimator remains slightly insensitive to the drastically change of the actual error, and the numerical results are generally pessimistic. This might because of the information loss was ignored during applying the Cauchy Schwarz inequality as well as the triangle inequality in the derivation process.

Figure B.3 describes the reason of slightly increased actual error near the end of the computational domain, equally well, the estimated error near the boundary of the bar element $\Omega = [0, 1]$. It is because the appearance of the relevantly large curvature of the exact solution for problem 2 near the end of the bar, and the *a posteriori* explicit error estimator successfully captured minor effects.

B.2.2.2 Error in L_2 norm

The specific derivation of explicit *a posteriori* error estimator in L_2 norm will not be described in details in this thesis, because the main idea is resemble to the derivation of the error in energy norm. The final form is:

Theorem B.2.4 *There exists a convex domain Ω such that $\partial\Omega = \mathcal{T}_D$, then the explicit a posteriori least square error estimator is defined as:*

$$\eta_{L_2(\Omega)} = \left\{ h_K^4 \left\| r \right\|_{L_2(K)}^2 + h_K^3 \left\| R \right\|_{L_2(\partial K)}^2 \right\}^{\frac{1}{2}} \tag{B.26}$$

Where r and R are the two types of residuals prescribed in (B.9) and (B.14). Then there exists a constant C depends on Ω and the shape of the elements K_i such that the global error estimator is given as:

$$\left\| e \right\|_{L_2(\Omega)}^2 \leq C \sum_{K \in \mathcal{T}} \eta_{L_2(K)}^2. \tag{B.27}$$

Proof : See Ainsworth M, Oden J T., section 2.4, Theorem 2.7 in [14] for details.

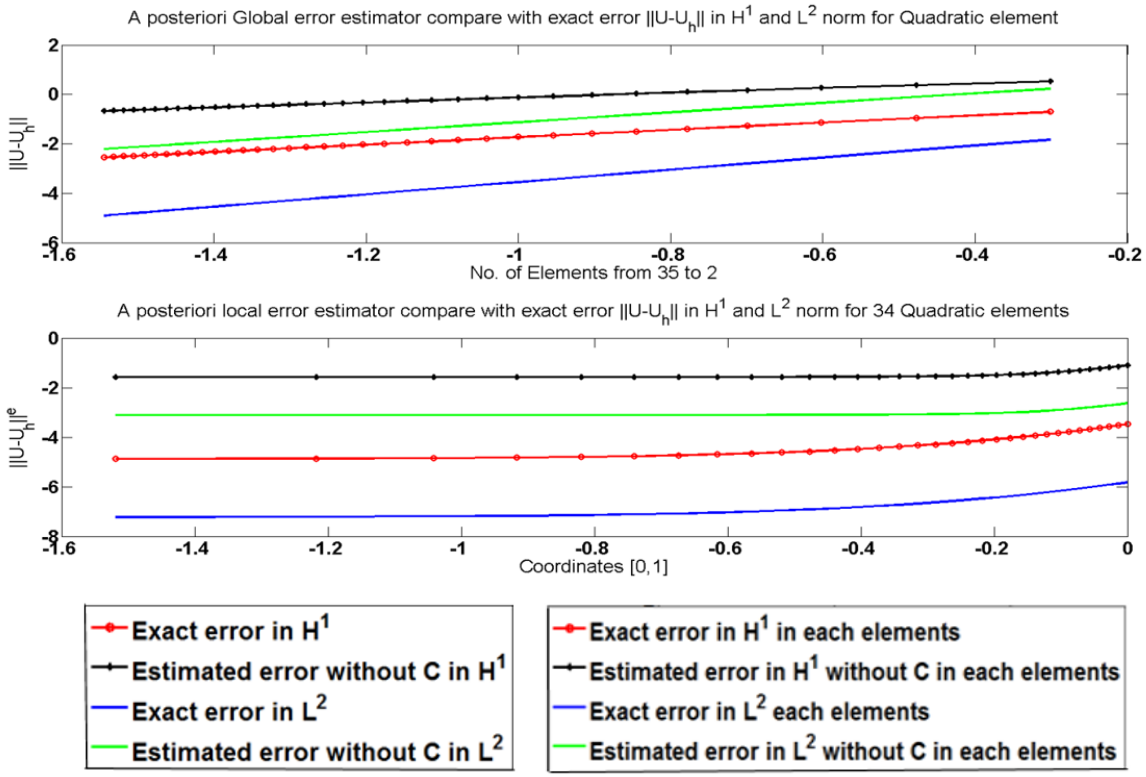

Figure B.4: A posteriori explicit error estimator based on residual for problem 2 in L_2 and H^1 norm, log - log plot

Figure B.4 illustrates the explicit error estimator in L_2 norm and H^1 norm respectively, both the estimated error and the exact error in L_2 norm are less and smoother when compared with the error in H^1 norm. Thus, the error indicators successfully captured the true scenarios. L_2 norm tends to underestimated the potential error when compares to the H^1 norm.

B.2.2.3 Error in L_∞ norm

The derivation of the L_∞ norm error estimator will be omitted (for details, see Anisworth [14]). The global point-wise error estimator and local indicator is given by:

Theorem B.2.5 *let the finite element problem be a pure Dirichlet boundary value problem, and the right hand side $f \in L_\infty(\Omega)$. In addition, $h_{min} \geq Ch^{\gamma}_{max}$ for $C > 0$ and $\gamma \geq 1$ are fixed value constants.*

$$\eta_\infty = \max_{K \in \mathcal{T}} h_K^2 \left\| r \right\|_{L_\infty(K)} + \max_{e \in \partial \mathcal{T}} h_e \left\| R \right\|_{L_\infty(e)}{}^{1} \tag{B.28}$$

$$\|e\|_{L_\infty(\Omega)} \leq C|log(h_{max})|^2\eta_\infty \tag{B.29}$$

where the logarithmic term can be regarded as a constant.

Proof See Ainsworth M, Oden J T.in section 2.5 [14] for details.

B.2.3 Conclusion

The local bound η_K plays an important role in adaptive refinement algorithm, since it indicates the distribution of the actual errors. If the estimated error estimator is relative large on a particular element, the actual error will be large in neighbour of that element too (patch of elements). Thus, the error estimators will point out the specific location on domain Ω which need to be refined.

In Ainsworth M, Oden J T Section 2.3 from [14], author states that an efficient estimator need not to be as accurate as the actual error, as long as it can imitate the behaviour of the actual error. In addition, both constant C independent of the mesh size should exists for the upper bound and lower bound of the error. Overall, the explicit *a posteriori* error estimator satisfied this condition.

B.2.4 An Implicit a Posteriori Error Estimator Based on Element Residual

The explicit error estimator presented in previous sections are generally pessimistic and insensitive to the changes of the error in micro-scale. It can be observed from the gap between estimated error and exact error in the graphs from previous sections, the gap represents the unknown constant. Moreover, the information loss was ignored while applying the Cauchy Schwarz inequality as well as the triangle inequality during the derivation process of the explicit error estimator. On the contrary, the implicit error estimator constructed based on the structure of the original problem, and involving solve a local boundary value problem with estimated error as unknown solutions. Therefore, it is more computational expensive than explicit error estimator.

Theoretically, the implicit error estimator and indicator are very sensitive to the changes of solution space and polynomial degree of bubble functions selected, indeed, the results of the error estimation can be vary for the same problem.

There are mainly two routines to obtain the implicit error estimator: the element residual method and the subdomain residual method [47], we will only focus on the element residual method itself since it inherited the ideas of element residual and

[1]Apologises for abuse of notation with error e and edge e used in different scenarios

provides more information than the later. Moreover, the local patch problems are expensive to evaluated.

Theorem B.2.6 *Suppose we have a boundary value problem like benchmark problem 2 in Eqn. (4.5). The finite element approximation is known to be u_h, then we have a local boundary value problem over each element $K \in \mathcal{T}$ of domain Ω such that:*

$$-\nabla \cdot (a\nabla e_h) + ce_h = f + \nabla \cdot (a\nabla u_h) - cu_h \text{ in } K \tag{B.30}$$

with Dirichlet boundary condition applied on the boundary edge of element K:

$$e_h = 0 \quad \forall e \subset \Gamma_D \tag{B.31}$$

and the Neumann boundary condition:

$$\begin{aligned} a\frac{\partial e_h}{\partial n} &= \left\langle a\frac{\partial u_h}{\partial n} \right\rangle - a\frac{\partial u_h}{\partial n} \quad \forall \quad e \in \partial K \backslash \Gamma_N \cup \Gamma_D \\ a\frac{\partial e_h}{\partial n} &= u_N - a\frac{\partial u_h}{\partial n} \quad \forall \quad e \subset \Gamma_N \end{aligned} \tag{B.32}$$

where $\left\langle a\frac{\partial u_h}{\partial n} \right\rangle$ is the approximation of the actual flux $a\frac{\partial u}{\partial n}$ jumps cross the element boundaries.

$$a\frac{\partial u}{\partial n} \approx \left\langle a\frac{\partial u_h}{\partial n} \right\rangle = \frac{1}{2}(a(\nabla u_h)_K \cdot n_K + a(\nabla u_h)_{K'} \cdot n_K). \tag{B.33}$$

Thus, its weak form is defined by the bilinear form:

$$\begin{aligned} a_K(e_K, v) &= \int_K (\nabla u \cdot \nabla v + cuv)dx \\ a_K(e_K, v) &= f_K(v) - a_K(u_h, v) + \int_{\partial K} \left\langle a\frac{\partial u_h}{\partial n} \right\rangle v ds \quad \forall v \in V_K \end{aligned} \tag{B.34}$$

where $V_K = v \in H^1(K) : v = 0\, on \partial K \cap \Gamma_D$*, we can then replace* e_K *by basis functions* ψ_K*.*

Proof : See Ainsworth M, Oden J T. section 3.3 in [14] and Babuška, Ivo chapter 7 in [34] for details.

Hence, the local error estimator is given by:

$$\eta_K = \|\psi_K\|_K \tag{B.35}$$

and the global error estimator is observed from the summation of the local errors.

$$\|e\| \approx \eta_h = \Big\{ \sum_{K \in \mathcal{T}} \eta_K^2 \Big\}^{\frac{1}{2}} \tag{B.36}$$

B.2.4.1 The Existence of Unique Solution

If a boundary value problem (e.g. problem 2) only has the Neumann boundary condition imposed on all of its boundaries, in addition, its absolute term vanishes (problem 2, $c = 0$). Consequently, this problem admits a solution if and only if it satisfies the compatibility condition as following:

Corollary B.2.7

$$\int_\Omega f dx + \oint_{\partial\Omega} h ds = 0. \tag{B.37}$$

Proof See Babuška, Ivo, Eqn. (7.15a)-(7.17) in [33].

For an implicit error estimator it means the right hand side of the bilinear form (B.34) equals to zero.

B.2.4.2 Bubble Functions

The infinite-dimensional space containing the actual error has to be approximated by a suitable finite dimensional subspace. A way of doing so is that we choose the subspace of V such that it will forms a coercivity bilinear form. These finite spaces contain some distinctive functions denoted as the bubble functions. The key point to construct such subspaces is to increase the order of spaces used to solve the original boundary value problem.

Bubble functions are routinely used modal shape functions for $p \geq 2$. In case the original finite element subspace V_h is used to obtain the approximation e_h of e, then a trivial solution of $e_h = 0$ will follows. Hence, one need to construct a wider space contains the bubble functions. The bubble functions is restricted to zero at the element vertices (boundaries) and non-zero in the interior of elements. Roughly speaking, They commonly have higher orders than the finite element solution space.

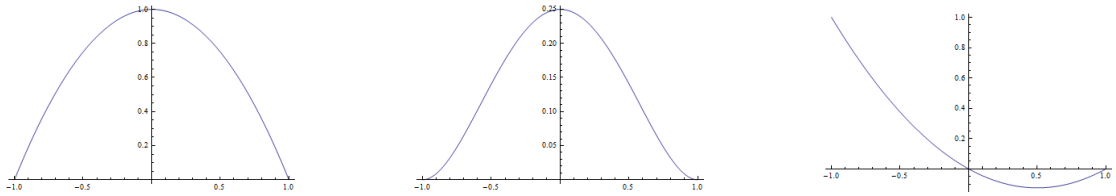

(a) Interior bubble function 1

(b) Interior bubble function 2

(c) Edge bubble function

Figure B.5: Example of bubble functions in edge element

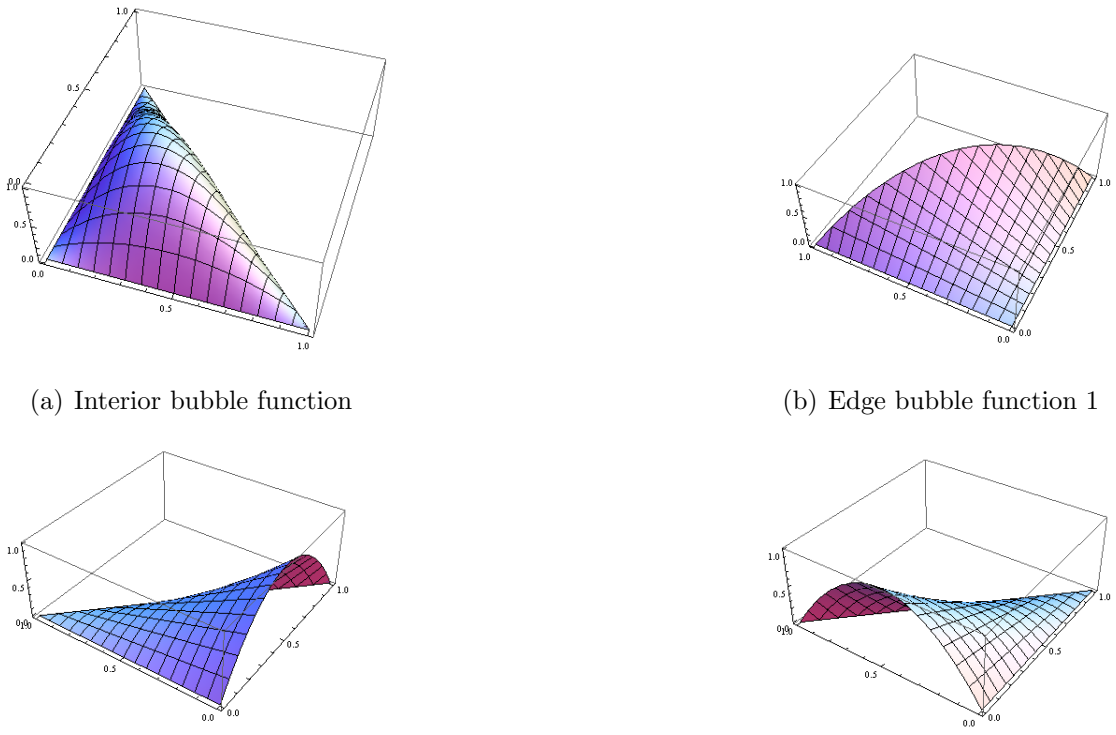

(a) Interior bubble function

(b) Edge bubble function 1

(c) Edge bubble function 2

(d) Edge bubble function 3

Figure B.6: Example of bubble functions in face element

The above graphs B.5 and B.6 depicted the bubble functions in one and two dimensions, they always vanish on the vertices of the elements. The interior bubble function are zero values outside of the elements of interests, and the edge bubble functions have value one at the edge shared by two adjacent elements.

B.2.4.3 Dirichlet Element Based Error Estimator

The implicit error estimator with approximation subspace contains the interior bubble function is referred to "Dirichlet element based error estimator" in Babuška, Ivo [33]. The estimated error $\tilde{e}_K$ belongs to:

Lemma B.2.8

$$\tilde{e}_K \in Y_K = \left\{ v | \int_{\mathcal{T}_h} \frac{\partial v}{\partial x} dx < \infty,\, v(x_{i+1}) = v(x_i) = 0 \right\} \tag{B.38}$$

Proof See Babuška Ivo section 7.1 in [33].

Proposition B.2.9

$$\begin{aligned} &\textit{Local indicator}: \quad \eta_K^{Dir} \equiv \|\tilde{e}_K\|_{Y_K} \\ &\textit{Global indicator}: \quad \eta_h^{Dir} \equiv \left(\sum_{K \in \mathcal{T}} (\eta_L)^2 \right)^{\frac{1}{2}} \end{aligned} \tag{B.39}$$

Theorem B.2.10 *Let $u \in V$ and $u_h \in V_h$ be as defined in Eqn. (4.6), and the problem satisfied the regularity condition (A.20), from proposition B.2.9 and lemma B.2.8, we have that:*

$$\begin{aligned} &\eta_K^{Dir} \leq \|e\|_e \leq \mathcal{K} \eta_K^{Dir} \\ &\mathcal{K} \leq \left(\frac{a_{max}}{a_{min}} \right) p^{\frac{1}{2}} \left(1 + \frac{c_{max}}{a_{max}} h_K^2 \right)^{\frac{1}{2}} p \end{aligned} \tag{B.40}$$

where $\|e\|_e$ is the true error in energy norm, and the error indicator in proposition (B.2.9) is a lower bound of the true error in finite element approximation.

Proof : See Babuška Ivo, theorem 7.2 - 7.3 in [34] for detailed proofs.

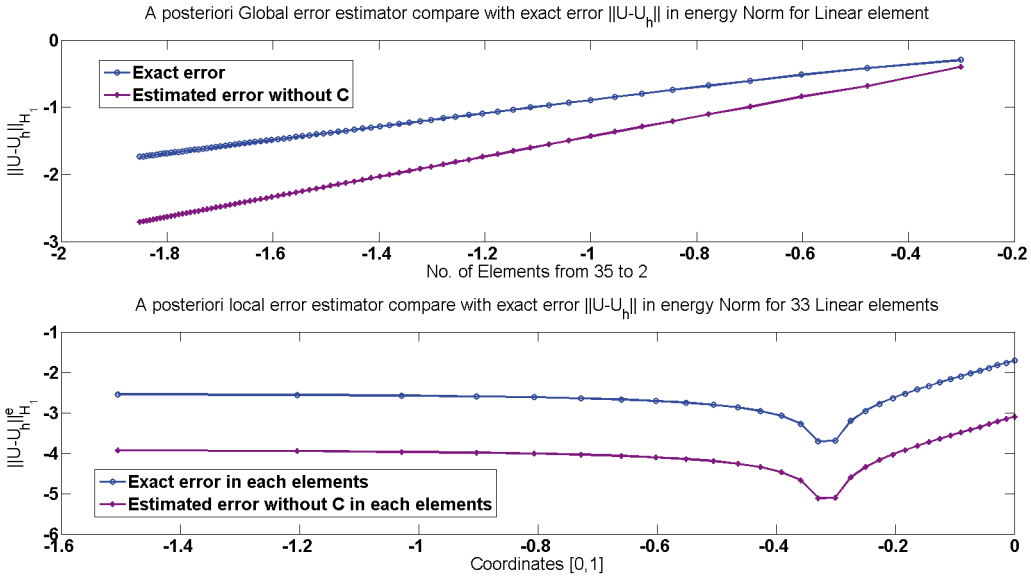

Figure B.7: Dirichlet element residual error indicator and estimator in 1D

Figure B.7 shows the results of implicit Dirichlet error estimator and indicator both below the actual error in energy norm for problem 2 with linear element. The good news is the local error indicators have successfully captured the trends of the actual error exactly. The defect is that the error indicator tends to underestimated the true error. The implicit error estimator converged faster than actual error in global sense.

B.2.4.4 Neumann Element Based Error Estimator

The Neumann element based error estimator can be observed by solving the Eqn. (B.30) with boundary conditions (B.31) and (B.32) in each elements, then adding them up by local errors (B.36).

Theorem B.2.11

$$\|e\|_e \approx \eta_h \equiv \eta_h^{Neu,U} \tag{B.41}$$

where $\eta_h^{Neu,U}$ *is the upper bound of the actual error obtained by solving a group of auxiliary linear system of equations.*

Proof : See Babuška, page 225-227 in [34] for detail proof.

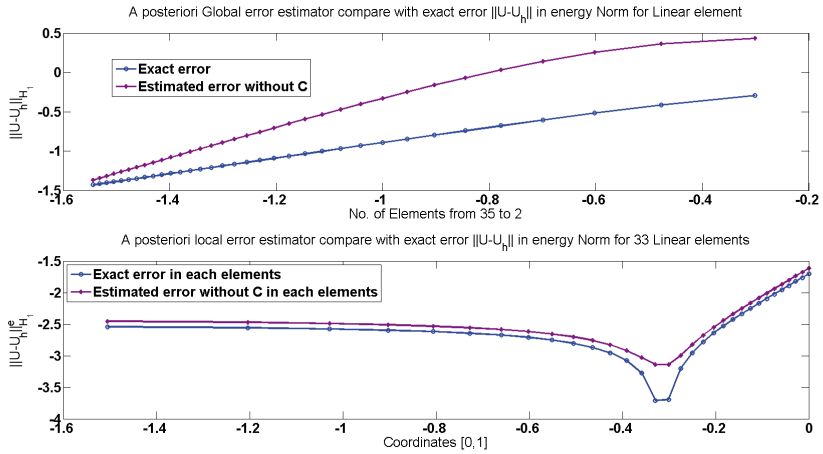

Figure B.8: Neumann element residual error estimator in 1D

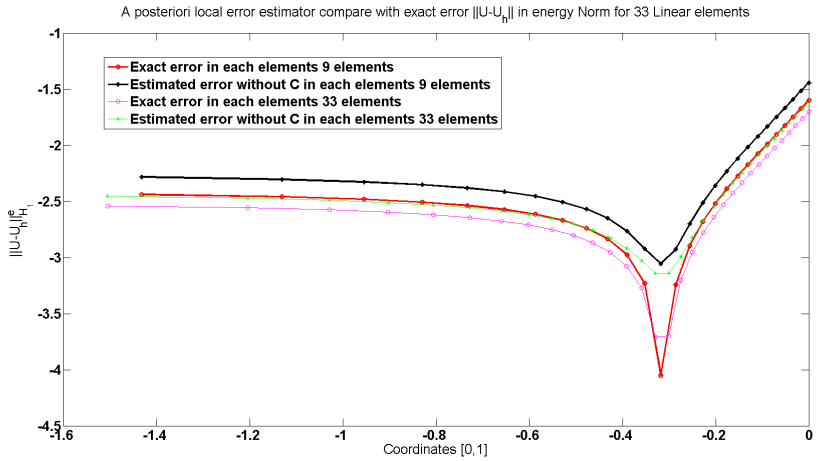

Figure B.9: Neumann element residual error indicator in 1D, solved with 9 elements and 33 elements respectively.

Figure B.8 and Figure B.9 reveal the fact that the *a posteriori* implicit Neumann error estimator converges to the true error as the element size h decreases. In Figure B.8, the implicit Neumann error indicator exhibits as an upper bound of the exact solution in both global and local levels, which coincides with the theory. The significant achievement of the Neumann error estimator is that the estimated error follows the exact error in domain coordinate-wise smoothly.

B.2.5 Conclusion

At this stage, regarding to previous analysis, we can conclude that the approximated error are heavily dependent on the subspace contains the bubble functions selected. Most importantly, a carefully selected subspace $Y_K \in V$ would leads to a well-posed problem. In case of 2D triangular or quadrilateral elements, Babuška, Ivo proposed several adequate subspaces which have been proved to be efficient

[33, 34]. Indeed, the results of the error estimation can be varied for the same problem based on error estimator applied. As a consequence, the following inequality holds:

Corollary B.2.12

$$\eta_K \leq C\Big\{h_K^2 \left\|r\right\|_{L_2(K)}^2 + \frac{1}{2}\sum_{e\subset\partial K} h_K \left\|R\right\|_{L_2(e)}^2\Big\}^{\frac{1}{2}} \tag{B.42}$$

where the right hand side of equation is the explicit error estimator in energy norm previously mentioned in (B.24). It is obvious that the implicit error estimator observed by solving a local linear system of equation is upper bounded by the explicit error estimator.

Overall, it is easy to say that the implicit error estimator like the one we presented in previous section are much complicated than the explicit error estimator. Indeed, its performance should be more accurate and robust than the explicit error estimator in theory (Ainsworth and Oden in [14], Bank, Randolph and Alan in [58]). Although the element residual global error estimator does not estimates the true error exactly, The local error indicator which can displays a clear distinction between "large" and "small" errors are still said to be effective to guide the local h & p refinement (Babuska Ivo [33]).

However, various implicit error estimators are found to offer similitude results as the explicit error estimators in both numerical tests and practical adaptivity refinements. This observation also coincides with the fact that uses of the true error (in case analytical solutions are known) as the error indicator does not always end up with the best quality mesh [8]. Hence, due to the computational cost when dealing with complicated and large psychical problems, the inexpensive explicit error estimators are more preferable than the expensive implicit error estimators [233].

B.3 Patch Recovery Based Methods: Gradient of Solutions

There are numerous engineering applications required the quantity of interests are not the finite element solution itself, but the gradient of the solution instead [318]. For instance, the elastic problems, stokes problems and the acoustic applications, the velocity and stress tensor are required for evaluation. The gradient of the potential is the velocity, and the stress or strain are calculated from the velocities and so on. These are the important physical quantities in particular engineering analysis.

The finite element spaces embodied are generally piecewise polynomial basis function space, which will leads to discontinuous & inaccurate derivative of the approximated solution at the interior boundary edge (face) across adjacent elements,

especially on the boundary of the domain Ω. The reason for this scenario to occur is because of the FEM is an approximation technique aim to the exact solution of the problem but not its derivatives. As for the derivative of the approximation solution, the actual error of the approximated gradient increases based on the approximated solution due to weaker condition. In linear approximation, the gradient of the solution is constant, thus definitely discontinuous across elements. The recovery-based method could also incorporates with the element residual error estimator positively, to give the latter a more accurate boundary data than itself for the underlying problems (Ainsworth, [14, 7]).

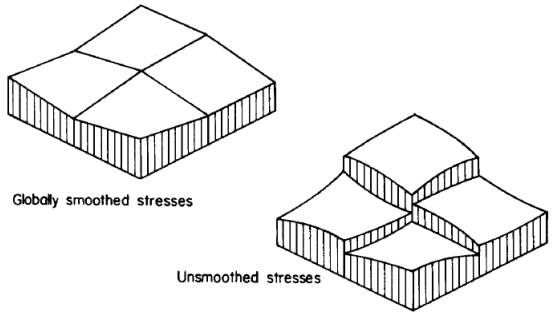

Figure B.10: Examples of smooth and non-smooth gradient of solution [7]

Proposition B.3.1 *Suppose $I_x u$ is an interpolant of a continuous function $u \in C(\bar{\Omega})$ in the finite element subspace, then the condition:*

$$I_x u \in X : \quad I_x u(x_i) = u(x_i),\ \forall i \in [\textit{nodes of } \mathcal{T}] \equiv \mathcal{N} \tag{B.43}$$

holds, where $[x_i : i \in \mathcal{N}]$ is the nodes of finite partition $\mathcal{T}$. If the basis function is Lagrange basis, then, the explicit interpolant is $I_x u = \sum_{i \in \mathcal{N}} u(x_i)\theta_i$. Theoretically, the interpolation delivers a quasi-optimal approximation from the finite subspace.

B.3.1 Averaging Method and Superconvergent Recovery

The averaging gradient method has been used in the development of *a posteriori* error estimator based on element residual. Alternatively, the gradient of solution can be calculated based on a weighted average of the flux terms between adjacent element boundaries. It intuitively estimated the discontinuous approximation of the true gradient. The very crucial fact for gradient recovery is that the gradient at the centroid of the elements are always superconvergent [326]. Babuška and Rheinboldt originally proposed a gradient recovery error estimator in 1D based on this fact in 1981 [48].

Lemma B.3.2 ***Consistency Condition*** *Let the recovery operator $\mathcal{G}_h$ together with the interpolation $\mathcal{G}_h(I_x u)$ be an approximation of the true gradient ∇u. In*

addition, assume u is a polynomial of degree $p+1$ on the patch $\tilde{K}$ associated with K, such that $u \in \mathbb{P}_{p+1}(\tilde{K})$, thus

$$\mathcal{G}_h(I_x u) = I_x \nabla u \; on \; element \, K \tag{B.44}$$

Localization Condition *If $x_g \in K$ and x_g can be any points in element K, then the recovered gradient $\mathcal{G}_h[u](x_g)$ depends only on values of ∇v sampled from neighbour elements $K^{'}$ from $\tilde{K}$.*

Boundedness and Linearity Conditions *Let $\mathcal{G}_h : V \mapsto V \times V$ be a linear operator, then*

$$\|\mathcal{G}_h[u]\|_{L_\infty(K)} \leq C|u|_{W^{1,\infty}(\tilde{K})} \; \forall K \in \mathcal{T} \; \forall u \in V \tag{B.45}$$

where C is a constant independent of element diameter h, and V denotes the finite element subspace. This condition interpret the fact that the recovered gradient is always bounded by a constant multiple the true gradient in the element patch surrounding K.

Theorem B.3.3 *Let $\mathcal{G}_h$ satisfies Lemma B.3.2 such that $u \in H^{p+2}(\tilde{K})$, and $\mathcal{T} \in \Omega$ be a partition of elements, $V_h \in V$ is the finite element subspace has polynomial of degree p. Then, there exists a positive constant C independent of h_K and u such that:*

$$\|\nabla u - \mathcal{G}_h(I_x u)\|_{L_2(K)} \leq C h_K^{p+1} |u|_{H^{p+2}(\tilde{K})}. \tag{B.46}$$

Proof See Babuška, Ivo Theorem 6.5, Theorem 6.6 [34] and Anisworth proof of Theorem 4.1 [14].

Since the finite element solutions have better accuracy than the linear interpolant operators, hence, we have

Corollary B.3.4 *Let $u \in H^{p+2}(\Omega)$, and the gradient recovery operator $\mathcal{G}_h$ satisfies Lemma B.3.2. Furthermore, $|u_h - I_x u|_{H^1(\Omega)} \leq C(u) h^{p+r}$ holds for $r \in (0, 1]$, then, the following also holds:*

$$\|\nabla u - \mathcal{G}_h(u_h)\|_{L_2(\Omega)} \leq C(u) h^{p+r} \tag{B.47}$$

for a positive constant C. Properties above are well known as the super-convergence since the order of h_K is one order higher than the polynomial order in the finite element subspace. The discussion about super-convergence results are referred to Krizek and Neitaanmaki in [198]. Consequently, the local error indicator for the general gradient recovery method are defined as:

$$\eta_K^{\mathcal{G}_h} = \|u - u_h\|_{H^1(K)} = \|u - u_h\|_{L_2(K)} + \|\mathcal{G}_h(u_h) - \nabla u_h\|_{L_2(K)} \tag{B.48}$$

Previously, we mentioned the gradient of u_h are discontinuous and inaccurate at element boundaries (nodal points in 1D), especially on the boundary of the domain. This is the main reason we need to impose the gradient recovery method and make this difference between solutions as small as possible in order to have a good approximation of the stress and strain. Moreover, it can also serves as an *a posteriori* error indicator.

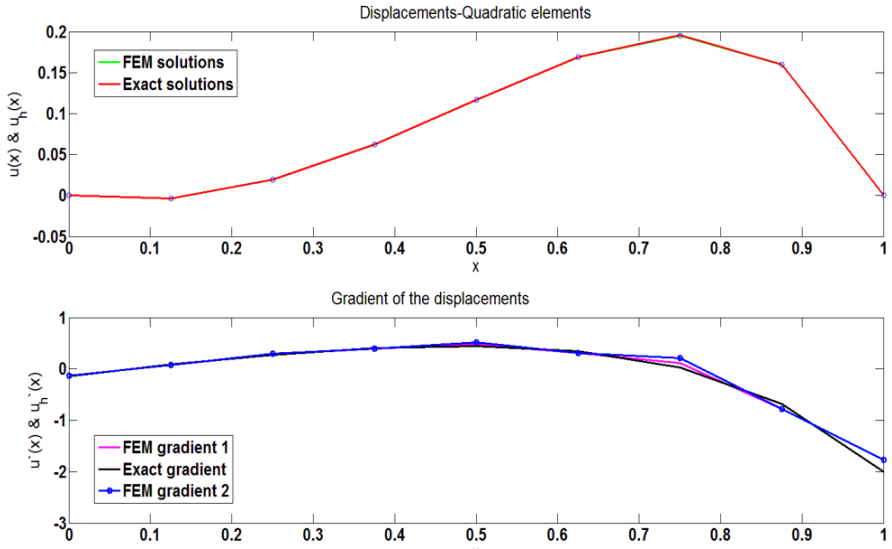

Figure B.11: Finite element solution and its gradient

The above Figure B.11 indicated the discontinuity of the gradient of finite element solution for problem 2 is specially large at the most bending part of the solution and the $\partial\Omega$. This observation is coincides with the results from *a posteriori* element residual method.

B.3.2 Z-Z Error Estimator

In earlier 1976, Barlow, John, *et al.* introduced how to find the super-convergence points in finite element method in his work [59]. Latterly, Mackinnon, R. J. and G. F. Carey in [226] demonstrated proofs of the special convergent property points in the domain of the finite element partition based on the expansion of Taylor series in 1D and 2D. In 2008, Pinto Junior and David Soares in [255] summarises three different types of gradient sampling points in one dimension and their various properties, as well as confirmed the centroid point of the element is not only the superconvergent point of the gradient of solution, but also the ultra convergence point with rate $\mathcal{O}(h^5)$.

Zienkiewicz and Zhu in [345] initially proposed the idea of super-convergence patch recovery techniques. In the first part of their paper, the benchmark examples and numerical results both for 1D and 2D elliptic equations are assessed,

whereas the second part of this paper Zienkiewicz and Zhu shows the effectivity index asymptotically converge to unity as the element size tends to zero [346]. The effectivity index of Z-Z estimator is superior when compares to other estimators like the global L_2 projection and the Hinton-Campbell extrapolation [168], and the adaptivity refinement algorithm is performed based on the error in energy norm and L_∞ norm. The Z-Z estimator also has been proven to be economical efficient and accuracy during evaluating process and the adaptivity schemes.

Zienkiewicz and Zhu in [341] emphasized in some cases where the Superconvergent Patch Recovery (SPR) method has been misunderstood, equally well, the dangerous of adding additional constraints on the original SPR. Most importantly, they present the inspiration of the new gradient recovery method named: REP (Recovery by Equilibrium in Patches). The superconvergent patch recovery technique is proved to have better performance than the element residual-based error estimators through many examples (Babuška, Strouboulis and Upadhyay in [41, 49]).

B.3.2.1 Implementation Procedures

Let i be an element vertex surrounded by a patch of elements $\mathcal{T}_i$ that shares the same vertex i. The values of the gradients at the sampling points of each elements in the patch $\mathcal{T}_i$ formed a recovered gradient at the vertex:

$$\sigma^* = P(x_i)\alpha \tag{B.49}$$

where P contains the monomials in the polynomial space of order up to the finite element subspace p, and α is a set of unknown coefficients. For example, the 1D problems with finite element subspace of order p has the following form:

$$P = [1, x, x^2, x^3, ..., x^p] \tag{B.50}$$

and the unknown coefficients

$$\alpha = [a_1, a_2, a_3, ..., a_{p+1}]^T \tag{B.51}$$

in three dimensions we have:

$$P = [1, x, y, z, x^2, xyz, y^2, z^2] \tag{B.52}$$

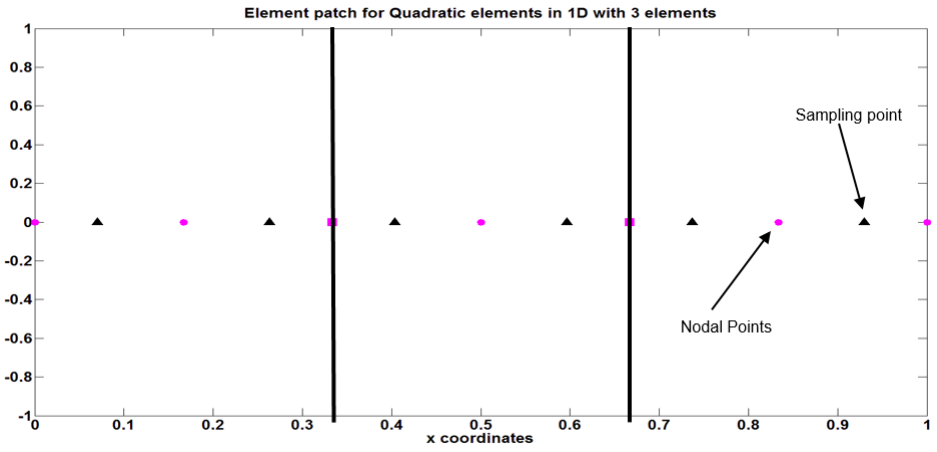

Figure B.12: Example of element patches in 1D with 4 sampling points per patch

where the purple $\cdot$ is the nodal points, and black Δ represents the sampling points. The sampling point is where the superconvergent property of the gradient of finite element solution holds. The coefficients α is determined in a least square fit sense which minimizes:

$$\mathcal{Z}(\alpha) = \sum_{K \subset \mathcal{T}_i} \left(\frac{\partial_h}{\partial x}(x_s) - P(x_s)^T \alpha \right)^2 \tag{B.53}$$

where x_s is the coordinates of the sampling points in each elements belong to $\mathcal{T}_i$. The Euler minimization condition implies in order to minimizes $\mathcal{Z}(\alpha)$, we need to solve the following local linear system of equations.

$$\alpha M = b \tag{B.54}$$

where the matrix M is defined as

$$M = \sum_{K \subset \mathcal{T}_i} P(x_s) P(x_s)^T \tag{B.55}$$

and the right hand side:

$$b = \sum_{K \subset \mathcal{T}_i} P(x_s)^T \frac{\partial u_h}{\partial x}(x_s). \tag{B.56}$$

Finally, the recovered gradients at each nodal points of the patch are interpreted as:

$$\mathcal{G}_h(u_h) = P(x_i)^T \alpha \tag{B.57}$$

where the recovered value of gradient σ^* is obtained by multiply the basis functions from the finite finite element subspace to the values of the gradient at the vertex points $\mathcal{G}_h(u_h)$, and if combined this estimator with the effectivity index (B.1), we can derive the following

Theorem B.3.5 *Assume $\|e^{scp}\|_e$ is the error estimator based on the recovered gradient of the finite element solution, then, the error estimator is said to be asymptotic exact if and only if*

$$\frac{\|e^{scp}\|_e}{\|e\|_e} \to 0 \text{ for } h \to 0 \,||\, p \to \infty \equiv \|e\|_e \to 0 \tag{B.58}$$

Proof The proof is very straightforward, in the assumption that the estimated error converges to zero at a higher rate than the actual error of the finite element approximation. Detailed proofs please refereed to Zienkowicz and Zhu in [346].

Corollary B.3.6 *The effectivity index for error estimator derived from gradient recovery has the following inequality:*

$$1 - \frac{\|\tilde{e}\|}{\|e\|} \leq \Theta \leq 1 + \frac{\|\tilde{e}\|}{\|e\|} \tag{B.59}$$

where e is the exact error, and $\|\tilde{e}\| = \|u - u_h^{sc}\|$ denotes the error of the recovered solution in specific norm. The importance of this corollary is that any gradient

recovery method gives higher rate of convergence than the finite element solution will be asymptotically exact.

The super-convergence points in each element are strongly depend on the shape functions chosen as well as the element type. Moreover, super-convergence points are slightly different from the Gaussian points for solution space of order greater or equal to cubic in one dimension [255]. In 1D case Mackinnon and Carey suggested that the super-convergent sampling points are coincide with the Gaussian points [226]. However, this is not always true for higher dimensions.

In the situation where order of element $p > 1$, there are inter-element nodes which will be evaluated more than one times by different patches, the values at these nodes can be taken by simply average out these different values. If the element nodes in the patch are also boundary nodes, these values on the nodes therefore can be determined by the interior element solely [345].

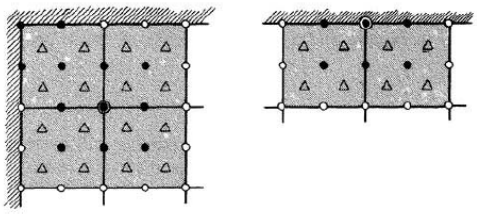

Figure B.13: Example of boundary element patches [345]

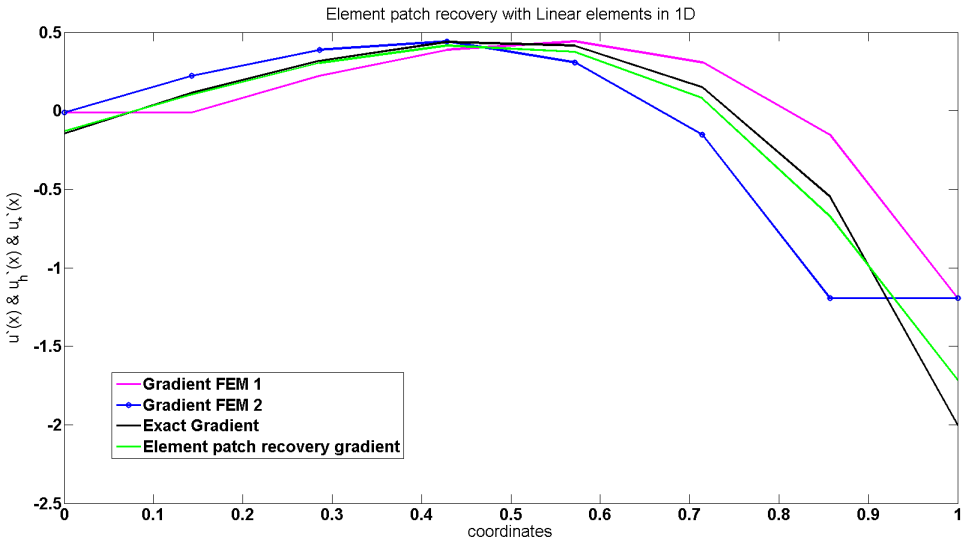

Figure B.14: Superconvergent patch recovery on linear elements

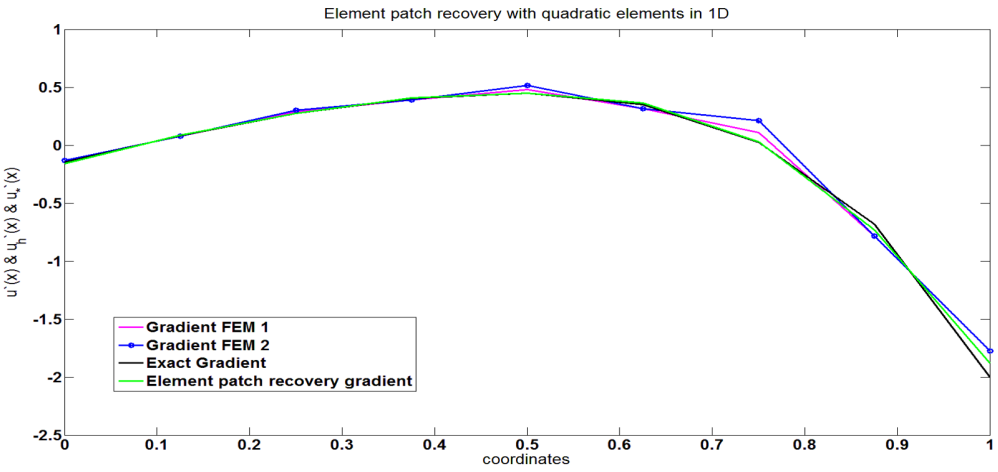

Figure B.15: Superconvergent patch recovery on quadratic elements

From the above graphs B.14 and B.15, we can no doubt see that the SPR (Superconvergent patch recovery) gradients have good agreement with the true gradient of the problem, it is intuitively a good results. We can thus use the SPR method to smoothing our gradient of solution, or applied as an estimator to implements the any adaptivity schemes. Even though, quantitative numerical tests are essential to further affirm the effectiveness of current method in higher dimensions.

B.3.3 Z-Z Error Estimator in L_∞ Norm

The error estimator in the point-wise norm is defined as:

$$\|u_h^{scp} - u_h\| = \max_{K\in\Omega} |(u_h - u_h)^2 + (\nabla u_h^{scp} - \nabla u_h)^2|^{\frac{1}{2}}$$

and the effectivity index adopted from Eqn. (B.1). The point-wise error is specialized to indicates the largest part of error occurs in the finite element domain Ω. We can observed from the Figure B.16, though the point-wise Z-Z estimator tends to overestimated the true error, the effectivity index interprets the point-wise error estimator is asymptotically converges to the actual error in L_∞ norm.

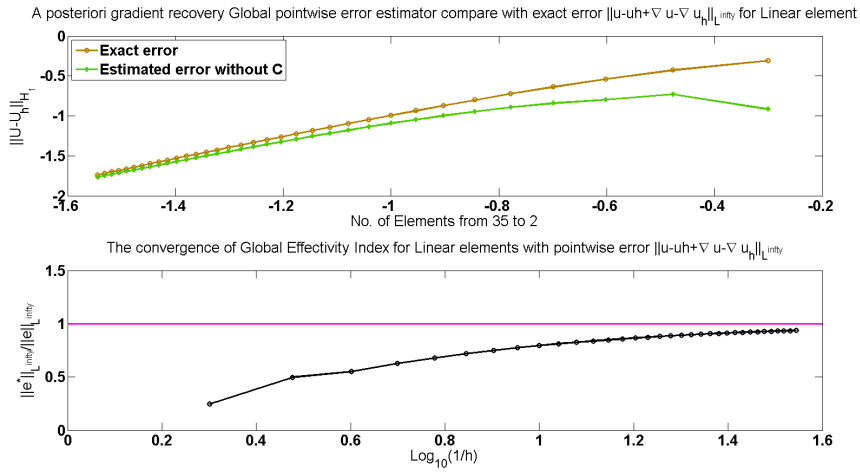

Figure B.16: Z-Z point-wise error estimator and the global effectivity index

B.3.4 Z-Z Error Estimator in Energy Norm

The *a posteriori* error estimator based on superconvergent patch recovery in energy norm is defined as:

$$\begin{aligned} \|e\|_e \equiv \|u-u_h\|_e &= \Big(\int_\Omega (u-u_h)^2 + (\nabla u - \nabla u_h)^2\Big)^{\frac{1}{2}} \\ \approx \|e^{scp}\|_e &= \Big(\int_\Omega (u_h-u_h)^2 + (\sigma^* - \nabla u_h)^2\Big)^{\frac{1}{2}} \end{aligned} \tag{B.60}$$

Hence the global error estimator in energy norm can be expressed as the summation of the local error indicators:

$$\|e^{scp}\|_e = \sum_{K\subset\mathcal{T}} \Big(\int_K (\sigma^* - \nabla u_h)^2\Big)^{\frac{1}{2}}.$$

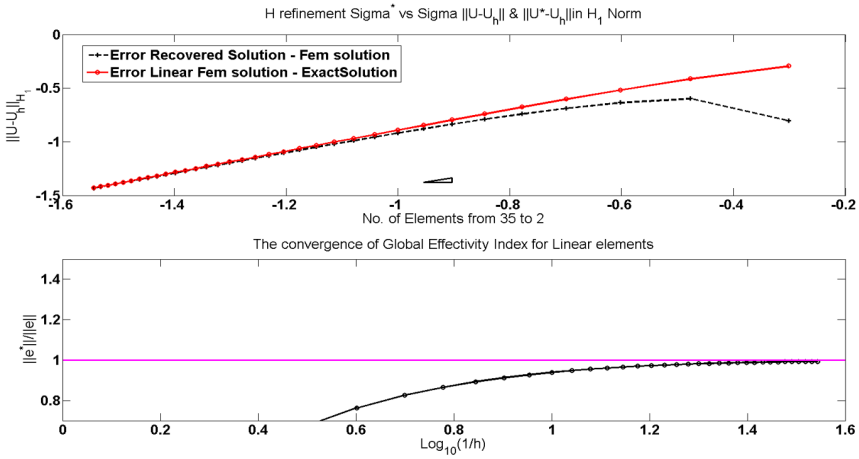

Figure B.17: Z-Z H^1 error estimator and effectivity index with linear element

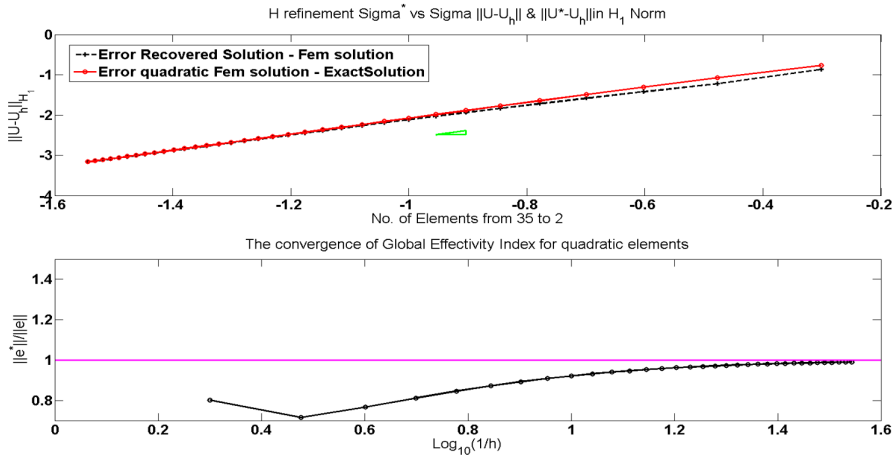

Figure B.18: Z-Z H^1 error estimator and effectivity index with quadratic element

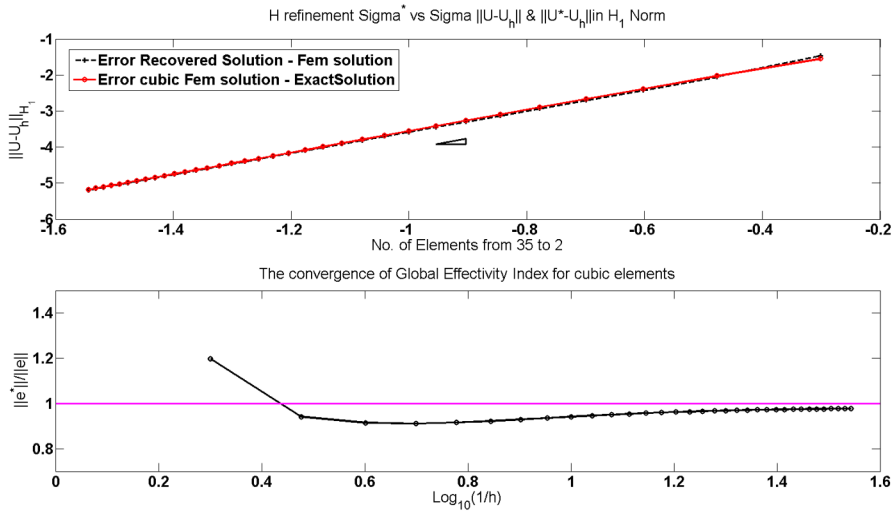

Figure B.19: Z-Z H^1 error estimator and effectivity index with cubic element

The above three Figures depicted the numerical results of our own codes derived from theorems in [345] and [346] by Zienkiewicz and Zhu. The benchmark problem 2 is solved and results are compared with analytical solution. The effectivity indices for element order $p = 1, 2, 3$ are asymptotically converge to 1, and the speed of convergence is superior when compared with other gradient recovery techniques like L_2 projection [329] and H-C extrapolation [168]. The recovered gradients are superconvergent for 1D elements of order $p = 1, 2, 3$, especially ultra-superconvergent for quadratic elements. Further numerical results and explanation of performance of Z-Z error estimator can be found in [340, 34] and [14].

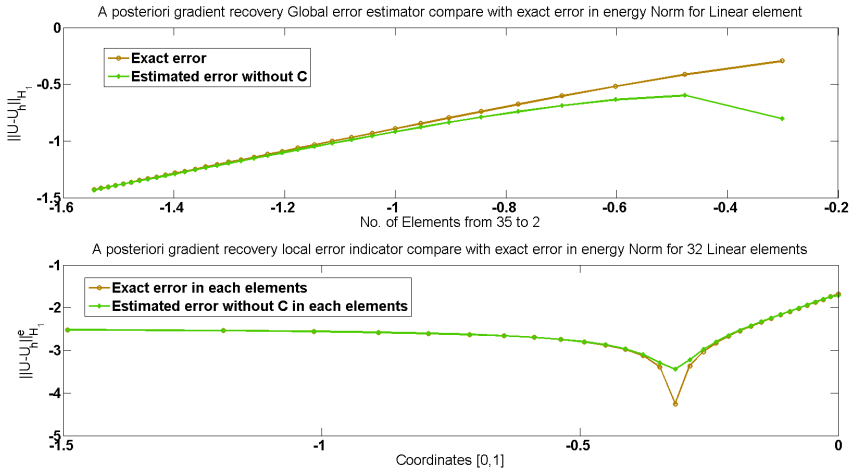

Figure B.20: Z-Z H^1 local error indicator - Linear element

In Figure B.20, the local Z-Z error indicator for linear element is interpreted. It can be compared with Figure B.1 and B.8, both the benchmark problem 2 is solved. It emphasized that the Z-Z error indicator is as good as the implicit element residual error estimator in the local sense, and even better efficiency than the implicit element residual on the computational cost side, since the implicit element residual indicator is very sensitive to the bubble function selected, and require solving a higher degree of linear system of equations in each elements. Nevertheless, the Z-Z indicator highly rely on the superconvergent property of the sampling points, and the position of the sampling points are somehow implicit to determined in higher dimensional elements with various geometry properties (simplex, pyramid, etc.) [346].

B.3.5 Conclusion

As expected, the major merits of the Z^2 error estimator are the economical cost and straightforward implementation. Moreover, since this type of estimator is based on the superconvergent property of the points within each elements instead of the structure of the original problem. Hence, it is robust and applicable to a wide range of engineering applications in practice. Nonetheless, the weakness of such estimators is that they do not account the error for the solution potential itself, but merely offer an effective recovered gradient of the FEM solution. Overall, all

three types of error estimator and indicator satisfied the qualified error estimator conditions 1-4 and 6 in section 4.4.

Appendix C

Architecture of MoFEM

C.1 Introduction

Finite element softwares are generally complex economical systems. They involve the process of managing mesh and topology related complexities, sparse algebra and complications related to approximation, integration or dense tensor algebra at integration point level.

Traditional finite element codes are element-centric (type of element defines approximation space and base) and therefore cannot exploit the potential of emerging approximation methods. The MoFEM software uses recent advances in finite element technology and modern data structures, enabling the efficient solution of difficult, multi-domain, multi-scale and multi-physics problems. In this code, design of data structures for approximation of fields variables are independent of the specific finite element (e.g. Lagrangian, Nedelec, Raviart-Thomas) being used, such that a finite element is constructed by a set of lower dimension entities on which the approximation fields are defined. Consequently, different approximation spaces such as: H^1, L_2, $H(curl)$ and $H(div)$ can be combined without constraints, in order to create the ability to solve complex problems efficiently. Arbitrary hierarchical polynomial basis can be used on element level (e.g. tetrahedra, triangles, hexahedra, prism, etc). The user defined data operator can act on fields directly associated with entities (vertices, edges, faces, volumes) rather than finite element itself.

In Figure C.1 below, the work distribution of such composed system in MoFEM is briefly outlined. The evaluation of hierarchical finite element approximation spaces are solely managed by MoFEM. For detailed informations please refer to [199].

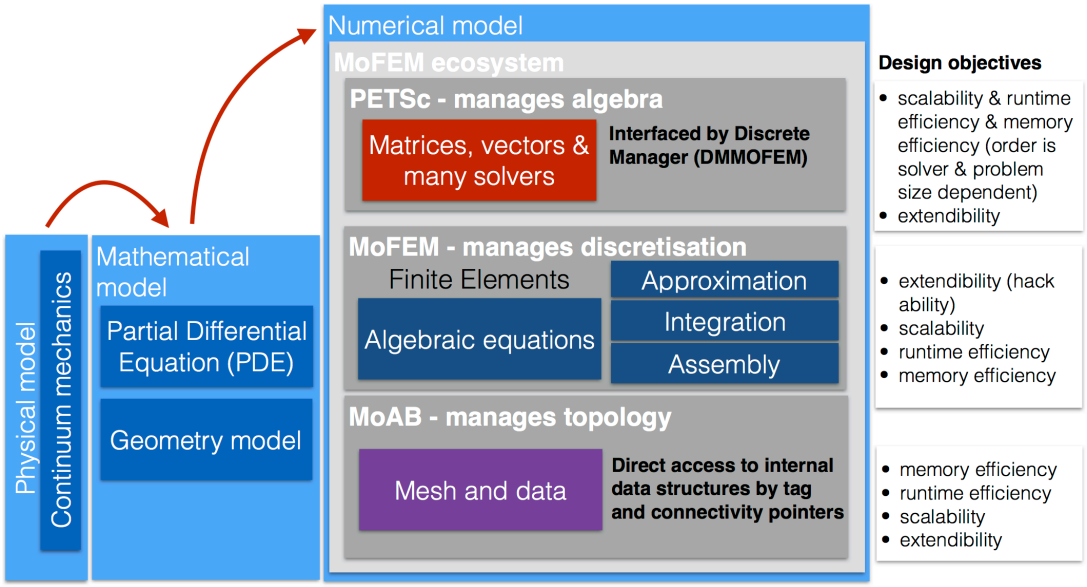

Figure C.1: Finite element analysis managing process [199]

In Figure C.2, a relationship between these softwares is addressed. The ecosystem of MoFEM integrated with Topology (MOAB and associated tools) and advanced scientific computing tools for Algebra (PETSc, and associated tools), which allows developers (/end user) to focus their attention on the development of finite element technology and/or physical applications under consideration. The resilience of the ecosystem is guaranteed because the underpinning components have sustainable funding, dynamic and established group of developers and significant user base.

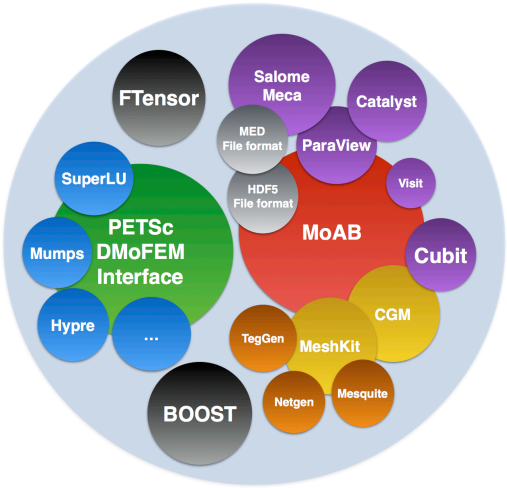

Figure C.2: Diagram of computational tools, the economic system of computational tools

In recent years, it has been recognised that there is a vast amount of literature describing and exemplifying the mixed formulation finite element method applied to different engineering applications [85, 61]. The solvability, stability and optimal convergence discretisation property of mixed FEM has been proven both analyti-

cally and numerically [84, 25]. Stringent comparison has been made between the least square method and the ultra-weak variational formulation in [152]. Two dimensional benchmark problems with regular and singular domain are resolved, the UW formulation outperforms the least square (LS) method in view of accuracy and conditioning for restricted degrees of freedom. The choice of approximation order for vector and scalar field basis of mixed FE are investigated throughly by Arnold, *et al.* in [26].

The University of Glasgow in house software MoFEM implemented the ultra-weak variational formulation method with hierarchical approximation basis for stationary transport / heat-conduction problems, both localized h and p adaptivities are available for analysis. This is another research direction for our current acoustic solver, an efficient and rigorous error estimator and adaptivity scheme can be developed upon the UW formulation, and extended to Helmholtz equation.

C.2 A Very Brief Description of the Parallel Computations

The partitioned mesh is required prior to the calculation, in order to support the parallel simulation. MoAB uses the ParMETIS library tool to initialise this feature [191, 308]. Intuitively speaking, it reads local meshes on each processors, and then stores the entities (e.g. vertices, edges) as tags or tagged sets (one set per part).

The complexities associated with parallel communications are hidden through the MoFEM interface using both PETSC and MOAB functions for management of distributed data. The MoFEM partitioning tool takes entities adjacent to elements and constructs an adjacency matrix that is partitioned using PETSC, which calls metis/parmetis, and/or other graph partitioning libraries [55]. In the partitioned mesh, each entity, which includes 3D entities and lower dimension adjacent entities, are assigned to a partition tag. MoFEM has its own mesh partitioning tools called MoFEM*part* that will partition the mesh and store as entity sets. In case the mesh has not created all the lower dimension adjacencies before partitioning, one should always use MoFEM to partition the mesh.

MoFEM takes care of setting elements and the distribution of degrees of freedom. Key functions are implemented in the **ProblemsManager** interface. The Function **ProblemsManager** deals with the number of degrees of freedom, setting local and global numbers, determining ghost DOFs, setting partition to finite elements, and everything else that is needed to construct parallel matrices in PETSC. During the matrix assembling process, every element that has attached a partition number equal to the rank of processors is evaluated.

In distributed memory systems, each processor (node) has its own memory, and data is stored locally. Thus, communication libraries are required to passing and receiving the data across local memories of each processors. The most commonly used communication library is the message passing interface (1992 [319, 162, 163]), which MPI is commonly chosen when compared to other alternatives (e.g. parallel

virtual machine [154]) because of its three features, portability, functionality and efficiency [294]. The MPI library tool is merely dealing with the communication part of the program and nothing else. The MPI supports a vast range of programming languages including C, C++ and FORTRAN. For details about how MPI is implemented, communicates and operates, please refer to [199] and [98].

C.3 Input Data for Polychromatic Wave Acoustic Solver in MoFEM

The main purpose of this section is to stipulate the format of time dependent input data supplied by the user of the acoustic solver in MoFEM. The algorithms of Polychromatic wave acoustic solver is introduced in section 5.4. First of all, A .txt file with two arrays: time steps and amplitudes are required to be defined in the following format:

t_m	$a(t_m)$
1	a_1
2	a_2
$\vdots$	$\vdots$
$M-1$	a_{M-1}

Table C.1: Format of input signal profiles

Table C.1 denotes the data of the discretised signal profile. It can either be polychromatic or monochromatic signal depending on different physical scenarios. As shown in Figure 5.6, the discretised input signals can be any user-defined shape. The simplest examples are square waves and sinusoidal waves.

The Fourier transformation is performed by the open source FFT library - "Keep It Simple, Stupid FFT" [80].

Appendix D

Non-Linear Time Dependant Thermal Governing Equation

D.1 Introduction

Thermal problems are the most fundamental variation of the Elliptic differential operator, and the Helmholtz problem is a special variation of coercive type Elliptic operator. Therefore, in order to implements the more complicated Helmholtz operator for modelling of acoustic wave propagation, the development of basic solver for the non-linear dynamic finite element problem with Elliptic structure is compulsory. Thus, the following works has been done in advance. The numerical examples and convergence results are tested.

D.2 Mathematical Formulation

Thermal equation plays an important role in the heat transfer engineering applications, it describes the energy transfer between different material bodies caused by temperature difference,

$$-\nabla^T \cdot (K\nabla T) = -Q + \rho c_p \frac{\partial T}{\partial t} \tag{D.1}$$

where $\rho c_p \frac{\partial T}{\partial t}$ is the unsteady term of the above equation. Explicitly, ρ is the material density, c_p represents the heat capacity, and $\frac{\partial T}{\partial t}$ generally denotes as $\dot{T}$ is the temperature rate of change with respect to time. $Q(x, y, z, t)$ is the inner heat generation (rate) per unit volume of the body. K denotes the heat conductivity, it

is a constant for isotropic material, otherwise, a 3×3 diagonal second order tensor is implied. The left hand side of the Thermal equation constitutes stiffness matrix only, which is the same as the stiffness term in Helmholtz equation despite the additional oscillatory mass term.

There are mainly three types of heat transfer, and they can be derived as boundary condition in the following way:

$$-K\nabla T \cdot n^T = q \text{ at any point of } \partial\Omega \tag{D.2}$$

is the heat flux boundary condition, where $n^T = [n_x, n_y, n_z]$ is the direction cosines of the normal to the surface and q is the flux density. Moreover, the convection boundary condition is:

$$-K\nabla T \cdot n^T = h(T_s - T_a) \text{ at any point of } \partial\Omega \tag{D.3}$$

where h is the known convection coefficients, T_s is the surface temperature and T_a is the ambient temperature. The heat convection occurs due to the movements of the fluids or air passing through the material body. The last set of boundary condition has many different forms, the typical one is:

$$-K\nabla T \cdot n^T = \sigma\epsilon(T_s^4 - T_\infty^4) \text{ at any point of } \partial\Omega \tag{D.4}$$

where σ is the Stefan-Boltzmann constant ($\sigma = 5.67 \cdot 10^{-8} W \cdot m^{-2} \cdot K^{-4}$), ϵ is the material emissivity of the body and T_∞ is the Kelvin temperature of the infinite environment. The term radiation existed due to the fact that the temperature is emitted from the surface of the body, when the temperature of the body is exceed absolute zero, and the body also have ability to absorb, reflect or transmit thermal radiation [276, 244]. Since the radiation boundary condition above has quartic terms involved, we need numerical methods like Newton Raphson to linearize the non-linear algebraic equation, then use linear solver such as Generalized Minimum Residual method (GMRES) to solve the problem. The procedure described in two steps as:

$$\begin{aligned} &1.\ J(x_n)\Delta x_n = -F(x_n) \\ &2.\ x_{n+1} = x_n + \Delta x_n \end{aligned} \tag{D.5}$$

such that $F(x_n)$ is the element residual vector of the system of algebraic equation in the iteration step n.

$$F(x_n) = b - A(x_n)x_n \tag{D.6}$$

and the Jacobian (tangent) matrix $J(x_n)$ is

$$J(x_n) = \frac{\partial F(x_n)}{\partial x_n} \tag{D.7}$$

for the Newton-Raphson method, it should be noticed that the choice of the tangent matrix does not affect the solution quality but merely the speed of convergence. The tangent matrix for the non-linear radiation BC is calculated as follows:

$$J(T)_{ij} = \int_{\partial\Omega} 4\sigma\epsilon T^3 N_i N_j ds \tag{D.8}$$

where i, j is the row and column indices of the Jacobian matrix [70].

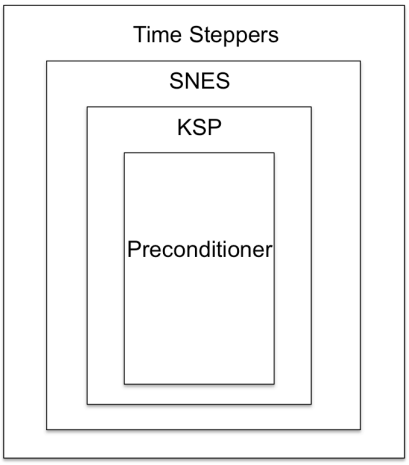

Figure D.1: The relationship between different solvers from PETSc in each iteration

As depicted in Figure D.1, during each iteration stpes, the TS (time step) solver calls the SNES (Non-linear method) solver. After linearization process, it subsequently calls the KSP (linear solver) to solve the preconditioned system of linear equations which applied algorithms such as GMRES or Richardson, etc. [55].

D.3 Numerical Results

In the two benchmark problems below, numerical results are compared between thermal conductive solver in MoFEM and commercial software Ansys to verify the correctness of implementation [22]. Beside the Ansys website, the first benchmark problem was also introduced in example 6.6.1 from the book: "Fundamental of the finite element method for Heat Conduction and Fluid flow" [244].

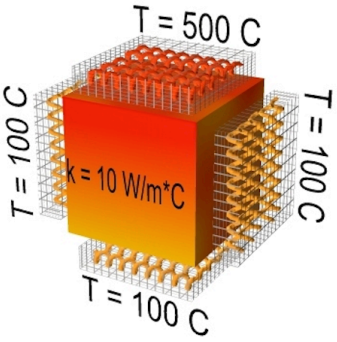

Figure D.2: Benchmark problem 1 [22]

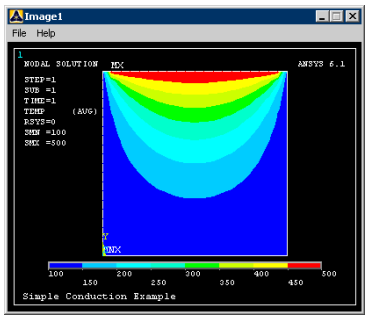

Figure D.3: Numerical result from Ansys [22]

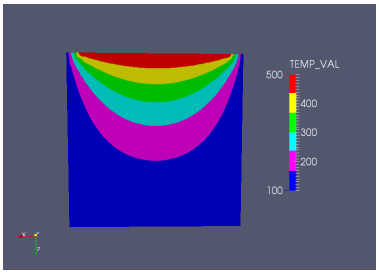

Figure D.4: Numerical result from MoFEM

In example 2, there is a zero convection boundary condition on the bottom of the unit cube, we thus apply the Generalized Minimal Residual method in the KSP solver and set the pre-conditioner to be incomplete LU factorization, then imposed the quadratic Legendre hierarchical shape functions. From both figures, it can be

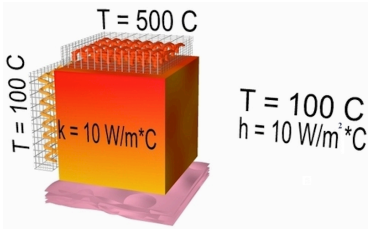

Figure D.5: Benchmark problem 2 [22]

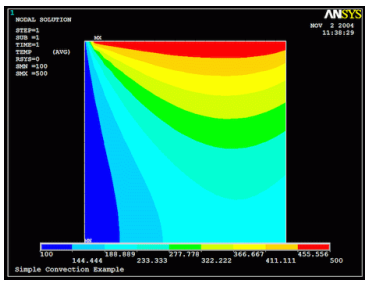

Figure D.6: Numerical result from Ansys [22]

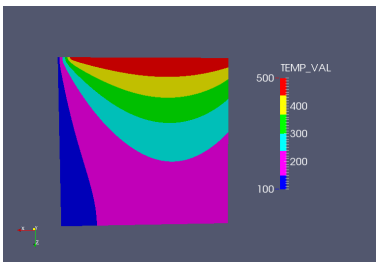

Figure D.7: Numerical result from MoFEM

said that qualitatively (intuitively) the results from thermal solver in MoFEM are consistent with the Ansys software.

D.4 Convergence Test

To this end, we adopt the Backward-Euler method as the time iteration scheme (TS), as well as the iterative Newton-line search method from SNES solver. The maximum iteration step used in previous examples is 100, and the absolute/relative convergence tolerance was set to 1e-8. We gradually increase the order of polynomials selected as Neumann BC from 1 to 4 (e.g. $\nabla T = T_s^n - T_a^n$, where T_s is constant and $n \in [1, 4]$). The motivation of this assessment is to study the rate of convergence while adopt the iterative methods to solve highly nonlinearity PDEs. Newton-line search method are found to be the best method for the test problem. Thus, we find out that:

- $\nabla T = T_s^n - T_a^n$ $n = 4$, the SNES solver converges sub-linearly. And it takes average of 10 time steps to reach the tolerance.
- $\nabla T = T_s^n - T_a^n$ $n = 3$, the SNES solver converges super-linearly. And it takes average of 4 time steps to reach the tolerance.
- $\nabla T = T_s^n - T_a^n$ $n = 2$, the SNES solver behaves approximately quadratic convergence. And it takes average of 3 time steps to reach the tolerance.

This test is omitted for case $n = 1$ since it is analogy to the general linear problems. The reason of slow rate of convergence occurs with higher order polynomials might because of the root multiplicity increased with polynomial orders. Thus, higher order elements are required in order to solve the physical problems with higher-order polynomial BCs.

Bibliography

[1] *Acoustic Wave Propagation in Microfluidic Application with Hierarchical Finite Element*. Zenodo, March 2016.

[2] *A-Priori Error Estimator based Hierarchical p Adaptivity Scheme for Acoustic Problems*. Zenodo, March 2017.

[3] Milton Abramowitz and Irene A Stegun. *Handbook of mathematical functions: with formulas, graphs, and mathematical tables*, volume 55. Courier Corporation, 1964.

[4] Milton Abramowitz, Irene A Stegun, et al. Handbook of mathematical functions. *Applied Mathematics Series*, 55:62, 1966.

[5] CJ Acott. The diving" law-ers": A brief resume of their lives. 1999.

[6] S Adjerid, M Aiffa, and JE Flaherty. Hierarchical finite element bases for triangular and tetrahedral elements. *Computer Methods in Applied Mechanics and Engineering*, 190(22):2925–2941, 2001.

[7] Mark Ainsworth. The influence and selection of subspaces for a posteriori error estimators. *Numerische Mathematik*, 73(4):399–418, 1996.

[8] Mark Ainsworth. Identification and a posteriori estimation of transported errors in finite element analysis. *Computer methods in applied mechanics and engineering*, 176(1):3–18, 1999.

[9] Mark Ainsworth. Discrete dispersion relation for hp-version finite element approximation at high wave number. *SIAM Journal on Numerical Analysis*, 42(2):553–575, 2004.

[10] Mark Ainsworth and Joe Coyle. Hierarchic finite element bases on unstructured tetrahedral meshes. *International journal for numerical methods in engineering*, 58(14):2103–2130, 2003.

[11] Mark Ainsworth and Alan Craig. A posteriori error estimators in the finite element method. *Numerische Mathematik*, 60(1):429–463, 1991.

[12] Mark Ainsworth and J Tinsley Oden. A unified approach to a posteriori error estimation using element residual methods. *Numerische Mathematik*, 65(1):23–50, 1993.

[13] Mark Ainsworth and J Tinsley Oden. A posteriori error estimation in finite element analysis. *Computer Methods in Applied Mechanics and Engineering*, 142(1):1–88, 1997.

[14] Mark Ainsworth and J Tinsley Oden. *A posteriori error estimation in finite element analysis*, volume 37. John Wiley & Sons, 2011.

[15] Mark Ainsworth and Bill Senior. Aspects of an adaptive hp-finite element method: Adaptive strategy, conforming approximation and efficient solvers. *Computer Methods in Applied Mechanics and Engineering*, 150(1):65–87, 1997.

[16] M Alghane, BX Chen, Yong Qing Fu, Yifan Li, JK Luo, and AJ Walton. Experimental and numerical investigation of acoustic streaming excited by using a surface acoustic wave device on a 128 ° yx-linbo3 substrate. *Journal of Micromechanics and Microengineering*, 21(1):015005, 2010.

[17] M Alghane, BX Chen, YQ Fu, Y Li, JK Luo, and AJ Walton. Experimental and numerical investigation of acoustic streaming excited by using a surface acoustic wave device on a 128 ° yx-linbo3 substrate. *Journal of Micromechanics and Microengineering*, 21(1):015005, 2011.

[18] M Alghane, YQ Fu, BX Chen, Y Li, MPY Desmulliez, and AJ Walton. Scaling effects on flow hydrodynamics of confined microdroplets induced by rayleigh surface acoustic wave. *Microfluidics and nanofluidics*, 13(6):919–927, 2012.

[19] Mansour Alghane, BX Chen, Yong Qing Fu, Yifan Li, Marc Phillipe Yves Desmulliez, Mazher-Iqbal Mohammed, and AJ Walton. Nonlinear hydrodynamic effects induced by rayleigh surface acoustic wave in sessile droplets. *Physical Review E*, 86(5):056304, 2012.

[20] Mansuor Mohamed Alghane. *Surface acoustic wave streaming in a microfluidic system*. PhD thesis, Heriot-Watt University, 2013.

[21] Patrick R Amestoy, Iain S Duff, and J-Y L'Excellent. Multifrontal parallel distributed symmetric and unsymmetric solvers. *Computer methods in applied mechanics and engineering*, 184(2):501–520, 2000.

[22] ansys. *Ansys examples*. retrieved from http://www.mece.ualberta.ca/tutorials/, on July 2014.

[23] Xavier Antoine, Helene Barucq, and Abderrahmane Bendali. Bayliss–turkel-like radiation conditions on surfaces of arbitrary shape. *Journal of Mathematical Analysis and Applications*, 229(1):184–211, 1999.

[24] Douglas N Arnold, Franco Brezzi, Bernardo Cockburn, and L Donatella Marini. Unified analysis of discontinuous galerkin methods for elliptic problems. *SIAM journal on numerical analysis*, 39(5):1749–1779, 2002.

[25] Douglas N Arnold, Richard S Falk, and Jay Gopalakrishnan. Mixed finite element approximation of the vector laplacian with dirichlet boundary conditions. *Mathematical Models and Methods in Applied Sciences*, 22(09):1250024, 2012.

[26] Douglas N Arnold, Richard S Falk, and Ragnar Winther. Differential complexes and stability of finite element methods i. the de rham complex. In *Compatible spatial discretizations*, pages 23–46. Springer, 2006.

[27] RM Arzt, E Salzmann, and K Dransfeld. Elastic surface waves in quartz at 316 mhz. *Applied Physics Letters*, 10(5):165–167, 1967.

[28] Harm Askes. Advanced spatial discretisation strategies for localised failure-mesh adaptivity and meshless methods. 2000.

[29] R Jeremy Astley. Numerical methods for noise propagation in moving flows, with application to turbofan engines. *Acoustical science and technology*, 30(4):227–239, 2009.

[30] John V Atanasoff and Philip J Hart. Dynamical determinitation of the elastic constants and their temperature coefficients for quartz. *Physical Review*, 59(1):85, 1941.

[31] Owe Axelsson and Janos Karatson. *Efficient preconditioned solution methods for elliptic partial differential equations*. Bentham Science Publishers, 2011.

[32] Abdul Kadir Aziz. *The mathematical foundations of the finite element method with applications to partial differential equations*. Academic Press, 2014.

[33] Ivo Babuška. *Accuracy estimates and adaptive refinements in finite element computations.* John Wiley & Sons, 1986.

[34] Ivo Babuška. *Finite Elements: An Introduction to the Method and Error Estimation.* Oxford University Press, 2011.

[35] Ivo Szabò Barna Babuška. *Introduction to Finite Element Analysis: Formulation, Verification and Validation*. John Wiley and Sons, 2011.

[36] I Babuška and BQ Guo. The h, p and hp version of the finite element method; basis theory and applications. *Advances in Engineering Software*, 15(3-4):159–174, 1992.

[37] I Babuska, F Ihlenburg, T Strouboulis, and SK Gangaraj. A posteriori error estimation for finite element solutions of helmholtz'equation-part ii: Estimation of the pollution error. *International Journal for Numerical Methods in Engineering*, 40(21):3883–3900, 1997.

[38] I Babuška, T Strouboulis, SK Gangaraj, and CS Upadhyay. Pollution error in the h-version of the finite element method and the local quality of the recovered derivatives. *Computer Methods in Applied Mechanics and Engineering*, 140(1-2):1–37, 1997.

[39] I Babuška, T Strouboulis, A Mathur, and CS Upadhyay. Pollution-error in the h-version of the finite-element method and the local quality of a-posteriori error estimators. *Finite Elements in Analysis and Design*, 17(4):273–321, 1994.

[40] I Babuška, T Strouboulis, and CS Upadhyay. A model study of the quality of a posteriori error estimators for linear elliptic problems. error estimation in the interior of patchwise uniform grids of triangles. *Computer Methods in Applied Mechanics and Engineering*, 114(3-4):307–378, 1994.

[41] I Babuška, T Strouboulis, and CS Upadhyay. A model study of the quality of a posteriori error estimators for linear elliptic problems. error estimation in the interior of patchwise uniform grids of triangles. *Computer Methods in Applied Mechanics and Engineering*, 114(3):307–378, 1994.

[42] I Babuška, T Strouboulis, CS Upadhyay, and SK Gangaraj. A posteriori estimation and adaptive control of the pollution error in the h-version of the finite element method. *International journal for numerical methods in engineering*, 38(24):4207–4235, 1995.

[43] Ivo Babuška, Michael Griebel, and Juhani Pitkäranta. The problem of selecting the shape functions for ap-type finite element. *International Journal for Numerical Methods in Engineering*, 28(8):1891–1908, 1989.

[44] Ivo Babuška, Frank Ihlenburg, Ellen T Paik, and Stefan A Sauter. A generalized finite element method for solving the helmholtz equation in two dimensions with minimal pollution. *Computer methods in applied mechanics and engineering*, 128(3-4):325–359, 1995.

[45] Ivo Babuška, Frank Ihlenburg, Ellen T Paik, and Stefan A Sauter. A generalized finite element method for solving the helmholtz equation in two dimensions with minimal pollution. *Computer Methods in Applied Mechanics and Engineering*, 128(3):325–359, 1995.

[46] Ivo Babuška and Jens M Melenk. The partition of unity method. *International journal for numerical methods in engineering*, 40(4):727–758, 1997.

[47] Ivo Babuška and Werner C Rheinboldt. A-posteriori error estimates for the finite element method. *International Journal for Numerical Methods in Engineering*, 12(10):1597–1615, 1978.

[48] Ivo Babuska and Werner C Rheinboldt. A posteriori error analysis of finite element solutions for one-dimensional problems. *SIAM Journal on Numerical Analysis*, 18(3):565–589, 1981.

[49] Ivo Babuška, T Strouboulis, CS Upadhyay, SK Gangaraj, and K Copps. Validation of a posteriori error estimators by numerical approach. *International journal for numerical methods in engineering*, 37(7):1073–1123, 1994.

[50] Ivo M Babuska and Stefan A Sauter. Is the pollution effect of the fem avoidable for the helmholtz equation considering high wave numbers? *SIAM Journal on numerical analysis*, 34(6):2392–2423, 1997.

[51] Ivo M Babuska and Stefan A Sauter. Is the pollution effect of the fem avoidable for the helmholtz equation considering high wave numbers? *SIAM review*, 42(3):451–484, 2000.

[52] J.E. Osborn Babuska I., U. Banerjee. *Quadrature error in meshless methods.* in preparation.

[53] I Babuvška and Werner C Rheinboldt. Error estimates for adaptive finite element computations. *SIAM Journal on Numerical Analysis*, 15(4):736–754, 1978.

[54] AJ Baker and PD Manhardt. Finite element analysis of aeroacoustic jet-flap flows. 1977.

[55] Satish Balay, J Brown, Kris Buschelman, Victor Eijkhout, W Gropp, D Kaushik, M Knepley, L Curfman McInnes, B Smith, and Hong Zhang. Petsc users manual revision 3.3. *Computer Science Division, Argonne National Laboratory, Argonne, IL*, 2012.

[56] S.S. Banach. *A course of functional analysis*. Kiev (In Ukrainian), 1948.

[57] Michael Bane, Rainer Keller, Michael Pettipher, and Ian Smith. A comparison of mpi and openmp implementations of a finite element analysis code. *Proceedings of Cray User Group Summit (CUG 2000)*, 2000.

[58] Randolph E Bank and Alan Weiser. Some a posteriori error estimators for elliptic partial differential equations. *Mathematics of Computation*, 44(170):283–301, 1985.

[59] John Barlow. Optimal stress locations in finite element models. *International Journal for Numerical Methods in Engineering*, 10(2):243–251, 1976.

[60] Robert G Bartle. *The elements of integration and Lebesgue measure*. John Wiley & Sons, 2014.

[61] KJ Bathe and H Saunders. Finite element procedures in engineering analysis, 1984.

[62] Klaus-Jürgen Bathe. *Finite element procedures*. Klaus-Jurgen Bathe, 2006.

[63] Alvin Bayliss, Max Gunzburger, and Eli Turkel. Boundary conditions for the numerical solution of elliptic equations in exterior regions. *SIAM Journal on Applied Mathematics*, 42(2):430–451, 1982.

[64] Alvin Bayliss and Eli Turkel. Radiation boundary conditions for wave-like equations. *Communications on Pure and applied Mathematics*, 33(6):707–725, 1980.

[65] Ahmet Teufik Becene. Parallel processing of finite strain, materially nonlinear and incompressible finite element analysis problems. 2003.

[66] Ari Ben-Menahem and Sarva Jit Singh. *Seismic waves and sources*. Springer Science & Business Media, 2012.

[67] Jean-Pierre Berenger. A perfectly matched layer for the absorption of electromagnetic waves. *Journal of computational physics*, 114(2):185–200, 1994.

[68] Vincent Bergeaud and Vincent Lefebvre. Salome. a software integration platform for multi-physics, pre-processing and visualisation. 2010.

[69] Jöran Bergh and Jorgen Lofstrom. *Interpolation spaces: an introduction*, volume 223. Springer Science & Business Media, 2012.

[70] Jean-Michel Bergheau and Roland Fortunier. *Finite element simulation of heat transfer*. John Wiley & Sons, 2013.

[71] Hadrien Bériot, Gwénaël Gabard, and Emmanuel Perrey-Debain. Analysis of high-order finite elements for convected wave propagation. *International journal for numerical methods in engineering*, 96(11):665–688, 2013.

[72] Hadrien Bériot, Albert Prinn, and Gwénaël Gabard. Efficient implementation of high-order finite elements for helmholtz problems. *International Journal for Numerical Methods in Engineering*, 2015.

[73] Christine Bernardi and Vivette Girault. A local regularization operator for triangular and quadrilateral finite elements. *SIAM Journal on Numerical Analysis*, 35(5):1893–1916, 1998.

[74] Daniel Bernoulli. Hydrodynamica. *Dulsecker. Consultable en ligne http://imgbase-scd-ulp. u-strasbg. fr/displayimage. php*, 1738.

[75] Peter Bettess. Infinite elements. *International Journal for numerical methods in engineering*, 11(1):53–64, 1977.

[76] D Beyssen, L Le Brizoual, O Elmazria, and P Alnot. Microfluidic device based on surface acoustic wave. *Sensors and Actuators B: Chemical*, 118(1):380–385, 2006.

[77] J Biermann and O von Estorff. Higher order finite and infinite acoustical elements based on ultraspherical polynomials. *Acta Acustica united with Acustica*, 99(5):759–769, 2013.

[78] Ted D Blacker, William J Bohnhoff, and Tony L Edwards. Cubit mesh generation environment. volume 1: Users manual. Technical report, Sandia National Labs., Albuquerque, NM (United States), 1994.

[79] Said Boluriaan and Philip J Morris. Acoustic streaming: from rayleigh to today. *International Journal of aeroacoustics*, 2(3):255–292, 2003.

[80] Mark Borgerding. Kiss fft. *http://sourceforge.net/projects/kissfft/*, 2014.

[81] Carlo L Bottasso, Stefano Micheletti, and Riccardo Sacco. The discontinuous petrov–galerkin method for elliptic problems. *Computer Methods in Applied Mechanics and Engineering*, 191(31):3391–3409, 2002.

[82] Dietrich Braess and Rüdiger Verfürth. A posteriori error estimators for the raviart–thomas element. *SIAM Journal on Numerical Analysis*, 33(6):2431–2444, 1996.

[83] Susanne C Brenner and Ridgway Scott. *The mathematical theory of finite element methods*, volume 15. Springer Science & Business Media, 2008.

[84] Franco Brezzi and Klaus-Jürgen Bathe. A discourse on the stability conditions for mixed finite element formulations. *Computer methods in applied mechanics and engineering*, 82(1-3):27–57, 1990.

[85] Franco Brezzi and Michel Fortin. *Mixed and hybrid finite element methods*, volume 15. Springer Science & Business Media, 2012.

[86] Alexander N Brooks and Thomas JR Hughes. Streamline upwind/petrov-galerkin formulations for convection dominated flows with particular emphasis on the incompressible navier-stokes equations. *Computer methods in applied mechanics and engineering*, 32(1-3):199–259, 1982.

[87] P Brunet, M Baudoin, O Bou Matar, and F Zoueshtiagh. Droplet displacements and oscillations induced by ultrasonic surface acoustic waves: a quantitative study. *Physical Review E*, 81(3):036315, 2010.

[88] Henrik Bruus. Acoustofluidics 2: Perturbation theory and ultrasound resonance modes. *Lab on a Chip*, 12(1):20–28, 2012.

[89] Thu-Hang Bui, Dat Nguyen Tien, Tung Bui Duc, and Trinh Chu Duc. 3-d finite element modeling of saw sensing system for liquids. In *Advanced Intelligent Mechatronics (AIM), 2012 IEEE/ASME International Conference on*, pages 782–787. IEEE, 2012.

[90] David S Burnett. A three-dimensional acoustic infinite element based on a prolate spheroidal multipole expansion. *The Journal of the Acoustical Society of America*, 96(5):2798–2816, 1994.

[91] James J Campbell and William R Jones. Propagation of surface waves at the boundary between a piezoelectric crystal and a fluid medium. *IEEE Transactions on Sonics and Ultrasonics*, 17(2):71–76, 1970.

[92] LM Campos. On 36 forms of the acoustic wave equation in potential flows and inhomogeneous media. *Applied Mechanics Reviews*, 60(4):149–171, 2007.

[93] CD Cantwell, SJ Sherwin, RM Kirby, and PHJ Kelly. From h to p efficiently: Strategy selection for operator evaluation on hexahedral and tetrahedral elements. *Computers & Fluids*, 43(1):23–28, 2011.

[94] William T Carter, T-L Sham, and Kincho H Law. A parallel finite element method and its prototype implementation on a hypercube. *Computers & structures*, 31(6):921–934, 1989.

[95] Paul Castillo, Bernardo Cockburn, Ilaria Perugia, and Dominik Schötzau. An a priori error analysis of the local discontinuous galerkin method for elliptic problems. *SIAM Journal on Numerical Analysis*, 38(5):1676–1706, 2000.

[96] Olivier Cessenat and Bruno Despres. Application of an ultra weak variational formulation of elliptic pdes to the two-dimensional helmholtz problem. *SIAM journal on numerical analysis*, 35(1):255–299, 1998.

[97] Olivier Cessenat and Bruno Després. Using plane waves as base functions for solving time harmonic equations with the ultra weak variational formulation. *Journal of Computational Acoustics*, 11(02):227–238, 2003.

[98] K Mani Chandy and Stephen Taylor. *An introduction to parallel programming*. Jones and Bartlett Publishers, Inc., 1992.

[99] JDN Cheeke and P Morisseau. Attenuation of rayleigh waves on a linbo3 crystal in contact with a liquid4he bath. *Journal of Low Temperature Physics*, 46(3-4):319–330, 1982.

[100] Huangxin Chen, Peipei Lu, and Xuejun Xu. A hybridizable discontinuous galerkin method for the helmholtz equation with high wave number. *SIAM Journal on Numerical Analysis*, 51(4):2166–2188, 2013.

[101] KN Chiang and RE Fulton. Concepts and implementation of parallel finite element analysis. *Computers & Structures*, 36(6):1039–1046, 1990.

[102] JR Cho and J Tinsley Oden. A priori modeling error estimates of hierarchical models for elasticity problems for plate-and shell-like structures. *Mathematical and computer modelling*, 23(10):117–133, 1996.

[103] K Christodoulou, O Laghrouche, MS Mohamed, and J Trevelyan. High-order finite elements for the solution of helmholtz problems. *Computers & Structures*, 191:129–139, 2017.

[104] Philippe G Ciarlet. *The finite element method for elliptic problems*, volume 40. Siam, 2002.

[105] Bernardo Cockburn, George E Karniadakis, and Chi-Wang Shu. The development of discontinuous galerkin methods. In *Discontinuous Galerkin Methods*, pages 3–50. Springer, 2000.

[106] David J Collins, Zhichao Ma, and Ye Ai. Highly localized acoustic streaming and size-selective submicrometer particle concentration using high frequency microscale focused acoustic fields. *Analytical chemistry*, 88(10):5513–5522, 2016.

[107] David Colton and Rainer Kress. *Inverse acoustic and electromagnetic scattering theory*, volume 93. Springer Science & Business Media, 2012.

[108] Ronald Cools. An encyclopaedia of cubature formulas. *Journal of complexity*, 19(3):445–453, 2003.

[109] Michael Cortis. *Numerical modelling of braided fibres for reinforced concrete*. PhD thesis, University of Glasgow, 2016.

[110] F Coulouvrat. On the equations of nonlinear acoustics. *J. Acoustique*, 5:321–359, 1992.

[111] Ben Cox. Acoustics for ultrasound imaging. *Lecture Notes, University College London*, 2013.

[112] A Del Grosso and G Righetti. Finite element techniques and artificial intelligence on parallel machines. *Computers & Structures*, 30(4):999–1007, 1988.

[113] L Demkowicz, Ph Devloo, and J Tinsley Oden. On an h-type mesh-refinement strategy based on minimization of interpolation errors. *Computer Methods in Applied Mechanics and Engineering*, 53(1):67–89, 1985.

[114] L Demkowicz, JT Oden, and T Strouboulis. Adaptive finite elements for flow problems with moving boundaries. part i: Variational principles and a posteriori estimates. *Computer methods in applied mechanics and engineering*, 46(2):217–251, 1984.

[115] L Demkowicz, JT Oden, and Tf Strouboulis. An adaptive p-version finite element method for transient flow problems with moving boundaries. In *Finite elements in fluids*, volume 1, pages 291–305, 1985.

[116] Leszek Demkowicz. *Computing with hp-ADAPTIVE FINITE ELEMENTS: Volume 1 One and Two Dimensional Elliptic and Maxwell problems*. CRC Press, 2006.

[117] Leszek Demkowicz, Jay Gopalakrishnan, and Antti H Niemi. A class of discontinuous petrov–galerkin methods. part iii: adaptivity. *Applied numerical mathematics*, 62(4):396–427, 2012.

[118] Leszek Demkowicz and Jayadeep Gopalakrishnan. A class of discontinuous petrov–galerkin methods. part i: The transport equation. *Computer Methods in Applied Mechanics and Engineering*, 199(23):1558–1572, 2010.

[119] Leszek Demkowicz and Jayadeep Gopalakrishnan. Analysis of the dpg method for the poisson equation. *SIAM Journal on Numerical Analysis*, 49(5):1788–1809, 2011.

[120] Leszek Demkowicz, J Tinsely Oden, Waldemar Rachowicz, and O Hardy. Toward a universal hp adaptive finite element strategy, part 1. constrained approximation and data structure. *Computer Methods in Applied Mechanics and Engineering*, 77(1-2):79–112, 1989.

[121] Leszek F Demkowicz and Jay Gopalakrishnan. An overview of the discontinuous petrov galerkin method. In *Recent Developments in Discontinuous Galerkin Finite Element Methods for Partial Differential Equations*, pages 149–180. Springer, 2014.

[122] Michael B Dentry, Leslie Y Yeo, and James R Friend. Frequency effects on the scale and behavior of acoustic streaming. *Physical Review E*, 89(1):013203, 2014.

[123] Arnaud Deraemaeker, Ivo Babuška, and Philippe Bouillard. Dispersion and pollution of the fem solution for the helmholtz equation in one, two and three dimensions. *International journal for numerical methods in engineering*, 46(4):471–499, 1999.

[124] Bruno Despres. Sur une formulation variationnelle de type ultra-faible. *Comptes rendus de l'Académie des sciences. Série 1, Mathématique*, 318(10):939–944, 1994.

[125] R Dias, EGD do Carmo, WJ Mansur, and CSG Monteiro. A discontinuous petrov–galerkin (dpg) formulation for the fem applied to the helmholtz equation for high wavenumbers. *Journal of the Brazilian Society of Mechanical Sciences and Engineering*, 39(5):1529–1544, 2017.

[126] Xiaoyun Ding, Peng Li, Sz-Chin Steven Lin, Zackary S Stratton, Nitesh Nama, Feng Guo, Daniel Slotcavage, Xiaole Mao, Jinjie Shi, Francesco Costanzo, et al. Surface acoustic wave microfluidics. *Lab on a Chip*, 13(18):3626–3649, 2013.

[127] Alexander A Doinikov. Acoustic radiation pressure on a compressible sphere in a viscous fluid. *Journal of Fluid Mechanics*, 267:1–22, 1994.

[128] Willy Dörfler. A convergent adaptive algorithm for poisson's equation. *SIAM Journal on Numerical Analysis*, 33(3):1106–1124, 1996.

[129] K Dransfeld and E Salzmann. Excitation, detection and attenuation of high-frequency elastic surface waves. *Physical acoustics*, 7:219–272, 2012.

[130] D Dreyer and O Von Estorff. Improved conditioning of infinite elements for exterior acoustics. *International Journal for Numerical Methods in Engineering*, 58(6):933–953, 2003.

[131] M Drolia, MS Mohamed, O Laghrouche, M Seaid, and J Trevelyan. Enriched finite elements for initial-value problem of transverse electromagnetic waves in time domain. *Computers & Structures*, 182:354–367, 2017.

[132] Jérôme Droniou. Non-coercive linear elliptic problems. *Potential Analysis*, 17(2):181–203, 2002.

[133] XY Du, Yong Qing Fu, JK Luo, AJ Flewitt, and WI Milne. Microfluidic pumps employing surface acoustic waves generated in zno thin films. *Journal of Applied Physics*, 105(2):024508, 2009.

[134] XY Du, ME Swanwick, Yong Qing Fu, JK Luo, AJ Flewitt, Dae-Sik Lee, Sunglyul Maeng, and WI Milne. Surface acoustic wave induced streaming and pumping in 128 y-cut linbo3 for microfluidic applications. *Journal of Micromechanics and Microengineering*, 19(3):035016, 2009.

[135] Yu Du and Haijun Wu. Preasymptotic error analysis of higher order fem and cip-fem for helmholtz equation with high wave number. *SIAM Journal on Numerical Analysis*, 53(2):782–804, 2015.

[136] Jürg Dual, Philipp Hahn, Ivo Leibacher, Dirk Möller, and Thomas Schwarz. Acoustofluidics 6: Experimental characterization of ultrasonic particle manipulation devices. *Lab on a Chip*, 12(5):852–862, 2012.

[137] Michael G Duffy. Quadrature over a pyramid or cube of integrands with a singularity at a vertex. *SIAM journal on Numerical Analysis*, 19(6):1260–1262, 1982.

[138] Ramani Duraiswami. *The Wave and Helmholtz Equations*. The University of Maryland College Park, February 3, 2006.

[139] Carl Eckart. Vortices and streams caused by sound waves. *Physical review*, 73(1):68, 1948.

[140] Tino Eibner and Jens Markus Melenk. Fast algorithms for setting up the stiffness matrix in hp-fem: a comparison. 2006.

[141] Britannica Online Encyclopedia. *Hydrodynamica*. Britannica Online Encyclopedia, Retrieved 2008-10-30.

[142] Björn Engquist and Andrew Majda. Absorbing boundary conditions for numerical simulation of waves. *Proceedings of the National Academy of Sciences*, 74(5):1765–1766, 1977.

[143] Miloš D Ercegovac and Jean-Michel Muller. Solving systems of linear equations in complex domain: Complex e-method. Technical report, LIP report no, 2007.

[144] Alexandre Ern and Jean-Luc Guermond. Evaluation of the condition number in linear systems arising in finite element approximations. *ESAIM: Mathematical Modelling and Numerical Analysis*, 40(1):29–48, 2006.

[145] L Euler. Principes généraux du mouvement des fluides, acad. roy. sci. belleslett. berlin (1755).

[146] Charbel Farhat, Isaac Harari, and Ulrich Hetmaniuk. A discontinuous galerkin method with lagrange multipliers for the solution of helmholtz problems in the mid-frequency regime. *Computer Methods in Applied Mechanics and Engineering*, 192(11):1389–1419, 2003.

[147] Charbel Farhat, Radek Tezaur, and Paul Weidemann-Goiran. Higher-order extensions of a discontinuous galerkin method for mid-frequency helmholtz problems. *International journal for numerical methods in engineering*, 61(11):1938–1956, 2004.

[148] Xiaobing Feng and Haijun Wu. Discontinuous galerkin methods for the helmholtz equation with large wave number. *SIAM Journal on Numerical Analysis*, 47(4):2872–2896, 2009.

[149] Isaac Fried. *Numerical solution of differential equations*. Academic Press, 2014.

[150] James Friend and Leslie Y Yeo. Microscale acoustofluidics: Microfluidics driven via acoustics and ultrasonics. *Reviews of Modern Physics*, 83(2):647, 2011.

[151] Gwenael Gabard, Pablo Gamallo, and Tomi Huttunen. A comparison of wave-based discontinuous galerkin, ultra-weak and least-square methods for wave problems. *International journal for numerical methods in engineering*, 85(3):380–402, 2011.

[152] Pablo Gamallo and RJ Astley. A comparison of two trefftz-type methods: the ultraweak variational formulation and the least-squares method, for solving shortwave 2-d helmholtz problems. *International journal for numerical methods in engineering*, 71(4):406–432, 2007.

[153] Michael Gedge and Martyn Hill. Acoustofluidics 17: Theory and applications of surface acoustic wave devices for particle manipulation. *Lab on a Chip*, 12(17):2998–3007, 2012.

[154] Al Geist. *PVM: Parallel virtual machine: a users' guide and tutorial for networked parallel computing*. MIT press, 1994.

[155] Jean-Frsedseric Gerbeau and Charbel Farhat. *The Finite Element Method for Fluid Mechanics*. CME 358 - INRIA Paris-Rocquencourt Stanford University, Spring 2009.

[156] K Gerdes and F Ihlenburg. On the pollution effect in fe solutions of the 3d-helmholtz equation. *Computer Methods in Applied Mechanics and Engineering*, 170(1):155–172, 1999.

[157] Christophe Geuzaine and Jean-François Remacle. Gmsh: A 3-d finite element mesh generator with built-in pre-and post-processing facilities. *International journal for numerical methods in engineering*, 79(11):1309–1331, 2009.

[158] Adrianna Gillman, Rabia Djellouli, and Mohamed Amara. A mixed hybrid formulation based on oscillated finite element polynomials for solving helmholtz problems. *Journal of computational and applied mathematics*, 204(2):515–525, 2007.

[159] Dan Givoli and Joseph B Keller. A finite element method for large domains. *Computer Methods in Applied Mechanics and Engineering*, 76(1):41–66, 1989.

[160] Peter Glynne-Jones, Puja P Mishra, Rosemary J Boltryk, and Martyn Hill. Efficient finite element modeling of radiation forces on elastic particles of arbitrary size and geometry. *The Journal of the Acoustical Society of America*, 133(4):1885–1893, 2013.

[161] LP Gor'Kov. On the forces acting on a small particle in an acoustical field in an ideal fluid. In *Soviet Physics Doklady*, volume 6, page 773, 1962.

[162] William Gropp, Ewing Lusk, and Anthony Skjellum. *Using MPI: portable parallel programming with the message-passing interface*, volume 1. MIT press, 1999.

[163] William Gropp, Ewing Lusk, and Rajeev Thakur. *Using MPI-2: Advanced features of the message-passing interface*. MIT press, 1999.

[164] Axel Grundmann and Hans-Michael Möller. Invariant integration formulas for the n-simplex by combinatorial methods. *SIAM Journal on Numerical Analysis*, 15(2):282–290, 1978.

[165] Björn Hammarström, Mikael Evander, Herve Barbeau, Mattias Bruzelius, Jörgen Larsson, Thomas Laurell, and Johan Nilsson. Non-contact acoustic cell trapping in disposable glass capillaries. *Lab on a Chip*, 10(17):2251–2257, 2010.

[166] Isaac Harari and Thomas JR Hughes. Galerkin/least-squares finite element methods for the reduced wave equation with non-reflecting boundary conditions in unbounded domains. *Computer methods in applied mechanics and engineering*, 98(3):411–454, 1992.

[167] ML Harbold and BN Steinberg. Direct experimental verification of creeping waves. *The journal of the Acoustical Society of America*, 45(3):592–603, 1969.

[168] E Hinton and JS Campbell. Local and global smoothing of discontinuous finite element functions using a least squares method. *International Journal for Numerical Methods in Engineering*, 8(3):461–480, 1974.

[169] Ralf Hiptmair, Andrea Moiola, and Ilaria Perugia. A survey of trefftz methods for the helmholtz equation. In *Building Bridges: Connections and Challenges in Modern Approaches to Numerical Partial Differential Equations*, pages 237–278. Springer, 2016.

[170] MJ Holmes, NG Parker, and MJW Povey. Temperature dependence of bulk viscosity in water using acoustic spectroscopy. In *Journal of Physics: Conference Series*, volume 269, page 012011. IOP Publishing, 2011.

[171] AF Horadam. Gegenbauer polynomials revisited. *Fibonacci Quart*, 23:294–299, 1985.

[172] Jacqueline Sanchez Hubert. *Vibration and coupling of continuous systems: asymptotic methods*. Springer Science & Business Media, 2012.

[173] Kenneth H Huebner, Donald L Dewhirst, Doughlas E Smith, and Ted G Byrom. *The finite element method for engineers*. John Wiley & Sons, 2008.

[174] Thomas JR Hughes, Leopoldo P Franca, and Gregory M Hulbert. A new finite element formulation for computational fluid dynamics: Viii. the galerkin/least-squares method for advective-diffusive equations. *Computer Methods in Applied Mechanics and Engineering*, 73(2):173–189, 1989.

[175] T Huttunen, JP Kaipio, and P Monk. An ultra-weak method for acoustic fluid–solid interaction. *Journal of Computational and Applied Mathematics*, 213(1):166–185, 2008.

[176] Tomi Huttunen, Pablo Gamallo, and R Jeremy Astley. Comparison of two wave element methods for the helmholtz problem. *International Journal for Numerical Methods in Biomedical Engineering*, 25(1):35–52, 2009.

[177] Tomi Huttunen, Jari P Kaipio, and Peter Monk. The perfectly matched layer for the ultra weak variational formulation of the 3d helmholtz equation. *International Journal for Numerical Methods in Engineering*, 61(7):1072–1092, 2004.

[178] Tomi Huttunen, Peter Monk, and Jari P Kaipio. Computational aspects of the ultra-weak variational formulation. *Journal of Computational Physics*, 182(1):27–46, 2002.

[179] F Ihlenburg, I Babuska, and S Sauter. Reliability of finite element methods for the numerical computation of waves. *Advances in Engineering Software*, 28(7):417–424, 1997.

[180] Frank Ihlenburg. *Finite element analysis of acoustic scattering*, volume 132. Springer Science & Business Media, 2006.

[181] Frank Ihlenburg and Ivo Babuška. Dispersion analysis and error estimation of galerkin finite element methods for the helmholtz equation. *International journal for numerical methods in engineering*, 38(22):3745–3774, 1995.

[182] Frank Ihlenburg and Ivo Babuška. Finite element solution of the helmholtz equation with high wave number part i: The h-version of the fem. *Computers & Mathematics with Applications*, 30(9):9–37, 1995.

[183] Frank Ihlenburg and Ivo Babuska. Finite element solution of the helmholtz equation with high wave number part ii: the hp version of the fem. *SIAM Journal on Numerical Analysis*, 34(1):315–358, 1997.

[184] Simona Irimie and Ph Bouillard. A residual a posteriori error estimator for the finite element solution of the helmholtz equation. *Computer methods in applied mechanics and engineering*, 190(31):4027–4042, 2001.

[185] Arieh Iserles. On the numerical quadrature of highly-oscillating integrals ii: Irregular oscillators. *IMA journal of numerical analysis*, 25(1):25–44, 2005.

[186] Arieh Iserles and Syvert P Nørsett. On quadrature methods for highly oscillatory integrals and their implementation. *BIT Numerical Mathematics*, 44(4):755–772, 2004.

[187] Mads JH Jensen, Jonas T Karlsen, and Henrik Bruus. Theory and simulation of the acoustic radiation force on a single microparticle in an ultrasonic standing wave including thermoviscous effects.

[188] ZJ Jiao, XY Huang, and Nam-Trung Nguyen. Scattering and attenuation of surface acoustic waves in droplet actuation. *Journal of Physics A: Mathematical and Theoretical*, 41(35):355502, 2008.

[189] PK Jimack and N Touheed. Developing parallel finite element software using mpi. *High Performance Computing for Computational Mechanics*, pages 15–38, 2000.

[190] Lukasz Kaczmarczyk. Mesh oriented finite element method. *http://userweb.eng.gla.ac.uk/lukasz.kaczmarczyk/MoFem/html/index.html*, Cephas, Accessed in 2013.

[191] George Karypis, Kirk Schloegel, and Vipin Kumar. Parmetis: Parallel graph partitioning and sparse matrix ordering library. *Version 1.0, Dept. of Computer Science, University of Minnesota*, 1997.

[192] Riyad Kechroud, Azzeddine Soulaimani, and Yousef Saad. Preconditionning techniques for the solution of the helmholtz equation by the finite element method. In *Computational Science and Its Applications—ICCSA 2003*, pages 847–858. Springer, 2003.

[193] Joseph B Keller and Dan Givoli. Exact non-reflecting boundary conditions. *Journal of computational physics*, 82(1):172–192, 1989.

[194] Louis V King. On the acoustic radiation pressure on spheres. In *Proceedings of the Royal Society of London A: Mathematical, Physical and Engineering Sciences*, volume 147, pages 212–240. The Royal Society, 1934.

[195] Kai Knoerzer, Pablo Juliano, Peter Roupas, and Cornelis Versteeg. *Innovative food processing technologies: advances in multiphysics simulation*. John Wiley & Sons, 2011.

[196] Daniel Köster. Numerical simulation of acoustic streaming on saw-driven biochips. ,, 2006.

[197] Daniel Köster. Numerical simulation of acoustic streaming on surface acoustic wave-driven biochips. *SIAM Journal on Scientific Computing*, 29(6):2352–2380, 2007.

[198] Michal Křížek and Pekka Neittaanmäki. On superconvergence techniques. *Acta Applicandae Mathematica*, 9(3):175–198, 1987.

[199] K. Lewandowski Xuan Meng Xiao-Yi Zhou Chris Pearce L. Kaczmarczyk, Z. Ullah. Mofem-v0.5.42, March 2017. http://mofem.eng.gla.ac.uk/mofem/html/.

[200] P Ladeveze, J-P Pelle, and Ph Rougeot. Error estimation and mesh optimization for classical finite elements. *Engineering Computations*, 8(1):69–80, 1991.

[201] O Laghrouche, P Bettess, E Perrey-Debain, and J Trevelyan. Plane wave basis finite-elements for wave scattering in three dimensions. *International Journal for Numerical Methods in Biomedical Engineering*, 19(9):715–723, 2003.

[202] O Laghrouche, P Bettess, E Perrey-Debain, and J Trevelyan. Wave interpolation finite elements for helmholtz problems with jumps in the wave speed. *Computer methods in applied mechanics and engineering*, 194(2):367–381, 2005.

[203] Omar Laghrouche, P Bettess, and RJ Astley. Modelling of short wave diffraction problems using approximating systems of plane waves. *International Journal for Numerical Methods in Engineering*, 54(10):1501–1533, 2002.

[204] Omar Laghrouche and PETER BETTESS. Short wave modelling using special finite elements. *Journal of Computational Acoustics*, 8(01):189–210, 2000.

[205] Omar Laghrouche, Peter Bettess, Emmanuel Perrey-Debain, and Jon Trevelyan. Wave interpolation finite elements for helmholtz problems with jumps in the wave speed. *Computer methods in applied mechanics and engineering*, 194(2):367–381, 2005.

[206] Omar Laghrouche, A El-Kacimi, and Jon Trevelyan. A comparison of nr-bcs for pufem in 2d helmholtz problems at high wave numbers. *Journal of Computational and Applied Mathematics*, 234(6):1670–1677, 2010.

[207] Omar Laghrouche and M Shadi Mohamed. Locally enriched finite elements for the helmholtz equation in two dimensions. *Computers & structures*, 88(23):1469–1473, 2010.

[208] S Langdon and SN Chandler-Wilde. Finite element methods for acoustic scattering. 2007.

[209] Bernard Le Mehaute. *An introduction to hydrodynamics and water waves*. Springer Science & Business Media, 2013.

[210] Paul H LeBlond and Lawrence A Mysak. *Waves in the Ocean*. Elsevier, 1981.

[211] Rolf Leis. *Initial boundary value problems in mathematical physics*. Courier Corporation, 2013.

[212] Huiyuan Li, Jiachang Sun, and Yuan Xu. Discrete fourier analysis, cubature, and interpolation on a hexagon and a triangle. *SIAM Journal on Numerical Analysis*, 46(4):1653–1681, 2008.

[213] Jörg Liesen and Zdenek Strakos. *Krylov subspace methods: principles and analysis*. Oxford University Press, 2013.

[214] Alice Lieu, Gwénaël Gabard, and Hadrien Bériot. A comparison of high-order polynomial and wave-based methods for helmholtz problems. *Journal of Computational Physics*, 321:105–125, 2016.

[215] James Lighthill. The fourth annual fairey lecture: The propagation of sound through moving fluids. *Journal of Sound and Vibration*, 24(4):471–492, 1972.

[216] James Lighthill. Acoustic streaming. *Journal of sound and vibration*, 61(3):391–418, 1978.

[217] Michael J Lighthill. On sound generated aerodynamically. ii. turbulence as a source of sound. *Proceedings of the Royal Society of London. Series A, Mathematical and Physical Sciences*, pages 1–32, 1954.

[218] Jacques Louis Lions and Enrico Magenes. *Non-homogeneous boundary value problems and applications*, volume 1. Springer Science & Business Media, 2012.

[219] MJ LlGHTHIll. On sound generated aerodynamically. i. *General Theory. Proc. Roy. Soc., ser. A*, 211:564–587, 1952.

[220] Daniel SH Lo. *Finite element mesh generation*. CRC Press, 2014.

[221] OpenCFD Ltd. *OpenFOAM user guide Version 1.5 Edition*. OpenCFD Ltd, 2008.

[222] JK Luo, YQ Fu, and WI Milne. Acoustic wave based microfluidics and lab-on-a-chip. 2013.

[223] T Luostari, T Huttunen, and P Monk. Improvements for the ultra weak variational formulation. *International Journal for Numerical Methods in Engineering*, 94(6):598–624, 2013.

[224] Ernst Mach. *The science of mechanics: A critical and historical account of its development*. Open court publishing Company, 1907.

[225] Ross JD Mackenzie. *A computational framework for modelling micro-scale fluids in the presence of surface tension*. PhD thesis, University of Glasgow, 2015.

[226] RJ Mackinnon and GF Carey. Superconvergent derivatives: A taylor series analysis. *International Journal for Numerical Methods in Engineering*, 28(3):489–509, 1989.

[227] M Made. Performance of parallel incomplete ldlt factorizations for solving acoustic wave propagation problems from industry. *Numerical linear algebra with applications*, 11(8-9):813–830, 2004.

[228] Arwind S Marathay. Fourier transform of the green's function for the helmholtz equation. *JOSA*, 65(8):964–965, 1975.

[229] Philip L Marston. Scattering of acoustic evanescent waves by circular cylinders: Partial wave series solution. *The Journal of the Acoustical Society of America*, 111(5):2378–2378, 2002.

[230] Vladimir Maz'ya. *Sobolev spaces*. Springer, 2013.

[231] John V McNicholas and H Überall. Creeping-wave theory and experiment. *The Journal of the Acoustical Society of America*, 46(3B):827–828, 1969.

[232] Jens M Melenk and Ivo Babuška. The partition of unity finite element method: basic theory and applications. *Computer methods in applied mechanics and engineering*, 139(1-4):289–314, 1996.

[233] William F Mitchell. A comparison of adaptive refinement techniques for elliptic problems. *ACM Transactions on Mathematical Software (TOMS)*, 15(4):326–347, 1989.

[234] DA Mitsoudis and M Plexousakis. A finite element method with nonlocal boundary conditions for the helmholtz equation with complex wavenumber in stratified waveguides. *Acta Acustica United with Acustica*, 95(4):753–756, 2009.

[235] Andrea Moiola and Euan A Spence. Is the helmholtz equation really sign-indefinite? *Siam Review*, 56(2):274–312, 2014.

[236] PETER Monk and Da-Qing Wang. A least-squares method for the helmholtz equation. *Computer Methods in Applied Mechanics and Engineering*, 175(1-2):121–136, 1999.

[237] SE Mousavi and N Sukumar. Generalized duffy transformation for integrating vertex singularities. *Computational Mechanics*, 45(2-3):127–140, 2010.

[238] A Müller, A Darga, and A Wixforth. Surface acoustic wave studies for chemical and biological sensors. *Nanoscale Devices-Fundamentals and Applications*, pages 3–13, 2006.

[239] Peter Barkholt Muller, Rune Barnkob, Mads Jakob Herring Jensen, and Henrik Bruus. A numerical study of microparticle acoustophoresis driven by acoustic radiation forces and streaming-induced drag forces. *Lab on a Chip*, 12(22):4617–4627, 2012.

[240] Nitesh Nama, Rune Barnkob, Zhangming Mao, Christian J Kähler, Francesco Costanzo, and Tony Jun Huang. Numerical study of acoustophoretic motion of particles in a pdms microchannel driven by surface acoustic waves. *Lab on a Chip*, 2015.

[241] Sergey Nazarov and Boris A Plamenevsky. *Elliptic problems in domains with piecewise smooth boundaries*, volume 13. Walter de Gruyter, 1994.

[242] Nam-Trung Nguyen, Audra H Meng, Justin Black, and Richard M White. Integrated flow sensor for in situ measurement and control of acoustic streaming in flexural plate wave micropumps. *Sensors and Actuators A: Physical*, 79(2):115–121, 2000.

[243] Nam-Trung Nguyen and Richard M White. Acoustic streaming in micromachined flexural plate wave devices: numerical simulation and experimental verification. *IEEE transactions on ultrasonics, ferroelectrics, and frequency control*, 47(6):1463–1471, 2000.

[244] Gennadiy P Nikishkov. *Programming Finite Elements in Java^{TM}*. Springer Science & Business Media, 2010.

[245] Oldrich Novotny. *Seismic Surface wave*. 1999.

[246] Wesley L Nyborg. Acoustic streaming due to attenuated plane waves. *The journal of the acoustical society of America*, 25(1):68–75, 1953.

[247] Assad A Oberai and Peter M Pinsky. A residual-based finite element method for the helmholtz equation. *International Journal for Numerical Methods in Engineering*, 49(3):399–419, 2000.

[248] J Tinsley Oden and Leszek Demkowicz. *Applied functional analysis*. CRC press, 2010.

[249] J Tinsley Oden, Serge Prudhomme, and Leszek Demkowicz. A posteriori error estimation for acoustic wave propagation problems. *Archives of Computational Methods in Engineering*, 12(4):343–389, 2005.

[250] J Tinsley Oden, Weihan Wu, and Mark Ainsworth. An a posteriori error estimate for finite element approximations of the navier-stokes equations. *Computer Methods in Applied Mechanics and Engineering*, 111(1-2):185–202, 1994.

[251] Haekwan Oh, Sangsik Yang, and Keekeun Lee. Development of surface acoustic wave-based microgyroscope utilizing progressive wave. *Japanese Journal of Applied Physics*, 49(6S):06GN16, 2010.

[252] E Perrey-Debain, O Laghrouche, P Bettess, and J Trevelyan. Plane-wave basis finite elements and boundary elements for three-dimensional wave scattering. *Philosophical Transactions of the Royal Society of London A: Mathematical, Physical and Engineering Sciences*, 362(1816):561–577, 2004.

[253] Steffen Petersen, Daniel Dreyer, and Otto von Estorff. Assessment of finite and spectral element shape functions for efficient iterative simulations of interior acoustics. *Computer methods in applied mechanics and engineering*, 195(44):6463–6478, 2006.

[254] N Anders Petersson, Ossian O'Reilly, Björn Sjögreen, and Samuel Bydlon. Discretizing singular point sources in hyperbolic wave propagation problems. *Journal of Computational Physics*, 321:532–555, 2016.

[255] David Soares Pinto Júnior. Studies on barlow points, gauss points and superconvergent points in 1d with lagrangian and hermitian finite element basis. *Computational & Applied Mathematics*, 27(3):275–303, 2008.

[256] Albert Prinn. *Efficient finite element methods for aircraft engine noise prediction*. PhD thesis, University of Southampton, 2014.

[257] Natalya Privorotskaya, Yi-Shao Liu, Jungchul Lee, Hongjun Zeng, John A Carlisle, Adarsh Radadia, Larry Millet, Rashid Bashir, and William P King. Rapid thermal lysis of cells using silicon–diamond microcantilever heaters. *Lab on a Chip*, 10(9):1135–1141, 2010.

[258] Aisha Qi, Leslie Y Yeo, and James R Friend. Interfacial destabilization and atomization driven by surface acoustic waves. *Physics of Fluids*, 20(7):074103, 2008.

[259] Alfio Quarteroni and Alberto Valli. *Numerical approximation of partial differential equations*, volume 23. Springer Science & Business Media, 2008.

[260] R Quintero and F Simonetti. Rayleigh wave scattering from sessile droplets. *Physical Review E*, 88(4):043011, 2013.

[261] Itzala Rabadan Malda, Emigdio Salazar Cordero, and Jose Angel Ortega Herrera. Petrov–galerkin's method hybrid with finite element into the helmholtz equation solution. part i. *The Journal of the Acoustical Society of America*, 112(5):2218–2218, 2002.

[262] M Rahman and T Michelitsch. A note on the formula for the rayleigh wave speed. *Wave Motion*, 43(3):272–276, 2006.

[263] RW Rambach, J Taiber, CML Scheck, C Meyer, J Reboud, JM Cooper, and T Franke. Visualization of surface acoustic waves in thin liquid films. *Scientific reports*, 6, 2016.

[264] Robert H Randall. *An introduction to acoustics*. Courier Corporation, 2012.

[265] Rolf Rannacher and Ridgway Scott. Some optimal error estimates for piecewise linear finite element approximations. *mathematics of computation*, 38(158):437–445, 1982.

[266] HT Rathod, B Venkatesudu, and KV Nagaraja. Gauss legendre quadrature formulas over a tetrahedron. *Numerical Methods for Partial Differential Equations*, 22(1):197–219, 2006.

[267] Thomas Rauber and Gudula Rünger. *Parallel programming: For multicore and cluster systems*. Springer Science & Business Media, 2013.

[268] Lord Rayleigh. On the circulation of air observed in kundt's tubes, and on some allied acoustical problems. *Philosophical Transactions of the Royal Society of London*, 175:1–21, 1884.

[269] Lord Rayleigh. On waves propagated along the plane surface of an elastic solid. *Proceedings of the London Mathematical Society*, 1(1):4–11, 1885.

[270] Julien Reboud, Yannyk Bourquin, Rab Wilson, Gurman S Pall, Meesbah Jiwaji, Andrew R Pitt, Anne Graham, Andrew P Waters, and Jonathan M Cooper. Shaping acoustic fields as a toolset for microfluidic manipulations in diagnostic technologies. *Proceedings of the National Academy of Sciences*, 109(38):15162–15167, 2012.

[271] A Renaudin, P Tabourier, V Zhang, JC Camart, and C Druon. Saw nanopump for handling droplets in view of biological applications. *Sensors and Actuators B: Chemical*, 113(1):389–397, 2006.

[272] Osborne Reynolds. An experimental investigation of the circumstances which determine whether the motion of water shall be direct or sinuous, and of the law of resistance in parallel channels. *Proceedings of the royal society of London*, 35(224-226):84–99, 1883.

[273] Osborne Reynolds. On the dynamical theory of incompressible viscous fluids and the determination of the criterion. *Philosophical Transactions of the Royal Society of London. A Vol. 186 (1895), pp. 123-164*, 1895.

[274] Antoine Riaud, Michael Baudoin, Oliver Bou Matar, Jean-Louis Thomas, and Philippe Brunet. Influence of viscosity on acoustic streaming in sessile droplets: an experimental and a numerical study with a streaming source spatial filtering (sssf) method. *arXiv preprint arXiv:1605.03762*, 2016.

[275] Béatrice Rivière, Mary F Wheeler, and Vivette Girault. A priori error estimates for finite element methods based on discontinuous approximation spaces for elliptic problems. *SIAM Journal on Numerical Analysis*, 39(3):902–931, 2001.

[276] W Lewis Roland, PERUMAL Nithiarasu, and KN Seetharamu. Fundamentals of the finite element method for heat and fluid flow, 2004.

[277] MP Rossow and IN Katz. Hierarchal finite elements and precomputed arrays. *International Journal for Numerical Methods in Engineering*, 12(6):977–999, 1978.

[278] Daniel Royer and Eugene Dieulesaint. *Elastic waves in solids II: generation, acousto-optic interaction, applications*. Springer Science & Business Media, 1999.

[279] Daniel Royer and Eugène Dieulesaint. Elastic waves in solids i: Free and guided propagation, translated by dp morgan. *Springer-Verlag, New York*, 2000.

[280] Yousef Saad. *Iterative methods for sparse linear systems*. SIAM, 2003.

[281] Bahaa EA Saleh, Malvin Carl Teich, and Bahaa E Saleh. *Fundamentals of photonics*, volume 22. Wiley New York, 1991.

[282] Subramanian KRS Sankaranarayanan and Venkat R Bhethanabotla. Numerical analysis of wave generation and propagation in a focused surface acoustic wave device for potential microfluidics applications. *Ultrasonics, Ferroelectrics, and Frequency Control, IEEE Transactions on*, 56(3):631–643, 2009.

[283] Subramanian KRS Sankaranarayanan, Stefan Cular, Venkat R Bhethanabotla, and Babu Joseph. Flow induced by acoustic streaming on surface-acoustic-wave devices and its application in biofouling removal: A computational study and comparisons to experiment. *Physical Review E*, 77(6):066308, 2008.

[284] Michael Schindler, Peter Talkner, and Peter Hänggi. Computing stationary free-surface shapes in microfluidics. *Physics of Fluids*, 18(10):103303, 2006.

[285] Lothar Schmid, David A Weitz, and Thomas Franke. Sorting drops and cells with acoustics: acoustic microfluidic fluorescence-activated cell sorter. *Lab on a Chip*, 14(19):3710–3718, 2014.

[286] Christoph T Schröder and Waymond R Scott Jr. On the complex conjugate roots of the rayleigh equation: The leaky surface wave. *The Journal of the Acoustical Society of America*, 110(6):2867–2877, 2001.

[287] G Schuster. Basic principles of wave propagation, 2011.

[288] Christoph Schwarzbach, Ralph-Uwe Börner, and Klaus Spitzer. Three-dimensional adaptive higher order finite element simulation for geo-electromagnetics—a marine csem example. *Geophysical Journal International*, 187(1):63–74, 2011.

[289] Mikkel Settnes and Henrik Bruus. Forces acting on a small particle in an acoustical field in a viscous fluid. *Physical Review E*, 85(1):016327, 2012.

[290] R Sevilla, S Fernández-Méndez, and A Huerta. Nurbs-enhanced finite element method. In *ECCOMAS CFD 2006: Proceedings of the European Conference on Computational Fluid Dynamics, Egmond aan Zee, The Netherlands, September 5-8, 2006*. Delft University of Technology; European Community on Computational Methods in Applied Sciences (ECCOMAS), 2006.

[291] S Shiokawa, Y Matsui, and T Ueda. Liquid streaming and droplet formation caused by leaky rayleigh waves. In *Ultrasonics Symposium, 1989. Proceedings., IEEE 1989*, pages 643–646. IEEE, 1989.

[292] Showko Shiokawa, Yoshikazu Matsui, and Toshihiko Ueda. Study on saw streaming and its application to fluid devices. *Japanese journal of applied physics*, 29(S1):137, 1990.

[293] Robert N Simpson, Michael A Scott, Matthias Taus, Derek C Thomas, and Haojie Lian. Acoustic isogeometric boundary element analysis. *Computer Methods in Applied Mechanics and Engineering*, 269:265–290, 2014.

[294] H Slim. An introduction to parallel programming, guide 48, version: 2.0. *Durham University, Durham, available at: www. dur. ac. uk/resources/its/info/guides/48ParallelProg. pdf (accessed 2 January 2013)*, 2010.

[295] Pavel Solin, Karel Segeth, and Ivo Dolezel. *Higher-order finite element methods*. CRC Press, 2003.

[296] Pavel Solin, Karel Segeth, and Ivo Dolezel. *Higher-order finite element methods*. CRC Press, 2003.

[297] Helen Song, Delai L Chen, and Rustem F Ismagilov. Reactions in droplets in microfluidic channels. *Angewandte chemie international edition*, 45(44):7336–7356, 2006.

[298] EA Spence. When all else fails, integrate by parts. *an overview of new and old variational formulations for linear elliptic PDEs, to appear in Unified Transform for Boundary Value Problems: Applications and Advances, AS Fokas and B. Pelloni, eds., SIAM*, 2014.

[299] CJ Strobl, A Rathgeber, A Wixforth, C Gauer, and J Scriba. Planar microfluidic processors. In *Ultrasonics Symposium, 2002. Proceedings. 2002 IEEE*, volume 1, pages 255–258. IEEE, 2002.

[300] Theofanis Strouboulis, Ivo Babuška, and Realino Hidajat. The generalized finite element method for helmholtz equation: theory, computation, and open problems. *Computer Methods in Applied Mechanics and Engineering*, 195(37):4711–4731, 2006.

[301] Theofanis Strouboulis, Realino Hidajat, and Ivo Babuška. The generalized finite element method for helmholtz equation. part ii: Effect of choice of handbook functions, error due to absorbing boundary conditions and its assessment. *Computer Methods in Applied Mechanics and Engineering*, 197(5):364–380, 2008.

[302] BA Szabo, PK Basu, DA Dunavant, and D Vasilopoulos. Adaptive finite element technology in integrated design and analysis. *Center for Computational Mechanics, Report WU/CCM-8*, 1(1), 1981.

[303] Barna A Szabo. Estimation and control error based on p-convergence. Technical report, WASHINGTON UNIV ST LOUIS MO CENTER FOR COMPUTATIONAL MECHANICS, 1984.

[304] Barna Aladar Szabo and Ivo BabuÂška. *Finite element analysis*. John Wiley & Sons, 1991.

[305] Ming K Tan, James R Friend, Omar K Matar, and Leslie Y Yeo. Capillary wave motion excited by high frequency surface acoustic waves. *Physics of Fluids*, 22(11):112112, 2010.

[306] Ming K Tan, James R Friend, and Leslie Y Yeo. Interfacial jetting phenomena induced by focused surface vibrations. *Physical Review Letters*, 103(2):024501, 2009.

[307] Timothy J Tautges. Canonical numbering systems for finite-element codes. *International Journal for Numerical Methods in Biomedical Engineering*, 26(12):1559–1572, 2010.

[308] Timothy James Tautges, Corey Ernst, Clint Stimpson, Ray J Meyers, and Karl Merkley. Moab: a mesh-oriented database. Technical report, Sandia National Laboratories, 2004.

[309] Douglas J Taylor. Evaluation of singular electric field integral equation (efie) matrix elements. Technical report, DTIC Document, 2001.

[310] Mark A Taylor, Beth A Wingate, and Len P Bos. A cardinal function algorithm for computing multivariate quadrature points. *SIAM Journal on Numerical Analysis*, 45(1):193–205, 2007.

[311] Radek Tezaur and Charbel Farhat. Three-dimensional discontinuous galerkin elements with plane waves and lagrange multipliers for the solution of mid-frequency helmholtz problems. *International journal for numerical methods in engineering*, 66(5):796–815, 2006.

[312] Radek Tezaur, Antonini Macedo, Charbel Farhat, and Rabia Djellouli. Three-dimensional finite element calculations in acoustic scattering using arbitrarily shaped convex artificial boundaries. *International Journal for Numerical Methods in Engineering*, 53(6):1461–1476, 2002.

[313] Lonny L Thompson and Peter M Pinsky. A galerkin least-squares finite element method for the two-dimensional helmholtz equation. *International Journal for numerical methods in engineering*, 38(3):371–397, 1995.

[314] Lony L Thompson and Peter M Pinsky. Complex wavenumber fourier analysis of the p-version finite element method. *Computational Mechanics*, 13(4):255–275, 1994.

[315] Thomas Toulorge, Christophe Geuzaine, Jean-François Remacle, and Jonathan Lambrechts. Robust untangling of curvilinear meshes. *Journal of Computational Physics*, 254:8–26, 2013.

[316] Eli Turkel, Charbel Farhat, and Ulrich Hetmaniuk. Improved accuracy for the helmholtz equation in unbounded domains. *International journal for numerical methods in engineering*, 59(15):1963–1988, 2004.

[317] Zahur Ullah. *Nonlinear solid mechanics analysis using the parallel selective element-free Galerkin method*. Durham theses. Durham University, 2013.

[318] Zahur Ullah, SA Grammatikos, MC Evernden, CJ Pearce, et al. Multi-scale computational homogenisation to predict the long-term durability of composite structures. *Computers & Structures*, 181:21–31, 2017.

[319] Thiti Vacharasintopchai. *A parallel implementation of the element-free Galerkin method on a network of PCs*. PhD thesis, Asian Institute of Technology, 2000.

[320] J Vanneste and O Bühler. Streaming by leaky surface acoustic waves. In *Proceedings of the Royal Society of London A: Mathematical, Physical and Engineering Sciences*, volume 467, pages 1779–1800. The Royal Society, 2011.

[321] Rüdiger Verfürth. A posteriori error estimators for the stokes equations. *Numerische Mathematik*, 55(3):309–325, 1989.

[322] Rüdiger Verfürth. A posteriori error estimation and adaptive mesh-refinement techniques. *Journal of Computational and Applied Mathematics*, 50(1-3):67–83, 1994.

[323] Pham Chi Vinh. Scholte-wave velocity formulae. *Wave Motion*, 50(2):180–190, 2013.

[324] O von Estorff, D Dreyer, and S Petersen. An efficient finite element-infinite element method for exterior acoustics simulation. *Proceedings of WCCM VI, Tsinghua University Press/Springer-Verlag, Beijing*, 2004.

[325] Peter EJ Vos, Spencer J Sherwin, and Robert M Kirby. From h to p efficiently: Implementing finite and spectral/hp element methods to achieve optimal performance for low-and high-order discretisations. *Journal of Computational Physics*, 229(13):5161–5181, 2010.

[326] Lars B Wahlbin. *Superconvergence in Galerkin finite element methods*. Springer, 1995.

[327] Dalei Wang, Radek Tezaur, Jari Toivanen, and Charbel Farhat. Overview of the discontinuous enrichment method, the ultra-weak variational formulation, and the partition of unity method for acoustic scattering in the medium frequency regime and performance comparisons. *International Journal for Numerical Methods in Engineering*, 89(4):403–417, 2012.

[328] Mary Fanett Wheeler. A priori l_2 error estimates for galerkin approximations to parabolic partial differential equations. *SIAM Journal on Numerical Analysis*, 10(4):723–759, 1973.

[329] MF Wheeler and JR Whiteman. Superconvergent recovery of gradients on subdomains from piecewise linear finite-element approximations. *Numerical methods for partial differential equations*, 3(1):65–82, 1987.

[330] Achim Wixforth. Acoustically driven planar microfluidics. *Superlattices and Microstructures*, 33(5):389–396, 2003.

[331] Achim Wixforth, Christoph Strobl, Ch Gauer, A Toegl, J Scriba, and Z v Guttenberg. Acoustic manipulation of small droplets. *Analytical and bioanalytical chemistry*, 379(7-8):982–991, 2004.

[332] WJ Xie, CD Cao, YJ Lü, ZY Hong, and B Wei. Acoustic method for levitation of small living animals. *Applied Physics Letters*, 89(21):214102, 2006.

[333] G Yagawa, G-W Ye, and S Yoshimura. A numerical integration scheme for finite element method based on symbolic manipulation. *International journal for numerical methods in engineering*, 29(7):1539–1549, 1990.

[334] Paul Yager, Gonzalo J Domingo, and John Gerdes. Point-of-care diagnostics for global health. *Annu. Rev. Biomed. Eng.*, 10:107–144, 2008.

[335] Leslie Y Yeo and James R Friend. Ultrafast microfluidics using surface acoustic waves. *Biomicrofluidics*, 3(1):012002, 2009.

[336] John Zehnpfennig, Gaurav Bahl, Matthew Tomes, and Tal Carmon. Surface optomechanics: Calculating optically excited acoustical whispering gallery modes in microspheres. *Optics Express*, 19(15):14240–14248, 2011.

[337] Fuzhen Zhang. *The Schur complement and its applications*, volume 4. Springer Science & Business Media, 2006.

[338] Linbo Zhang, Tao Cui, Hui Liu, et al. A set of symmetric quadrature rules on triangles and tetrahedra. *J. Comput. Math*, 27(1):89–96, 2009.

[339] Pengfei Zhu and Junhui Hu. Fem analyses of acoustic streaming in a water droplet at the center of an ultrasonic stage. In *Piezoelectricity, Acoustic Waves, and Device Applications (SPAWDA), 2014 Symposium on*, pages 146–149. IEEE, 2014.

[340] OC Zienkiewicz and JZ Zhu. The superconvergent patch recovery (spr) and adaptive finite element refinement. *Computer Methods in Applied Mechanics and Engineering*, 101(1):207–224, 1992.

[341] OC Zienkiewicz and JZ Zhu. Superconvergence and the superconvergent patch recovery. *Finite elements in analysis and design*, 19(1):11–23, 1995.

[342] OC Zienkiewicz, JZ Zhu, and NG Gong. Effective and practical h–p-version adaptive analysis procedures for the finite element method. *International Journal for Numerical Methods in Engineering*, 28(4):879–891, 1989.

[343] Olgierd C Zienkiewicz and Jian Z Zhu. A simple error estimator and adaptive procedure for practical engineerng analysis. *International Journal for Numerical Methods in Engineering*, 24(2):337–357, 1987.

[344] Olgierd Cecil Zienkiewicz and Robert Leroy Taylor. The finite element method, vol. 1, 1989.

[345] Olgierd Cecil Zienkiewicz and Jian Zhong Zhu. The superconvergent patch recovery and a posteriori error estimates. part 1: The recovery technique. *International Journal for Numerical Methods in Engineering*, 33(7):1331–1364, 1992.

[346] Olgierd Cecil Zienkiewicz and Jian Zhong Zhu. The superconvergent patch recovery and a posteriori error estimates. part 2: Error estimates and adaptivity. *International Journal for Numerical Methods in Engineering*, 33(7):1365–1382, 1992.

[347] Jeff Zitelli, Ignacio Muga, Leszek Demkowicz, Jayadeep Gopalakrishnan, David Pardo, and Victor M Calo. A class of discontinuous petrov–galerkin methods. part iv: The optimal test norm and time-harmonic wave propagation in 1d. *Journal of Computational Physics*, 230(7):2406–2432, 2011.

[348] Gerhard W Zumbusch. *Symmetric hierarchical polynomials for the hp-version of finite elements*. Konrad-Zuse-Zentrum für Informationstechnik Berlin [ZIB], 1993.